Bimetallic Branched Nanoparticles with a Tunable Branch Number, Surface Facets and Composition for Enhanced Oxygen Evolution Reaction Electrocatalysts

By
Munkhshur Myekhlai

UNSW
SYDNEY

A thesis in fulfilment of the requirements for the degree of
Doctor of Philosophy

School of Chemistry
Faculty of Science
The University of New South Wales
August 2021

Thesis/Dissertation Sheet

Surname/Family Name	**: Myekhlai**
Given Name/s	**: Munkhshur**
Abbreviation for degree as give in the University calendar	**: PhD**
Faculty	**: Science**
School	**: Chemistry**
Thesis Title	**: Bimetallic Branched Nanoparticles with a Tunable Branch Number, Surface Facets and Composition for Enhanced Oxygen Evolution Reaction Electrocatalysts**

Abstract

The electrochemical water splitting reaction, which consists of hydrogen reduction at the cathode and oxygen evolution (OER) at the anode, is one of the core processes for the utilization of sustainable and green energy sources. However, the sluggish kinetics of the oxygen evolution reaction requires a higher overpotential than the theoretical potential (1.23 V). Engineering a high-performance electrocatalyst is an avenue to improve the reaction kinetics for OER. Bimetallic branched nanoparticles offer substantial benefits for OER electrocatalysts; which include a greatly increased exposed surface area, highly crystalline *hcp* branches and stable surfaces. This thesis aims to design branched nanoparticles as electrocatalysts for enhanced OER in the following ways: (i) extending the cubic-core hexagonal-branch growth approach for a new bimetallic (Co, Au) system, (ii) leveraging the advantages of the Ru-Pd branched nanoparticles by tuning the surface facets and branch number, and (iii) making branched nanoparticles consisting of a cubic core (Pd) and alloyed branches (RuCo).

Chapter one discusses the literature on the oxygen evolution reaction and Co- and Ru-based electrocatalysts for OER as well as the organic solution-phase synthesis method. The limiting factors of Co- and Ru- based catalysts and the strategies for improving their catalytic performance are also summarized. Also outlined is the fundamental understanding for synthesizing metallic nanoparticles using a seed-mediated growth approach in an organic solution phase and controlling the shape and size of the final products. Chapter two describes the synthetic methodology, sample purification, ink preparation for electrochemical measurements and characterization techniques in more detail. Chapter three provides the synthetic approaches and challenges in making Co and Ru branched nanoparticles. Chapter four compares the OER catalytic activity and stability of the Co-Au branched nanoparticles with the Co-Au core-shell and Co_3O_4 nanoparticles in alkaline media. The improved catalytic performance of the branched nanoparticles can be attributed to the formation of an active and stable oxide layer on the branch surface. Chapter five investigates the effect of branch number, and surface facets on the catalytic properties of the Ru-Pd branched nanoparticles with tunable branch number and surface facets. It is found that tuning surface facets and branch length is essential for enhancing catalytic performance by increasing the exposure of more active sites and improving the accessibility of the catalytic surface to the catalytic reaction. Chapter six explores alloyed branched nanoparticles consisting of a Pd core and RuCo branches and assesses their catalytic activity for OER electrocatalysts. It is demonstrated that Co leaching during catalytic activation in acid solution increases the exposure of highly catalytically active sites on the branch surface resulting in enhanced catalytic activity. Chapter seven concludes the overall results and achievements of this thesis and also discusses future opportunities.

COPYRIGHT STATEMENT

Signed ……

Date ……...

AUTHENTICITY STATEMENT

‘I certify that the Library deposit digital copy is a direct equivalent of the final officially approved version of my thesis.’

Signed ……

Date ……..

ORIGINALITY STATEMENT

'I hereby declare that this submission is my own work and to the best of my knowledge it contains no materials previously published or written by another person, or substantial proportions of material which have been accepted for the award of any other degree or diploma at UNSW or any other educational institution, except where due acknowledgement is made in the thesis. Any contribution made to the research by others, with whom I have worked at UNSW or elsewhere, is explicitly acknowledged in the thesis. I also declare that the intellectual content of this thesis is the product of my own work, except to the extent that assistance from others in the project's design and conception or in style, presentation and linguistic expression is acknowledged.'

Signed ……

Date ……..

Inclusion of Publications Statement

UNSW is supportive of candidates publishing their research results during their candidature as detailed in the UNSW Thesis Examination Procedure.

Publications can be used in their thesis in lieu of a Chapter if:

- The candidate contributed greater than 50% of the content in the publication and is the "primary author", ie. the candidate was responsible primarily for the planning, execution and preparation of the work for publication
- The candidate has approval to include the publication in their thesis in lieu of a Chapter from their supervisor and Postgraduate Coordinator.
- The publication is not subject to any obligations or contractual agreements with a third party that would constrain its inclusion in the thesis

Please indicate whether this thesis contains published material or not:

☐ This thesis contains no publications, either published or submitted for publication

☐ Some of the work described in this thesis has been published and it has been documented in the relevant Chapters with acknowledgement

☒ This thesis has publications (either published or submitted for publication) incorporated into it in lieu of a chapter and the details are presented below

CANDIDATE'S DECLARATION

I declare that:

- I have complied with the UNSW Thesis Examination Procedure
- where I have used a publication in lieu of a Chapter, the listed publication(s) below meet(s) the requirements to be included in the thesis.

Candidate's Name	**Signature**	**Date (dd/mm/yy)**
Munkhshur Myekhlai		

POSTGRADUATE COORDINATOR'S DECLARATION

I declare that:

- the information below is accurate
- where listed publication(s) have been used in lieu of Chapter(s), their use complies with the UNSW Thesis Examination Procedure
- the minimum requirements for the format of the thesis have been met.

PGC's Name	PGC's Signature	Date (dd/mm/yy)
Alex William Donald		

For each publication incorporated into the thesis in lieu of a Chapter, provide all of the requested details and signatures required.

Details of publication #1:

Full title: *Increasing the Formation of Active Sites on Highly Crystalline Co Branched Nanoparticles for Improved Oxygen Evolution Reaction Electrocatalysis*

Authors: *Munkhshur Myekhlai, Tania M. Benedetti, Lucy Gloag, Vinicius R. Gonçales, Soshan Cheong, Hsiang-Sheng Chen, J. Justin Gooding, and Richard D. Tilley*

Journal or book name: *ChemCatChem*

Volume/page numbers: Volume 12, Issue. 11, pages 3126-3131

Date accepted/ published: 20 March, 2020

Status	*Published*	✗	*Accepted and In press*		*In progress (submitted)*	

The Candidate's Contribution to the Work

- Synthesized Co-Au branched, Co-Au core shell, and Co_3O_4 nanoparticles
- Characterized nanocrystals using low-resolution electron microscopy
- Performed electrocatalytic experiments including cyclic voltammertry, chronopotentiometry, electrochemical impedance spectroscopy
- Drafted and proofread manuscript

Location of the work in the thesis and/or how the work is incorporated in the thesis:

In lieu of Chapter 4

PRIMARY SUPERVISOR'S DECLARATION

I declare that:

- the information above is accurate
- this has been discussed with the PGC and it is agreed that this publication can be included in this thesis in lieu of a Chapter
- All of the co-authors of the publication have reviewed the above information and have agreed to its veracity by signing a 'Co-Author Authorisation' form.

Primary Supervisor's name	**Primary Supervisor's signature**	**Date (dd/mm/yy)**
Richard D. Tilley		

Details of publication #2:

Full title: *Controlling the number of branches and surface facets of Pd-core Ru-branched nanoparticles to make highly active oxygen evolution reaction electrocatalysts*

Authors: *Munkhshur Myekhlai, Tania M. Benedetti, Lucy Gloag, Agus R. Poerwoprajitno, Soshan Cheong, Wolfgang Schuhmann, J. Justin Gooding, and Richard D. Tilley*

Journal or book name: *Chemistry-A European Journal (Chem. Eur.J)*

Volume/page numbers: *Volume 26, Issue. 67, pages 15501-15504*

Date accepted/ published: *25 August, 2020*

Status	*Published*	✗	*Accepted and In press*		*In progress (submitted)*	

The Candidate's Contribution to the Work

- Synthesized Pd seeds, Ru-Pd branched nanoparticles
- Characterized nanocrystals using low-resolution electron microscopy, XRD
- Performed electrocatalytic experiments including cyclic voltammertry, chronopotentiometry
- Drafted and proofread manuscript

Location of the work in the thesis and/or how the work is incorporated in the thesis:

In lieu of Chapter 5

PRIMARY SUPERVISOR'S DECLARATION

I declare that:

- the information above is accurate
- this has been discussed with the PGC and it is agreed that this publication can be included in this thesis in lieu of a Chapter
- All of the co-authors of the publication have reviewed the above information and have agreed to its veracity by signing a 'Co-Author Authorisation' form.

Primary Supervisor's name	**Primary Supervisor's signature**	**Date**
Richard D. Tilley		**(dd/mm/yy)**

Acknowledgements

It has been an amazing journey over the past four years of my life, full of learning, stress, frustration, and plenty of joy. I am grateful every day at UNSW to be surrounded by an abundance of opportunity, immense beauty, and some of the most impressive and kind people in the world. The successful completion of this thesis and the achievement of my degree would not have been possible without the support of my mentors, colleagues, family, and friends.

I would like to begin by thanking Professor Richard Tilley, my Ph.D. supervisor, for his guidance and mentorship along this journey. I am very grateful for the opportunity you provided in allowing me to relocate to Australia to pursue my PhD, and I hope this will be a stepping stone for further accomplishments in my life.

I would like to thank my co-supervisor, Professor Justin Gooding, for his incredible intellect and ability to comprehend a range of topics that I remain unsure about to an extent. I am incredibly grateful for your support throughout the research process.

In honor of my wonderful lab supervisor and cool lab sister, Dr Tânia Benedetti, none of this work would have been possible without your constant support and guidance. I would like to thank you for teaching me so much about electrochemistry. I am forever grateful to you for your encouragement. Without your presence in the lab, it would be a much darker place.

Dr. James Webb, you have been an integral part of my dissertation as my mentor and lab brother. Clearly, life in the lab would be much harder without you, who not only sustain the operation and culture of a large group like this but cares about everyone in the lab (so much so that you proofread my thesis!). You are a magnificent individual, and I greatly admire your support.

I am grateful to you, Dr. Lucy Gloag, for helping me during this period, particularly your comments and advice on nanoparticle synthesis and my first and second papers.

Thank you, Dr. Andrew McGrath, for all of your valuable advice and assistance during the early stages of my Ph.D. endeavor.

Many thanks to Hsiang-Sheng (Johnson) Chen, Dr. Soshan Cheong, Dr. Richard Webster, and Zeno Rizqi Ramadhan for conducting HRTEM and EDX mapping analysis for my particles.

It is my pleasure to thank Dr. Vinicius Gonçales for XPS analysis of my samples and your kindness.

It is my privilege to thank the staff at the electron microscope unit at UNSW, especially, Sean Lim, Katie Levick, and Qiang Zhu, for teaching me how to operate TEM and obtain beautiful but scientifically meaningful images.

I would like to thank Dr. Ruoming Tian and Dr. Yu Wang for teaching me how to operate the XRD instrument and obtain high-quality data.

Thank you, Parisa, for your support when life becomes challenging in various ways. I will always cherish our memories.

It is greatly appreciated to have a friend like you, Xueqian. Thank you for all of your support and companionship.

I would also like to thank Kristine for your lunch, coffee catch-ups, and your inspiration. Thanks for being so kind and supportive, Wenxian.

Cong, you are a wonderful friend, and I sincerely appreciate your generosity, kindness, and support.

Thank you very much, Frederik, for being a good friend and providing assistance.

Thanks to Patrick and Peter, I feel energized after speaking with you. I would also like to thank Patrick for teaching me Autodesk and Peter for his comments on my presentations.

Thank you, Ali, for being a good friend. I am grateful for the help you provided, Johnson.

I am grateful for Toby's assistance in my Ph.D. journey; it has made the process easier and more enjoyable. I greatly appreciate your time and effort.

I appreciate your guidance and support, Dr. Cameron. The lessons I have learned from you have been invaluable to me.

Special thanks to Leo and Matthew for your wonderful help in proofreading my thesis and improving it substantially.

To other great lab mates on level seven: Stephanie, Kuan, Johanna, Shreedhar, Milad, Kim, Saiful, Yosef, Qinyu, Joe, Daniel, Han Han, Sam, Danielle, Lily, Zeno, Agus, Kevin: Thank you all for some great time, some good company, and a great work environment to come into every day.

I would like to thank Emma and Yang for your continued support. I am so grateful that someone is thinking about my well-being and career. I will always remember everything you've done for me.

I would like to express my gratitude to Giang, you, and your family for being great flatmates in Sydney.

I highly appreciate the continuous support and cooperation from Dr. Battsengel, Dr. Gunpilmaa, Dr. Uranchimeg, and Tseveendorj.

Dr. Munkhbayar -your contribution to this journey is invaluable. I am grateful for your assistance and continued support.

I would like to thank you for always having my back, Govigerel. My appreciation goes out to you for constantly pushing me to do better and for

helping me achieve my goals. You make sure that I stay on the right track at all times, and I am grateful to you for this.

I would also like to thank the UNSW Scientia Scholarship. Through this financial support, I enjoyed four years of financially carefree living, which allowed me to focus on my research and develop other skills in preparation for my future career.

Last, I would like to express my sincere gratitude to my dad, Myekhlai, mother, Nergui, and my brothers, Luvsangombo and Tsegtsbaatar, for their unconditional support. I am grateful for my family, but there are no words to express how grateful I am. I would not be the person I am today without your help. Love you always.

Abstract

The electrochemical water splitting reaction, which consists of hydrogen reduction at the cathode and oxygen evolution (OER) at the anode, is one of the core processes for the utilization of sustainable and green energy sources. However, the sluggish kinetics of the oxygen evolution reaction requires a higher overpotential than the theoretical potential (1.23 V). Engineering a high-performance electrocatalyst is an avenue to improve the reaction kinetics for OER. Bimetallic branched nanoparticles offer substantial benefits for OER electrocatalysts; which include a greatly increased exposed surface area, highly crystalline *hcp* branches and stable surfaces. This thesis aims to design branched nanoparticles as electrocatalysts for enhanced OER in the following ways: (i) extending the cubic-core hexagonal-branch growth approach for a new bimetallic (Co, Au) system, (ii) leveraging the advantages of the Ru-Pd branched nanoparticles by tuning the surface facets and branch number, and (iii) making branched nanoparticles consisting of a cubic core (Pd) and alloyed branches (RuCo).

Chapter one discusses the literature on the oxygen evolution reaction and Co- and Ru-based electrocatalysts for OER as well as the organic solution-phase synthesis method. The limiting factors of Co- and Ru- based catalysts and the strategies for improving their catalytic performance are also summarized. Also outlined is the fundamental understanding for synthesizing metallic nanoparticles using a seed-mediated growth approach in an organic solution phase and controlling the shape and size of the final products. Chapter two describes the synthetic methodology, sample purification, ink preparation for electrochemical measurements and characterization techniques in more detail. Chapter three provides the synthetic approaches and challenges in making Co and Ru branched

nanoparticles. Chapter four compares the OER catalytic activity and stability of the Co-Au branched nanoparticles with the Co-Au core-shell and Co_3O_4 nanoparticles in alkaline media. The improved catalytic performance of the branched nanoparticles can be attributed to the formation of an active and stable oxide layer on the branch surface. Chapter five investigates the effect of branch number, and surface facets on the catalytic properties of the Ru-Pd branched nanoparticles with tunable branch number and surface facets. It is found that tuning surface facets and branch length is essential for enhancing catalytic performance by increasing the exposure of more active sites and improving the accessibility of the catalytic surface to the catalytic reaction. Chapter six explores alloyed branched nanoparticles consisting of a Pd core and RuCo branches and assesses their catalytic activity for OER electrocatalysts. It is demonstrated that Co leaching during catalytic activation in acid solution increases the exposure of highly catalytically active sites on the branch surface resulting in enhanced catalytic activity. Chapter seven concludes the overall results and achievements of this thesis and also discusses future opportunities.

List of Publications

1. M. Myekhlai, T. M. Benedetti, L. Gloag, V. R. Gonçales, S. Cheong, H.-S. Chen, J. J. Gooding, R. D. Tilley. *Increasing the Formation of Active Sites on Highly Crystalline Co Branched Nanoparticles for Improved Oxygen Evolution Reaction Electrocatalysis. ChemCatChem,* **2020.**
2. M. Myekhlai, T. M. Benedetti, L. Gloag, A. R. Poerwoprajitno, S. Cheong, W. Schuhmann, J. J. Gooding, R. D. Tilley. *Controlling the Number of Branches and Surface Facets of Pd-Core Ru-Branched Nanoparticles to Make Highly Active Oxygen Evolution Reaction Electrocatalysts. Chem. Eur. J.* **2020.**
3. P. Moazzam, M. Myekhlai, A. Alinezhad, F. A. Alshawawreh, P. Bakthavathsalam, V. R. Goncales, R. D. Tilley, J. J. Gooding. Ultrasensitive detection of programmed death-ligand 1 (PD-L1) in whole blood using dispersible electrodes. ChemComm, **2021.**
4. M. Batmunkh, M. Myekhlai, A. S. R. Bati, S. Sahlos, A. D. Slattery, T. M. Benedetti,V. R. Gonçales, C. T. Gibson, J. J. Gooding, R. D. Tilley, J. G. Shapter. Microwave-assisted synthesis of black phosphorus quantum dots: efficient electrocatalyst for oxygen evolution reaction. J. Mater. Chem. A, **2019.**

Conference presentations

Oral presentation. Electrochemical Division of the Royal AustraliaChemical Institute (EDRACI), **2019,** Australia.

Oral presentation. International Conference on Materials for Advanced Technology (ICMAT), **2019,** Singapore**.**

Oral presentation. ACS National Meeting & Exposition, **2019,** USA

Table of Contents

Copyright Statement ..... **iii**

Authenticity Statement ..... **iii**

Originality Statement ..... **iv**

Inclusion of Publications Statement ..... **v**

Acknowledgements ..... **ix**

Abstract ..... **xiii**

List of publications ..... **xv**

List of Figures ..... **xx**

List of Tables ..... **xv**

List of Abbreviations and Synonyms ..... **xvii**

Chapter 1: Introduction **1**

1.1 Motivation 2

1.2 Electrochemical Water Splitting 3

1.3 Oxygen Evolution Reaction 4

1.4 Catalytic trend for oxygen evolution reaction 7

1.4.1 Cobalt oxide (CoO_x) -based electrocatalysts 7

1.4.2 Ru-based electrocatalysts 15

1.5 Organic solution phase synthesis method 24

1.5.1 Bimetallic branched nanoparticles 26

1.6 Project aims 28

1.7 References 30

Chapter 2: Synthesis and Characterization Methods 48

2.1 Overview 49

2.2 Synthesis and Purification Methods 50

2.2.1 Fischer-Porter bottle synthesis 50

2.2.2 Thermal decomposition 51

2.2.3 Post-synthesis, cleaning, purification, and storage 52

2.2.4 Sample preparation for electron microscopy characterization 53

2.2.5 Sample preparation for X-ray diffraction and X-ray photoelectron spectroscopy …… 53
2.2.6 Nanoparticles loading on carbon …… 54
2.3 TEM-based techniques ……... 55
2.3.1 Basic principles of TEM ……. 55
2.3.2 TEM characterization ……. 58
2.3.3 HRTEM characterization ……... 58
2.3.4 High-angle annular dark-field scanning transmission electron microscopy (HAADF-STEM) analysis …… 60
2.3.5 Scanning Transmission Electron Microscopy-Energy Dispersive X-ray Spectroscopy (STEM-EDX) ……. 61
2.4 X-Ray Powder Diffraction (XRD) ……. 62
2.5 X-ray photoelectron spectroscopy (XPS) ……... 64
2.6 Electrochemical characterizations ……. 65
2.6.1 Catalysts ink preparation …… 66
2.6.2 Catalytic activation …… 66
2.6.3 OER activity ……. 66
2.6.4 Stability test ……... 67
2.6.5 Electrochemical surface area ……. 68
2.6.6 Electrochemical impedance spectroscopy ……. 68
2.7 References ……. 69
Chapter 3. Optimisation of the synthesis of Co-Au and Ru-Pd branched nanoparticles ……. 72
3.1 Chapter Overview ……... 73
3.2 Co-Au branched nanoparticles synthesis …… 74
3.2.1 Experiment 1-3: Effect of precursor to seed ratio …… 76
3.2.2 Experiment 4: Effect of the type of precursor ……. 80
3.2.3 Experiment 4-6: Time-resolved experiments ……. 82
3.3 Ru branched nanoparticles with controlled surface facets and branch numbers ……... 86
3.3.1 Pd seeds with tunable sizes ……. 87
3.3.2 Au seeds with different seed sizes ……... 92
3.3.3 Ru-Pd branched nanoparticles with tunable branch size and branch number ……. 95

3.3.3.1 Experiment 15: The effect of surfactant impurity 96
3.3.3.2 The effect of precursor to seed ratio 97
3.3.3.3 Experiment 20-23: The effect of seed size on the branch number 101
3.4 Conclusions 105
3.5 References 105
Chapter 4. Increasing the Formation of Active Sites on Highly Crystalline Co Branched Nanoparticles for Improved Oxygen Evolution Reaction Electrocatalysis 110
4.1 Summary 111
Declaration for Chapter 4 112
Chapter 5. Controlling the Number of Branches and Surface Facets of Pd-Core Ru-Branched Nanoparticles to Make Highly Active Oxygen Evolution Reaction Electrocatalysts 132
5.1 Summary 133
Declaration for Chapter 5 134
Chapter 6. Increasing the exposure of highly active sites on RuCo-Pd alloyed branched nanoparticles for improved oxygen evolution reaction electrocatalysis 153
6.1 Introduction 154
6.2 Synthesis of RuCo-Pd branched nanoparticles 157
6.2.1 Syntheses using cobalt (II) acetylacetonate as the Co precursor 158
6.2.2 Syntheses using cobalt (III) acetylacetonate as the precursor 164
6.2.3 Two-step synthesis using $Co(acac)_3$ as the precursor 169
6.3 Electrocatalytic properties of RuCo-Pd branched nanoparticles ... 175
6.4 Conclusions 185
6.5 References 187
Chapter 7. Conclusion and Future Work 192
7.1 Conclusions 193
7.1.1 Co branched nanoparticles 195
7.1.2 Ru-Pd branched nanoparticles 196
7.1.3 RuCo-Pd alloyed branched nanoparticles 197
7.2 Future Work 199
7.3 References 201

List of Figures

Chapter 1: Introduction

Figure 1.1. Schematic illustration of the electrochemical water splitting process …… 3

Figure 1.2 OER volcano trend for metal oxides …….. 6

Figure 1.3. TEM images of Au-CoOx core-shell nanoparticles and related polarization curves: **(a)** Au@Co_3O_4 core-shell NCs[57], inset: related histogram, **(b)** Au@Co/C (Au_9Co_{91})[58], **(c)** AuNCs@$Co(OH)_2$ Au-rod-$Co(OH)_2$ core-shell nanoparticles[59], **(d)** Au@CoOx[42] …… 12

Figure 1.4. (a-d) Schema of engineering the surface of SC CoO NRs. **(e)** High magnification TEM image of SC CoO NR. Scale bar, 20 nm. **(f)** High-resolution HAADF-STEM image SC CoO NR. Inset: Selected area electron diffraction pattern from [110] zone axis. Scale bar = 2 nm. **(g)** The catalytic activity study by linear sweep voltammetry (LSV) of SC, PC CoO NRs, and commercial RuO_2 catalysts. Inset: Tafel plots. (**h-i)** Intrinsic OER activity of SC CoO NCs and PC CoO NCs ……. 13

Figure 1.5. (a) TEM image of Ru octahedral nanocrystals, (b) HAADF-STEM image and EDX mapping of an octahedral nanocrystal, (c) HRTEM image of a branched nanoparticle and magnified part in the black box showing the {200} and {111} facets …….. 19

Figure 1.6 (a) Schematic illustration of a hierarchical 4H/fcc Ru NT, (b) TEM image of hierarchical 4H/fcc Ru NTs, (c) HAADF-STEM image and EDX mapping of an individual hierarchical 4H/fcc Ru NTs, (d) HER activities of 4H/fcc Ru NTs, 4H/fcc Au-Ru nanowires, 4H/fcc Au, Pt/C, Ru/C, and commercial Pt/C, (e) Catalytic stability of 4H/fcc Ru NCs …… 21

Figure 1.7. (a) TEM image of Pd-Ru branched nanoparticles, (b) HAADF-STEM image and EDX mapping of an branched nanoparticle, (c) HRTEM image of a branched nanoparticle showing the {10-11} and {0001} facets, magnified part in the black box, and corresponding model showing the atomic arrangement of the particle, (d) OER activities of Pd-Ru branched and sphere nanoparticles, and (e) Stability test of the branched nanoparticles. 22

Figure 1.8 Diagram of the classic Lamer-Dinegar model. Reproduced from Xia et al ……... 24

Figure 1.9. (a) Models showing a branch of the nanocrystal in which lateral sides passivated by ODPA molecules and a tetrapod CdTe nanocrystal. ZB-zinc blende -cubic phase, WZ -wurtzite -hexagonal phase and Cd atoms -yellow, Te atoms -blue. (b) TEM image of CdTe branched nanocrystal synthesized at Cd/Te 3:1 and Cd/ODPA 1:5 …… 27

Chapter 2: Synthesis and Characterization Methods

Figure 2.1. A Fischer-Porter bottle showing the bivalves and location of the reaction mixture …….. 51

Figure 2.2. Schematic of a thermal composition setup in a two-neck flask. One neck is for the condenser and N_2/Ar flow, and another neck is for the injection …….. 52

Figure 2.3. Co spherical nanoparticles loaded onto carbon black (Vulcan XC72) using different quantities of surfactant (OAm): (a) a higher quantity (b) a lower quantity, and (c) an optimized quantity …… 54

Figure 2.4. Schematic illustration of a TEM ……... 56

Figure 2.5. Diagrams showing the two fundamental functions of the TEM imaging system: (a) producing the diffraction pattern on the screen and (b) generating an image on the screen ……. 57

Figure 2.6. (a) A low-resolution TEM image of RuCo-Pd branched nanoparticles used in Chapter 6, (b) A diagram showing how to determine the dimensions of a branched nanocrystal …….. 58

Figure 2.7. (a) TEM image of a Co branch. (b) HRTEM image of part of the branch in (a) indicated by the red box. (c) FFT of the HRTEM image at the oxide surface (purple box) indexed to a cubic <110> zone axis. (d) FFT of the HRTEM image at the core region (blue box) indexed to a hexagonal <01-10> zone axis. The lattice measurements of 2.0 Å at the core, and 2.1 Å and 2.4 Å at the shell regions are consistent with the lattice spacings of hcp Co{0002}, cubic CoO{200} and cubic CoO{111}, respectively …… 59

Figure 2.8. HAADF-STEM images of Co-Au core shell nanoparticles and (b) a Co-Au core-shell nanoparticle …… 61

Figure 2.9. STEM-EDX elemental maps of Au (yellow), Co (pink) and O (green) of a Co spherical nanoparticle …… 62

Figure 2.10. Illustration of Bragg's law in a simplified form ……. 63

Figure 2.11. Schematic illustration of a three-electrode electrochemical setup showing the working, counter, and reference electrodes …… 65

Chapter 3. Optimisation of the synthesis of Co-Au and Ru-Pd branched nanoparticles

Figure 3.1. TEM images of Au-Co particles synthesized at different Co precursor to Au seed ratios: (a) Au-Co core-shell nanoparticles (10:1) and (c, e) Co-Au branched nanoparticles with different branch numbers and lengths (50:1 and 100 :1, respectively), (b) branch numbers, (d, f) branch lengths of the branched nanoparticles. Scale bars = 50 nm ……. 78

Figure 3.2. TEM image of the particles synthesized using $Co(laurate)_2$ as the Co precursor and corresponding size distribution …….. 81

Figure 3.3. Time-resolved synthesis. (a) proposed growth mechanism, (b) Initial gold seeds and nanoparticles formed after (b) 30 min, (c) 45 min, and (c) 24 h reaction periods ……. 90

Figure 3.4. TEM images of small Pd seeds synthesized by a one-pot reaction and larger Pd seeds synthesized by a seed-mediated method by varying the precursor to seed ratio. (a) small Pd seeds with an average diameter of 3.5 ± 0.4 nm (b) precursor to seed ratio: 0.005, Pd seeds with an average diameter 6.6 ± 0.7 nm, (c) 0.025, 8.7 ± 0.7 nm, (d) 0.05, 11.5 ± 0.8 nm …… 91

Figure 3.5. TEM images of Au seeds synthesized at different temperatures and their corresponding histograms. (a) 60 ºC, 14.0 ± 2.7 nm, (b) 70 ºC, 8.9 ± 1.1 nm, (c) 80 ºC, 7.6 ± 0.8 nm, (d) 90 ºC, 7.1± 1.0 nm …….. 94

Figure 3.6 Au seed size as a function of reaction temperature for the synthesis of Au seeds. Representative TEM images of each sample are shown in the plot. Scale bar = 5 nm …… 95

Figure 3.7. Ru-Pd branched nanoparticles using 70% grade oleylamine ….. 97

Figure 3.8. The effect of precursor to seed ratio at (a) 5 :1, (b) 8: 1, (c) 24 : 1, and (d) 50 : 1 molar ratios …… 100

Figure 3.9. Multi-branched Ru-Pd nanoparticles using Pd seeds of different sizes. (a) 3.5 ± 0.4nm, (b) 6.0 ± 0.7 nm, (c) 8.7 ± 0.7 nm, and (d) 11.5 ± 0.8 nm Pd seeds ……. 103

Chapter 6. Increasing the exposure of highly active sites on RuCo-Pd alloyed branched nanoparticles for improved oxygen evolution reaction electrocatalysis

Figure 6.1. (a-d) TEM images of RuCo-Pd nanoparticles synthesized using $Co(acac)_2$ and (e-h) corresponding size distributions. Scale bar, 10 nm …… 160

Figure 6.2. (a) HAADF-STEM image and (b-d) corresponding STEM-EDX elemental maps of Ru (pink), Co (green) of RuCo-Pd branched nanoparticles (Exp.3) and overlay of elemental maps in (b) and (c). EDX maps were taken by Hsiang-sheng Chen …… 161

Figure 6.3. (a-d) SAED patterns of RuCo-Pd nanoparticles synthesized using $Co(acac)_2$, (e) SAED indexed to hcp-Ru, and (f) XRD pattern of corresponding SAED pattern. Pink lines: JCPDC no. 06-0663 (hcp-Ru). Green lines: JCPDC no. 65-8976 (hcp-CoRu) …… 162

Figure 6.4. (a) TEM image of the particles synthesized using $Co(acac)_3$ as the Co precursor and (b) corresponding size distributions of core diameter (5.1 ± 0.7 nm), branch width (5.6 ± 0.8 nm), and branch length (18.4 ± 3.0 nm), (c-f) HAADF-STEM image, STEM-EDX elemental maps of Co (pink), 165

Ru (green) of RuCo-Pd branched nanoparticles, and overlay of elemental maps, (g) EDX spectrum of the sample and elemental composition in at%. HAADF-STEM image and EDX maps were taken by Hsiang-sheng Chen …

Figure 6.5. (a) SAED and (b) XRD pattern of the sample. The characteristic peaks of hcp-Ru and hcp-RuCo are marked by pink and blue, respectively. Pink lines: JCPDS no. 04-4608 (hcp-Ru). Blue lines: JCPDS no. 65-8976 (hcp-CoRu) ……. 166

Figure 6.6. (a) TEM image of the particles synthesized using $Co(acac)_3$ as the Co precursor and (b) EDS spectrum of the sample and elemental composition in at%, (c-f) HAADF-STEM image, STEM-EDX elemental maps of Co (green), Ru (pink) of RuCo-Pd branched nanoparticles, and overlay of elemental maps. HAADF-STEM image and EDX-maps were taken by Zeno Rizqi Ramadhan …….. 171

Figure 6.7. (a) SAED and (b) XRD pattern of the sample. The characteristic peaks of hcp-Ru and hcp-RuCo are marked by pink and blue, respectively. Pink lines: JCPDS no. 04-4608 (hcp-Ru). Blue lines: JCPDS no. 65-8976 (hcp-CoRu) ……. 171

Figure 6.8. (a) HRTEM image of a branched nanoparticle. (b) HRTEM image of part of the branch in (a) indicated by the blue box and corresponding FFT indexed to a hexagonal <01$\bar{1}$0> zone axis. (c) HRTEM image of the core region in (a) indicated by the orange box and corresponding FFT indexed to a cubic <110> zone axis. HRTEM image was taken by Zeno Rizqi Ramadhan …….. 173

Figure 6.9. TEM images of the particles (a) after 4 h reaction and (b) after 24 h reaction …… 174

Figure 6.10. Size distributions of core diameter, branch width, and branch length of the particles (a) after 4 h reaction and (b) after 24 h reaction …….. 174

Figure 6.11. Anodic scan of the 5th cycle of cyclic voltammetry to show the geometric activities (a) Ru-Pd branched nanoparticles, (b) RuCo-Pd branched nanoparticles 1, and (c) RuCo-Pd branched nanoparticles 2 …… 177

Figure 6.12. CVs measured for (a) Ru-Pd branched nanoparticles, (b) RuCo-Pd branched nanoparticles 1, and (c) RuCo-Pd branched nanoparticles 2 in 0.1 M $HClO_4$. Corresponding plots of the current at 1.15 V vs. the scan rate. 178

Figure 6.13. Anodic scan of the 5th cycle of cyclic voltammetry to show the specific activities (a) Ru-Pd branched nanoparticles, (b) RuCo-Pd branched nanoparticles 1, and (c) RuCo-Pd branched nanoparticles 2 …….. 179

Figure 6.14. Catalytic stability tests for the catalysts. (a) changes in activity vs. cycle and (b) changes in specific activity vs. cycle. Ru-Pd branched nanoparticle (grey), RuCo-Pd branched nanoparticles 1 (blue), and (c) RuCo-Pd branched nanoparticles 2 (red) ……. 180

Figure 6.15. CVs measured in alkaline solution (0.1 M NaOH) before and after running CVs in acid solution (0.1 M $HClO_4$) for (a-b) RuCo-Pd branched nanoparticles 1 and (c-d) RuCo-Pd branched nanoparticles 2 …… 181

Figure 6.16. Comparison of surface areas before and after Co leaching. CVs measured in alkaline solution (0.1 M NaOH) at 100 mV s^{-1} before and after running CVs in acid solution (0.1 M $HClO_4$), and the plots of current at 1.05 V vs. the scan rate for (a-b) RuCo-Pd branched nanoparticles 1 and (c-d) RuCo-Pd branched nanoparticles 2 ……. 182

Figure 6.17. Comparison of the Co content in the RuCo-Pd 2 catalyst before and after electrochemical activation. **(a-b)** Eds spectras of the catalysts before and after running CVs in acid solution (0.1 M $HClO_4$), and (c) the schematic illustration of the formation of active surface after running CVs in acid solution. Black circles indicated that the vacancies of Co after Co leaching from the catalyst's surface …… 183

Figure 6.18 Schematic illustration of the synthesis for (a) RuCo-Pd alloyed branched nanoparticles with the Co distribution around the beginning of branches and (b) RuCo-Pd alloyed branched nanoparticles with the Co distribution though branches ……... 185

Figure 6.19 Catalytic activities of the catalysts. (a) anodic scan of the 5th cycle of cyclic voltammetry to show the OER activities and (b) Comparison of the specific activities of RuCo-Pd 1, RuCo-Pd 2, and Ru-Pd catalysts obtained at an overpotential of 260 mV ……... 186

List of Tables

Chapter 3. Optimisation of the synthesis of Co-Au and Ru-Pd branched nanoparticles

Table 1.1. Summary of recently reported Co-based OER catalysts ……. 8

Table 1.2. Summary of recently reported Ru-based OER catalysts …….. 16

Table 3.1. The experimental conditions applied for the precursor to seed ratio on the synthesis of Co-Au branched nanoparticles …….. 77

Table 3.2. The experimental conditions applied for the effect of precursor on the synthesis of Co-Au nanoparticles ……. 81

Table 3.3. The experimental conditions applied for the effect of reaction time on the synthesis of Co-Au nanoparticles …….. 83

Table 3.4. The experimental conditions applied for the synthesis of small Pd seeds …… 88

Table 3.5. The experimental conditions applied for the synthesis of Pd nanoparticles with different sizes …… 89

Table 6. The experimental conditions applied for the synthesis of Au nanoparticles with different sizes …… 92

Table 3.7. The experimental conditions applied for the synthesis of Ru-Pd branched nanoparticles using 70 % oleylamine surfactant …….. 96

Table 3.8. The experimental conditions applied when varying the precursor to seed ratio on the synthesis of Ru-Pd branched nanoparticles ……... 98

Table 3.9. The experimental conditions applied for the synthesis of Ru-Pd branched nanoparticles with controlled branch number ……. 102

Chapter 6. Increasing the exposure of highly active sites on RuCo-Pd alloyed branched nanoparticles for improved oxygen evolution reaction electrocatalysis

Table 6.1. The experimental conditions a applied for the synthesis of RuCo-Pd nanoparticles using $Co(acac)_2$ as the Co precursor varying the ratio of $Ru(acac)_3$ to $Co(acac)_2$ …… 159

Table 6-2. The experimental conditions applied to synthesize RuCo-Pd nanoparticles using $Co(acac)_3$ as the Co precursor …….. 164

Table 6.3. Indexing the diffraction rings of the sample ……. 167

Table 6.4. The experimental conditions applied for the synthesis of RuCo-Pd nanoparticles using $Co(acac)_3$ as the Co precursor ……. 170

Table 6.5. Indexing the diffraction rings of the sample ……... 182

List of Abbreviations and Synonyms

3D	three-dimensional
acac	acetylacetonate
CV	cyclic voltammogram
DFT	density functional theory
EDX	Energy dispersive X-ray spectroscopy
ECSA	electrochemical surface area
EIS	electrochemical impedance spectroscopy
fcc	face centred cubic
HAADF	high angle annular dark field
hcp	hexagonal close packed
HDA	hexadecylamine
HER	hydrogen evolution reaction
HRTEM	high resolution transmission electron microscopy
OAm	Oleylamine
OER	oxygen evolution reaction
STEM	scanning transmission electron microscopy
TEM	transmission electron microscopy
TOP	trioctylphosphine

XRD	X-ray diffraction
XPS	X-ray photoelectron microscopy

Chapter 1

Introduction

1.1 Motivation

Energy plays a crucial role in our society, and fossil fuels have been used as a conventional energy resource until now[1, 2]. However, fossil fuels resources are being depleted, while climate change, air pollution, and the ecological devastation from traditional energy sources continue to increase[1, 2]. To tackle this problem, nations have started searching for new renewable and sustainable energy sources and energy storage systems, including solar cells, fuel cells, and lithium batteries[3-5].

Emerging sustainable energy sources such as fuel cells and solar cells use hydrogen (H_2) as an energy carrier, which is the fuel of the future, to produce energy[2, 6]. Nevertheless, producing and storing H_2 is very challenging due to its low energy density and high flammability, which limits the implementation of these alternative energy sources to widespread practical use[7]. Therefore, finding a solution to produce and store H_2 effectively and safely is of great importance for the future of these sustainable energy sources.

A promising route for producing H_2 is via an electrochemical water splitting process[8, 9]. In this reaction, electricity is generated through H_2 bond breaking, producing water as waste[8, 9]. However, the efficiency of this reaction is limited by the kinetically slow oxygen evolution reaction (OER) at the anode, which is slower than the hydrogen evolution reaction at the cathode[10, 11]. Thus, designing an efficient and cheaper electrocatalyst for OER is of great significance in improving the reaction kinetics and reducing the devices' cost. Although a number of studies have been published on developing efficient electrocatalysts for OER, further improvements are essential to make it economically viable for practical use[5, 12, 13]. Therefore,

the following chapters will focus on developing highly efficient OER catalysts.

1.2 Electrochemical water splitting

The water splitting reaction is a core process in electrochemical energy storage/conversion applications, including fuel cells, solar cells, and lithium-ion batteries[14-16]. The electrochemical water splitting reaction consists of two half-reactions: hydrogen reduction at the cathode and oxygen evolution at the anode, as shown in Figure 1.1[13, 14].

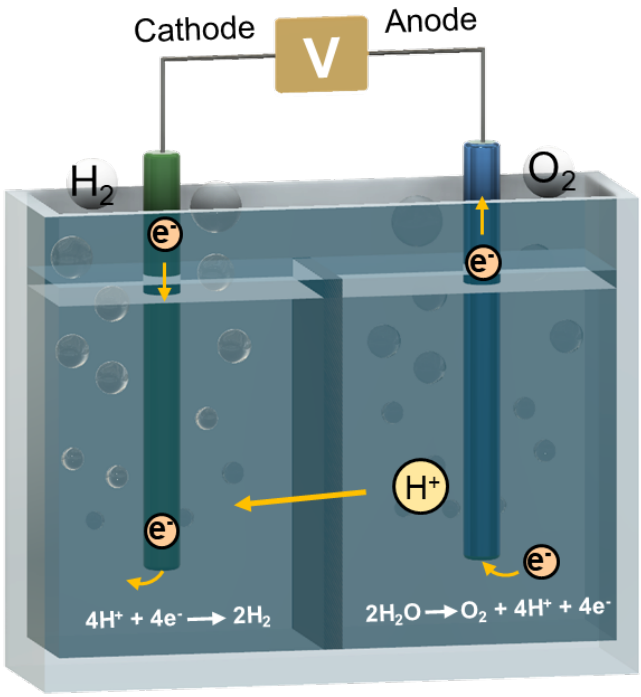

Figure 1.1. Schematic illustration of the electrochemical water splitting process.

The produced hydrogen can be further used as a fuel for clean energy sources[13, 14]. However, oxygen evolution reaction takes place via a complex four-electron transfer mechanism, which affects the reaction kinetics[13, 14]. Therefore, understanding the general principles and mechanism and identifying the rate-determining steps of this reaction is important for

designing a novel and efficient electrocatalyst for OER in order to improve its reaction kinetics.

1.3 Oxygen evolution reaction (OER)

OER is a reaction happening at the anodes in water splitting processes and is a multi-step four-electron transfer reaction[13, 17, 18]. Owing to its slow kinetics, this reaction requires a higher overpotential than the theoretical potential (1.23 V), which lowers the hydrogen production efficiency of the water-splitting reaction[13, 17, 18]. Generally, OER can proceed in both acidic (Eqn 1.1) and alkaline environments (Eqn 1.2)[13, 18, 19].

$$2H_2O_{(l)} \rightarrow O_{2(g)} + 4H^+ + 4e^- \quad (1.1)$$

$$4OH^- \rightarrow O_{2(g)} + 2H_2O_{(l)} + 4e^- \quad (1.2)$$

In an acidic environment, oxygen molecules were generated by water oxidation, whereas in neutral and alkaline environments, oxygen was produced via hydroxyl ion oxidation[13, 18, 19]. The general OER in acidic and alkaline conditions are discussed in more detail below.

In an acidic media, OER can proceed by the following four-electron transfer pathway (Eqn 1.3-1.6)[13, 18, 19]:

$$M + H_2O_{(l)} \rightarrow MOH + H^+ + e^- \quad (1.3)$$

$$MOH \rightarrow MO + H^+ + e^- \quad (1.4)$$

$$2MO \rightarrow 2M + O_{2(g)} \quad \text{or} \quad (1.5)$$

$$MO + H_2O_{(l)} \rightarrow MOOH + H^+ + e^- \quad (1.6)$$

$$MOOH \rightarrow M + O_{2(g)} + H^+ + e^- \quad (1.6)$$

where M denotes a catalyst's surface.

OER under an alkaline environment can proceed by the following four-electron transfer pathway (Eqn 1.9-1.13)[13, 18, 19]:

$$M + OH^- \rightarrow MOH + e^- \quad (1.9)$$

$$MOH + OH^- \rightarrow MO + H_2O_{(l)} + e^- \quad (1.10)$$

$$2MO \rightarrow 2M + O_{2(g)} \text{ or} \quad (1.11)$$

$$MO + OH^- \rightarrow MOOH + e^- \quad (1.12)$$

$$MOOH + OH^- \rightarrow M + O_{2(g)} + H_2O_{(l)} + e^- \quad (1.13)$$

After two electrons are transferred, the OER can proceed by two routes: (i) via direct recombination of oxygen and (ii) generating MOOH as an intermediate and producing oxygen molecules[13, 18, 19]. Both acidic and alkaline OER produces the same intermediates (OH_{ads}, O_{ads}, OOH_{ads})[18-21]. In addition to the reaction steps, elucidating the interaction between the reaction intermediates and catalyst surface is essential to gain insight into the reaction mechanism[18-21]. Thus, several theoretical studies have been conducted to understand: (i) the interaction of catalyst surface and water; (ii) the formation of O-O bond; (iii) the reaction thermodynamics/energies; and (iv) the adsorption property/surface reactivity[22-25].

In an ideal catalyst, the formation steps of intermediates including OH_{ads}, O_{ads}, and OOH_{ads} each require the same amount of Gibbs-free energy (1.23 eV)[26, 27]. However, one step in the reaction often becomes limited due to slow kinetics on the catalyst surface, which requires a high overpotential to overcome. According to the Sabatier principle and the "volcano" trend shown in Figure 1.2, an ideal catalyst should bind to the reaction intermediates not too weakly or strongly[5].

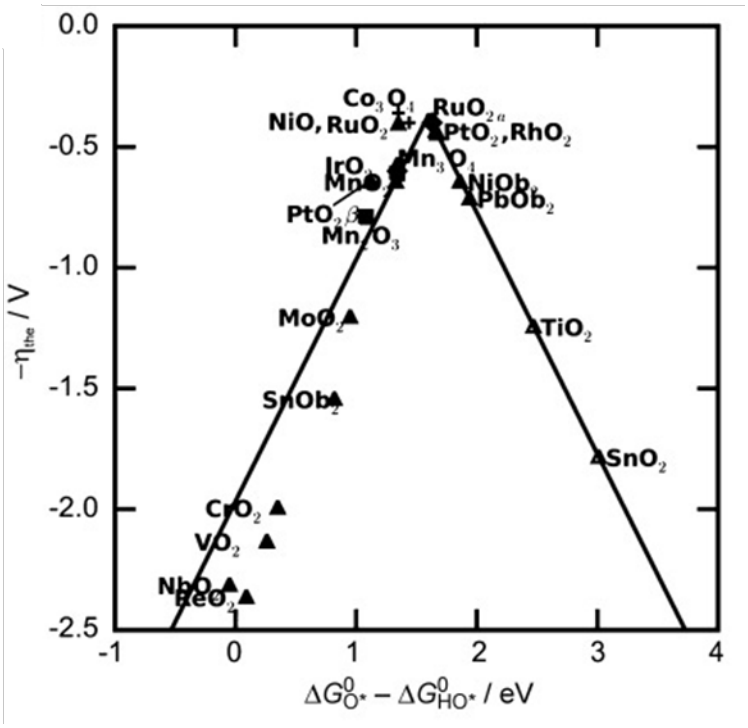

Figure 1.2. OER volcano trend for metal oxides. Reproduced from Isabela et al. [28]

The stronger binding energy between the oxygen and metal surface results in limited proton-electron transfer between O* or OH*, while weaker binding energy between the oxygen and catalyst surface shows the limited proton-electron transfer to O_2* or formation of the O-O bond[15, 22].

Therefore, unravelling the rate-limiting step of the reaction and modifying the binding energy between the catalyst surface and intermediates is essential for designing an efficient catalyst.

1.4 Catalytic trend for OER

The noble metal oxides RuO_2 and IrO_2 have been the most active catalysts for OER[29-31]. However, Ru-based catalysts dissolve easily at the potential relevant to OER in acidic and basic solutions, and both Ru and Ir metals are expensive and have limited availability[32, 33]. Because of the scarcity of noble metals, sustainable energy sources based on OER cannot be implemented as an alternative energy source to fossil fuels[12, 34]. Therefore, transition metal oxides and their hybrid materials have attracted much attention in recent years, and the OER on the transition metal-based electrocatalysts are stable in alkaline media[12, 21, 35]. However, the catalytic activities of these catalysts' family are still much lower than the noble metal-based catalysts[12, 21, 35]. In the following sections, 1.4.1 and 1.4.2, the recent advancements in CoO_x- and Ru-based electrocatalysts will be discussed, followed by the question of what improvements could be made for designing efficient OER catalysts.

1.4.1 Cobalt oxide (CoOx) -based electrocatalysts

Among transition metal and their oxide-based electrocatalysts, CoO_x (CoO, Co_2O_3, and Co_3O_4) based catalysts for OER have been widely studied due to their earth-abundance and promising catalytic activity and stability in alkaline media[23, 36-40]. However, the overpotentials of these catalysts are still higher than precious metals such as Ru and Ir. Therefore, improving the catalytic performance of CoO_x-based catalysts is important to its potential application.

Extensive efforts have been undertaken to enhance their catalytic performance by modifying electronic properties[41, 42], surface[43, 44] and crystalline structures[45]. The electrocatalytic properties of recently reported Co-based catalysts for OER are summarized in Table 1.1.

Table 1.1. Summary of recently reported Co-based OER catalysts.

Catalyst	Electrolyte	Activity	Tafel slope / mV dec^{-1}	Stability	Ref.
CoNi-SAs/NC	1 M KOH	340 mV@10 mA cm^{-2}	58.7	-	[46]
IrCo-N-C	0.1 M KOH	330 mV@10 mA cm^{-2}	79.0	2000 CV cycles	[47]
Co@N-C/PCNF	1 M KOH	289 mV@10 mA cm^{-2}	91.8	10 h @ 10mA cm^{-2}	[48]
L-Co_3O_4 NSs	1 M KOH	290 mV@10 mA cm^{-2}	76.0	20 h @ 20 mA cm^{-2}	[49]
V-Co_3O_4	0.1 M KOH	351 mV@10 mA cm^{-2}	-	-	[50]
Co-Co_2P@NCNTs	1 M KOH	350 mV@10 mA cm^{-2}	-	11 h @ 1.7 V_{RHE}	[51]
CoO_x@CoN_y/NCNF	0.1 M KOH	450 mV@10 mA cm^{-2}	85.6	-	[52]
Fe_3O_4@CoO NCs	0.1 M KOH	390 mV@10 mA cm^{-2}	89.3	3000 CV cycles	[53]
$Cu(OH)_2$@CoNiCH NTs/CF	1 M KOH	288 mV@30 mA cm^{-2}	74.0	1000 CV cycles	[54]
Co_3O_4/CoS	0.1 M KOH	349 mV@10 mA cm^{-2}	66.6	1000 CV cycles	[55]
Co_3O_4/$Fe_{0.33}Co_{0.66}P$	1 M KOH	215 mV@50 mA cm^{-2}	59.8	3000 CV cycles	[56]
Au@Co_3O_4/C	0.1 M KOH	350 mV@10 mA cm^{-2}	60.0	5 h@1.54 V	[57]
AuNCs@$Co(OH)_2$	0.1 M KOH	350 mV@10 mA cm^{-2}	72.0	600 CV cycles	[58]
Au@CoOx	1 M KOH	367 mV@10 mA cm^{-2}	92.0	2 h@10 mA cm^{-2}	[42]
$P_{8.6}$-Co_3O_4/NF	1 M KOH	260 mV@10 mA cm^{-2}	60.0	25 h@ 1.7 V_{RHE}	[59]

1D nanorod Co_3O_4	1 M KOH	414 mV@10 mA cm^{-2}	70	24 h@10	[60]
2D nanosheet		374 mV@10 mA cm^{-2}	65	mA cm^{-2}	
Co_3O_4		433 mV@10 mA cm^{-2}	72		
3D nanocube Co_3O_4					
Co_3O_4-R hexagonal platelets					[61]
Co_3O_4-2.5	0.1 M KOH	354 mV@0.1 mA cm^{-2}	51.0	-	
Co_3O_4-5.0		364 mV@0.1 mA cm^{-2}	53.0		
Co_3O_4-7.5		375 mV@0.1 mA cm^{-2}	57.0		
R -the ratios of (111)/(110) facets					
0.1Fe-CoNiO/NF	1.0 M KOH	240 mV@10 mA cm^{-2}	-	-	[62]
Co_3O_4/CeO_2 NHs	1.0 M KOH	270 mV@10 mA cm^{-2}	60.0	10 h@10 mA cm^{-2}	[63]
Co-C_3N_4/CNT	1.0 M KOH	380 mV@10 mA cm^{-2}	68.4	3000 CV cycles	[64]
SC CoO NRs	1.0 M KOH	330 mV@10 mA cm^{-2}	44.0	-	[65]
ODAC-CoO-30	0.1 M KOH	364 mV@10 mA cm^{-2}	68.6	12 h@10 mA cm^{-2}	[66]
CoO/hi-Mn_3O_4	1.0 M KOH	378 mV@10 mA cm^{-2}	61.0	2 h@10 mA cm^{-2}	[65]
Co_3O_4/N-rmGO	0.1 M KOH	310 mV@10 mA cm^{-2}	67.0	1500 CV cycles	[41]
CoO/CoFe LDH	1.0 M KOH	254 mV@10 mA cm^{-2}	34.0	12 h@10 mA cm^{-2}	[67]

Controlling the metal oxide during oxidation reactions is an effective strategy for enhancing the catalytic properties of catalysts[68, 69]. The surface structure of the oxide affects the catalytic activity by changing the electronic properties[43, 65] and the density of active sites present at the surface[70, 71]. For example, the Sharp group demonstrated that cobalt hydroxide, $Co(OH)_2$, is more active than the spinel Co_3O_4 because its open and layered structure provides fast charge transfer and thus, enables a higher number of active sites[72]. Later, they found that the $Co(OH)_2$ oxidizes to form active CoO(OH) phase during catalytic activation using spectroscopic techniques, an active surface to promote the formation of active sites further[73]. In contrast, the spinel Co_3O_4 phase partially converts to CoO(OH). This concept has been further investigated by the Strasser group to understand the transformation of the CoO_x catalysts (a crystalline spinel Co_3O_4, a wurtzite w-CoO, a rock salt rs-CoO, and a heterogenite CoOOH) during OER at the atomic scale with the help of spectroscopic techniques and surface voltammetry coupled with theoretical calculations[74]. Except for crystalline Co_3O_4, which retains its structure, other CoO_x catalysts convert irreversibly to active $CoO_x(OH)_y$ phase after OER conditioning. The activity trend was observed in the order of Co_3O_4 < w-CoO < rs-CoO < CoOOH. The excellent activity of CoOOH catalyst can be attributed to the formation of $CoO_x(OH)_y$ surface, which contains both μ_2-O and μ_2-OH sites responsible for the generation of O-O bond and deprotonation of water molecules, and its 3D cross-linked layered structure. Therefore, for highly OER active Co-based catalytic nanoparticles, control over the Co-oxide surface structure with retention of the lower oxidation state $Co(OH)_2$ at the surface is a desirable requirement.

Furthermore, improving the electronic properties of CoO_x-based electrocatalysts is a promising approach for enhancing their catalytic

activity. One efficient way to enhance the electronic conductivities of CoO_x catalysts is to synthesize hybrid materials using different substrates/cores such as graphene[41], carbon nanotubes[75], and metals [76, 77]. There are a number of studies that have aimed to develop Co and Au-based hybrid material electrocatalysts. For example, Yeo and Bell (2011) first reported that Au substrate has enhanced the catalytic activity of cobalt oxide the most when compared with other metal substrates, including Pt, Pd, Cu, and Co, owing to its high electronegativity[77]. Following this paper, considerable studies have been carried out to synthesize cobalt oxide and Au hybrid materials for OER **(Figure 1.3 a-b)**. Zhuang et al. (2014) synthesized monodispersed Au-Co_3O_4 core-shell nanoparticles and compared these with a mixture of Au and Co_3O_4 nanoparticles Figure 1.3a[57]. The core-shell NPs show enhanced catalytic property, and they confirmed that core-shell structure has a strong synergistic effect between core and shell. Lu et al. (2016) investigated the effect of the composition of Au and cobalt oxide in Au@Co_3O_4 nanoparticles on catalytic activity for OER Figure 1.3b[78]. Zhou et al. (2016) synthesized AuNCs@$Co(OH)_2$ by depositing $Co(OH)_2$ on Au nanorods and evaluated their OER activity Figure 1.3c[58]. Jaramillo's group (2017) reported the synthesis of Au and 3d transition metal oxide core-shell nanoparticles using a wet chemical method and investigated their electrocatalytic properties Figure 1.3d[42].

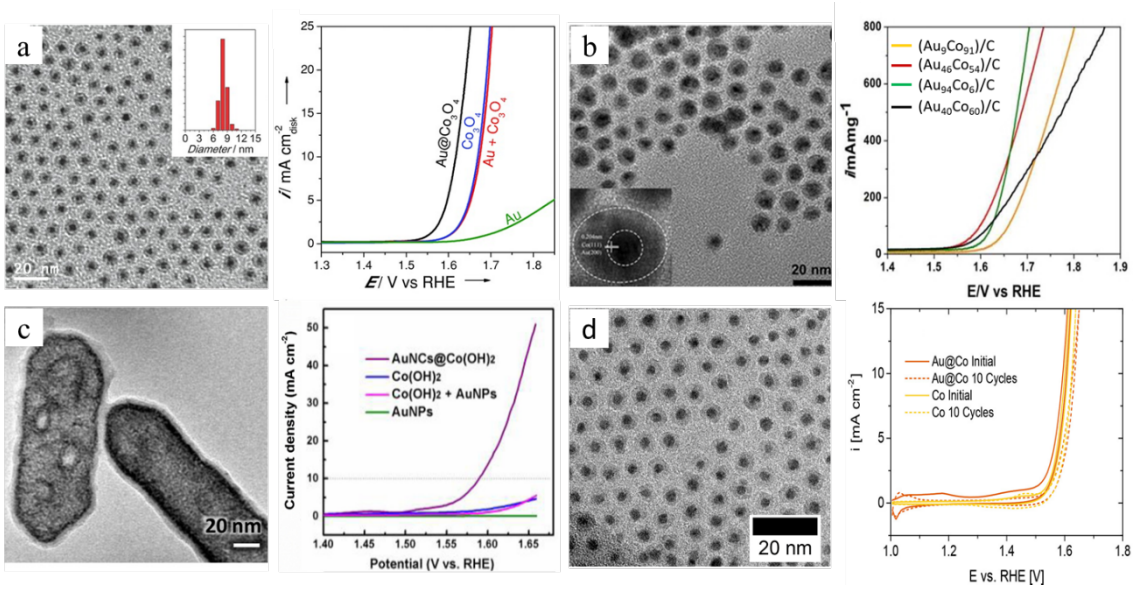

Figure 1.3. TEM images of Au-CoOx core-shell nanoparticles and related polarization curves: **(a)** Au@Co_3O_4 core-shell NCs[57], inset: related histogram, **(b)** Au@Co/C (Au_9Co_{91})[78], **(c)** AuNCs@$Co(OH)_2$ Au-rod-$Co(OH)_2$ core-shell nanoparticles[58], **(d)** Au@CoOx[42]. Reproduced with permission from Zhuang et al[57], Lu et al[78], Zhou et al[58], and Strickler et al[42].

Based on these studies, it can be concluded that the Au cores improve the catalytic activity of cobalt oxide for the following reasons: (i) Reaction kinetics are improved because Au acts as an electron sink and oxidizes Co from Co^{II}/Co^{III} to the more active Co^{IV}. (ii) Presenting Au cores/substrates increases the binding energy of Co shells due to the d-band shift, which decreases the activation energy of the total reaction.

In addition, controlling the shape of Co catalysts is a promising approach for designing efficient electrocatalysts [20, 65, 79]. Shaped nanoparticles have defined facets, which have different atomic arrangements and distribution of surface atoms, resulting in changes in the charge-transfer properties and binding energies between catalytic active sites and reaction intermediates [20, 79].

For example, Chen et al. investigated the facet-dependent catalytic activity and stability of Co_3O_4 on OER in alkaline media[79]. In this study, well-defined cubic, truncated octahedra, and octahedra Co_3O_4 nanoparticles were compared for their activity in the OER. The results showed that octahedra nanoparticles exposing predominantly (111) surfaces show greater catalytic activity than the other catalysts, whereas cubic nanoparticles, which expose predominantly (100) surfaces, exhibit higher stability. These results correlate with the higher Co ion density and higher reactivity of (111) facets and lower surface energy of (100) facets. The Qiao group reported the synthesis of one-dimensional cobalt oxide nanorods by creating oxygen vacancies on pyramidal nanofacets (Figure 1.4)[65].

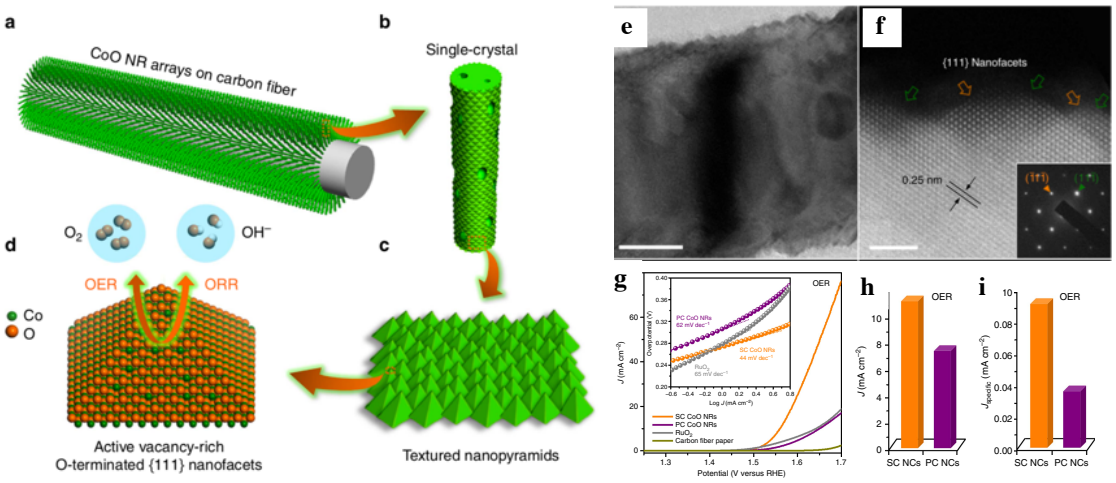

Figure 1.4. (a-d) Schema of engineering the surface of SC CoO NRs. **(e)** High magnification TEM image of SC CoO NR. Scale bar, 20 nm. **(f)** High-resolution HAADF-STEM image SC CoO NR. Inset: Selected area electron diffraction pattern from [110] zone axis. Scale bar = 2 nm. **(g)** The catalytic activity study by linear sweep voltammetry (LSV) of SC, PC CoO NRs, and commercial RuO_2 catalysts. Inset: Tafel plots. (**h-i)** Intrinsic OER activity of SC CoO NCs and PC CoO NCs. Reproduced with permission from Ling et al.[65]

These nanorods exhibit enhanced catalytic activity for both ORR and OER (Figure 1.4). The superior electrocatalytic properties were explained by a rapid charge transfer in the 1D structure and optimal adsorption energies between reaction intermediates and the catalyst surface (Figure 1.4).

Branched nanoparticles are of significant interest as electrocatalysts owing to their three-dimensional (3D), crystalline, and faceted structures[80-83]. Inspired by the recent advances in branched nanoparticle electrocatalysts and based on the previous studies mentioned above, it can be seen that designing Co branched nanoparticles with a 3D structure is a promising way to improve the OER activities of Co-based catalysts due to the following reasons: (i) the low index facets on branches might enable the formation of more active $Co(OH)_2$ layer in the near-surface region, (ii) 1D morphology of branches improves the charge transfer on the surface, (iii) 3D structures provide high surface area.

1.4.2 Ru -based electrocatalysts

Ru is the most active OER electrocatalyst that requires very low overpotential to generate a large anodic current density[32, 33, 84, 85]. As shown in the Volcano plot, Ru catalyst binds moderately to oxygen intermediates that promote oxygen adsorption and desorption processes on its surface[32, 33, 84, 85]. As a result, this exhibits excellent catalytic activity for OER[32, 33, 84]. However, Ru is unstable at the potential relevant to OER at low pH conditions because it oxidizes to soluble products at this condition, according to the Pourbaix diagram[32, 33, 84]. Furthermore, its high cost and fast dissolution rate limit the benefits of Ru electrocatalysts in practical application[32, 33, 84]. Therefore, reducing the amount of Ru by enhancing its catalytic activity and stability is crucial to enable the large-scale use of Ru in OER.

Until now, extensive research efforts have been undertaken to improve the performance of Ru-based catalysts[32, 33, 84]. The catalytic activity of Ru nanocrystals can be improved by modifying its surface[81, 82, 86] and electronic structures[87, 88]. The most common strategies to improve the electrocatalytic properties of Ru catalysts include (i) synthesizing Ru nanocrystals with well-defined size and shape and controlled crystal-phase[87, 89, 90], (ii) making bimetallic Ru-based catalysts such as core-shell, alloy, and doped nanoparticles[91-93], and (iii) compositing Ru with carbon-based nanomaterials[85]. The electrocatalytic properties of recently reported Ru-based catalysts for OER are summarized in Table 1.2.

Table 1.2. Summary of recently reported Ru-based OER catalysts.

Catalysts	Electrolyte	Activity	Tafel slope / mV dec-1	Stability	Ref.
Ru@IrO_x	0.5 M H_2SO_4	282 mV@10 mA cm^{-2}	69.1	24 h@1.5 V_{RHE}	[94]
RuCu alloy NCs	0.5 M H_2SO_4	270 mV@10 mA cm^{-2}	75.8	24 h@10 mA cm^{-2}	[95]
Mn-RuO_2	0.5 M H_2SO_4	158 mV@10 mA cm^{-2}	43.0	10 h@10 mA cm^{-2}	[96]
Cu-doped RuO_2	0.5 M H_2SO_4	188 mV@10 mA cm^{-2}	44.0	8 h@10 mA cm^{-2}	[97]
hollow Pt/NiO/RuO_2	0.1 M $HClO_4$	239 mV@10 mA cm^{-2}	52.0	2000 CV cycles	[98]
Co-RuIr alloy	0.1 M $HClO_4$	235 mV@10 mA cm^{-2}	66.9	25 h@10 mA cm^{-2}	[93]
Co-doped RuO_2 NWs	0.5 M H_2SO_4 1.0 M KOH	200 mV@10 mA cm^{-2} 235 mV@10 mA cm^{-2}	60.0 62.0	1000 CV cycles under both conditions	[99]
$Cr_{0.6}Ru_{0.4}O_2$	0.5 M H_2SO_4	178 mV@10 mA cm^{-2}	58.0	10 h@10 mA cm^{-2}	[100]
Ru_1-Pt_3Cu	0.1 M $HClO_4$	220 mV@10 mA cm^{-2}	-	28 h@10 mA cm^{-2}	[85]
RuO_2 nanosheets	0.5 M H_2SO_4	260 mV@10 mA cm^{-2}	54.0	2 h@10 mA cm^{-2}	[101]
$NaRuO_2$ nanosheets	0.1 M $HClO_4$	255 mV@10 mA cm^{-2}	38.0	6 h@1 mA cm^{-2}	[102]
Ultrafine defective RuO_2	0.5 M H_2SO_4	179 mV@10 mA cm^{-2}	36.9	20 h@10 mA cm^{-2}	[103]
RuCu nanosheets	0.5 M H_2SO_4	236 mV@10 mA cm^{-2}	40.4	12 h@10 mA cm^{-2}	[104]
fcc-Ru octahedra	0.5 M H_2SO_4	168 mV@10 mA cm^{-2}	47.8	-	[90]

fcc-Ru truncated cubes	0.5 M H_2SO_4	189 mV@10 mA cm^{-2}	51.2	-	[90]
$CaCu_3Ru_4O_{12}$	0.5 M H_2SO_4	171 mV@10 mA cm^{-2}	40.0	24 h@10 mA cm^{-2}	[105]
$RuIrO_x$ nano-netcages	0.5 M H_2SO_4	233 mV@10 mA cm^{-2}	42.0	3000 CV cycles	[106]
a-RuTe PNRs	0.5 M H_2SO_4	245 mV@10 mA cm^{-2}	47.0	24 h@7 mA cm^{-2}	[107]
Pd-Ru core-shell NPs (1.2 nm shell)	0.1 M $HClO_4$	220 mV@10 mA cm^{-2}	-	-	[108]
Au-Ru branched NPs	0.1 M $HClO_4$	220 mV@10 mA cm^{-2}	62.0	1000 CV cycles	[82]
Pd-Ru branched NPs	0.1 M $HClO_4$	225 mV@10 mA cm^{-2}	61.0	2 h@η=250 mV	[81]

Controlling the shape of Ru nanoparticles is one of the viable strategies to enhance the catalytic properties by altering their surface structure.

The surface facets of Ru nanocrystals play a key role in their catalytic properties[20, 84]. The chemical reactivity of catalysts is strongly dependent on the exposed facets of nanocrystals owing to their different surface energies and atomic coordination numbers[20, 84]. A number of reports have been undertaken to elucidate the effect of the surface structure of Ru on its catalytic performance[86, 109-112]. For instance, Kelsey et al. investigated the effect of (100) and (110) surfaces of RuO_2 and IrO_2 on the OER in alkaline media by growing rutile films on substrates[109]. More open Ru (100) and Ir (100) surfaces showed greater activity than the (110) surfaces because of the higher availability of Ru atoms.

Further studies demonstrated that there is no linear relationship between the number of coordinatively unsaturated Ru sites (Ru_{cus}) and catalytic activity as the (100) (7 $Ru_{cus}\,nm^{-2}$) and (101) (8 $Ru_{cus}\,nm^{-2}$) facets exhibited 7- and 2.5-fold higher activities than the (110) (5 $Ru_{cus}\,nm^{-2}$)[113]. This correlation suggested that the catalytic activities depend not only on the number of coordinatively unsaturated atoms but also on the reaction intermediates and the interaction between Ru_{cus} and water molecules. Recent work conducted by Reshma et al. supports this presumption[86]. They investigated OER on three different (100), (101), and (110) RuO_2 surfaces by operando analysis coupled with DFT computation to elucidate the reaction mechanism at the molecular level. The increased intrinsic activities on (100) and (101) Ru_{cus} surfaces can be attributed to the decreased adsorption energies to intermediates depending on the local environments of Ru_{cus}, which results in improved reaction kinetics on the rate-determining step (the dehydrogenation of -OO-H).

These studies highlighted that synthesizing nanoparticle with well-defined surface facets is of great significance for engineering electrocatalysts.

Control over surface structures can be achieved by tuning the shape[89, 90] and crystal structure[81, 82, 87] of Ru nanocrystals. The significant improvements of catalytic activities in OER, HER, and other catalytic reactions were obtained by designing shape-controlled Ru nanocrystals including porous Ru nanocrystals[114], Ru dendrites[115], plates[116], nanosheets[102], cubic Ru nanoparticles[102], etc. For example, the Xia group recently developed *fcc*-Ru octahedra nanocrystals with preferential exposure of (111) facets using a seed-mediated growth approach (Figure 1.5)[90].

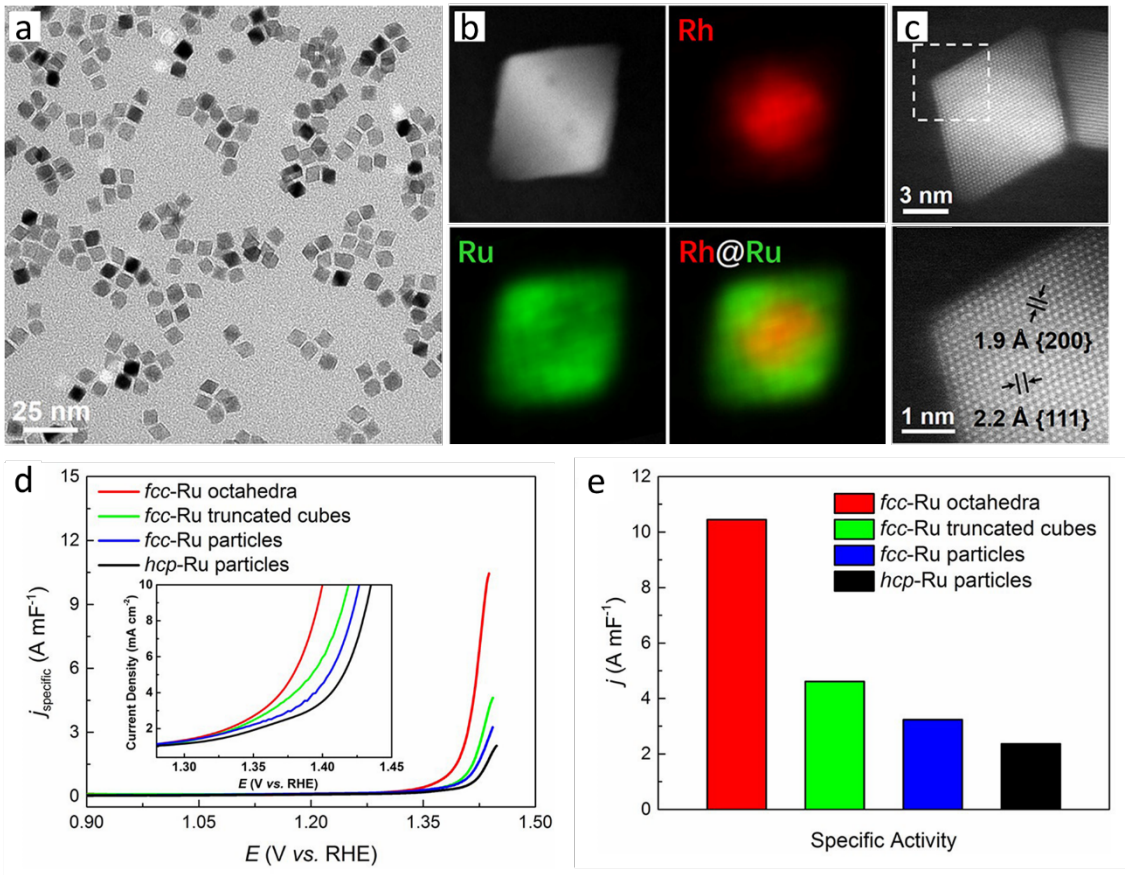

Figure 1.5. (a) TEM image of Ru octahedral nanocrystals, (b) HAADF-STEM image and EDX mapping of an octahedral nanocrystal, (c) HRTEM image of a branched nanoparticle and magnified part in the black box showing the {200} and {111} facets. Reproduced with permission from Zhao et al.[90]

The effect of crystal-phase and facets on the catalytic activity was then systematically investigated by comparing the octahedra nanocrystals with fcc-Ru truncated nanocubes, *hcp*- and *fcc*-Ru nanocrystals. They found that (111) facets are more active than the (100) facets, and fcc-crystalline structure is more efficient than hcp-Ru for catalyzing OER. The reasons behind the enhanced catalytic properties of Ru octahedra nanocrystals were not explained in this work.

In addition to shape control, considerable efforts have been devoted to improving the catalytic performance of Ru by tuning its crystal properties. Controlling the crystal phase modifies the surface and electronic structures of the catalyst by restructuring all the atoms and thus improving its catalytic performance. For instance, Li et al. synthesized highly crystalline *hcp*-Ru nanocrystals through thermal annealing, which significantly enhanced HER catalytic activity and stability compared to those with poor crystallinity. Furthermore, the Xia group developed various hollow *fcc*-Ru nanocrystals such as cubic, octahedral, and icosahedra nanocages via a seed-mediated approach. These nanoparticles showed improved catalytic activities toward ammonia synthesis. Hierarchical 4H/fcc Ru nanotubes with novel crystal phase have been recently synthesized by Zhang et al., and they exhibited excellent HER activities in alkaline media (Figure 1.6).

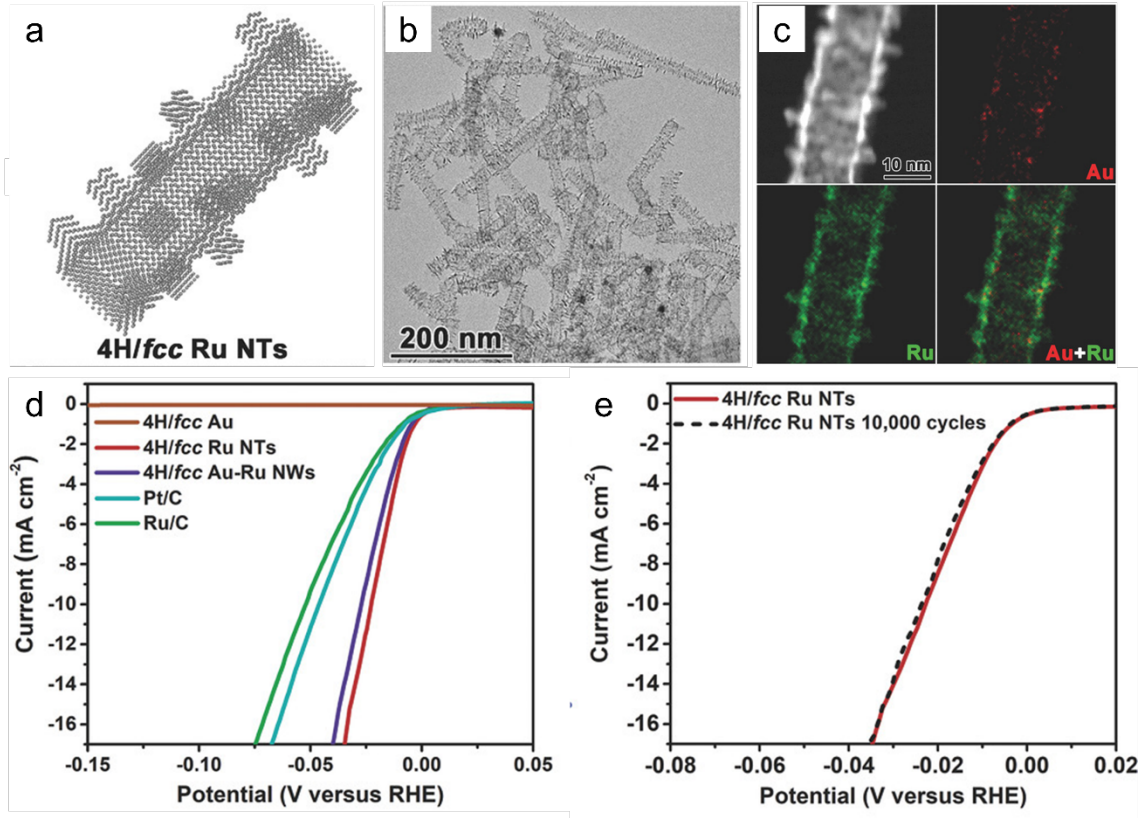

Figure 1.6. (a) Schematic illustration of a hierarchical 4H/fcc Ru NT, (b) TEM image of hierarchical 4H/fcc Ru NTs, (c) HAADF-STEM image and EDX mapping of an individual hierarchical 4H/fcc Ru NTs, (d) HER activities of 4H/fcc Ru NTs, 4H/fcc Au-Ru nanowires, 4H/fcc Au, Pt/C, Ru/C, and commercial Pt/C, (e) Catalytic stability of 4H/fcc Ru NCs. Reproduced with permission from Lu et al.[87]

The enhanced activities of nanocrystals with controlled crystallinity can be attributed to the change in surface energy depending on exposed facets[87, 89, 117]. In addition to the novel crystal phase, the excellent HER activity of 4H/fcc Ru NTs can be ascribed to (i) enhanced charge transfer due to its 1D structure, (ii) efficient utilization of atoms due to the defects on their surface and hollow structure[87].

Combining the control of shape and crystal structure, our group (Gloag et al.) has recently developed three-dimensional *hcp*-Ru branched nanoparticles using a cubic-core hexagonal-growth approach[81, 82] (Figure 1.7).

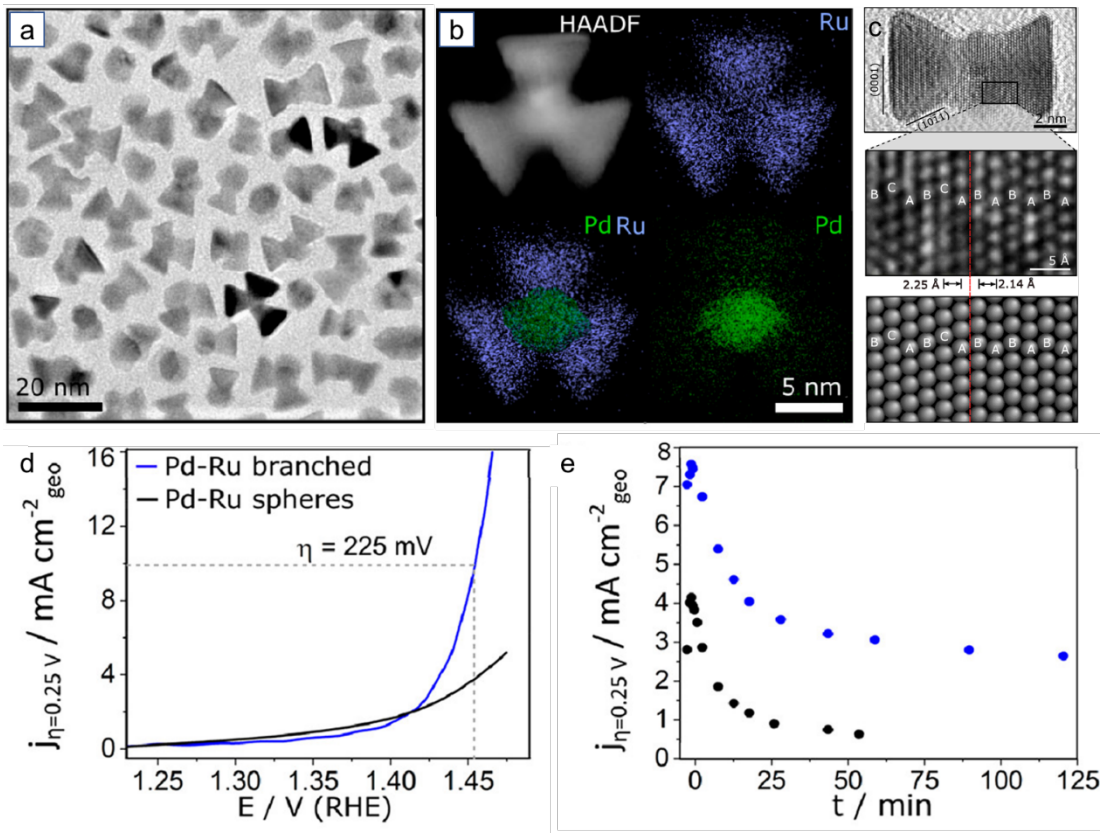

Figure 1.7. (a) TEM image of Pd-Ru branched nanoparticles, (b) HAADF-STEM image and EDX mapping of a branched nanoparticle, (c) HRTEM image of a branched nanoparticle showing the {10-11} and {0001} facets, magnified part in the black box, and corresponding model showing the atomic arrangement of the particle, (d) OER activities of Pd-Ru branched and sphere nanoparticles, and (e) Stability test of the branched nanoparticles. Reproduced from Lucy et al. [81]

These branched nanoparticles showed superior catalytic performance compared to polycrystalline Ru. The basis for the enhancement of catalytic performance are potentially due to (i) the slow dissolution rate of low indexed *hcp*- {10-11} and {0001} facets and (ii) the highly exposed surface area of three-dimensional structure.

The aim here is to leverage the advantages of the Ru-Pd branched nanoparticles by tuning the surface facets and branch number. It is also hypothesized that the number of active sites on Ru branches would increase

by engineering alloyed branched nanoparticles growing RuCo branches on a Pd core.

Although great progress has been made on synthesizing 3D branched nanoparticles for OER, synthesizing 3D bimetallic nanoparticles has been very challenging. Therefore, colloidal nanoparticle synthesis will be discussed in the next section.

1.5 Organic solution phase syntheses method

The physical and chemical properties of nanoparticles strongly depend on their size, shape, composition, and structure. Therefore, it is important to synthesize nanoparticles with a well-defined structure. Solution phase organic synthetic methods have been extensively studied to prepare monodispersed nanoparticles in terms of size and shape[118-121]. Understanding the mechanism of synthesis and the effect of reaction parameters on the final nanocrystals is crucial to synthesize nanocrystals with controlled size and shape. The mechanism is expected to be based on the classic Lamer-Dinegar model shown in Figure 1.8[122-124].

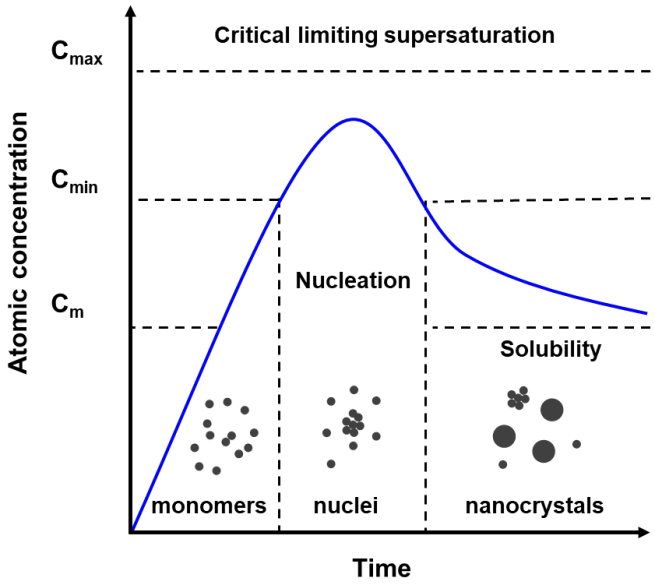

Figure 1.8. Diagram of the classic Lamer-Dinegar model. Reproduced from Xia et al.[122]

The Lamer-Dinegar model consists of three main stages including (i) nucleation, in which a precursor is either decomposed or reduced to the zero-valent metallic atoms, (ii) evolution of nuclei or the formation of seeds when

the atomic concentration reaches the supersaturation point, and (iii) growth stage where atoms continue to deposit on the surface of the nanocrystals.

Using a one-pot approach, both homogeneous (or self-nucleation) and heterogeneous nucleation occur concurrently, which can result in polydispersed nanoparticles in terms of size and shape. On the contrary, during a seed-mediated approach, heterogeneous nucleation, in which adatoms grow on the well-defined seed surface, occurs in monodispersed nanoparticles in terms of size and shape. In seed-mediated growth, the nanocrystal size can be controlled by separating nucleation events from the growth stage and using a capping agent. The final nanocrystals shape can be controlled by seed structures[123], the rate of adatom diffusion to a surface[121], as well as surfactants[122, 125].

Firstly, the crystallinity or internal structure of a seed nanocrystal is one of the main parameters that affects the final nanocrystal structure[123]. The final nanocrystal shape depends on the lattice mismatch between a seed and second metal and the energy difference between exposed facets of a seed.

Reaction parameters, including the precursor and seed concentration, temperature, and pressure, also play key roles in synthesizing thermodynamically and kinetically controlled nanoparticles. Furthermore, both thermodynamics and kinetics play important roles in the evolution of nanocrystals with different geometric shapes[121]. When nanocrystals are grown under thermodynamic control, the diffusion rate of adatoms is higher than that of the deposition rate resulting in thermodynamically stable spherical nanoparticles. On the other hand, when the nanocrystals grow under kinetic control when the deposition rate of adatoms is higher than the diffusion rate of the adatoms. In other words, adatoms grow directly on the

crystal facets with higher energy resulting in shaped or branched nanoparticles.

Finally, the surfactants play an essential role in the synthesis of nanocrystals in the solution phase. Firstly, surfactants adsorb to the nanoparticle surface and reduce agglomeration. Surfactants can also passivate particular facets resulting in anisotropic growth. The most common surfactants in solution phase synthesis are alkylphosphine oxides, alkylphosphonic acids, alkyl phosphines, fatty acids, amines, and nitrogen-containing aromatics[126]. Surfactants can be chosen based on adhesion energy to the nanocrystal and steric hindrance.

Therefore, all reaction parameters play important roles in developing nanoparticles with controlled size and shape.

1.5.1 Bimetallic branched nanoparticles

Since the breakthrough work of Alivisatos group on branched CdTe nanocrystals synthesis using polymorphism growth in organic solution-phase, polymorphism growth has been widely used to synthesize branched semiconductor nanocrystals with well-defined structures[119, 127]. In this work, they synthesized CdTe tetrapods using a cubic-core hexagonal-branch growth approach (a type of seed-mediated growth) in organic solution-phase synthesis (Figure 1.9). The reaction consists of two stages. Firstly, the cubic CdTe phase forms in the nucleation stage at a lower temperature. Then, at a higher temperature in the presence of n-octadecylphosphonic acids (ODPA) acids as a surfactant, the hexagonal CdTe branches grow on the {111} facets of the cubic phase. The formation of two phases occurs at two different temperatures owing to their energy discrepancies. The growth of hexagonal branches along the c-axis can be attributed to (i) the identical atomic

arrangements between {111} and {0001} facets of cubic and hexagonal structures and (ii) the passivated lateral facets ({$10\bar{1}0$}) of branches by the ODPA.

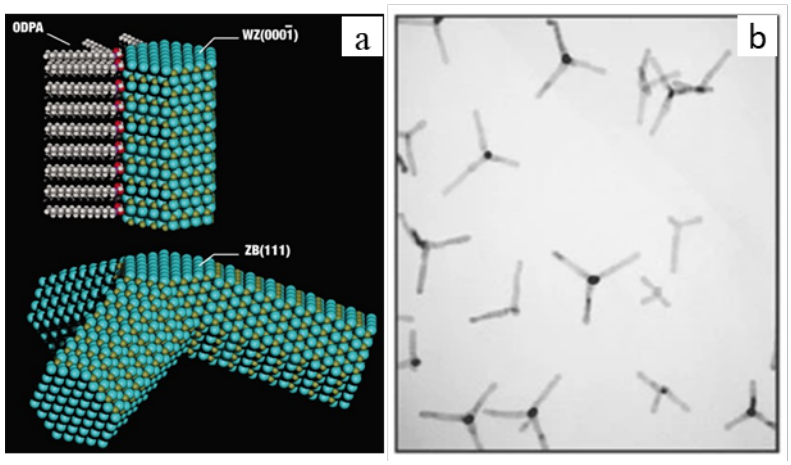

Figure 1.9. (a) Models showing a branch of the nanocrystal in which lateral sides passivated by ODPA molecules and a tetrapod CdTe nanocrystal. ZB-zinc blende -cubic phase, WZ -wurtzite -hexagonal phase and Cd atoms -yellow, Te atoms -blue. (b) TEM image of CdTe branched nanocrystal synthesized at Cd/Te 3:1 and Cd/ODPA 1:5. Reproduced from Manna et al.[127]

Furthermore, previous research in our group confirmed that the polymorphism growth can be used to synthesize other branched metallic nanostructures[128]. With these merits, extensive works have been published for the synthesis of metallic branched nanocrystals[81-83]. However, there is a limited number of studies for the bimetallic branched nanoparticles with a well-defined structure.

1.6 Project aims

This dissertation focuses on the development of bimetallic branched nanoparticles for improved OER electrocatalysts. The goal of this thesis are the following four aims.

Aim 1 (Chapter 3) is to develop a synthetic protocol for the synthesis of novel Co branched nanoparticles and to determine the experimental conditions for controlling the branch length and number of Ru branched nanoparticles. The initial step for this goal is to synthesize the cubic Au and Pd seeds with tunable sizes. The next step is optimizing the reaction parameters to grow Co or Ru branches on the seeds. The resultant branched nanoparticles will be further used as OER electrocatalysts in Chapters 3 and 4.

Aim 2 (Chapter 4) is to understand the formation of active sites on highly crystalline Co branched nanoparticles for OER. In order to achieve this, Co branched nanoparticles consisting of a Co shell over an Au core and Co branches will be synthesized using a cubic-core hexagonal-branch approach in an organic solution phase. The effect of the branched nanoparticle oxide layer on active site formation during OER will be compared to Co spherical and CoO_x nanoparticles. This part of the project is hoped to contribute to the development of electrocatalysts by introducing a new bimetallic (Co-Au) branched nanoparticle and providing a method of control over the surface oxides on nanoparticles.

Aim 3 (Chapter 5) is to study the effect of surface facets and branch number of Ru-Pd branched nanoparticles for OER. First, Pd-Ru branched nanoparticles with controlled branch length and branch number will be synthesized using a seed-mediated approach, tuning surface facets by varying the branch length. Second, a systematic exploration of the OER

process on branched nanoparticles as a function of branch length and branch number. This is aimed at exploring the advantages of branched nanoparticles as electrocatalysts fully.

Aim 4 (Chapter 6) is to elucidate the catalytic reaction of RuCo-Pd branched nanoparticles consisting of RuCo alloyed branches and a Pd core for OER. The first step towards this goal is to synthesize RuCo-Pd alloyed branched nanoparticles. The next step is to examine the effect of Co leaching during electrochemical pre-treatment on the formation of new active sites on Ru branches and, therefore, on their catalytic performance. Finally, this approach may be applied to other electrocatalysts to improve their catalytic performance.

1.7 References

1. Chu, S.; Majumdar, A., Opportunities and challenges for a sustainable energy future. *Nature* **2012,** *488* (7411), 294-303.

2. Turner, J. A., Sustainable Hydrogen Production. *Science* **2004,** *305* (5686), 972-974.

3. Moriarty, P.; Honnery, D., Intermittent renewable energy: The only future source of hydrogen? *International Journal of Hydrogen Energy* **2007,** *32* (12), 1616-1624.

4. Turner, J. A., A Realizable Renewable Energy Future. *Science* **1999,** *285* (5428), 687-689.

5. Seh, Z. W.; Kibsgaard, J.; Dickens, C. F.; Chorkendorff, I.; Norskov, J. K.; Jaramillo, T. F., Combining theory and experiment in electrocatalysis: Insights into materials design. *Science* **2017,** *355* (6321).

6. Anantharaj, S.; Aravindan, V., Developments and Perspectives in 3d Transition-Metal-Based Electrocatalysts for Neutral and Near-Neutral Water Electrolysis. *Advanced Energy Materials* **2019,** *10* (1).

7. Ball, M.; Weeda, M., The hydrogen economy – Vision or reality? . *International Journal of Hydrogen Energy* **2015,** *40* (25), 7903-7919.

8. Wei, C.; Rao, R. R.; Peng, J.; Huang, B.; Stephens, I. E. L.; Risch, M.; Xu, Z. J.; Shao-Horn, Y., Recommended Practices and Benchmark Activity for Hydrogen and Oxygen Electrocatalysis in Water Splitting and Fuel Cells. *Adv Mater* **2019,** *31* (31), e1806296.

9. Hwang, J.; Rao, R. R.; Giordano, L.; Katayama, Y.; Yu, Y.; Shao-Horn, Y., Perovskites in catalysis and electrocatalysis. *Science* **2017,** *358* (6364), 751-756.

10. Li, Z.; Ji, S.; Liu, Y.; Cao, X.; Tian, S.; Chen, Y.; Niu, Z.; Li, Y., Well-Defined Materials for Heterogeneous Catalysis: From Nanoparticles to Isolated Single-Atom Sites. *Chem Rev* **2019**.

11. Hu, C.; Zhang, L.; Gong, J., Recent progress made in the mechanism comprehension and design of electrocatalysts for alkaline water splitting. *Energy & Environmental Science* **2019,** *12* (9), 2620-2645.

12. Zhao, C. X.; Liu, J. N.; Wang, J.; Ren, D.; Li, B. Q.; Zhang, Q., Recent advances of noble-metal-free bifunctional oxygen reduction and evolution electrocatalysts. *Chem Soc Rev* **2021,** *50* (13), 7745-7778.

13. Suen, N. T.; Hung, S. F.; Quan, Q.; Zhang, N.; Xu, Y. J.; Chen, H. M., Electrocatalysis for the oxygen evolution reaction: recent development and future perspectives. *Chem Soc Rev* **2017,** *46* (2), 337-365.

14. Tee, S. Y.; Win, K. Y.; Teo, W. S.; Koh, L. D.; Liu, S.; Teng, C. P.; Han, M. Y., Recent Progress in Energy-Driven Water Splitting. *Adv Sci (Weinh)* **2017,** *4* (5), 1600337.

15. Huang, Z.-F.; Wang, J.; Peng, Y.; Jung, C.-Y.; Fisher, A.; Wang, X., Design of Efficient Bifunctional Oxygen Reduction/Evolution Electrocatalyst: Recent Advances and Perspectives. *Advanced Energy Materials* **2017,** *7* (23).

16. Katsounaros, I.; Cherevko, S.; Zeradjanin, A. R.; Mayrhofer, K. J., Oxygen electrochemistry as a cornerstone for sustainable energy conversion. *Angew Chem Int Ed Engl* **2014,** *53* (1), 102-21.

17. An, L.; Wei, C.; Lu, M.; Liu, H.; Chen, Y.; Scherer, G. G.; Fisher, A. C.; Xi, P.; Xu, Z. J.; Yan, C. H., Recent Development of Oxygen Evolution Electrocatalysts in Acidic Environment. *Adv Mater* **2021,** *33* (20), e2006328.

18. Fabbri, E.; Habereder, A.; Waltar, K.; Kötz, R.; Schmidt, T. J., Developments and perspectives of oxide-based catalysts for the oxygen evolution reaction. *Catal. Sci. Technol.* **2014,** *4* (11), 3800-3821.

19. Hong, W. T.; Risch, M.; Stoerzinger, K. A.; Grimaud, A.; Suntivich, J.; Shao-Horn, Y., Toward the rational design of non-precious transition metal oxides for oxygen electrocatalysis. *Energy & Environmental Science* **2015,** *8* (5), 1404-1427.

20. Strasser, P.; Gliech, M.; Kuehl, S.; Moeller, T., Electrochemical processes on solid shaped nanoparticles with defined facets. *Chem Soc Rev* **2018,** *47* (3), 715-735.

21. Han, L.; Dong, S.; Wang, E., Transition-Metal (Co, Ni, and Fe)-Based Electrocatalysts for the Water Oxidation Reaction. *Adv Mater* **2016,** *28* (42), 9266-9291.

22. Tao, H. B.; Fang, L.; Chen, J.; Yang, H. B.; Gao, J.; Miao, J.; Chen, S.; Liu, B., Identification of Surface Reactivity Descriptor for Transition Metal Oxides in Oxygen Evolution Reaction. *J Am Chem Soc* **2016,** *138* (31), 9978-85.

23. García-Mota, M.; Bajdich, M.; Viswanathan, V.; Vojvodic, A.; Bell, A. T.; Nørskov, J. K., Importance of Correlation in Determining Electrocatalytic Oxygen Evolution Activity on Cobalt Oxides. *The Journal of Physical Chemistry C* **2012,** *116* (39), 21077-21082.

24. Chen, J.; Selloni, A., Water Adsorption and Oxidation at the Co3O4 (110) Surface. *The Journal of Physical Chemistry Letters* **2012,** *3* (19), 2808-2814.

25. Li, X.; Siegbahn, P. E., Water oxidation mechanism for synthetic Co-oxides with small nuclearity. *J Am Chem Soc* **2013,** *135* (37), 13804-13.

26. Jiao, Y.; Zheng, Y.; Jaroniec, M.; Qiao, S. Z., Design of electrocatalysts for oxygen- and hydrogen-involving energy conversion reactions. *Chem Soc Rev* **2015,** *44* (8), 2060-86.

27. Zhang, M.; de Respinis, M.; Frei, H., Time-resolved observations of water oxidation intermediates on a cobalt oxide nanoparticle catalyst. *Nat Chem* **2014,** *6* (4), 362-7.

28. Man, I. C.; Su, H. Y.; Calle-Vallejo, F.; Hansen, H. A.; Martínez, J. I.; Inoglu, N. G.; Kitchin, J.; Jaramillo, T. F.; Nørskov, J. K.; Rossmeisl, J., Universality in Oxygen Evolution Electrocatalysis on Oxide Surfaces. *ChemCatChem* **2011,** *3* (7), 1159-1165.

29. Lee, Y.; Suntivich, J.; May, K. J.; Perry, E. E.; Shao-Horn, Y., Synthesis and Activities of Rutile IrO2 and RuO2 Nanoparticles for Oxygen Evolution in Acid and Alkaline Solutions. *J Phys Chem Lett* **2012,** *3* (3), 399-404.

30. Reier, T.; Nong, H. N.; Teschner, D.; Schlögl, R.; Strasser, P., Electrocatalytic Oxygen Evolution Reaction in Acidic Environments - Reaction Mechanisms and Catalysts. *Advanced Energy Materials* **2017,** *7* (1).

31. Shi, Y.; Lyu, Z.; Zhao, M.; Chen, R.; Nguyen, Q. N.; Xia, Y., Noble-Metal Nanocrystals with Controlled Shapes for Catalytic and Electrocatalytic Applications. *Chem Rev* **2021,** *121* (2), 649-735.

32. Axet, M. R.; Philippot, K., Catalysis with Colloidal Ruthenium Nanoparticles. *Chem Rev* **2020**.

33. Yu, J.; He, Q.; Yang, G.; Zhou, W.; Shao, Z.; Ni, M., Recent Advances and Prospective in Ruthenium-Based Materials for Electrochemical Water Splitting. *ACS Catalysis* **2019,** *9* (11), 9973-10011.

34. Wu, Z. P.; Lu, X. F.; Zang, S. Q.; Lou, X. W., Non-Noble-Metal-Based Electrocatalysts toward the Oxygen Evolution Reaction. *Advanced Functional Materials* **2020,** *30* (15).

35. Subbaraman, R.; Tripkovic, D.; Chang, K. C.; Strmcnik, D.; Paulikas, A. P.; Hirunsit, P.; Chan, M.; Greeley, J.; Stamenkovic, V.; Markovic, N. M., Trends in activity for the water electrolyser reactions on 3d M(Ni,Co,Fe,Mn) hydr(oxy)oxide catalysts. *Nat Mater* **2012,** *11* (6), 550-7.

36. Indra, A.; Menezes, P. W.; Sahraie, N. R.; Bergmann, A.; Das, C.; Tallarida, M.; Schmeisser, D.; Strasser, P.; Driess, M., Unification of catalytic water oxidation and oxygen reduction reactions: amorphous beat crystalline cobalt iron oxides. *J Am Chem Soc* **2014,** *136* (50), 17530-6.

37. Risch, M.; Ringleb, F.; Kohlhoff, M.; Bogdanoff, P.; Chernev, P.; Zaharieva, I.; Dau, H., Water oxidation by amorphous cobalt-based oxides: in situ tracking of redox transitions and mode of catalysis. *Energy & Environmental Science* **2015,** *8* (2), 661-674.

38. Artero, V.; Chavarot-Kerlidou, M.; Fontecave, M., Splitting water with cobalt. *Angew Chem Int Ed Engl* **2011,** *50* (32), 7238-66.

39. Deng, X.; Tüysüz, H., Cobalt-Oxide-Based Materials as Water Oxidation Catalyst: Recent Progress and Challenges. *ACS Catalysis* **2014,** *4* (10), 3701-3714.

40. Ullman, A. M.; Brodsky, C. N.; Li, N.; Zheng, S. L.; Nocera, D. G., Probing Edge Site Reactivity of Oxidic Cobalt Water Oxidation Catalysts. *J Am Chem Soc* **2016,** *138* (12), 4229-36.

41. Liang, Y.; Li, Y.; Wang, H.; Zhou, J.; Wang, J.; Regier, T.; Dai, H., Co(3)O(4) nanocrystals on graphene as a synergistic catalyst for oxygen reduction reaction. *Nat Mater* **2011,** *10* (10), 780-6.

42. Strickler, A. L.; Escudero-Escribano, M. A.; Jaramillo, T. F., Core-Shell Au@Metal-Oxide Nanoparticle Electrocatalysts for Enhanced Oxygen Evolution. *Nano Lett* **2017,** *17* (10), 6040-6046.

43. Tan, C. S.; Hsu, S. C.; Ke, W. H.; Chen, L. J.; Huang, M. H., Facet-dependent electrical conductivity properties of Cu2O crystals. *Nano Lett* **2015,** *15* (3), 2155-60.

44. Ling, T.; Yan, D. Y.; Wang, H.; Jiao, Y.; Hu, Z.; Zheng, Y.; Zheng, L.; Mao, J.; Liu, H.; Du, X. W.; Jaroniec, M.; Qiao, S. Z., Activating cobalt(II) oxide nanorods for efficient electrocatalysis by strain engineering. *Nat Commun* **2017,** *8* (1), 1509.

45. Liu, J. X.; Su, H. Y.; Sun, D. P.; Zhang, B. Y.; Li, W. X., Crystallographic dependence of CO activation on cobalt catalysts: HCP versus FCC. *J Am Chem Soc* **2013,** *135* (44), 16284-7.

46. Han, X.; Ling, X.; Yu, D.; Xie, D.; Li, L.; Peng, S.; Zhong, C.; Zhao, N.; Deng, Y.; Hu, W., Atomically Dispersed Binary Co-Ni Sites in Nitrogen-Doped Hollow Carbon Nanocubes for Reversible Oxygen Reduction and Evolution. *Adv Mater* **2019,** *31* (49), e1905622.

47. Xiao, M.; Zhu, J.; Li, S.; Li, G.; Liu, W.; Deng, Y.-P.; Bai, Z.; Ma, L.; Feng, M.; Wu, T.; Su, D.; Lu, J.; Yu, A.; Chen, Z., 3d-Orbital Occupancy Regulated Ir-Co Atomic Pair Toward Superior Bifunctional Oxygen Electrocatalysis. *ACS Catalysis* **2021,** *11* (14), 8837-8846.

48. Lu, Q.; Wu, H.; Zheng, X.; Chen, Y.; Rogach, A. L.; Han, X.; Deng, Y.; Hu, W., Encapsulating Cobalt Nanoparticles in Interconnected N-Doped Hollow Carbon Nanofibers with Enriched CoNC Moiety for Enhanced Oxygen Electrocatalysis in Zn-Air Batteries. *Adv Sci (Weinh)* **2021,** *8* (20), e2101438.

49. Lu, Y.; Li, C.; Zhang, Y.; Cao, X.; Xie, G.; Wang, M.; Peng, D.; Huang, K.; Zhang, B.; Wang, T.; Junsheng, W.; Huang, Y., Engineering of cation and anion vacancies in Co3O4 thin nanosheets by laser irradiation for more advancement of oxygen evolution reaction. *Nano Energy* **2021,** *83*.

50. Rao, Y.; Chen, S.; Yue, Q.; Kang, Y., Optimizing the Spin States of Mesoporous Co3O4 Nanorods through Vanadium Doping for Long-Lasting and Flexible Rechargeable Zn–Air Batteries. *ACS Catalysis* **2021,** *11* (13), 8097-8103.

51. Wu, M.; Zhang, G.; Chen, N.; Hu, Y.; Regier, T.; Rawach, D.; Sun, S., Self-Reconstruction of Co/Co2P Heterojunctions Confined in N-Doped Carbon Nanotubes for Zinc–Air Flow Batteries. *ACS Energy Letters* **2021**, 1153-1161.

52. Yoon, K. R.; Hwang, C. K.; Kim, S. H.; Jung, J. W.; Chae, J. E.; Kim, J.; Lee, K. A.; Lim, A.; Cho, S. H.; Singh, J. P.; Kim, J. M.; Shin, K.; Moon, B. M.; Park, H. S.; Kim, H. J.; Chae, K. H.; Ham, H. C.; Kim, I. D.; Kim, J. Y., Hierarchically Assembled Cobalt Oxynitride Nanorods and N-Doped Carbon Nanofibers for Efficient Bifunctional Oxygen Electrocatalysis with Exceptional Regenerative Efficiency. *ACS Nano* **2021**.

53. Zhou, L.; Deng, B.; Jiang, Z.; Jiang, Z. J., Shell thickness controlled core-shell Fe3O4@CoO nanocrystals as efficient bifunctional catalysts for the oxygen reduction and evolution reactions. *Chem Commun (Camb)* **2019,** *55* (4), 525-528.

54. Kang, J.; Sheng, J.; Xie, J.; Ye, H.; Chen, J.; Fu, X.-Z.; Du, G.; Sun, R.; Wong, C.-P., Tubular Cu(OH)2 arrays decorated with nanothorny Co–Ni bimetallic carbonate hydroxide supported on Cu foam: a 3D hierarchical core–shell efficient electrocatalyst for the oxygen evolution reaction. *Journal of Materials Chemistry A* **2018,** *6* (21), 10064-10073.

55. Min, K.; Kim, S.; Lee, E.; Yoo, G.; Ham, H. C.; Shim, S. E.; Lim, D.; Baeck, S.-H., A hierarchical Co3O4/CoS microbox heterostructure as a highly efficient bifunctional electrocatalyst for rechargeable Zn–air batteries. *Journal of Materials Chemistry A* **2021,** *9* (32), 17344-17352.

56. Zhang, X.; Li, J.; Yang, Y.; Zhang, S.; Zhu, H.; Zhu, X.; Xing, H.; Zhang, Y.; Huang, B.; Guo, S.; Wang, E., Co3 O4 /Fe0.33 Co0.66 P Interface Nanowire for Enhancing Water Oxidation Catalysis at High Current Density. *Adv Mater* **2018,** *30* (45), e1803551.

57. Zhuang, Z.; Sheng, W.; Yan, Y., Synthesis of monodispere Au@Co3O4 core-shell nanocrystals and their enhanced catalytic activity for oxygen evolution reaction. *Adv Mater* **2014,** *26* (23), 3950-5.

58. Zhou, Y.; Zeng, H. C., Metal–Hydroxide and Gold–Nanocluster Interfaces: Enhancing Catalyst Activity and Stability for Oxygen Evolution Reaction. *The Journal of Physical Chemistry C* **2016,** *120* (51), 29348-29357.

59. Wang, Z.; Liu, H.; Ge, R.; Ren, X.; Ren, J.; Yang, D.; Zhang, L.; Sun, X., Phosphorus-Doped Co3O4 Nanowire Array: A Highly Efficient Bifunctional Electrocatalyst for Overall Water Splitting. *ACS Catalysis* **2018,** *8* (3), 2236-2241.

60. Sidhureddy, B.; Dondapati, J. S.; Chen, A., Shape-controlled synthesis of Co3O4 for enhanced electrocatalysis of the oxygen evolution reaction. *Chem Commun (Camb)* **2019,** *55* (25), 3626-3629.

61. Xu, Y.; Zhang, F.; Sheng, T.; Ye, T.; Yi, D.; Yang, Y.; Liu, S.; Wang, X.; Yao, J., Clarifying the controversial catalytic active sites of Co3O4 for the oxygen evolution reaction. *Journal of Materials Chemistry A* **2019,** *7* (40), 23191-23198.

62. Kong, Q.; Bai, W.; Bai, F.; An, X.; Feng, W.; Zhou, F.; Chen, Q.; Wang, Q.; Sun, C., FeCoNi Ternary Spinel Oxides Nanosheets as High Performance Water Oxidation Electrocatalyst. *ChemCatChem* **2020,** *12* (8), 2209-2214.

63. Liu, Y.; Ma, C.; Zhang, Q.; Wang, W.; Pan, P.; Gu, L.; Xu, D.; Bao, J.; Dai, Z., 2D Electron Gas and Oxygen Vacancy Induced High Oxygen Evolution Performances for Advanced Co3 O4 /CeO2 Nanohybrids. *Adv Mater* **2019,** *31* (21), e1900062.

64. Zheng, Y.; Jiao, Y.; Zhu, Y.; Cai, Q.; Vasileff, A.; Li, L. H.; Han, Y.; Chen, Y.; Qiao, S. Z., Molecule-Level g-C3N4 Coordinated Transition Metals as a New Class of Electrocatalysts for Oxygen Electrode Reactions. *J Am Chem Soc* **2017,** *139* (9), 3336-3339.

65. Ling, T.; Yan, D. Y.; Jiao, Y.; Wang, H.; Zheng, Y.; Zheng, X.; Mao, J.; Du, X. W.; Hu, Z.; Jaroniec, M.; Qiao, S. Z., Engineering surface atomic structure of single-crystal cobalt (II) oxide nanorods for superior electrocatalysis. *Nat Commun* **2016,** *7*, 12876.

66. Tian, Y.; Liu, X.; Xu, L.; Yuan, D.; Dou, Y.; Qiu, J.; Li, H.; Ma, J.; Wang, Y.; Su, D.; Zhang, S., Engineering Crystallinity and Oxygen Vacancies of Co(II) Oxide Nanosheets for High Performance and Robust Rechargeable Zn–Air Batteries. *Advanced Functional Materials* **2021,** *31* (20).

67. Gao, Z. W.; Ma, T.; Chen, X. M.; Liu, H.; Cui, L.; Qiao, S. Z.; Yang, J.; Du, X. W., Strongly Coupled CoO Nanoclusters/CoFe LDHs Hybrid as a Synergistic Catalyst for Electrochemical Water Oxidation. *Small* **2018,** *14* (17), e1800195.

68. Kelly, C. H. W.; Benedetti, T. M.; Alinezhad, A.; Gooding, J. J.; Tilley, R. D., Controlling Metallic Nanoparticle Redox Properties for

Improved Methanol Oxidation Reaction Electrocatalysis. *ChemCatChem* **2019,** *11* (24), 5989-5993.

69. Kelly, C. H. W.; Benedetti, T. M.; Alinezhad, A.; Schuhmann, W.; Gooding, J. J.; Tilley, R. D., Understanding the Effect of Au in Au–Pd Bimetallic Nanocrystals on the Electrocatalysis of the Methanol Oxidation Reaction. *The Journal of Physical Chemistry C* **2018,** *122* (38), 21718-21723.

70. Xie, X.; Li, Y.; Liu, Z. Q.; Haruta, M.; Shen, W., Low-temperature oxidation of CO catalysed by Co(3)O(4) nanorods. *Nature* **2009,** *458* (7239), 746-9.

71. Wang, H. Y.; Hung, S. F.; Chen, H. Y.; Chan, T. S.; Chen, H. M.; Liu, B., In Operando Identification of Geometrical-Site-Dependent Water Oxidation Activity of Spinel Co3O4. *J Am Chem Soc* **2016,** *138* (1), 36-9.

72. Yang, J.; Cooper, J. K.; Toma, F. M.; Walczak, K. A.; Favaro, M.; Beeman, J. W.; Hess, L. H.; Wang, C.; Zhu, C.; Gul, S.; Yano, J.; Kisielowski, C.; Schwartzberg, A.; Sharp, I. D., A multifunctional biphasic water splitting catalyst tailored for integration with high-performance semiconductor photoanodes. *Nat Mater* **2017,** *16* (3), 335-341.

73. Favaro, M.; Yang, J.; Nappini, S.; Magnano, E.; Toma, F. M.; Crumlin, E. J.; Yano, J.; Sharp, I. D., Understanding the Oxygen Evolution Reaction Mechanism on CoOx using Operando Ambient-Pressure X-ray Photoelectron Spectroscopy. *J Am Chem Soc* **2017,** *139* (26), 8960-8970.

74. Bergmann, A.; Jones, T. E.; Martinez Moreno, E.; Teschner, D.; Chernev, P.; Gliech, M.; Reier, T.; Dau, H.; Strasser, P., Unified structural motifs of the catalytically active state of Co(oxyhydr)oxides during the electrochemical oxygen evolution reaction. *Nature Catalysis* **2018,** *1* (9), 711-719.

75. Aijaz, A.; Masa, J.; Rosler, C.; Xia, W.; Weide, P.; Botz, A. J.; Fischer, R. A.; Schuhmann, W.; Muhler, M., Co@Co3O4 Encapsulated in Carbon Nanotube-Grafted Nitrogen-Doped Carbon Polyhedra as an Advanced Bifunctional Oxygen Electrode. *Angew Chem Int Ed Engl* **2016,** *55* (12), 4087-91.

76. Wu, L.; Li, Q.; Wu, C. H.; Zhu, H.; Mendoza-Garcia, A.; Shen, B.; Guo, J.; Sun, S., Stable Cobalt Nanoparticles and Their Monolayer Array as an Efficient Electrocatalyst for Oxygen Evolution Reaction. *J Am Chem Soc* **2015,** *137* (22), 7071-4.

77. Yeo, B. S.; Bell, A. T., Enhanced activity of gold-supported cobalt oxide for the electrochemical evolution of oxygen. *J Am Chem Soc* **2011,** *133* (14), 5587-93.

78. Lu, A.; Peng, D. L.; Chang, F.; Skeete, Z.; Shan, S.; Sharma, A.; Luo, J.; Zhong, C. J., Composition- and Structure-Tunable Gold-Cobalt Nanoparticles and Electrocatalytic Synergy for Oxygen Evolution Reaction. *ACS Appl Mater Interfaces* **2016,** *8* (31), 20082-91.

79. Chen, Z.; Kronawitter, C. X.; Koel, B. E., Facet-dependent activity and stability of Co(3)O(4) nanocrystals towards the oxygen evolution reaction. *Phys Chem Chem Phys* **2015,** *17* (43), 29387-93.

80. Zhang, Z.; Liu, G.; Cui, X.; Chen, B.; Zhu, Y.; Gong, Y.; Saleem, F.; Xi, S.; Du, Y.; Borgna, A.; Lai, Z.; Zhang, Q.; Li, B.; Zong, Y.; Han, Y.; Gu, L.; Zhang, H., Crystal Phase and Architecture Engineering of Lotus-Thalamus-Shaped Pt-Ni Anisotropic Superstructures for Highly Efficient Electrochemical Hydrogen Evolution. *Advanced Materials* **2018,** *30* (30), 1801741.

81. Gloag, L.; Benedetti, T. M.; Cheong, S.; Marjo, C. E.; Gooding, J. J.; Tilley, R. D., Cubic-Core Hexagonal-Branch Mechanism To Synthesize

Bimetallic Branched and Faceted Pd-Ru Nanoparticles for Oxygen Evolution Reaction Electrocatalysis. *J Am Chem Soc* **2018,** *140* (40), 12760-12764.

82. Gloag, L.; Benedetti, T. M.; Cheong, S.; Li, Y.; Chan, X. H.; Lacroix, L. M.; Chang, S. L. Y.; Arenal, R.; Florea, I.; Barron, H.; Barnard, A. S.; Henning, A. M.; Zhao, C.; Schuhmann, W.; Gooding, J. J.; Tilley, R. D., Three-Dimensional Branched and Faceted Gold-Ruthenium Nanoparticles: Using Nanostructure to Improve Stability in Oxygen Evolution Electrocatalysis. *Angew Chem Int Ed Engl* **2018,** *57* (32), 10241-10245.

83. Cao, Z.; Chen, Q.; Zhang, J.; Li, H.; Jiang, Y.; Shen, S.; Fu, G.; Lu, B. A.; Xie, Z.; Zheng, L., Platinum-nickel alloy excavated nano-multipods with hexagonal close-packed structure and superior activity towards hydrogen evolution reaction. *Nat Commun* **2017,** *8*, 15131.

84. Zhao, M.; Xia, Y., Crystal-phase and surface-structure engineering of ruthenium nanocrystals. *Nature Reviews Materials* **2020**.

85. Yao, Y.; Hu, S.; Chen, W.; Huang, Z.-Q.; Wei, W.; Yao, T.; Liu, R.; Zang, K.; Wang, X.; Wu, G.; Yuan, W.; Yuan, T.; Zhu, B.; Liu, W.; Li, Z.; He, D.; Xue, Z.; Wang, Y.; Zheng, X.; Dong, J.; Chang, C.-R.; Chen, Y.; Hong, X.; Luo, J.; Wei, S.; Li, W.-X.; Strasser, P.; Wu, Y.; Li, Y., Engineering the electronic structure of single atom Ru sites via compressive strain boosts acidic water oxidation electrocatalysis. *Nature Catalysis* **2019,** *2* (4), 304-313.

86. Rao, R. R.; Kolb, M. J.; Giordano, L.; Pedersen, A. F.; Katayama, Y.; Hwang, J.; Mehta, A.; You, H.; Lunger, J. R.; Zhou, H.; Halck, N. B.; Vegge, T.; Chorkendorff, I.; Stephens, I. E. L.; Shao-Horn, Y.,

Operando identification of site-dependent water oxidation activity on ruthenium dioxide single-crystal surfaces. *Nature Catalysis* **2020**.

87. Lu, Q.; Wang, A. L.; Cheng, H.; Gong, Y.; Yun, Q.; Yang, N.; Li, B.; Chen, B.; Zhang, Q.; Zong, Y.; Gu, L.; Zhang, H., Synthesis of Hierarchical 4H/fcc Ru Nanotubes for Highly Efficient Hydrogen Evolution in Alkaline Media. *Small* **2018,** *14* (30), e1801090.

88. Mao, J.; He, C. T.; Pei, J.; Chen, W.; He, D.; He, Y.; Zhuang, Z.; Chen, C.; Peng, Q.; Wang, D.; Li, Y., Accelerating water dissociation kinetics by isolating cobalt atoms into ruthenium lattice. *Nat Commun* **2018,** *9* (1), 4958.

89. Zhao, M.; Hood, Z. D.; Vara, M.; Gilroy, K. D.; Chi, M.; Xia, Y., Ruthenium Nanoframes in the Face-Centered Cubic Phase: Facile Synthesis and Their Enhanced Catalytic Performance. *ACS Nano* **2019,** *13* (6), 7241-7251.

90. Zhao, M.; Chen, Z.; Lyu, Z.; Hood, Z. D.; Xie, M.; Vara, M.; Chi, M.; Xia, Y., Ru Octahedral Nanocrystals with a Face-Centered Cubic Structure, {111} Facets, Thermal Stability up to 400 degrees C, and Enhanced Catalytic Activity. *J Am Chem Soc* **2019,** *141* (17), 7028-7036.

91. Jackson, A.; Strickler, A.; Higgins, D.; Jaramillo, T. F., Engineering Ru@Pt Core-Shell Catalysts for Enhanced Electrochemical Oxygen Reduction Mass Activity and Stability. *Nanomaterials (Basel)* **2018,** *8* (1).

92. Zhang, D.; Zhao, H.; Huang, B.; Li, B.; Li, H.; Han, Y.; Wang, Z.; Wu, X.; Pan, Y.; Sun, Y.; Sun, X.; Lai, J.; Wang, L., Advanced Ultrathin RuPdM (M = Ni, Co, Fe) Nanosheets Electrocatalyst Boosts Hydrogen Evolution. *ACS Cent Sci* **2019,** *5* (12), 1991-1997.

93. Shan, J.; Ling, T.; Davey, K.; Zheng, Y.; Qiao, S. Z., Transition-Metal-Doped RuIr Bifunctional Nanocrystals for Overall Water Splitting in Acidic Environments. *Adv Mater* **2019,** *31* (17), e1900510.

94. Shan, J.; Guo, C.; Zhu, Y.; Chen, S.; Song, L.; Jaroniec, M.; Zheng, Y.; Qiao, S.-Z., Charge-Redistribution-Enhanced Nanocrystalline Ru@IrOx Electrocatalysts for Oxygen Evolution in Acidic Media. *Chem* **2019,** *5* (2), 445-459.

95. Li, Y.; Zhou, W.; Zhao, X.; Cheng, W.; Su, H.; Zhang, H.; Liu, M.; Liu, Q., Donutlike RuCu Nanoalloy with Ultrahigh Mass Activity for Efficient and Robust Oxygen Evolution in Acid Solution. *ACS Applied Energy Materials* **2019,** *2* (10), 7483-7489.

96. Chen, S.; Huang, H.; Jiang, P.; Yang, K.; Diao, J.; Gong, S.; Liu, S.; Huang, M.; Wang, H.; Chen, Q., Mn-Doped RuO2 Nanocrystals as Highly Active Electrocatalysts for Enhanced Oxygen Evolution in Acidic Media. *ACS Catalysis* **2019,** *10* (2), 1152-1160.

97. Su, J.; Ge, R.; Jiang, K.; Dong, Y.; Hao, F.; Tian, Z.; Chen, G.; Chen, L., Assembling Ultrasmall Copper-Doped Ruthenium Oxide Nanocrystals into Hollow Porous Polyhedra: Highly Robust Electrocatalysts for Oxygen Evolution in Acidic Media. *Adv Mater* **2018**, e1801351.

98. Oh, A.; Kim, H. Y.; Baik, H.; Kim, B.; Chaudhari, N. K.; Joo, S. H.; Lee, K., Topotactic Transformations in an Icosahedral Nanocrystal to Form Efficient Water-Splitting Catalysts. *Adv Mater* **2019,** *31* (1), e1805546.

99. Wang, J.; Ji, Y.; Yin, R.; Li, Y.; Shao, Q.; Huang, X., Transition metal-doped ultrathin RuO2 networked nanowires for efficient overall water splitting across a broad pH range. *Journal of Materials Chemistry A* **2019,** *7* (11), 6411-6416.

100. Lin, Y.; Tian, Z.; Zhang, L.; Ma, J.; Jiang, Z.; Deibert, B. J.; Ge, R.; Chen, L., Chromium-ruthenium oxide solid solution electrocatalyst for highly efficient oxygen evolution reaction in acidic media. *Nat Commun* **2019,** *10* (1), 162.

101. Kong, X.; Xu, K.; Zhang, C.; Dai, J.; Norooz Oliaee, S.; Li, L.; Zeng, X.; Wu, C.; Peng, Z., Free-Standing Two-Dimensional Ru Nanosheets with High Activity toward Water Splitting. *ACS Catalysis* **2016,** *6* (3), 1487-1492.

102. Laha, S.; Lee, Y.; Podjaski, F.; Weber, D.; Duppel, V.; Schoop, L. M.; Pielnhofer, F.; Scheurer, C.; Müller, K.; Starke, U.; Reuter, K.; Lotsch, B. V., Ruthenium Oxide Nanosheets for Enhanced Oxygen Evolution Catalysis in Acidic Medium. *Advanced Energy Materials* **2019,** *9* (15).

103. Ge, R.; Li, L.; Su, J.; Lin, Y.; Tian, Z.; Chen, L., Ultrafine Defective RuO2

Electrocatayst Integrated on Carbon Cloth for Robust Water Oxidation in Acidic Media. *Advanced Energy Materials* **2019,** *9* (35).

104. Yao, Q.; Huang, B.; Zhang, N.; Sun, M.; Shao, Q.; Huang, X., Channel-Rich RuCu Nanosheets for pH-Universal Overall Water Splitting Electrocatalysis. *Angew Chem Int Ed Engl* **2019,** *58* (39), 13983-13988.

105. Miao, X.; Zhang, L.; Wu, L.; Hu, Z.; Shi, L.; Zhou, S., Quadruple perovskite ruthenate as a highly efficient catalyst for acidic water oxidation. *Nat Commun* **2019,** *10* (1), 3809.

106. Zhuang, Z.; Wang, Y.; Xu, C. Q.; Liu, S.; Chen, C.; Peng, Q.; Zhuang, Z.; Xiao, H.; Pan, Y.; Lu, S.; Yu, R.; Cheong, W. C.; Cao, X.; Wu, K.; Sun, K.; Wang, Y.; Wang, D.; Li, J.; Li, Y., Three-dimensional open nano-netcage electrocatalysts for efficient pH-universal overall water splitting. *Nat Commun* **2019,** *10* (1), 4875.

107. Wang, J.; Han, L.; Huang, B.; Shao, Q.; Xin, H. L.; Huang, X., Amorphization activated ruthenium-tellurium nanorods for efficient water splitting. *Nat Commun* **2019,** *10* (1), 5692.

108. Gloag, L.; Benedetti, T. M.; Cheong, S.; Webster, R. F.; Marjo, C. E.; Gooding, J. J.; Tilley, R. D., Pd-Ru core-shell nanoparticles with tunable shell thickness for active and stable oxygen evolution performance. *Nanoscale* **2018,** *10* (32), 15173-15177.

109. Stoerzinger, K. A.; Qiao, L.; Biegalski, M. D.; Shao-Horn, Y., Orientation-Dependent Oxygen Evolution Activities of Rutile IrO2 and RuO2. *J Phys Chem Lett* **2014,** *5* (10), 1636-41.

110. Danilovic, N.; Subbaraman, R.; Chang, K. C.; Chang, S. H.; Kang, Y. J.; Snyder, J.; Paulikas, A. P.; Strmcnik, D.; Kim, Y. T.; Myers, D.; Stamenkovic, V. R.; Markovic, N. M., Activity-Stability Trends for the Oxygen Evolution Reaction on Monometallic Oxides in Acidic Environments. *J Phys Chem Lett* **2014,** *5* (14), 2474-8.

111. Chang, S. H.; Danilovic, N.; Chang, K. C.; Subbaraman, R.; Paulikas, A. P.; Fong, D. D.; Highland, M. J.; Baldo, P. M.; Stamenkovic, V. R.; Freeland, J. W.; Eastman, J. A.; Markovic, N. M., Functional links between stability and reactivity of strontium ruthenate single crystals during oxygen evolution. *Nat Commun* **2014,** *5*, 4191.

112. Chang, S. H.; Connell, J. G.; Danilovic, N.; Subbaraman, R.; Chang, K. C.; Stamenkovic, V. R.; Markovic, N. M., Activity-stability relationship in the surface electrochemistry of the oxygen evolution reaction. *Faraday Discuss* **2014,** *176*, 125-33.

113. Roy, C.; Rao, R. R.; Stoerzinger, K. A.; Hwang, J.; Rossmeisl, J.; Chorkendorff, I.; Shao-Horn, Y.; Stephens, I. E. L., Trends in Activity and Dissolution on RuO2 under Oxygen Evolution Conditions: Particles versus

Well-Defined Extended Surfaces. *ACS Energy Letters* **2018,** *3* (9), 2045-2051.

114. Drouet, S.; Creus, J.; Colliere, V.; Amiens, C.; Garcia-Anton, J.; Sala, X.; Philippot, K., A porous Ru nanomaterial as an efficient electrocatalyst for the hydrogen evolution reaction under acidic and neutral conditions. *Chem Commun (Camb)* **2017,** *53* (85), 11713-11716.

115. Gao, K.; Wang, Y.; Wang, Z.; Zhu, Z.; Wang, J.; Luo, Z.; Zhang, C.; Huang, X.; Zhang, H.; Huang, W., Ru nanodendrites composed of ultrathin fcc/hcp nanoblades for the hydrogen evolution reaction in alkaline solutions. *Chem Commun (Camb)* **2018,** *54* (36), 4613-4616.

116. Yoon, D.; Lee, J.; Seo, B.; Kim, B.; Baik, H.; Joo, S. H.; Lee, K., Cactus-Like Hollow Cu2-x S@Ru Nanoplates as Excellent and Robust Electrocatalysts for the Alkaline Hydrogen Evolution Reaction. *Small* **2017,** *13* (29).

117. Li, Y.; Zhang, L. A.; Qin, Y.; Chu, F.; Kong, Y.; Tao, Y.; Li, Y.; Bu, Y.; Ding, D.; Liu, M., Crystallinity Dependence of Ruthenium Nanocatalyst toward Hydrogen Evolution Reaction. *ACS Catalysis* **2018,** *8* (7), 5714-5720.

118. Li, Q.; Sun, S., Recent advances in the organic solution phase synthesis of metal nanoparticles and their electrocatalysis for energy conversion reactions. *Nano Energy* **2016,** *29*, 178-197.

119. Cozzoli, P. D.; Pellegrino, T.; Manna, L., Synthesis, properties and perspectives of hybrid nanocrystal structures. *Chem Soc Rev* **2006,** *35* (11), 1195-208.

120. Gilroy, K. D.; Ruditskiy, A.; Peng, H. C.; Qin, D.; Xia, Y., Bimetallic Nanocrystals: Syntheses, Properties, and Applications. *Chem Rev* **2016,** *116* (18), 10414-72.

121. Xia, Y.; Xia, X.; Peng, H. C., Shape-Controlled Synthesis of Colloidal Metal Nanocrystals: Thermodynamic versus Kinetic Products. *J Am Chem Soc* **2015,** *137* (25), 7947-66.

122. Xia, Y.; Xiong, Y.; Lim, B.; Skrabalak, S. E., Shape-controlled synthesis of metal nanocrystals: simple chemistry meets complex physics? *Angew Chem Int Ed Engl* **2009,** *48* (1), 60-103.

123. Xia, Y.; Gilroy, K. D.; Peng, H. C.; Xia, X., Seed-Mediated Growth of Colloidal Metal Nanocrystals. *Angew Chem Int Ed Engl* **2017,** *56* (1), 60-95.

124. LaMer, V. K.; Dinegar, R. H., Theory, Production and Mechanism of Formation of Monodispersed Hydrosols. *Journal of the American Chemical Society* **1950,** *72* (11), 4847-4854.

125. Tao, A. R.; Habas, S.; Yang, P., Shape Control of Colloidal Metal Nanocrystals. *Small* **2008,** *4* (3), 310-325.

126. Yin, Y.; Alivisatos, A. P., Colloidal nanocrystal synthesis and the organic–inorganic interface. *Nature* **2004,** *437*, 664.

127. Manna, L.; Milliron, D. J.; Meisel, A.; Scher, E. C.; Alivisatos, A. P., Controlled growth of tetrapod-branched inorganic nanocrystals. *Nat Mater* **2003,** *2* (6), 382-5.

128. LaGrow, A. P.; Cheong, S.; Watt, J.; Ingham, B.; Toney, M. F.; Jefferson, D. A.; Tilley, R. D., Can polymorphism be used to form branched metal nanostructures? *Adv Mater* **2013,** *25* (11), 1552-6.

Chapter 2

Synthesis and Characterization Methods

2.1 Overview

In this chapter, the synthetic techniques used to design nanocrystals, post-synthetic approaches for further characterizations will be explored. In particular, the principles, theories, and applications of TEM-based techniques, X-ray diffractometers, and X-ray photoelectron spectroscopies will be discussed. This section describes electrochemical analyses, such as cyclic voltammetry (CV), chronoamperometry, and electrochemical impedance spectroscopy (EIS), that were used to evaluate the catalytic performance of the nanocrystals.

2.2 Synthesis and purification methods

2.2.1 Fischer-Porter bottle synthesis

A Fischer-Porter bottle was used as the main apparatus for conducting the synthesis of Au, Pd seeds, as well as Co, Ru, RuCo branched nanoparticles. Fischer-Porter bottles act as a pressure reaction vessel that accommodates the use of different gases to reduce metallic precursors. A range of shape-controlled metallic nanoparticles has been synthesized via Fischer-Porter bottle reactions under H_2 or CO atmospheres, including Co, Ni nanorods[1, 2], Fe, Ni nanocubes[3, 4], and Ru, Pd branches[5-7]. H_2 was employed as a weak reducing agent during synthesis, which helped control the atomic concentration of metal atoms (Co, Ru) and prevented unwanted homogeneous nucleation during synthesis.

For a typical Fischer-Porter bottle synthesis, the precursor, seeds, and surfactant components are dissolved in an organic solvent. Once this reaction solution has been prepared, the mixture is then transferred to a Fischer-Porter bottle (Figure 2.1), where it is degassed under vacuum and pressurized with 3 bar hydrogen (Figure 2.1). Upon successful pressurization, the Fischer-Porter bottle is then placed in an oil bath on a hot plate at a set reaction temperature.

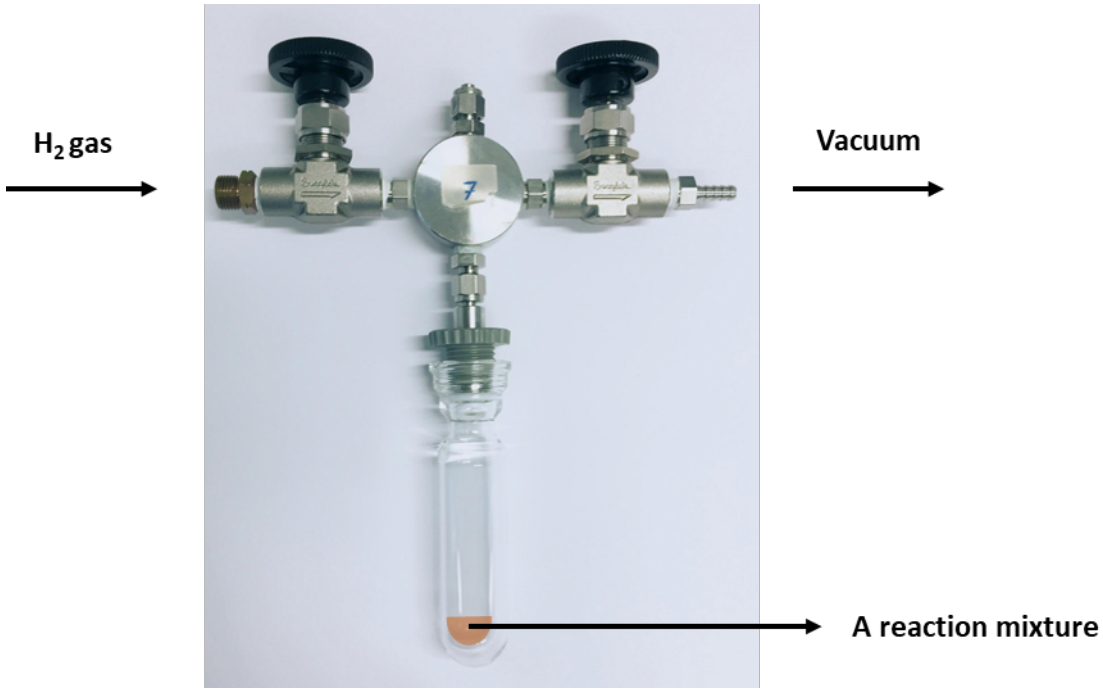

Figure 2.1. A Fischer-Porter bottle showing the bivalves and location of the reaction mixture.

Among the disadvantages of Fischer-Porter bottle synthesis are the inability to stir the solution during the reactions, the inability to take aliquots, and the inability to employ hot injections and secondary injections. Injection methods provide greater control over the reaction[8] and result in more uniform nanoparticles[9, 10].

2.2.2 Thermal decomposition

Thermodynamic decomposition is a solution-phase benchtop synthetic process in which metallic precursors are heated above their decomposition temperature and are then stabilized through the action of a surfactant in order to form nanocrystals. Long-chain amine surfactants are commonly used along with an organic solvent for synthesizing nanoparticles due to the strong interactions between metal and ligand species. When heated to high temperatures, these long-chain amine surfactants act as weak reducing agents

which aid in nanoparticle formation[11]. Additionally, many of these surfactants exist in liquid form at the required reaction temperatures, making them suitable for use as reaction solvents. Due to this, it is possible to synthesize nanoparticles with just one chemical simultaneously acting as a solvent, surfactant, and reducing agent.

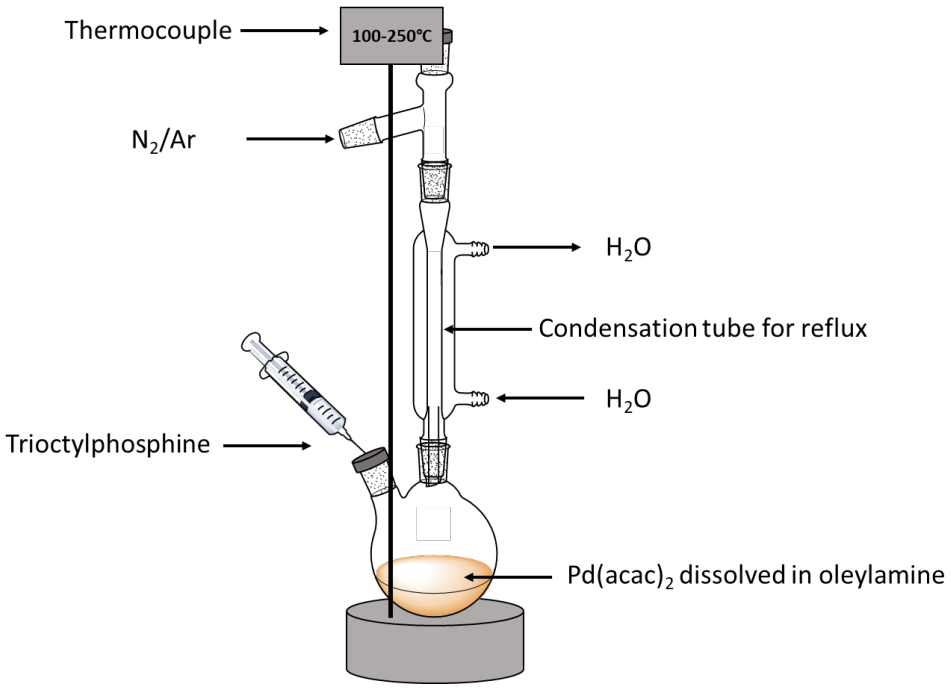

Figure 2.2. Schematic of a thermal composition setup in a two-neck flask. One neck is for the condenser and N_2/Ar flow, and another neck is for the injection.

In this work, thermal decomposition was used to synthesize small Pd seeds by reducing $Pd(acac)_2$ precursor using a modified literature method[6, 12, 13]. Oleylamine served as both a reducing agent and a solvent, while TOP was used as a surfactant.

2.2.3 Post-synthesis, cleaning, purification, and storage

Generally, centrifugation is used to separate the nanoparticles from the solution they are dispersed in, owing to their much higher density. Any

remaining precursor and excess surfactant are cleaned as well. After synthesis, all particles were stored in mesitylene. For further characterizations and electrochemical analysis, particles were first transferred to a centrifuge tube (2-50 mL), and a 1:1 ratio of solvent (mostly toluene) and antisolvent (usually ethanol) mixture were added to the sample. Cleaning was performed 2-5 times via centrifugation at a rotation speed of 4000-14000 rpm. The volume of the centrifuge tube, the number of centrifugal cycles, and rotation speeds were selected based on various considerations such as the amount/volume of particles, characterization method, and nanoparticle size. The following chapters provide detailed information on the purification process for each particle (Chapters 3, 4, 5, and 6).

2.2.4 Sample preparation for electron microscopy characterization

After purification, the diluted suspension of nanoparticles was prepared in toluene and then drop-cast onto 400 mesh formvar-coated Cu grids for low-resolution TEM analysis. For high-resolution TEM and STEM analysis, a dilute suspension of nanoparticles in toluene was drop-cast onto a thin carbon Cu grid. Toluene evaporates more slowly than hexane/ethanol, promoting the formation of well-ordered nanocrystal arrays.

2.2.5 Sample preparation for X-ray diffraction and X-ray photoelectron spectroscopy

The samples used for synchrotron X-ray diffraction (XRD) and X-ray photoelectron spectroscopy were prepared using a similar method to that described in Section 2.2.4. The key difference was that several drops of a concentrated nanoparticle solution were dropped onto a single-crystalline silicon wafer and then slowly evaporated to form a ticker smooth layer for

the XPS analysis. In order to obtain the XRD measurements, the samples were drop-casted from a highly concentrated nanoparticle solution in toluene onto a silicon holder with zero background. This process was repeated until the sample fully covered the holder.

2.2.6 Nanoparticles loading on carbon

Several electrocatalytic reactions were investigated using the Co particles loaded on carbon in this thesis. Nanoparticles were first deposited on a carbon black support material via sonication. In a typical carbon loading process, the sample and carbon support were dissolved in an organic solvent and sonicated until the nanoparticles adhered to the support. Adjusting the amount of surfactant incorporated was paramount to the dispersion on the carbon support.

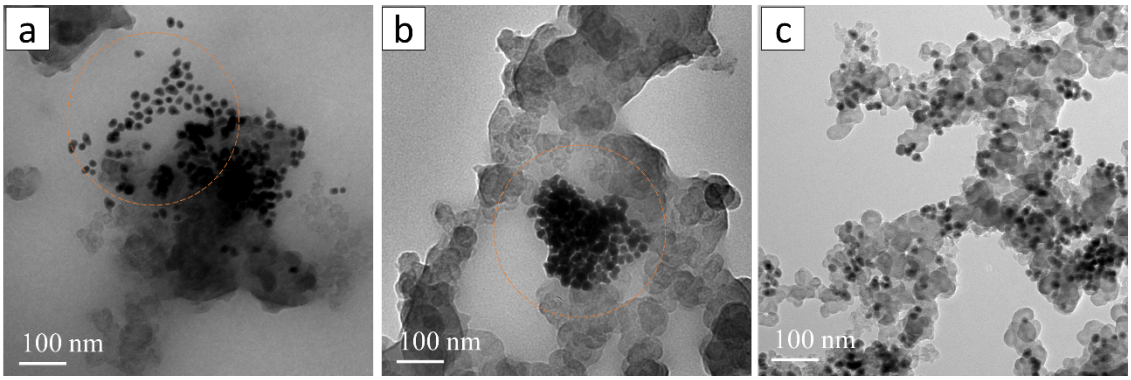

Figure 2.3. Co spherical nanoparticles loaded onto carbon black (Vulcan XC72) using different quantities of surfactant (OAm): (a) a higher quantity, (b) a lower quantity, and (c) an optimized quantity.

An increased amount of surfactant reduces the physical interactions between the carbon support and nanoparticles. As a result, the nanoparticles are unable to adhere to the carbon support (Figure 2.3a). Due to the higher surface energy of the nanoparticles, aggregated nanoparticles are deposited on the support material when a smaller amount of surfactant is used (Figure

2.3b). Optimizing the amount of surfactant ensures that the nanoparticles are dispersed well on the carbon support (Figure 2.3c).

2.3 TEM-based techniques

The morphological and crystalline structures, as well as elemental composition of nanoparticles were primarily characterized using TEM-based techniques in this study. The methods include TEM and high-resolution TEM imaging (HRTEM), selected area electron diffraction (SAED), scanning TEM imaging (STEM), energy-dispersive X-ray spectroscopy (EDX), and STEM-EDX mapping.

2.3.1 Basic principles of TEM

The working principle and theory underlying TEM-based techniques are discussed in more detail in the texts of Williams and Carter " Transmission electron microscopy, a textbook for material science"[14] and Luo "A Practical Guide to Transmission Electron Microscopy"[15]. A brief overview of the topic is presented here to assist in understanding the technique.

TEM operation works under the same principles as light microscopy, except that electrons are used in place of a light source. As the wavelength of electrons is significantly smaller than that of light, the resolution achieved by a TEM image is of a much higher order of magnitude than that of a light microscope[14, 15]. Thus, TEMs are capable of unveiling the finest details of nanomaterial structure at the atomic level.

A general diagram of a TEM is shown in Figure 2.4. The instrument can be split into three main parts: the illumination system, objective lens/stage, and imaging system[14].

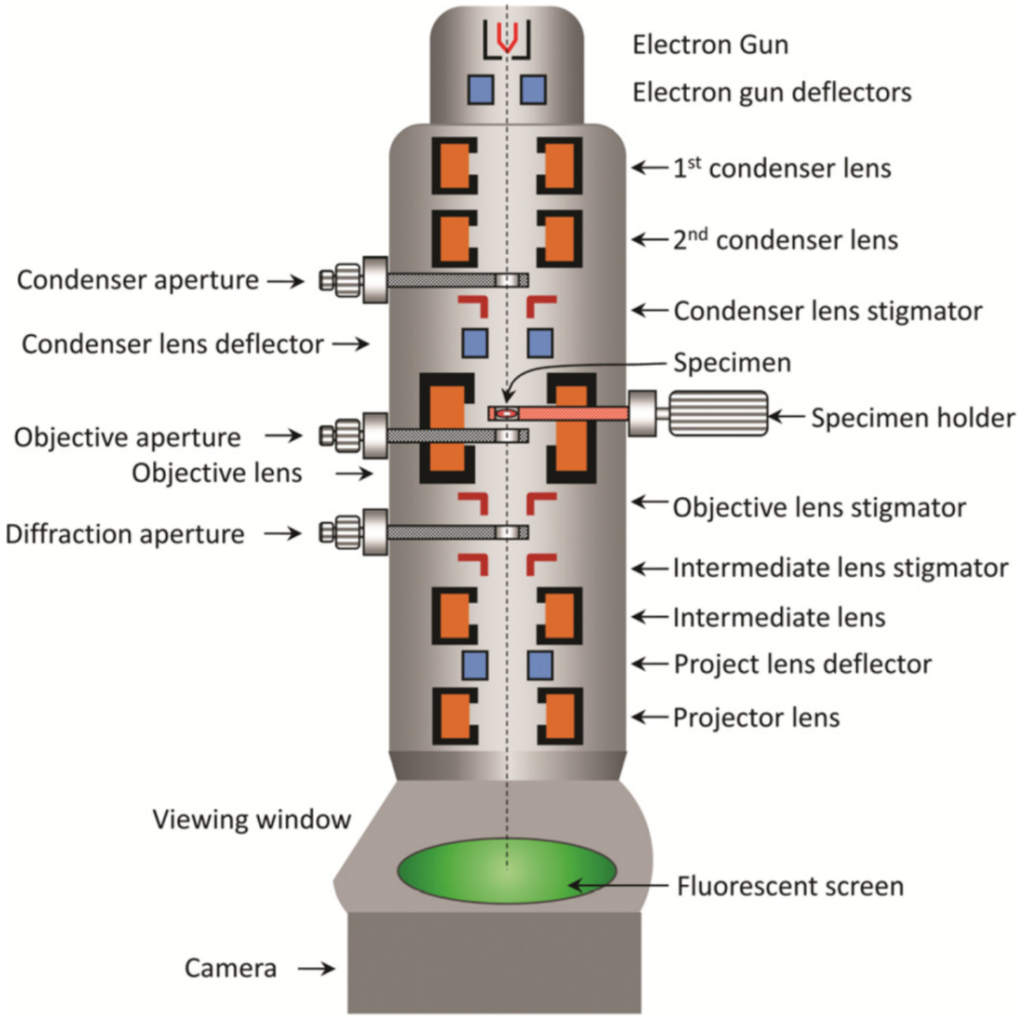

Figure 2.4. Schematic illustration of a TEM. Reproduced from the work of Luo.[15]

In the illumination system, electrons generated from the electron gun are made to pass through a series of condenser lenses to the specimen. The illumination system can be operated in either two principal modes, which are parallel beam and convergent beam settings. TEM imaging and diffraction are conducted using the first mode, whilst scanning TEM (STEM) imaging is linked with the second setting.[14]

The next component is the objective lens/stage, which is the crucial part of a TEM. In this region, electron beams interact with the specimen, resulting in selected area diffraction patterns (SAED) and bright-field/dark-field TEM

images. The length of the region along the column is no longer than 1 cm.[14] The transmitted electrons through the specimen pass through the objective lens, thereby creating a diffraction pattern or an image. A diffraction pattern is created by projecting the electrons onto the screen exclusively using the SAED aperture, as illustrated in Figure 2.5a. On the other hand, an image is produced by projecting the electrons onto the screen whilst only applying the objective aperture while removing the SAED aperture, as depicted in Figure 2.5b.[14, 15]

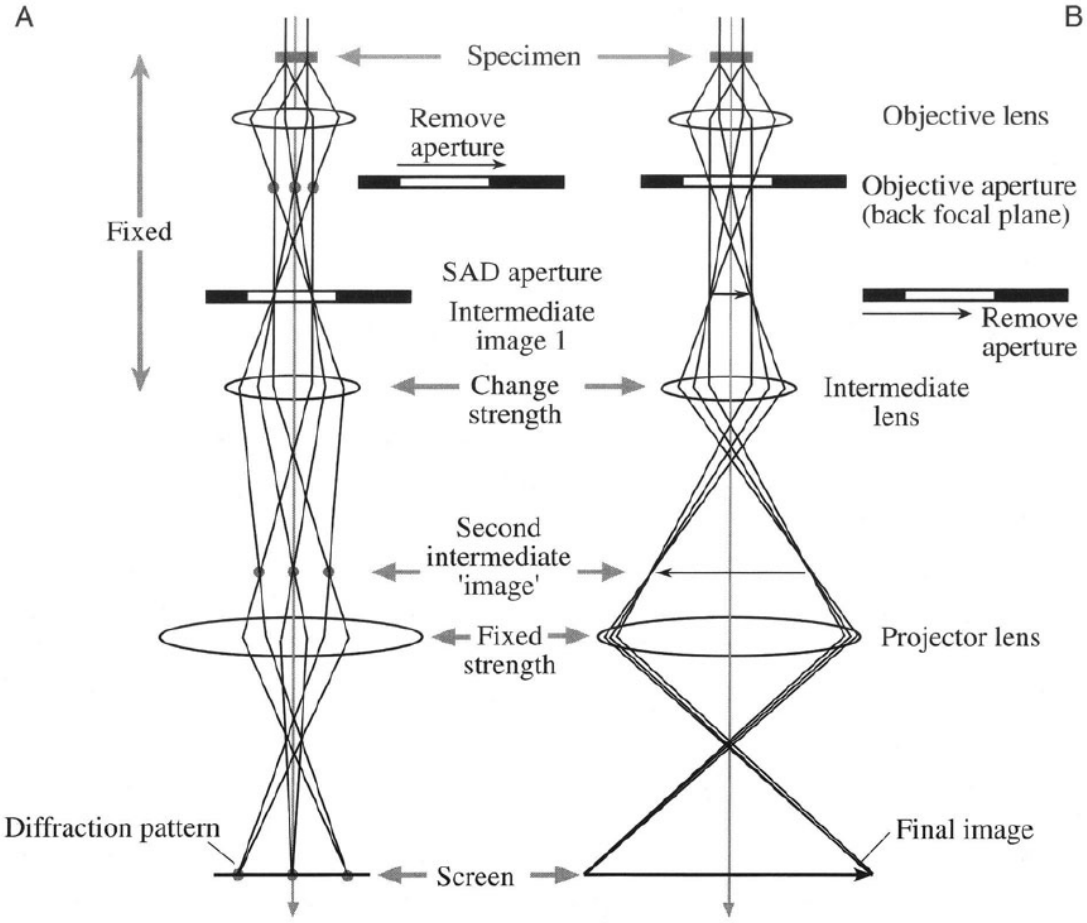

Figure 2.5. Diagrams showing the two fundamental functions of the TEM imaging system: (a) producing the diffraction pattern on the screen and (b) generating an image on the screen. Reproduced from the work of Williams and Carter.[14]

Finally, both imaging systems utilize multiple lenses to increase the magnification and improve the focus of the images or the diffraction pattern generated by the objective lens on the viewing screen.[14, 15]

2.3.2 TEM characterization

In this study, low-resolution TEM imaging was conducted on a Philips CM200 operated at 200 kV to characterize the shape and size of the resultant nanocrystals. A TEM image of the alloyed RuCo-Pd branched nanoparticles discussed in Chapter 6 is illustrated in Figure 2.6a.

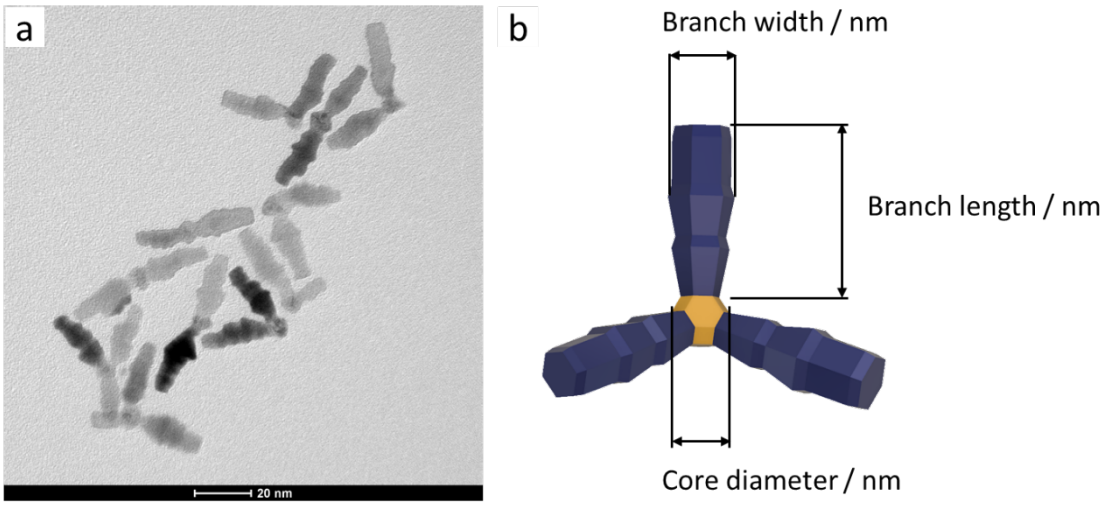

Figure 2.6. (a) A low-resolution TEM image of RuCo-Pd branched nanoparticles used in Chapter 6, (b) A diagram showing how to determine the dimensions of a branched nanocrystal.

Nanoparticle size was examined for more than 100 particles using ImageJ software. Branched nanoparticle dimensions were determined by measuring the branch width, branch length, and core diameter (Figure 2.6b).

2.3.3 HRTEM characterization

High-resolution TEM and STEM-EDX were performed on a JEOL JEM-F200 (200 kV, cold field emission gun) equipped with an annular dark field

detector and a JEOL windowless 100 mm^2 silicon drift X-ray detector. The HRTEM imaging was used to analyze the atomic arrangements and crystalline structures of nanocrystals. Figure 2.7a-b illustrates an example HRTEM image of a Co branch as a part of a Co-Au nanoparticle, which was investigated in Chapter 4. Gatan Microscopy Suite (GMS) Software was used to determine atomic spacings from these HRTEM images.

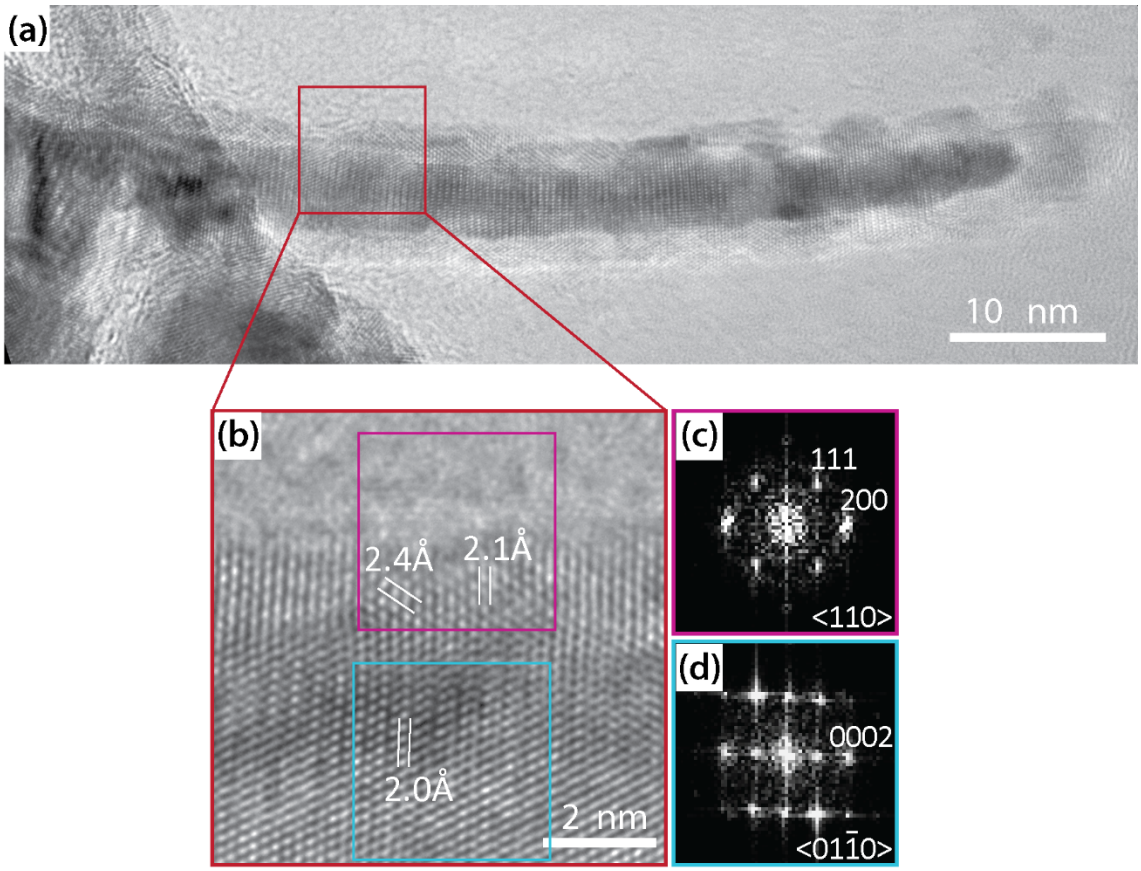

Figure 2.7. (a) TEM image of a Co branch. (b) HRTEM image of part of the branch in (a) indicated by the red box. (c) FFT of the HRTEM image at the oxide surface (purple box) indexed to a cubic <110> zone axis. (d) FFT of the HRTEM image at the core region (blue box) indexed to a hexagonal <01-10> zone axis. The lattice measurements of 2.0 Å at the core, and 2.1 Å and 2.4 Å at the shell regions are consistent with the lattice spacings of hcp Co{0002}c, cubic CoO{200} and cubic CoO{111}, respectively. This image was obtained and analyzed by Soshan Cheong.

Fast-Fourier transform (FFT) operations were additionally used to further examine the crystal structure, as well as the orientation, of nanoparticles. The pattern observed on a simple FFT would correlate to a reciprocal lattice. The presence of additional spots can result from twins, defects, or superstructures and can provide information about the crystal's growth mechanism.[14] In general, an FFT can be obtained using the ImageJ EM software program. This provides a reciprocal image, which is comparable to the reciprocal lattice of a crystal. Figure 2.7 c-d shows the FFT patterns for the surface oxide and the branch core of the Co-Au nanoparticle, respectively, which are used to determine the crystalline structures of each part.

2.3.4 High-angle annular dark-field scanning transmission electron microscopy (HAADF-STEM) analysis

HAADF-STEM analysis was performed for examining any phase differences in nanoparticle structure due to their image contrast. A HAADF-STEM image is obtained by detecting all the scattered electrons using an annular detector.[14] Figure 2.8 illustrates an example HAADF-STEM of Co spherical nanoparticles consisting of a Au-core Co-shell coated with an oxide layer (Co_3O_4). These particles will be discussed in Chapter 5.

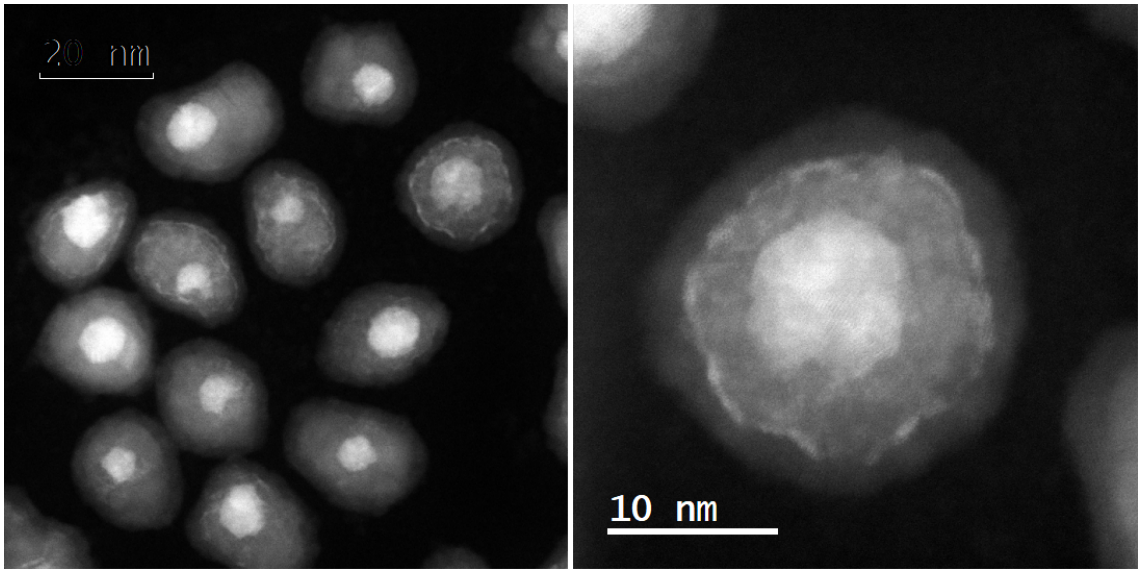

Figure 2.8. HAADF-STEM images of Co-Au core-shell nanoparticles and (b) a Co-Au core-shell nanoparticle. This image was obtained by Hsiang-Sheng Cheng.

It can be clearly seen in Figure 2.8 that the core-shell structure is coated with an oxide layer due to their difference in atomic masses.

2.3.5 Scanning Transmission Electron Microscopy-Energy Dispersive X-ray Spectroscopy (STEM-EDX)

In this study, STEM-EDX analysis was performed to examine nanoparticle chemical composition. In this technique, STEM imaging and EDX spectroscopy are combined to produce maps indicating the locations of individual elements in a particle.[14] In EDX, when a high-energy beam hits an element, core electrons are removed from the element, and the vacancies are filled by high-energy electrons, which produce X-rays. There are characteristic X-ray spectra for each element, which allows the identification of elements present by comparing their spectral identity to an elemental database. When coupled with STEM, spectra are identified from each point where the beam crosses, resulting in an elemental map that is overlaid with a STEM image. The STEM-EDX data is converted to images using

Pathfinder software. An example of STEM-EDX mapping of Co-Au core-shell nanoparticles is shown in Figure 2.9.

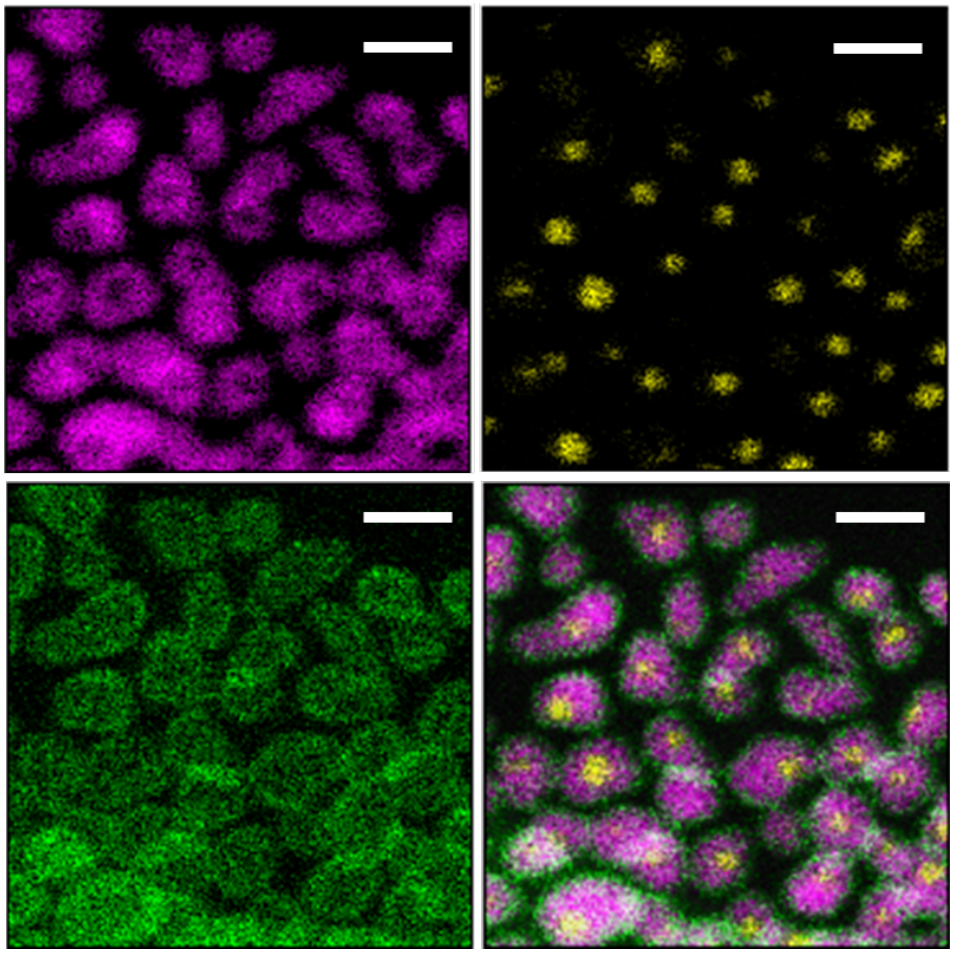

Figure 2.9. STEM-EDX elemental maps of Au (yellow), Co (pink), and O (green) of a Co spherical nanoparticle. This image was obtained by Hsiang-Sheng Cheng.

2.4 X-Ray Powder Diffraction (XRD)

XRD analysis was conducted to examine the crystalline structures of the nanoparticles. When the incident radiation interacts with a crystal lattice, and its wavelength is comparable to the interplanar spacing (d) of the crystal, the radiation will scatter or diffract.[16] The position of these diffracted rays or reflections can be determined using Bragg's law (shown in Figure 2.10):

$$n\lambda = 2d_{hkl}\sin\theta \qquad \text{(Eq.2.1)}$$

where n is an integer, λ is the X-ray wavelength, θ is the diffraction angle, and d_{hkl} -is the interplanar spacing. A simplified illustration of Bragg's law is shown in Figure 2.10.[16]

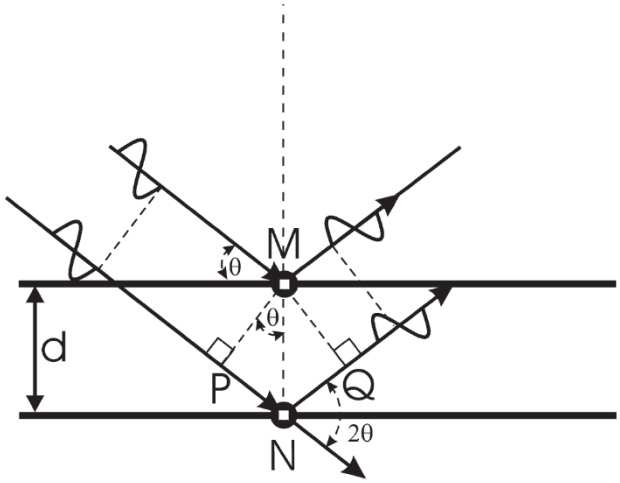

Figure 2.10. Illustration of Bragg's law in a simplified form. This figure was reproduced from the work of Dinnebier.[16]

By determining the diffraction angle, elemental d-spacing can be found and indexed using the lattice parameters of the specimen.

An Empyrean-II powder diffractometer fitted with a 10 mm slit was used to investigate the crystalline structure of nanoparticles using a Co source. In powder X-ray diffraction (XRD), a rotating detector collects X-rays diffracted from a solid sample at a range of angles. A spectrum of peaks is then constructed based on the angles and corresponding intensities of each peak. Further analysis of these XRD patterns can be performed via database comparison and correlating them with a specific structure. Highscore software was used to process the XRD data in this work.

2.5 X-ray photoelectron spectroscopy (XPS)

XPS was performed to examine the chemical composition of the synthesized nanocrystals and the binding energies of each element. XPS involves the measurement of photoelectrons generated when the solid surface is irradiated by a beam of X-rays. These emitted photoelectrons have quantifiable kinetic energy, which is dependent upon its binding energy in the atom, as shown in Eq. 2.2.

$$E_{binding} = h\nu - E_{kinetic} - \phi \qquad (2.2)$$

where $E_{binding}$ is the binding energy, $E_{kinetic}$ is the kinetic energy, h is Planck's constant, ν is the frequency of the incident photon, and the ϕ is the work function of the spectrometer.

The chemical composition of a sample, and the respective oxidation states of each element, can be determined by interpreting the intensity of a detected peak and its corresponding binding energy.

XPS analysis was performed on an ESCALab 250 Xi (Thermo Scientific) spectrometer with a monochromated Al Kα source. The pressure in the analysis chamber during measurements was < 108 mbar. The pass energy and step size for narrow scans were 20 eV and 0.1 eV, respectively, with a take-off angle normal to the sample surface. Spectral analysis was performed using Avantage 4.73 software, and the curve fitting was carried out using a mixture of Gaussian–Lorentzian functions.

2.6 Electrochemical characterizations

All electrochemical measurements were acquired using an Autolab potentiostat running with Nova 2 software. All experiments were performed using a three-electrode cell, with the working electrode kept at a 1600 rpm rotation.

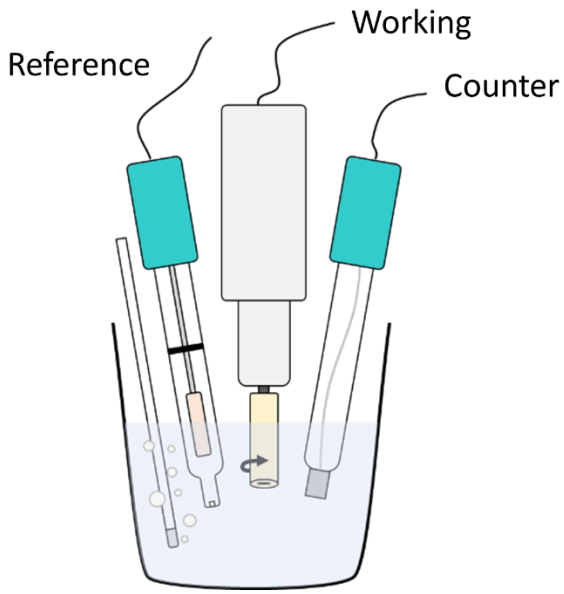

Figure 2.11. Schematic illustration of a three-electrode electrochemical setup showing the working, counter, and reference electrodes.

In alkaline media, a 1 mol L^{-1} KOH solution was used as the electrolyte. A Pt-mesh and Hg|HgO|1 mol L^{-1} NaOH was used as the counter electrode and reference electrode, respectively.

In acidic media, a 0.1 M HClO4 solution was used as the electrolyte. A Pt-mesh and Ag|AgCl|3 M NaCl were used as the counter electrode and reference electrode, respectively.

All potentials were converted to the reversible hydrogen electrode (RHE) by measuring the potential between the reference electrode and a freshly

prepared standard reference electrode (SHE), whilst taking into consideration electrolyte pH.

2.6.1 Catalysts ink preparation

As described in Section 2.2.5, Co nanoparticles were adhered to a carbon support, yielding 20 wt% Co. In contrast, Ru-Pd and RuCo-Pd nanoparticles were used directly in these experiments. The nanoparticles (carbon loaded nanoparticles) (2.5 mg) were dispersed in toluene (1000 μL) and Nafion 0.5 % v/v (20 μL) to make a catalytic ink. The working electrode was prepared by drop-casting the electrocatalysts (15 μL) and Nafion (0.05 % v/v, 5 μL) onto the glassy carbon surface (0.196 cm2 area). For the Co catalysts, the actual wt % of Co was determined by ICP-OES.

2.6.2 Catalytic activation

Catalytic activation was performed prior to the catalytic activity tests in order to reduce surface oxides and remove surfactants.

Any surface Co oxides that formed due to air exposure was removed by keeping the potential at -0.3 V (RHE) for 3 minutes. In the case of Ru catalysts, the catalytic activation was carried out by running several cycles of cyclic voltammetry (CV) scans to remove surfactant material.

2.6.3 OER activity

Electrocatalysis was used to determine the catalytic activities of the catalysts for the OER. In alkaline OER, CVs were collected at 100 mV s^{-1} in 1.0 mol L^{-1} of KOH within the potential window of -0.3 V vs. and 1.7 V (RHE). For acidic OER, CVs were recorded at 50 mV s^{-1} in 0.1 mol L^{-1} of HCl within the potential range of 1.0 V and 1.55 V (RHE).

By analyzing the collected CVs data, the catalytic activity, catalyst oxidation state, and reaction kinetics were determined. The oxidation peaks of CVs may provide information concerning the transformation of the catalysts and the formation of catalytic active sites during OER. Anodic scans of the voltammograms were used to determine OER activity. Geometric and specific activities of the catalysts were calculated by normalizing the current to that of the electrode area and electrochemical surface area, respectively. Data acquired from the anodic scans of CVs were used to construct plots of the overpotential versus current density. Contained in the gradient of these curves was the Tafel slope, which were used to explain the reaction kinetics of the electrocatalysis.

2.6.4 Stability test

Chronopotentiometry techniques and CVs were used to evaluate the catalytic stability of the catalysts.

Chronopotentiometry is a galvanostatic method in which the current at the working electrode is held at a constant level for a given period of time, whilst the potential is measured as a function of time. Chronopotentiometry measurements were conducted at a geometric current density of 10 mA cm^{-2} for 2 hours. Other experimental conditions, including the amount of particles, scan rate, and electrodes, were kept consistent to those incorporated in the activity tests.

Stability was then evaluated by computing the difference between the maximum catalytic activity and the activity after 200, 400, 800, and 1000 OER cycles. Cyclic voltammetry measurements for the stability tests were performed under the same conditions as those used for the activity tests. For determining faradaic efficiency, the amount of dissolved Ru after 5, 10, 100,

200, and 500 cycles was firstly found using ICP-MS. The Faradaic efficiencies of the electrocatalysts for these given cycles were then determined from the charge of Ru and the total charge.

2.6.5 Electrochemical surface area

The electrochemical surface area (ECSA) of the catalysts was determined from the slope of the capacitive current versus scan rate plots. To obtain a capacitance value, particles prepared without a carbon support were first dispersed in toluene. The exact concentration of this solution was determined using ICP-OES, and this same mass of catalyst was added onto the glassy carbon surface across all samples. Cyclic voltammetry measurements within the capacitive potential range were performed at 5, 10, 20, and 50 mV s^{-1} scan rates. The obtained capacitance was then used to calculate the ECSA using the corresponding specific capacitance.

2.6.6 Electrochemical impedance spectroscopy

Electrochemical impedance spectroscopy (EIS) measurements were carried out using the same experimental setup described above using particles prepared without a carbon support. After five potentiodynamic cycles, EIS measurements were performed from 10000 Hz to 0.1 Hz at 1.61 V (RHE) and 10 mV amplitudes. Before each EIS measurement, pretreatment was carried out for three minutes under the same potential used for measurement, after which the current was constant. EIS spectra fitting was done using a Voigt circuit with two-time constants (R(QR)(QR)) and ‘’ZSimp.Win 3.22’’ software.

2.7 References

1. Dumestre, F.; Chaudret, B.; Amiens, C.; Fromen, M.-C.; Casanove, M.-J.; Renaud, P.; Zurcher, P., Shape Control of Thermodynamically Stable Cobalt Nanorods through Organometallic Chemistry. *Angewandte Chemie International Edition* **2002,** *41* (22), 4286-4289.
2. Cordente, N.; Respaud, M.; Senocq, F.; Casanove, M.-J.; Amiens, C.; Chaudret, B., Synthesis and Magnetic Properties of Nickel Nanorods. *Nano Letters* **2001,** *1* (10), 565-568.
3. LaGrow, A. P.; Ingham, B.; Cheong, S.; Williams, G. V.; Dotzler, C.; Toney, M. F.; Jefferson, D. A.; Corbos, E. C.; Bishop, P. T.; Cookson, J.; Tilley, R. D., Synthesis, alignment, and magnetic properties of monodisperse nickel nanocubes. *J Am Chem Soc* **2012,** *134* (2), 855-8.
4. McGrath, A. J.; Cheong, S.; Henning, A. M.; Gooding, J. J.; Tilley, R. D., Size and shape evolution of highly magnetic iron nanoparticles from successive growth reactions. *Chem Commun (Camb)* **2017,** *53* (84), 11548-11551.
5. Cheong, S.; Watt, J.; Ingham, B.; Toney, M. F.; Tilley, R. D., In Situ and Ex Situ Studies of Platinum Nanocrystals: Growth and Evolution in Solution. *Journal of the American Chemical Society* **2009,** *131* (40), 14590-14595.
6. Gloag, L.; Benedetti, T. M.; Cheong, S.; Marjo, C. E.; Gooding, J. J.; Tilley, R. D., Cubic-Core Hexagonal-Branch Mechanism To Synthesize Bimetallic Branched and Faceted Pd-Ru Nanoparticles for Oxygen Evolution Reaction Electrocatalysis. *J Am Chem Soc* **2018,** *140* (40), 12760-12764.
7. Gloag, L.; Benedetti, T. M.; Cheong, S.; Li, Y.; Chan, X. H.; Lacroix, L. M.; Chang, S. L. Y.; Arenal, R.; Florea, I.; Barron, H.; Barnard,

A. S.; Henning, A. M.; Zhao, C.; Schuhmann, W.; Gooding, J. J.; Tilley, R. D., Three-Dimensional Branched and Faceted Gold-Ruthenium Nanoparticles: Using Nanostructure to Improve Stability in Oxygen Evolution Electrocatalysis. *Angew Chem Int Ed Engl* **2018,** *57* (32), 10241-10245.

8. Kwon, S. G.; Hyeon, T., Formation mechanisms of uniform nanocrystals via hot-injection and heat-up methods. *Small* **2011,** *7* (19), 2685-702.

9. Kang, Y.; Ye, X.; Murray, C. B., Size- and shape-selective synthesis of metal nanocrystals and nanowires using CO as a reducing agent. *Angew Chem Int Ed Engl* **2010,** *49* (35), 6156-9.

10. Yin, Y.; Alivisatos, A. P., Colloidal nanocrystal synthesis and the organic–inorganic interface. *Nature* **2005,** *437* (7059), 664-670.

11. Mourdikoudis, S.; Liz-Marzán, L. M., Oleylamine in Nanoparticle Synthesis. *Chemistry of Materials* **2013,** *25* (9), 1465-1476.

12. Wang, X.; Choi, S. I.; Roling, L. T.; Luo, M.; Ma, C.; Zhang, L.; Chi, M.; Liu, J.; Xie, Z.; Herron, J. A.; Mavrikakis, M.; Xia, Y., Palladium-platinum core-shell icosahedra with substantially enhanced activity and durability towards oxygen reduction. *Nat Commun* **2015,** *6*, 7594.

13. Sang-Wook Kim, J. P., Youngjin Jang, Yunhee Chung,; Sujin Hwang, a. T. H., Synthesis of Monodisperse Palladium Nanoparticles *Nano Lett* **2003,** *3* (9), 1289-1291.

14. Williams, D. B.; Carter, C. B.; Spence, J. C. H., *Transmission electron microscopy. a textbook for materials science 4, 4*. 2009.

15. Luo, Z.; ProQuest, A practical guide to transmission electron microscopy. **2016**.

16. Dinnebier, R. E.; Billinge, S. J. L.; Le Bail, A.; Madsen, I.; Cranswick, L. M. D.; Cockcroft, J. K.; Norby, P.; Zuev, A. D.; Fitch, A.; Rodriguez-Carvajal, J.; Giacovazzo, C.; Von Dreele, R. B.; Scardi, P.; Popa, N. C.; Allmann, R., Powder Diffraction Theory and Practice. **2008**.

Chapter 3

Optimization of the synthesis of Co-Au and Ru-Pd branched nanoparticles

3.1 Chapter Overview

This chapter covers the synthetic approaches used in fabricating Co-Au and Ru-Pd branched nanoparticles for improved oxygen evolution reaction in Chapters 4 and 5 of this thesis.

Successful syntheses of Co-Au branched nanoparticles, and Ru-Pd branched nanoparticles with precisely controlled branch numbers and branch size, as well as any synthetic challenges in making these particles, are explained below in more detail.

3. 2 Co-Au branched nanoparticles synthesis

3D-bimetallic branched nanoparticles consisting of a Au-core and highly crystalline *hcp*-Co-branches were synthesized to develop a Co electrocatalyst with excellent catalytic performance as described in Section 1.4.1. A cubic-core hexagonal-branch approach was used to grow Co branches on a Au-core, as this method has been successfully implemented in designing a wide range of metallic branched nanoparticles systems.[1-4] It is imperative that the basic experimental parameters, including reactants and experimental conditions (i.e. temperature, pressure, time) be determined prior to nanoparticle synthesis. The pioneering work on this approach by the Alivisatos group suggests that, excluding seeds, other experimental parameters such as solvent, reducing agent, and surfactant can be chosen based on the previous works conducted on similar metallic nanoparticles (Section 1.5)[5]. Thus, in accordance with earlier literature work on Co nanorods[6, 7] and other branched nanoparticles[1, 3], $Co(acac)_2$ and $Co(laurate)_2$, hexadecylamine (HDA), and mesitylene were selected as the precursors, surfactant, and solvent species, respectively. These particular reagents were chosen for the following reasons: (i) $Co(acac)_2$ was chosen as a precursor because $M(acac)_x$ precursors are generally used for organic solution-phase synthesis due to their solubility and low decomposition temperatures[1, 3]. In addition, $Co(laurate)_2$ was selected due to its carboxylate anions[6, 7]. (ii) HDA and other long-chain amine surfactants were employed well to stabilize the lateral facets of hcp-Co, which enable the growth of Co nanorods[6]. (iii) The choice of mesitylene was made due to its higher boiling point (164.7°C) and ability to dissolve the organometallic complexes. Furthermore, Au cores were used as the template for growing Co branches in this synthesis as they

are a common seed material, with exceptional durability and well-defined structure[8].

The reduction rate and the reaction time also play a crucial role in the growth of nanocrystals[8, 9]. The use of a weak reducing agent permits the reduction of the Co slowly, thereby controlling the concentration of Co atoms and preventing homogeneous nucleation during the synthesis[8, 9]. In our group, we use a Fischer-Porter bottle reaction vessel, as the incorporation of H_2 atmospheres can be performed under a controlled environment. These bottles also provide precise control over temperature and pressure. In particular, reaction temperatures of 140°C and a 24-hour time period were incorporated according to the synthetic conditions of Co nanorods[6, 7]. It is important for the reaction temperature to be able to decompose the metallic precursor and for the reaction time to provide time to facilitate the formation of the final product[6, 7].

Prior to synthesis, Au seeds were prepared according to a previously published method by Anna in our group[10]. Then, to grow cobalt branches, this Au seed solution was added to a solution containing cobalt(II) acetylacetonate and hexadecylamine dissolved in mesitylene. This reaction mixture was then transferred to a Fischer-Porter bottle, where it was left to react under 3 bar hydrogen at 140°C for 24 hours. After this time, H_2 was released, and the final product was purified twice using a 1:1 toluene and ethanol solution at 8000 rpm.

Using this approach, the successful synthesis of Co-Au branched nanoparticles was achieved by optimizing the precursor to seed ratio, precursor type, and reaction time.

3.2.1 Experiment 1-3: Effect of precursor to seed ratio.

In order to determine the optimal precursor to seed ratio, a series of experiments were designed with differing precursor to seed parameters. Variations in precursor ratio can alter the deposition and surface diffusion rates of metallic atoms, changing the final shape of nanocrystals[9]. The precursor to seed ratio can affect the growth pattern of the secondary metal on the seed as it changes the available atomic concentration of metal per seed. To find this optimal precursor to seed ratio when synthesizing Co-Au branched nanoparticles, three experiments were performed at varying precursor to seed ratios (10:1 to 30:1 and 100:1 Co:Au). By doing so, the effect of precursor to seed ratio on the final architecture of synthesized Co-Au branched nanoparticles could be investigated.

Experimental

For these experiments, the Au seed solution was added to a solution containing 0.25 mmol cobalt(II) acetylacetonate (0.065 g) as a precursor and 5 eq. mol of hexadecylamine (0.3018 g) as a surfactant dissolved in 2 mL of mesitylene. The amount of Au seed was varied in order to achieve ratios of Co to Au at 10:1, 30:1, and 100:1 while the amount of $Co(acac)_2$ was kept constant. The reaction mixture was then taken place under 3 bar hydrogen at 140^{o}C for 24 hours. After the reaction, H_2 was released, and purification was done twice using toluene and ethanol solution (1:1 volume ratio) at 8000 rpm. Co_3O_4 nanoparticles were also synthesized using the same method without the Au seeds (Chapter 4). These experimental set-ups are summarized in Table 3.1 below.

Table 3.1. The experimental conditions applied for the precursor to seed ratio on the synthesis of Co-Au branched nanoparticles.

Exp. #	Co: Au ratio	The amount of Co, mmol	The amount of Au seeds, mmol	Temp., °C	Time, h
1	10:1	0.25	0.025	140	24
2	30:1	0.25	0.0084	140	24
3	100:1	0.25	0.0025	140	24

Results

A noticeable colour change in solution from purple-red to black was a good indicator of the formation of Co nanoparticles in solution. To support these initial observations, Figure 3.1 shows the representative low-resolution TEM images of as-synthesized Co-Au nanoparticles using a Co: Au ratio of 10: 1, 30: 1, and 100: 1, respectively.

When a Co : Au ratio of 10: 1 was applied, Au-Co core-shell nanoparticles with an average diameter of 19.4±2.3 nm were formed. When the Co: Au ratio was increased to 30 :1, each nanoparticle would typically have 1-2 Co branches, with branch length of 21.3 ± 8.0 nm and width of 9.0 ±1.0 nm being obtained. These branches grow from a 25.0 ±3.2 nm nanoparticle core, which itself is of a core-shell structure. When the Co : Au ratio was further increased to 100 : 1, each nanoparticle would have 3 -5 branches, with branch length of 63.4 ±12.3 nm and width of 9.3 ± 1.4 nm, being formed. The core diameter of these branched nanoparticles was determined to be 33.2 ± 5.4 nm.

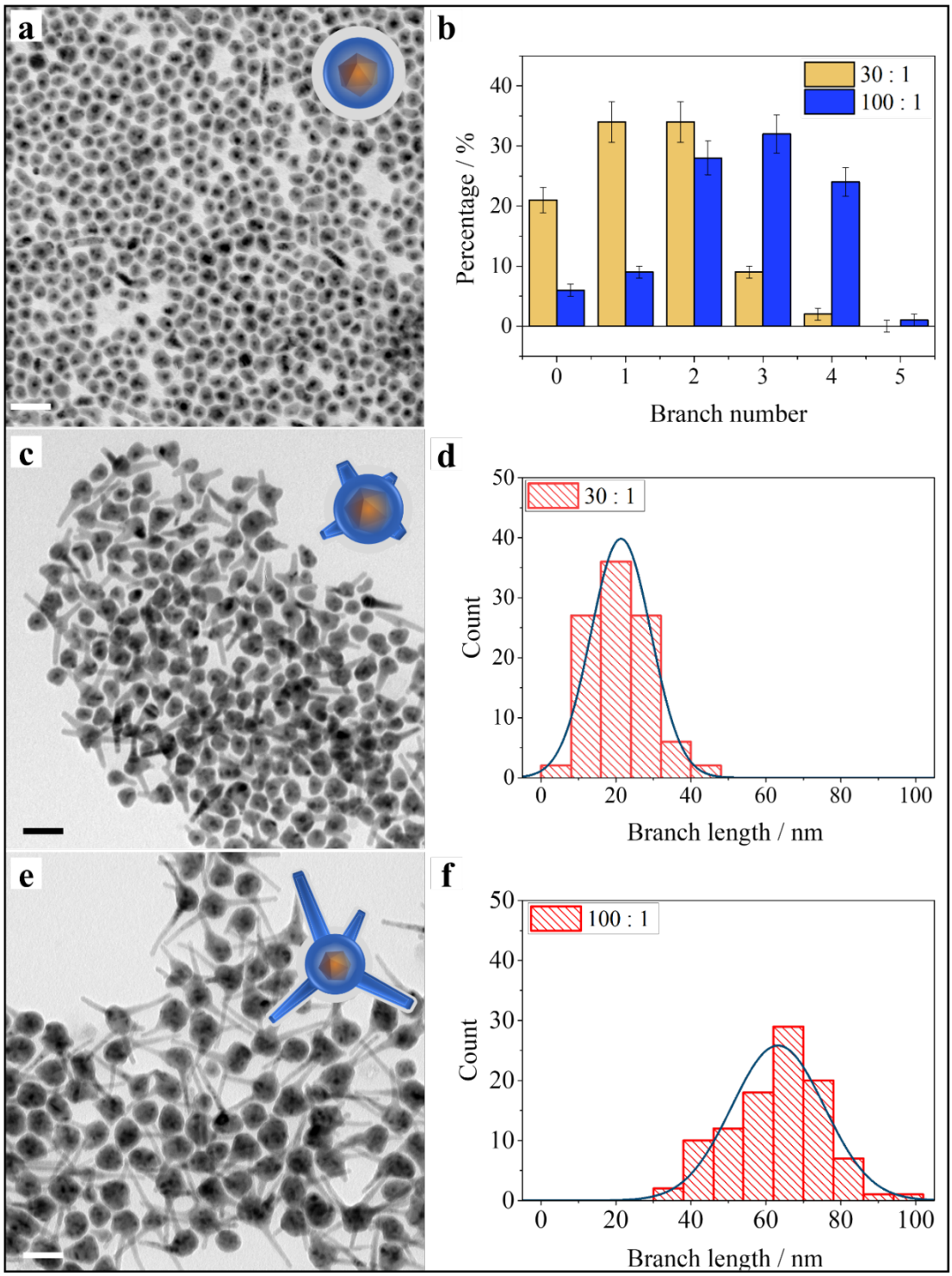

Figure 3.1. TEM images of Au-Co particles synthesized at different Co precursor to Au seed ratios: (a) Au-Co core-shell nanoparticles (10:1) and (c, e) Co-Au branched nanoparticles with different branch numbers and lengths (30:1 and 100 :1, respectively), (b) branch numbers, (d, f) branch lengths of the branched nanoparticles. Scale bars = 50 nm.

Discussion

Noticeable effects of the precursor to seed ratio on branch number and branch size were observed in the growth of these Co-Au branched nanoparticles. At a lower precursor to seed ratio (10: 1), Au-Co core-shell (Co -spherical) nanoparticles were formed. With an increase in precursor to seed ratio (30 : 1), branched nanoparticles were obtained. The high precursor to seed ratio (100 : 1) further increased the branch number and length of these branched nanoparticles.

The formation of a Co shell can be attributed to the large lattice mismatch difference (8.1 %) between fcc-Au(111) (2.36 Å) and hcp-Co(0001) (2.17 Å), which is higher than 5.0 %. A similar growth pattern was also obtained for the formation of Ru-Au branched nanoparticles, where Ru shell formed on the Au core followed by the growth of Ru branches[2].

The growth rate along hcp {0001} facets is higher than that of hcp {10-11} facets since surfactant molecules stabilize these hcp {10-11} facets during reaction. Due to their faster growth rate, Co adatoms grow continuously along this c-axis, thus increasing Co branch length. The number of branches is also increased at higher precursor to seed ratios since the larger core in branched nanoparticles provides a higher exposed surface area for nucleation sites.

Overall, it can be demonstrated that the shape of these Co-Au nanoparticles as well as their resultant branch number and branch length, can be tuned by varying this precursor to seed ratio.

3.2.2 Experiment 4: Effect of the type of precursor

In order to explore the effect of the precursor type on the final shape of Co-Au nanoparticles, a separate series of experiments were constructed using two types of Co precursors with different solubilities and decomposition rates. The choice of a suitable precursor is important for synthesizing nanoparticles with tunable size and shape. For example, the Chaudret group compared two types of Co precursors, namely, $Co_2(CO)_8$ and $Co(\eta_3\text{-}C_8H_{13})(\eta_4\text{-}C_8H_{12})$ (an organometallic precursor), for the synthesis of Co nanoparticles[6]. The use of a $Co_2(CO)_8$ precursor yielded polydisperse Co nanoparticles, whereas $Co(\eta_3\text{-}C_8H_{13})(\eta_4\text{-}C_8H_{12})$ yielded monodisperse Co nanoparticles. They found out that the decomposition rate, solubility, and by-products of these precursors can affect the growth mode of nanoparticles by changing its reaction kinetics. For these reasons, I chose $Co(laurate)_2$ and $Co(acac)_2$ as Co precursors to investigate the role of precursors on the growth of Co on Au cores since $M(laurate)_x$ and $M(acac)_x$ are common precursors used in nanoparticle synthesis.

Experimental

Two experiments were conducted, one of which used the same protocol for synthesizing Co-Au branched nanoparticles as described in Exp. 3. Experiment 4 also used a similar approach, except for replacing $Co(acac)_2$ with $Co(laurate)_2$. These changes are summarised in Table 3.2.

Table 3.2. The experimental conditions applied for the effect of precursor on the synthesis of Co-Au nanoparticles.

Exp. #	Cobalt precursor	Precursor to seed ratio	Surfactant	Temp., °C	Time, h
3	$Co(acac)_2$	100 : 1	Hexadecylamine	140	24
4	Co(II) laurate	100 : 1	Hexadecylamine	140	24

Results

A similar change in reaction solution colour from purple to brown-black was used to denote the formation of Co nanoparticles. A representative TEM image of the nanoparticles formed using $Co(laurate)_2$ is shown in Figure 3.2. Polydisperse Co-Au core-shell nanoparticles with an average diameter of 30.0 ± 5.4 nm were formed when cobalt(II) laurate was used as a precursor.

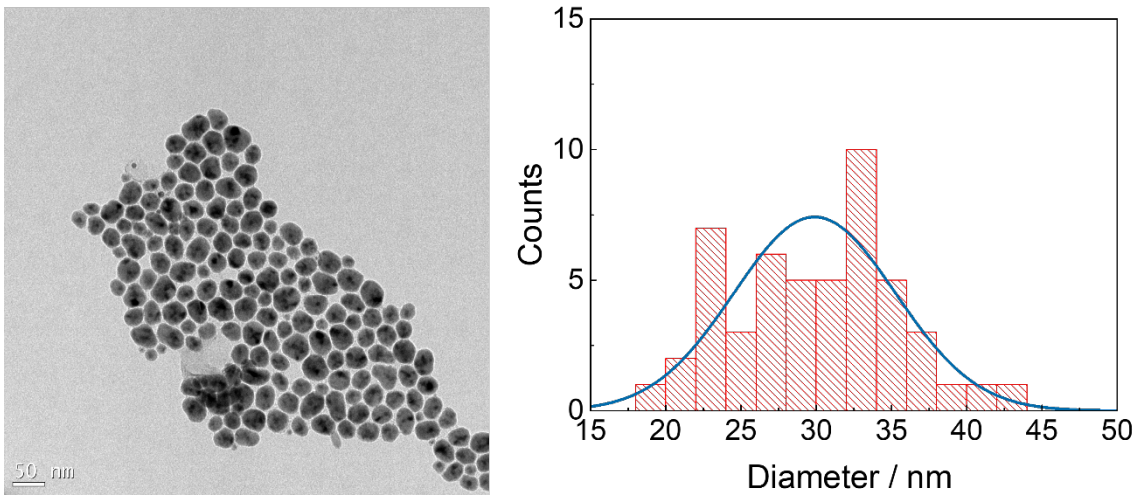

Figure 3.2. TEM image of the particles synthesized using $Co(laurate)_2$ as the Co precursor with a corresponding size distribution.

Discussion

The Chaudret group has previously reported that the decomposition rate of a precursor plays a critical role in the nucleation step and growth of nanoparticles[7]. In this work, it was shown that a higher precursor decomposition rate enabled anisotropic growth while a slower decomposition rate enabled the formation of a spherical core[7]. Thus, the formation of polydisperse Au-Co core-shell nanoparticles can be linked to the slower decomposition rate of $Co(laurate)_2$ precursor compared to $Co(acac)_2$.

3.2.3 Experiment 4-6: Time-resolved experiments.

To further understand the growth mechanism of these Co-Au branched nanoparticles, time-resolved experiments were carried out. The schematic illustration and corresponding TEM images of Au seeds and nanoparticles synthesized after 30 min, 45 min, and 24 h are shown in Figure 6. From these studies, it can be seen that the growth mechanism of these branched nanoparticles consists of the following steps: (i) the synthesis of initial gold seeds, (ii) the formation of Co shell, and (iii) the growth of Co branches.

Experimental

These experiments were performed under the same reaction conditions as those used to synthesize Co-Au branched nanoparticles in Exp. 3, except for varying the reaction time period. These changes are summarized in Table 3.3.

Table 3.3. The experimental conditions applied for the effect of reaction time on the synthesis of Co-Au nanoparticles.

Exp. #	Cobalt precursor	Precursor to seed ratio	Surfactant	Temp., °C	Time
5	$Co(acac)_2$	100 : 1	Hexadecylamine	140	30 min
6	$Co(acac)_2$	100 : 1	Hexadecylamine	140	45 min
3	$Co(acac)_2$	100 : 1	Hexadecylamine	140	24 h

Results

The schematic illustration and TEM images of synthesized Au seeds and nanoparticles after 30 min, 45 min, and 24 h of reaction time are shown in Figure 3.2. Core-shell nanoparticles were obtained after 30 min of reaction, indicating the formation of an outer Co shell over Au seeds. After 45 min, short branches were formed from this Co shell, with differences in image contrast highlighting changes in elemental composition between Co and Au regions. Branched nanoparticles with a larger core and longer branch lengths of 63 ± 12 nm were obtained after 24 h, indicating that adatoms of Co grow on the shell and promote the continuous growth of branches along the c-axis.

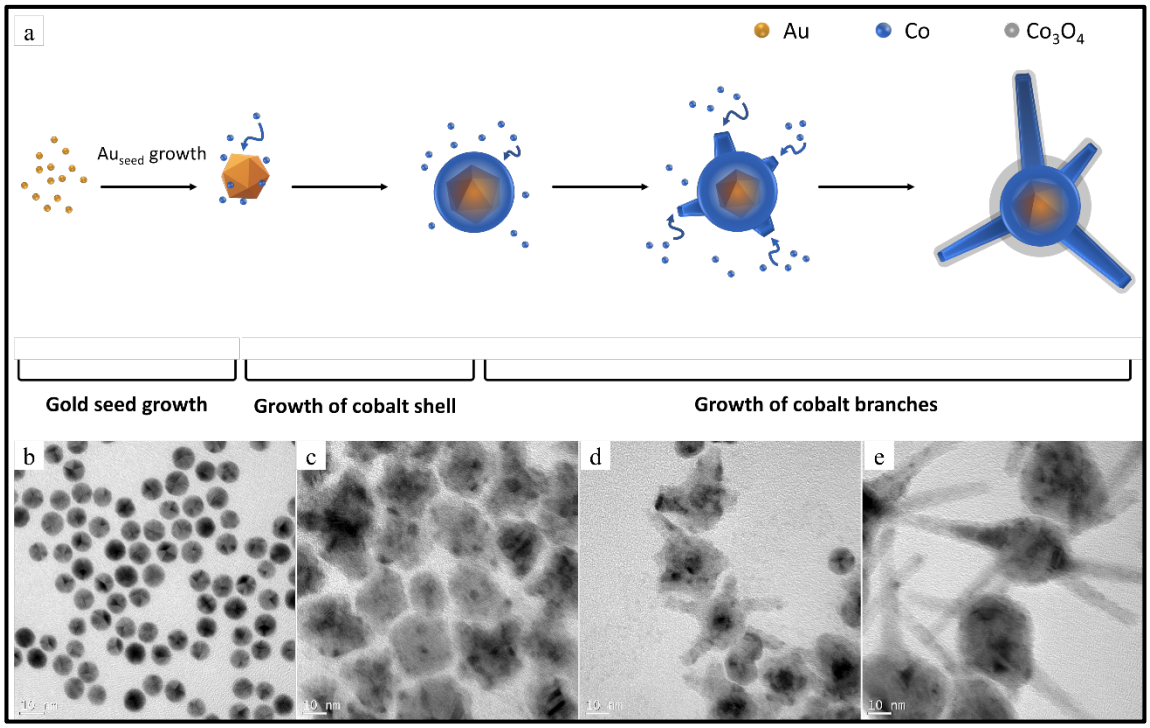

Figure 3.3. Time-resolved synthesis. (a) proposed growth mechanism, (b) initial gold seeds and nanoparticles formed after (b) 30 min, (c) 45 min, and (c) 24 h reaction periods.

Discussion

In a generic cubic-core hexagonal-branch growth mechanism, hcp-branches grow on an fcc-core along the c-axis due to the preferential alignment of atoms on the {111} and {0001} facets[5]. To understand this growth mechanism for the Co-Au branched nanoparticle system, time-resolved reactions were performed. The formation pathway of these branched nanoparticles was shown to consist of the following steps: (i) the synthesis of initial Au seeds, (ii) the formation of an outer Co shell, and (iii) the growth of Co branches. Outer Co shells formed over Au seeds during the first stage of the reaction are promoted due to the large lattice mismatch difference between surface atoms at the Au{111} and Co{0001} planes (8.1 % mismatch). Furthermore, this Co shell reduces the mismatch between surface atoms, enabling the growth of branches along the c-axis during subsequent

stages of the reaction. The formation of this shell is consistent with the previous report on the synthesis of Ru-Au branched nanoparticles, where the mismatch between Ru and Au is also higher than 5.0 %.[2]

3.3 Ru branched nanoparticles with controlled surface facets and branch numbers

This project aims to synthesize Ru branched nanoparticles with precisely controlled surface facets and branch numbers for improved OER. The surface facets can be controlled by tuning Ru branch length.

A cubic-core hexagonal-branch approach was used to make Ru-Pd branched nanoparticles in this study. The synthesis protocol of Ru-Pd branched nanoparticles developed by one of our group members (Gloag et al.) was applied to the following experiments with a few modifications[1]. In seed-mediated growth, seed structures[8], the rate of adatom diffusion[9, 11], and surfactants[12] all play a significant role in determining the resultant shape and size of the final nanoparticles. Hence, the precursor to seed ratio and seed size were selected as the variable parameters in the synthesis of Ru nanoparticles for controlling the branch length and number, respectively.

Branch length and, thus, surface facets of Ru branched nanoparticles can be controlled by altering the precursor to seed ratio. Because branch side facets ($\{10\bar{1}1\}$) of branches are passivated by surfactant molecules, the Ru adatoms could be continuously deposited on the base facets ($\{0001\}$), thus increasing in length.

Furthermore, the branch number of Ru nanoparticles can be modified by varying the size of the seed. For instance, a larger cubic seed is expected to expose more $\{111\}$ surfaces to deposit Ru adatoms, leading to an increase in branch number.

To achieve a successful synthesis of Ru branched nanoparticles with strict control over branch size and number, we first synthesized well-defined Pd

and Au cubic seeds with precise dimensions. The choice of Pd and Au seeds was made due to their well-defined and stable structures, making them great candidates for nanoparticle synthesis[8, 13]. Using these seeds, Ru branched nanoparticles with controlled branch lengths and numbers were then synthesized by optimizing synthetic conditions, including the precursor to seed ratio, seed size, and surfactant type.

3.3.1 Pd seeds with tunable sizes

The goal of these experiments is to synthesize Pd seeds with tunable sizes. A thermal composition method was first used to make small Pd seeds, and a seed-mediated growth approach was then used to obtain larger Pd seeds by growing Pd atoms onto smaller seeds. Previously established methods for the synthesis of Pd seeds were applied for the following experiments with a few modifications[14, 15]. In order to increase the shell thickness of Pd surrounding these small seeds, the precursor to seed ratio was varied with the aim of promoting Pd atom growth. It was hypothesized that Pd seeds with tunable sizes could be achieved using a similar seed-mediated approach by varying the precursor to seed ratio based on earlier works on Pd icosahedra[15] and core-shell nanocrystals[16-18]. For instance, Graham et al. reported the synthesis of Pd icosahedra seeds (12.9 ± 0.7 nm) using a seed-mediated approach[15]. In this synthesis, a Pd shell formed on a Pd core (5.8 ± 0.4 nm) via the slow reduction of $Pd(acac)_2$ in the presence of hexadecylamine as the surfactant and hydrogen as the reducing agent. In addition, studies conducted on the synthesis of core-shell nanoparticles[16-18] have shown that shell thickness can be controlled by varying the precursor to seed ratio.

Thus, Pd seeds (3.5 ±0.4 nm) were first synthesized using a thermal decomposition method according to previously published works[1, 14].

Subsequent experiments (Experiments 8-10) were then conducted using varying precursor to seed ratios in order to synthesize larger Pd seeds with controlled sizes.

Experimental

Synthesis of small Pd seeds. Small Pd seeds were synthesized via a thermal decomposition method according to a previously published protocol[1, 14, 19]. $Pd(acac)_2$ (0.16 mmol, Sigma-Aldrich, 99 %) was dissolved in 5 mL of oleylamine (Sigma-Aldrich, 70 %) in a 25 mL three-neck flask equipped with a magnetic stirrer bar. The reaction mixture was then heated to 100 °C under an Ar atmosphere for 30 min. After this time, 0.25 mL of trioctylphosphine (TOP, Sigma-Aldrich, 97 %) was added to the reaction mixture. The temperature was then raised to 250°C at a rate of 3 °C min^{-1} and held for 30 min. Once complete, the mixture was cooled down under Ar, and purification via centrifugation was performed 4-5 times using ethanol and toluene (1:1 volume ratio) at 14000 rpm. The purified Pd seeds were kept in mesitylene (Sigma-Aldrich, 98 %) for further experiments.

Table 3.4. The experimental conditions applied for the synthesis of small Pd seeds.

Exp. #	Pd precursor, mmol	Solvent/Surfactant	Temp. ramp/ °C min^{-1}	Temp. / °C	Time
7	0.16	Oleylamine/ TOP	3	100	30
				250	30

Synthesis of larger Pd seeds. Larger Pd seeds were synthesized using a similar seed-mediated approach, with a slight modification made to the

synthesis of the Pd icosahedra nanocrystals[15]. Bis(acetonitrile) dichloropalladium ($PdCl_2(CH_3CN_2)$) (0.05 mmol, Sigma-Aldrich, 99 %) and 10 eq. molar hexadecylamine (0.5 mmol, Sigma-Aldrich, 90 %) was first dissolved in toluene (1.0 mL). Pre-synthesized Pd seeds (3.5 ±0.4 nm) (0.00125-0.0125 mmol) and toluene (10 mL, Chem-Supply, 99.9 %) were then added to this solution. The reaction mixture was then kept under a 3 bar hydrogen atmosphere at 25°C for 2 hours. Once complete, H_2 was released, and purification of the seeds via centrifugation was performed 4-5 times using an ethanol and toluene solution (1:1 volume ratio) at 14000 rpm. The synthesized Pd seeds were kept in mesitylene for further studies. The size of the Pd seeds was tuned by varying the precursor to seed ratio.

Table 3.5. The experimental conditions applied for the synthesis of Pd nanoparticles with different sizes.

Exp. #	Pd^{2+}: Pd^0 ratio	Pd precursor, mmol	Pd seeds, mmol	Temp. / °C	Time
8	4	0.05	0.0125	25	2
9	20	0.05	0.0025	25	2
10	40	0.05	0.00125	25	2

Results

When synthesizing small Pd seeds, the initial reaction mixture of $Pd(acac)_2$, oleylamine, and TOP appeared yellow in colour. This transitioned to a black appearance upon reaction, indicating the formation of Pd seeds. Figure 3.3a shows the representative low-resolution TEM image and related histogram of these as-synthesized small Pd seeds. The small Pd seeds are monodisperse, with an average diameter of 3.5 ± 0.4 nm, as supported by

corresponding histogram data. These small Pd seeds (3.5 ± 0.4) nm were then used to make larger Pd seeds.

Larger Pd seeds were synthesized using a seed-mediated approach. A change in solution colour from orange-yellow to black was indicative of the reaction reaching completion. Figure 3b-d shows the representative low-resolution TEM images and corresponding histograms of the larger Pd seeds with controlled sizes. The polycrystalline octahedral Pd seeds with an average diameter of 6.0 ±0.7 nm, 8.7 ±0.7 nm, and 11.5 ±0.8 nm were obtained by varying the Pd^{2+}:Pd^{0} ratio from 0.005 to 0.025 and 0.05, respectively.

Discussion

As shown in Figure 3.3, control over the size of Pd nanoparticles was achieved by varying the amount of precursor with respect to the amount of Pd seeds. For seed-mediated growth, determining the amount of precursor needed is essential, as suitable concentration will help suppress homogeneous nucleation and promote the formation of our desired product[8, 13]. By calculating the total surface area of the seeds based on the morphological and quantitative analysis such as TEM and ICP-MS data, we can find the amount of precursor needed to make the final product[8]. Several studies have been conducted towards synthesizing nanoparticles with the controlled shell thicknesses by varying the precursor to seed ratio using a seed-mediated growth approach[16, 20]. For instance, the Xia's group (2014) synthesized Pd@PtnL core−shell nanocubes with tuneable shell thicknesses from one to six atomic layers[17]. The thickness of the Pd shell was achieved by altering the amount of Pd precursor. Gloag et al. reported the synthesis of Pd-Ru core-shell nanoparticles with different shell thicknesses by changing the molar ratio of Ru precursor to Pd seeds[21].

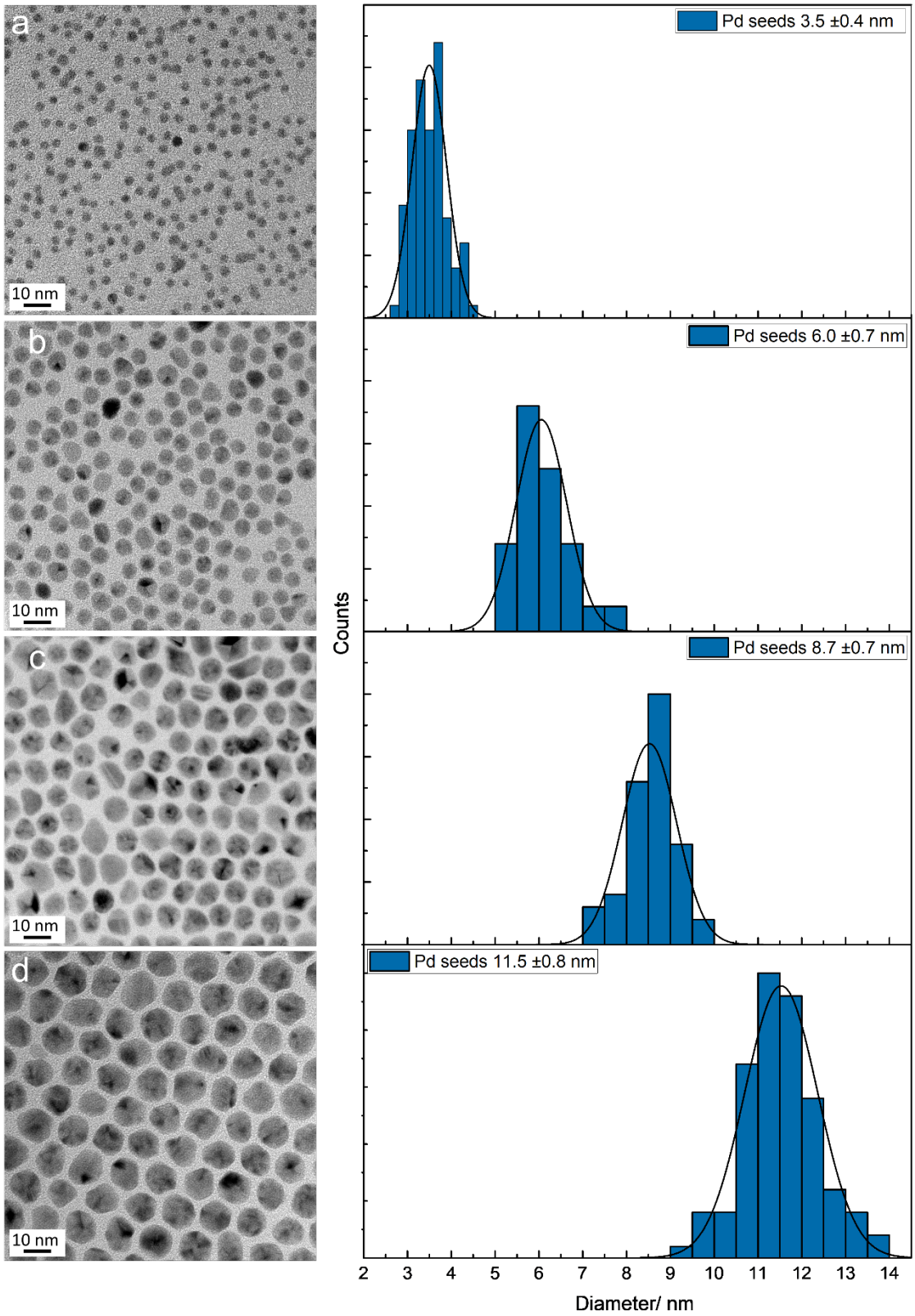

Figure 3.4. TEM images of small Pd seeds synthesized by a one-pot reaction and larger Pd seeds synthesized by a seed-mediated method by varying the precursor to seed ratio. (a) small Pd seeds with an average diameter of 3.5 ± 0.4 nm (b) precursor to seed ratio: 0.005, Pd seeds with an average diameter 6.6 ± 0.7 nm, (c) 0.025, 8.7 ± 0.7 nm, (d) 0.05, 11.5 ± 0.8 nm.

3.3.2 Au seeds with different seed sizes

Au seeds were synthesized via a Fischer-Porter bottle synthesis approach according to a previously established method by our research group (Henning et al.)[10]. The reaction temperature, which influences the rate of nucleation and seed formation, was varied in order to obtain Au seeds with tunable sizes[8].

Experimental

Hexadecylamine (1.072 g, 4.4 mmol) was first dissolved in toluene (4.0 mL), followed by the addition of gold (III) chloride hydrate (0.079g, 0.4 mmol) to this solution. The reaction mixture was placed under a 3 bar hydrogen atmosphere for 24 hours. The reaction temperatures were varied from 60 to 90°C. Once complete, H_2 was released, and purification via centrifuge was conducted twice using a toluene and ethanol solution (1:1 volume ratio) at 8000 rpm. The final, Au seeds were then kept in mesitylene for further syntheses. The experiments shown in Table 3.6 were performed to obtain Au seeds with tunable sizes.

Table 3.6. The experimental conditions applied for the synthesis of Au nanoparticles with different sizes.

Exp. #	Au precursor, mmol	Surfactant	Temp. / °C	Time
11	4.4	Hexadecylamine	**60**	24
12	4.4	Hexadecylamine	**70**	24
13	4.4	Hexadecylamine	**80**	24
14	4.4	Hexadecylamine	**90**	24

Results

During Au seed synthesis, the initial reaction mixture of Au precursor ($HAuCl_4 \bullet 3H_2O$) and hexadecylamine appeared as a shade of golden yellow. Upon reaction completion, this solution colour transitioned to a purple hue, indicating the formation of Au seeds. Figures 3.4 a-d exhibits the representative low-resolution TEM images and corresponding size distributions of the as-synthesized Au seeds. It can be noted that, at 60°C, the largest Au seeds with an average diameter of 14.0 ± 2.7 nm were obtained.

Figure 3.6 illustrates an inverse relationship between Au seed size and reaction temperature. Monodisperse cubic Au seeds with an average diameter of 8.9 ± 0.1 nm, 7.6 ± 0.8 nm, and 7.1 ± 1.0 nm were obtained at different reaction temperatures of 70°C, 80°C, and 90°C, respectively. Insets in Figures 3.4 a-d provide insight into the SAED patterns of these Au seeds with different sizes, similar crystalline structures are obtained for each Au seeds. Specifically, diffraction rings in these SAED patterns confirm that these Au nanoparticles are structured in an fcc arrangement.

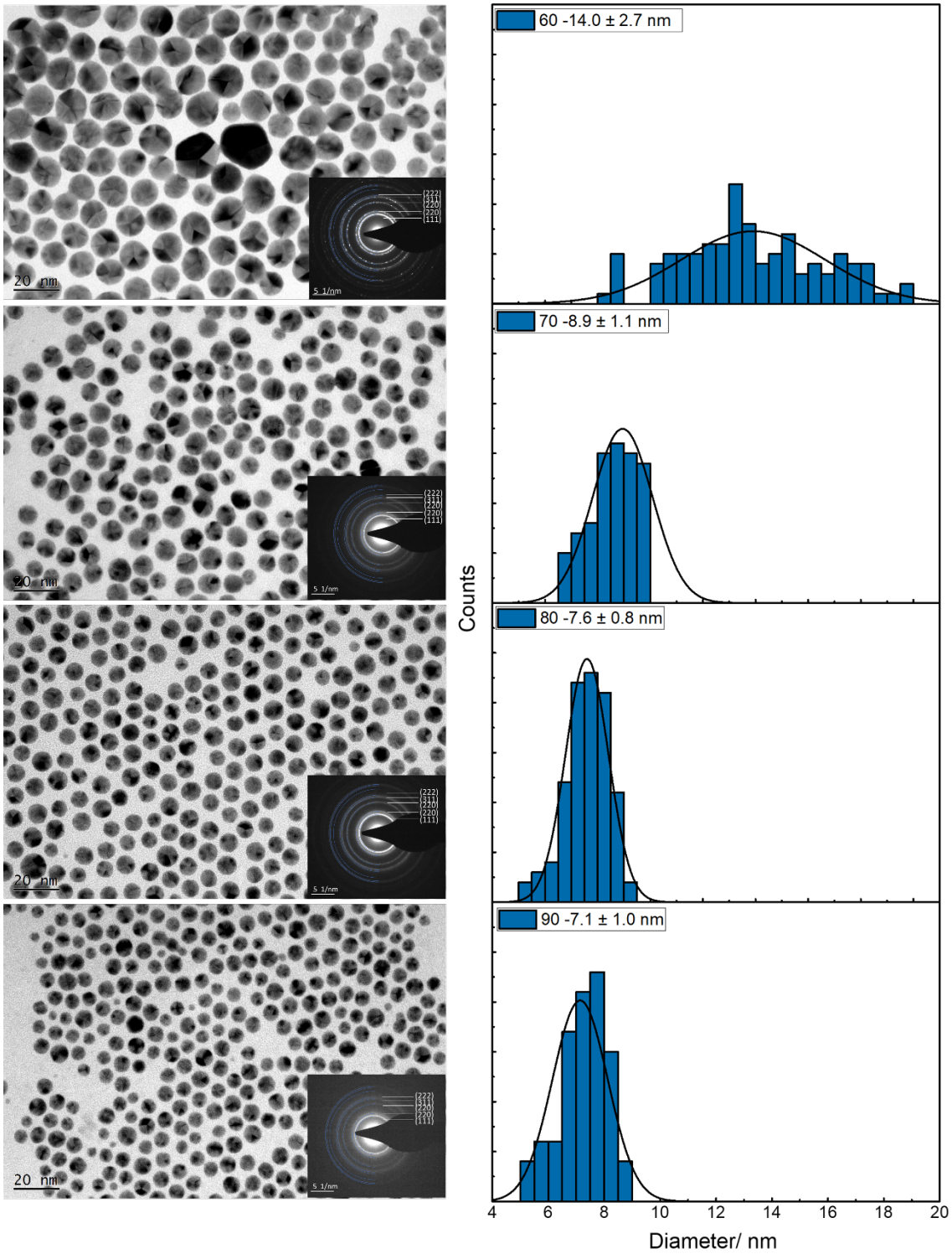

Figure 3.5. TEM images of Au seeds synthesized at different temperatures and their corresponding histograms. (a) 60 ºC, 14.0 ± 2.7 nm, (b) 70 ºC, 8.9 ± 1.1 nm, (c) 80 ºC, 7.6 ± 0.8 nm, (d) 90 ºC, 7.1± 1.0 nm.

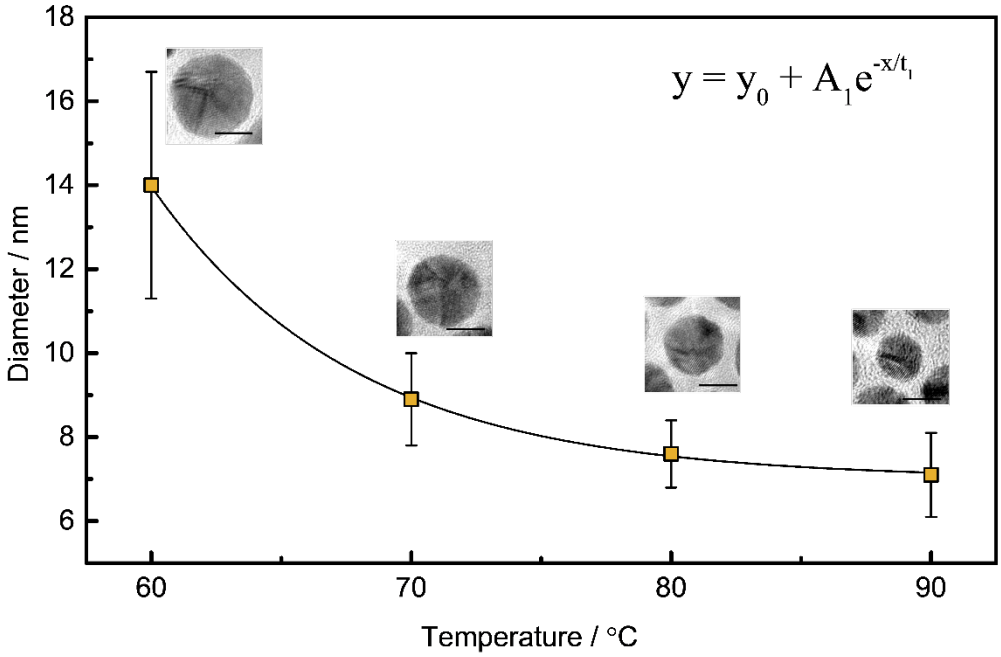

Figure 3.6 Au seed size as a function of reaction temperature for the synthesis of Au seeds. Expdec1 function was used for fitting and the corresponding equation is shown in the plot. Where y is the particle diameter at T temperature, y_0 is the particle's initial diameter at T_0, x is the temperature, T, and A_1 and t_1 are constants. Representative TEM images of each sample are shown in the plot. Scale bar = 5 nm.

Discussion

From these figures, I can conclude that there exists a positive relation between reaction temperature and reaction kinetics during solution-phase synthesis of the Au nanocrystals. Increasing the reaction temperature has a significant impact on the nucleation stage of nanocrystal growth, ultimately changing their resultant size and shape. As reaction temperature increases, the number of nuclei increases, resulting in smaller nanoparticles.

3.3.3 Ru-Pd branched nanoparticles with tunable branch size and branch number

Control over the branch number and branch size of Ru-Pd branched nanoparticles was achieved via optimization of the precursor to seed ratio,

seed size, and surfactant parameters. A summary of key experimental conditions and notable findings are presented below.

3.3.3.1 Experiment 15: The effect of surfactant impurity

The technical grade of purchased oleylamine is usually 70 %, which contains both short and long-chain primary alkylamines. A set of experiments were first conducted using this grade of oleylamine surfactant.

Table 3-7. The experimental conditions applied for the synthesis of Ru-Pd branched nanoparticles using 70 % oleylamine surfactant.

Exp. #	Ru : Pd ratio	$Ru(acac)_3$, mmol	$Pd(acac)_2$, mmol	Surfactant	Temp., °C	Time, h
15	24 : 1	0.05	0.0021	Oleylamine	140	24

Experimental

These experiments were performed according to the standard protocol of synthesizing Ru-Pd branched nanoparticles using the purchased oleylamine surfactant.

Results

Figure 3.7 shows the representative low-resolution TEM images of Ru-Pd nanoparticles synthesized using 70% grade oleylamine. The resultant nanoparticles are polydisperse in both size and shape.

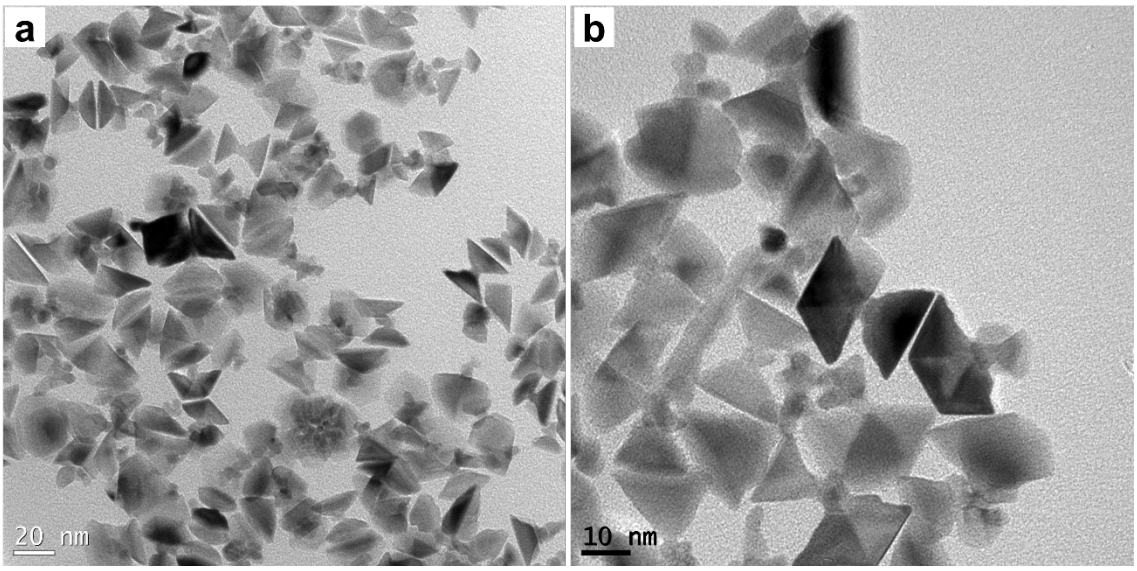

Figure 3.7. Ru-Pd branched nanoparticles using 70% grade oleylamine.

Discussion

As stated earlier, technical grade oleylamine typically contains both short and long-chain alkylamines. As a result, the binding energy between nanoparticles surface are different for these alkylamines, yielding irregularly shaped, polydisperse nanoparticles. Based on this analysis, 70% oleylamine was distilled for further syntheses.

3.3.3.2 The effect of precursor to seed ratio

The precursor to seed ratio has been shown to affect the growth mode of a metallic species during seeded growth by changing its reaction kinetics. This was observed when growing Co atoms on Au seeds in experiments 1-3 of Section 3.2.1, that the resultant shape, branch length, and branch number of the final nanoparticles was tuned by altering the Co to Au ratio. Based on these findings, Experiments 16-19 were conducted towards synthesize Ru branched nanoparticles with controlled branch length by changing the precursor to seed ratio.

Experimental

Pd-Ru branched nanoparticles. The synthesis of Pd-Ru branched nanoparticles was first carried out via an organic-phase solution seed-mediated approach according to a previously published method in our group.[1] To grow *hcp*-Ru branches, a 3.5 nm Pd seed solution (0.001 -0.01 mmol) was added to a mixture containing Ru (III) acetylacetonate (0.05 mmol, Sigma-Aldrich, 97 %) precursor and 5 eq. mol of oleylamine (82 µL) surfactant dissolved in 1 mL of mesitylene. Four sets of experiments were conducted, in which the ratio of Ru to Pd was varied from 5:1 to 8:1, 24:1, and 50:1. Each reaction mixture was then kept under a 3-bar hydrogen atmosphere at 140°C for 24 hours. Once complete, H_2 was released, and purification via centrifugation was conducted twice using a methanol and toluene solution (1:1 volume ratio) at 4000 rpm.

Table 3.8. The experimental conditions applied when varying the precursor to seed ratio on the synthesis of Ru-Pd branched nanoparticles.

Exp. #	Ru : Pd ratio	$Ru(acac)_3$, mmol	$Pd(acac)_2$, mmol	Temp., °C	Time, h
16	5 : 1	0.05	0.01	140	24
17	8 : 1	0.05	0.00625	140	24
18	24 : 1	0.05	0.0021	140	24
19	50 : 1	0.05	0.001	140	24

Results

Each reaction mixture was initially dark-red in colour prior to the Fischer-Porter bottle reaction. And this colour transitioned to a brown-black shade post-reaction, indicative of the formation of Ru-Pd nanoparticles.

Figures 3.8 a-d show the representative TEM images of the Ru-Pd nanoparticles synthesized with varying precursor to seed ratios. At a 5:1 molar ratio, a mixture of spherical and branched nanoparticles had formed. The formation of these spherical nanoparticles can be attributed to the higher number of nucleation sites at this lower precursor to seed ratios. This was also observed in previously published work in which Ru-Pd core-shell nanoparticles were synthesized at a lower than 2:1 ratio[21]. When increased to 8:1, monodisperse branched nanoparticles were obtained, indicating equivalence of adatoms to nucleation sites. At a ratio of 24:1, longer branched nanoparticles were formed. The formation of these longer branches can be correlated to the additional growth of Ru adatoms on branch tips. When this ratio was further increased to 50:1, the formation of non-uniform Ru branched nanoparticles was observed, which can be linked to an excess amount of Ru adatoms in solution.

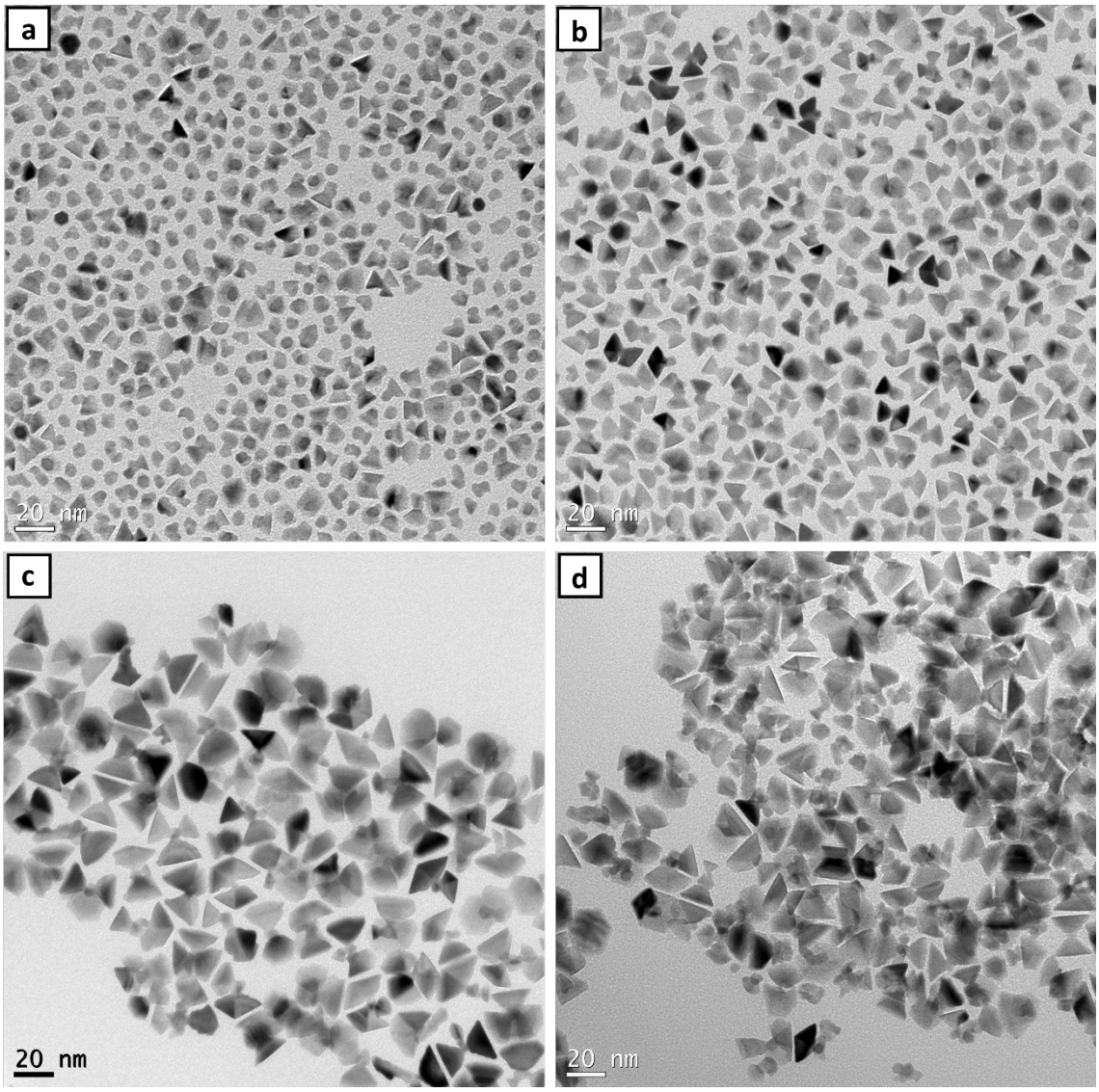

Figure 3.8. The effect of precursor to seed ratio at (a) 5 :1, (b) 8: 1, (c) 24 : 1, and (d) 50 : 1 molar ratios.

Discussion

During seed-mediated growth, the size and shape of synthesized nanoparticle products can be manipulated by varying the precursor to seed ratio[8, 9, 13]. In these set of experiments, different precursor to seed ratios resulted in the formation of (i) a mixture of core-shell and branched nanoparticles (5:1), (ii) branched nanoparticles with controlled branch sizes (8:1, 24:1), and (iii) a

mixture of branched nanoparticles and irregular shaped small nanoparticles (50:1).

These noticeable changes can be attributed to the following respective reasons: (i) a lower number of Ru(III) precursor ions relative to Pd precursor altering the reaction kinetic by increasing the diffusion rate of Ru adatoms. (ii) an optimization in the precursor to seed ratio enabling the continuous growth of Ru adatoms along the c-axis (<111> direction). (iii) a higher number of Ru(III) precursor ions resulting in homogenous nucleation.

3.3.3.3 Experiment 20-23: The effect of seed size on the branch number

I performed a set of experiments to obtain Ru-Pd branched nanoparticles with tunable branch numbers. It has been demonstrated that heterogeneous nucleation of metallic atoms can occur on particular seed sites through variation of the underlying reaction kinetics[22-26]. The Xia group, for instance, investigated the effect of the nucleation and growth rates of Ag on Pd cubic seeds through variation of specific reaction parameters, including the precursor injection rate, capping agent, reductant species, and reaction temperature[25]. Through these experiments, they found that Ag atoms could be selectively deposited on a specific number of Pd seed facets by regulating these reaction kinetics, resulting in the formation of Pd-Ag bimetallic core-shell nanocrystals. Using this, I hypothesize that the number of available Pd seed facets for depositing Ru atoms can be tuned by changing the Pd seed size, thus resulting in nanoparticle products with tunable branch numbers. To help explore this, experiments 20-23 were conducted such that the size of incorporated Pd seeds was varied between trials.

Experimental

Pd-Ru multi-branched nanoparticles with 11 nm long branches. Pd-Ru multi-branched nanoparticles were synthesized according to the same protocol used for designing Pd-Ru branched nanoparticles with 11 nm long branches. An identical precursor to seed ratio of 24:1 was incorporated, whilst Pd seeds with sizes of 3.5 ± 0.4 nm, 6.0 ± 0.7nm, 8.7 ± 0.7 nm, and 11.5 ± 0.8 were used.

Table 3-9. The experimental conditions applied for the synthesis of Ru-Pd branched nanoparticles with controlled branch numbers.

Exp. #	Ru : Pd ratio	Pd seeds size, nm	Temp., °C	Time, h
20	24:1	3.5 ± 0.4	140	24
21	24:1	6.0 ± 0.7	140	24
22	24:1	8.7 ± 0.7	140	24
23	24:1	11.5 ± 0.8	140	24

Results

Branched nanoparticles with 2-4 branches were observed when the 3.5 nm Pd seeds were used during synthesis. When the Pd seed size was increased from 3.5 nm to 6 nm and 8.7 nm, the average number of branches has also increased to within 3-5, with multiple branching also taking place. As seed size was further increased to 11.5 nm, irregularly shaped multi-branched nanoparticles were obtained.

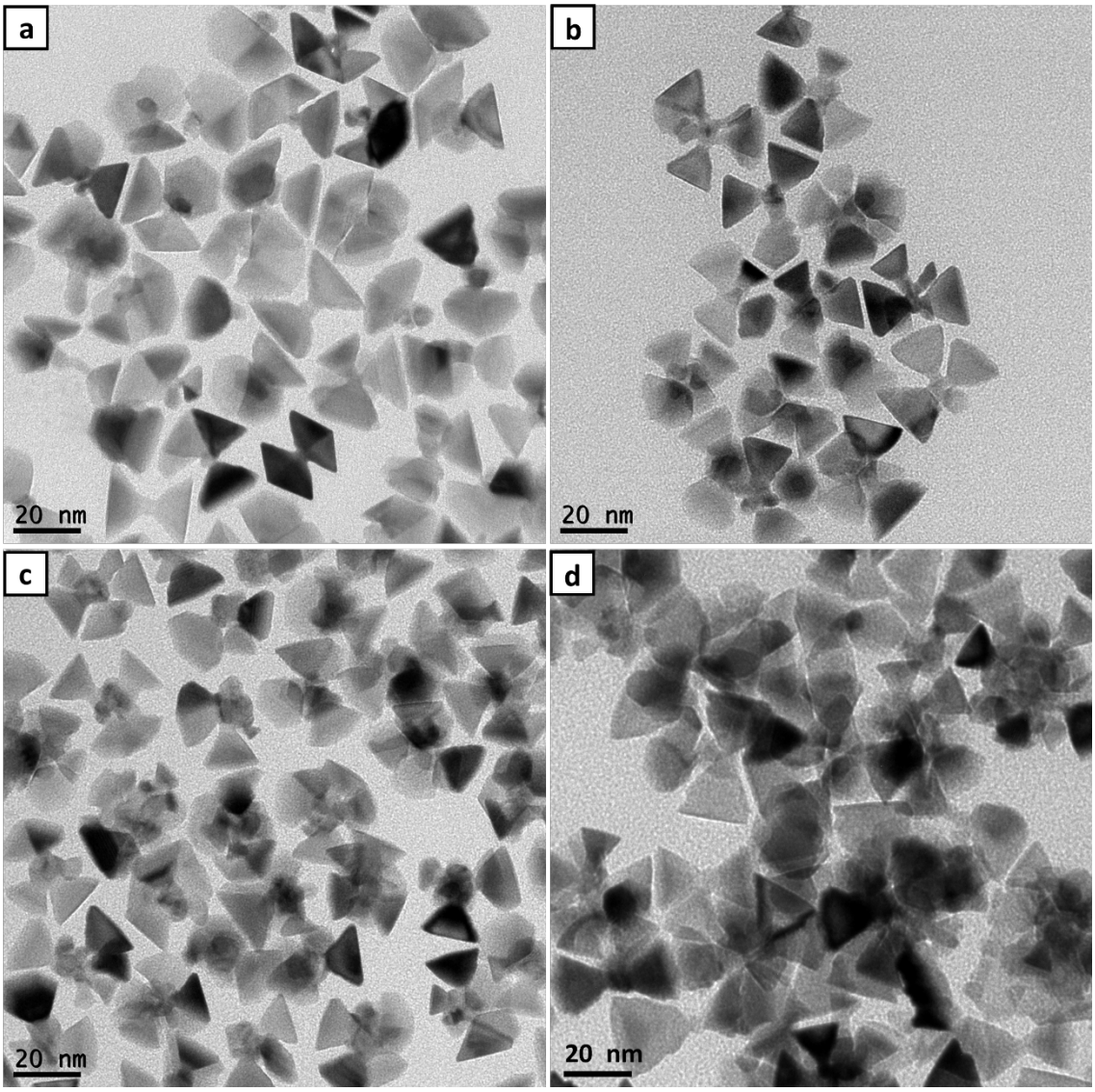

Figure 3.9. Multi-branched Ru-Pd nanoparticles using Pd seeds of different sizes. (a) 3.5 ± 0.4nm, (b) 6.0 ± 0.7 nm, (c) 8.7 ± 0.7 nm, and (d) 11.5 ± 0.8 nm Pd seeds.

Discussion

Larger Pd seeds increased the number of Ru-branches. Truncated octahedron seeds have 8 {111} facets and 6 {100} facets, while cubic-icosahedron seeds possess 20 {111} facets[8]. For the growth of Ru on Pd seeds (which have a truncated octahedron shape), deposition can be made to occur on a controlled number of Pd seed facets by simply changing the Pd seed size. An increase in Pd seed size led to the formation of multi-branched

Ru-Pd nanoparticles. When small Pd seeds were used during the reaction, Ru deposition only occurred on 2-3 8{111} Pd facets. Ru adatoms were continually deposited to these facets due to the surfactant hindrance, thereby resulting in the formation of Ru-Pd branched nanoparticles with 2-3 branches. When larger Pd seeds were used, deposition occurred over more {111} facets, leading to the formation of multi-branched Ru-Pd nanoparticles. As the Pd seed size was further increased to 11.5 nm, irregularly shaped nanoparticles were obtained. Ru atoms nucleation occurred on all {111} faces of these large Pd seeds, thus altering the growth mechanism of these branches.

3.4 Conclusion

These results demonstrated that a cubic-core hexagonal-branch growth approach in an organic solution-phase environment could lead to the successful synthesis of bimetallic-branched nanoparticles with controlled surface facets and branch numbers.

The growth mechanism of Co-Au branched nanoparticles with highly-crystalline *hcp*-Co branches was first investigated. The precursor to seed ratio, the type of precursor, and reaction time were found to be critical parameters in deciding the overall growth of *hcp*-Co branches on the Au-core.

The use of well-defined seeds with controlled size and shape is also important for the formation of branched nanoparticles. Control over the size of Au seeds was made possible by adjusting reaction temperature. Larger Pd seeds were also synthesized through variation of the precursor to seed ratio within the confines of a seed-mediated growth approach. Bringing all these synthetic parameters together and investigating their effect on a different bimetallic Ru-Pd system, it was similarly noted that the precursor to seed ratio, surfactant, and seed size played a critical role in the tuning of branch size and branch number during the growth of Ru branched nanoparticles.

The catalytic properties of these Co-Au and Ru-Pd branched nanoparticles will be explored in Chapters 3 and 4.

3.5 References

1. Gloag, L.; Benedetti, T. M.; Cheong, S.; Marjo, C. E.; Gooding, J. J.; Tilley, R. D., Cubic-Core Hexagonal-Branch Mechanism To Synthesize Bimetallic Branched and Faceted Pd-Ru Nanoparticles for Oxygen Evolution Reaction Electrocatalysis. *J Am Chem Soc* **2018,** *140* (40), 12760-12764.

2. Gloag, L.; Benedetti, T. M.; Cheong, S.; Li, Y.; Chan, X. H.; Lacroix, L. M.; Chang, S. L. Y.; Arenal, R.; Florea, I.; Barron, H.; Barnard, A. S.; Henning, A. M.; Zhao, C.; Schuhmann, W.; Gooding, J. J.; Tilley, R. D., Three-Dimensional Branched and Faceted Gold-Ruthenium Nanoparticles: Using Nanostructure to Improve Stability in Oxygen Evolution Electrocatalysis. *Angew Chem Int Ed Engl* **2018,** *57* (32), 10241-10245.

3. Cao, Z.; Chen, Q.; Zhang, J.; Li, H.; Jiang, Y.; Shen, S.; Fu, G.; Lu, B. A.; Xie, Z.; Zheng, L., Platinum-nickel alloy excavated nano-multipods with hexagonal close-packed structure and superior activity towards hydrogen evolution reaction. *Nat Commun* **2017,** *8*, 15131.

4. LaGrow, A. P.; Cheong, S.; Watt, J.; Ingham, B.; Toney, M. F.; Jefferson, D. A.; Tilley, R. D., Can polymorphism be used to form branched metal nanostructures? *Adv Mater* **2013,** *25* (11), 1552-6.

5. Manna, L.; Milliron, D. J.; Meisel, A.; Scher, E. C.; Alivisatos, A. P., Controlled growth of tetrapod-branched inorganic nanocrystals. *Nat Mater* **2003,** *2* (6), 382-5.

6. Dumestre, F.; Chaudret, B.; Amiens, C.; Fromen, M.-C.; Casanove, M.-J.; Renaud, P.; Zurcher, P., Shape Control of Thermodynamically Stable Cobalt Nanorods through Organometallic Chemistry. *Angewandte Chemie International Edition* **2002,** *41* (22), 4286-4289.

7. Ciuculescu, D.; Dumestre, F. d. r.; Comesaña-Hermo, M.; Chaudret, B.; Spasova, M.; Farle, M.; Amiens, C., Single-Crystalline Co Nanowires: Synthesis, Thermal Stability, and Carbon Coating. *Chemistry of Materials* **2009,** *21* (17), 3987-3995.

8. Xia, Y.; Gilroy, K. D.; Peng, H. C.; Xia, X., Seed-Mediated Growth of Colloidal Metal Nanocrystals. *Angew Chem Int Ed Engl* **2017,** *56* (1), 60-95.

9. Xia, Y.; Xia, X.; Peng, H. C., Shape-Controlled Synthesis of Colloidal Metal Nanocrystals: Thermodynamic versus Kinetic Products. *J Am Chem Soc* **2015,** *137* (25), 7947-66.

10. Henning, A. M.; Watt, J.; Miedziak, P. J.; Cheong, S.; Santonastaso, M.; Song, M.; Takeda, Y.; Kirkland, A. I.; Taylor, S. H.; Tilley, R. D., Gold-palladium core-shell nanocrystals with size and shape control optimized for catalytic performance. *Angew Chem Int Ed Engl* **2013,** *52* (5), 1477-80.

11. Tao, A. R.; Habas, S.; Yang, P., Shape Control of Colloidal Metal Nanocrystals. *Small* **2008,** *4* (3), 310-325.

12. Xia, Y.; Xiong, Y.; Lim, B.; Skrabalak, S. E., Shape-controlled synthesis of metal nanocrystals: simple chemistry meets complex physics? *Angew Chem Int Ed Engl* **2009,** *48* (1), 60-103.

13. Gilroy, K. D.; Yang, X.; Xie, S.; Zhao, M.; Qin, D.; Xia, Y., Shape-Controlled Synthesis of Colloidal Metal Nanocrystals by Replicating the Surface Atomic Structure on the Seed. *Adv Mater* **2018,** *30* (25), e1706312.

14. Sang-Wook Kim, J. P., Youngjin Jang, Yunhee Chung,; Sujin Hwang, a. T. H., Synthesis of Monodisperse Palladium Nanoparticles *Nano Lett* **2003,** *3* (9), 1289-1291.

15. Graham, L.; Collins, G.; Holmes, J. D.; Tilley, R. D., Synthesis and catalytic properties of highly branched palladium nanostructures using seeded growth. *Nanoscale* **2016,** *8* (5), 2867-74.

16. Wang, X.; Choi, S. I.; Roling, L. T.; Luo, M.; Ma, C.; Zhang, L.; Chi, M.; Liu, J.; Xie, Z.; Herron, J. A.; Mavrikakis, M.; Xia, Y., Palladium-platinum core-shell icosahedra with substantially enhanced activity and durability towards oxygen reduction. *Nat Commun* **2015,** *6*, 7594.

17. Xie, S.; Choi, S. I.; Lu, N.; Roling, L. T.; Herron, J. A.; Zhang, L.; Park, J.; Wang, J.; Kim, M. J.; Xie, Z.; Mavrikakis, M.; Xia, Y., Atomic layer-by-layer deposition of Pt on Pd nanocubes for catalysts with enhanced activity and durability toward oxygen reduction. *Nano Lett* **2014,** *14* (6), 3570-6.

18. Kelly, C. H. W.; Benedetti, T. M.; Alinezhad, A.; Gooding, J. J.; Tilley, R. D., Controlling Metallic Nanoparticle Redox Properties for Improved Methanol Oxidation Reaction Electrocatalysis. *ChemCatChem* **2019,** *11* (24), 5989-5993.

19. Gao, Q.; Ju, Y. M.; An, D.; Gao, M. R.; Cui, C. H.; Liu, J. W.; Cong, H. P.; Yu, S. H., Shape-controlled synthesis of monodisperse PdCu nanocubes and their electrocatalytic properties. *ChemSusChem* **2013,** *6* (10), 1878-82.

20. Wang, X.; Vara, M.; Luo, M.; Huang, H.; Ruditskiy, A.; Park, J.; Bao, S.; Liu, J.; Howe, J.; Chi, M.; Xie, Z.; Xia, Y., Pd@Pt Core-Shell Concave Decahedra: A Class of Catalysts for the Oxygen Reduction Reaction with Enhanced Activity and Durability. *J Am Chem Soc* **2015,** *137* (47), 15036-42.

21. Gloag, L.; Benedetti, T. M.; Cheong, S.; Webster, R. F.; Marjo, C. E.; Gooding, J. J.; Tilley, R. D., Pd-Ru core-shell nanoparticles with tunable

shell thickness for active and stable oxygen evolution performance. *Nanoscale* **2018,** *10* (32), 15173-15177.

22. Lim, B.; Kobayashi, H.; Yu, T.; Wang, J.; Kim, M. J.; Li, Z.-Y.; Rycenga, M.; Xia, Y., Synthesis of Pd−Au Bimetallic Nanocrystals via Controlled Overgrowth. *Journal of the American Chemical Society* **2010,** *132* (8), 2506-2507.

23. He, G.; Zeng, J.; Jin, M.; Zhang, H.; Lu, N.; Wang, J.; Kim, M. J.; Xia, Y., A Mechanistic Study on the Nucleation and Growth of Au on Pd Seeds with a Cubic or Octahedral Shape. *ChemCatChem* **2012,** *4* (10), 1668-1674.

24. Xia, X.; Xia, Y., Symmetry breaking during seeded growth of nanocrystals. *Nano Lett* **2012,** *12* (11), 6038-42.

25. Zhu, C.; Zeng, J.; Tao, J.; Johnson, M. C.; Schmidt-Krey, I.; Blubaugh, L.; Zhu, Y.; Gu, Z.; Xia, Y., Kinetically controlled overgrowth of Ag or Au on Pd nanocrystal seeds: from hybrid dimers to nonconcentric and concentric bimetallic nanocrystals. *J Am Chem Soc* **2012,** *134* (38), 15822-31.

26. Gilroy, K. D.; Hughes, R. A.; Neretina, S., Kinetically controlled nucleation of silver on surfactant-free gold seeds. *J Am Chem Soc* **2014,** *136* (43), 15337-45.

Chapter 4

Increasing the formation of active sites on highly crystalline Co branched nanoparticles for improved oxygen evolution reaction electrocatalysis

Publication One

Munkhshur Myekhlai, Tania M. Benedetti, Lucy Gloag, Vinicius R. Gonçales, Soshan Cheong, Hsiang-Sheng Chen, J. Justin Gooding, and Richard D. Tilley, ***ChemCatChem,*** 2020, 12, 3126 –3131.

Reproduced with the permission from Willey

4.1 Summary

The publication “Increasing the Formation of Active Sites on Highly Crystalline Co Branched Nanoparticles for Improved Oxygen Evolution Reaction Electrocatalysis” has been used in lieu of this chapter. The aim of this chapter is to understand the formation of catalytically active sites on highly crystalline hcp Co branched nanoparticles for the OER. First, It was hypothesized that designing highly crystalline *hcp* Co branched nanoparticles would provide a more catalytically stable surface under OER conditions, with possible retention of $Co(OH)_2$ on the nanoparticle surface, and which would thereby result in an increased density of catalytically active sites for improved OER performance. Therefore, Co branched nanoparticles were first synthesized, and their catalytic activities were then evaluated in comparison to Co spherical nanoparticles and Co_3O_4 nanoparticles. The results indicated that Co branched nanoparticles were the most catalytically active and stable, followed by Co spherical nanoparticles and Co_3O_4 oxide nanoparticles. In particular, we concluded that the origin of improved catalytic activity observed in the Co spherical nanoparticles and Co branched nanoparticles in comparison with the Co_3O_4 nanoparticles lies within the biphasic oxide surfaces composed of Co_3O_4 and $Co(OH)_2$. This is because the more catalytically active $Co(OH)_2$ surface is retained on the branched nanoparticles during OER due to the low indexed facets present on the *hcp* branches, and which thereby resulted in the greater catalytic activity observed.

Declaration for Chapter 4

Author	Contributions
Munkhshur Myekhlai	Synthesized Co-Au branched, Co-Au core shell, and Co_3O_4 nanoparticles Characterized nanocrystals using low-resolution electron microscopy Performed electrocatalytic experiments including cyclic voltammertry, chronopotentiometry, electrochemical impedance spectroscopy Drafted and proofread manuscript
Tania M. Benedetti	Training of student in electrochemistry techniques Provided knowledge of electrocatalysis Guidance and direction for project Proofread and writing of manuscript
Lucy Gloag	Experimental design Proofread manuscript
Vinicius R. Gonçales	Characterizations of nanocatalysts via XPS and processing the data Proofread manuscript
Soshan Cheong	Characterizations of nanocatalysts via high-resolution TEM and processed the image Proofread manuscript
Hsiang-Sheng Chen	Characterizations of nanocatalysts via high-resolution TEM and STEM-EDX mapping Proofread manuscript
J. Justin Gooding	Experimental design Provided fundamental understanding of key electrocatalysis ideas Proofread manuscript
Richard D. Tilley	Experimental design Provided fundamental understanding of key electrocatalysis ideas Proofread manuscript

Inclusion of Publications Statement

UNSW is supportive of candidates publishing their research results during their candidature as detailed in the UNSW Thesis Examination Procedure.

Publications can be used in their thesis in lieu of a Chapter if:

- The candidate contributed greater than 50% of the content in the publication and is the "primary author", ie. the candidate was responsible primarily for the planning, execution and preparation of the work for publication
- The candidate has approval to include the publication in their thesis in lieu of a Chapter from their supervisor and Postgraduate Coordinator.
- The publication is not subject to any obligations or contractual agreements with a third party that would constrain its inclusion in the thesis

Please indicate whether this thesis contains published material or not:

☐ This thesis contains no publications, either published or submitted for publication

☐ Some of the work described in this thesis has been published and it has been documented in the relevant Chapters with acknowledgement

☒ This thesis has publications (either published or submitted for publication) incorporated into it in lieu of a chapter and the details are presented below

CANDIDATE'S DECLARATION

I declare that:

- I have complied with the UNSW Thesis Examination Procedure
- where I have used a publication in lieu of a Chapter, the listed publication(s) below meet(s) the requirements to be included in the thesis.

Candidate's Name	**Signature**	**Date (dd/mm/yy)**
Munkhshur Myekhlai		

POSTGRADUATE COORDINATOR'S DECLARATION

I declare that:

- the information below is accurate
- where listed publication(s) have been used in lieu of Chapter(s), their use complies with the UNSW Thesis Examination Procedure
- the minimum requirements for the format of the thesis have been met.

PGC's Name	**PGC's Signature**	**Date (dd/mm/yy)**
Alex William Donald		

For each publication incorporated into the thesis in lieu of a Chapter, provide all of the requested details and signatures required.

Details of publication #1:

Full title: *Increasing the Formation of Active Sites on Highly Crystalline Co Branched Nanoparticles for Improved Oxygen Evolution Reaction Electrocatalysis*

Authors: *Munkhshur Myekhlai, Tania M. Benedetti, Lucy Gloag, Vinicius R. Gonçales, Soshan Cheong, Hsiang-Sheng Chen, J. Justin Gooding, and Richard D. Tilley*

Journal or book name: *ChemCatChem*

Volume/page numbers: Volume 12, Issue. 11, pages 3126-3131

Date accepted/ published: 20 March, 2020

Status	*Published*	✗	*Accepted and In press*		*In progress (submitted)*	

The Candidate's Contribution to the Work

- Synthesized Co-Au branched, Co-Au core shell, and Co_3O_4 nanoparticles
- Characterized nanocrystals using low-resolution electron microscopy
- Performed electrocatalytic experiments including cyclic voltammertry, chronopotentiometry, electrochemical impedance spectroscopy
- Drafted and proofread manuscript

Location of the work in the thesis and/or how the work is incorporated in the thesis:

In lieu of Chapter 4

PRIMARY SUPERVISOR'S DECLARATION

I declare that:

- the information above is accurate
- this has been discussed with the PGC and it is agreed that this publication can be included in this thesis in lieu of a Chapter
- All of the co-authors of the publication have reviewed the above information and have agreed to its veracity by signing a 'Co-Author Authorisation' form.

Primary Supervisor's name	**Primary Supervisor's signature**	**Date (dd/mm/yy)**
Richard D. Tilley		

Increasing the Formation of Active Sites on Highly Crystalline Co Branched Nanoparticles for Improved Oxygen Evolution Reaction Electrocatalysis

Munkhshur Myekhlai,[a] Tania M. Benedetti,*[a] Lucy Gloag,[a] Vinicius R. Gonçales,[a] Soshan Cheong,[b] Hsiang-Sheng Chen,[a] J. Justin Gooding,[a, c] and Richard D. Tilley*[a, b]

The electrocatalysis of the oxygen evolution reaction (OER) at the surface of oxidized metal electrocatalysts is highly dependent on the structure and composition of the surface oxide. Here, Au core- Co branched nanoparticles were synthesized using a cubic-core hexagonal-branch growth approach in a slow reductive solution synthesis, resulting in highly crystalline metallic *hcp* Co branches. Electrochemical surface oxidation of the Co branched nanoparticles resulted in formation of $Co(OH)_2$ that enable the formation of a higher number of active sites under OER conditions compared to Co_3O_4. Differently from polycrystalline spherical Au–Co core-shell nanoparticles, the oxidized structure on the Co branched nanoparticle surface is retained with electrochemical cycling, resulting in improved OER activity and stability.

Introduction

Producing H_2 as fuel by water electrolysis is a sustainable way to store energy from renewable intermittent energy sources such as wind and solar.[1] However, this process is limited by the much slower oxidation of water into O_2 at the anode side of the electrolyzer.[2] Among earth-abundant alternatives as electrocatalysts for the oxygen evolution reaction (OER), Co oxide provides good activity in both neutral and alkaline environments[3] although higher overpotentials compared to precious metals such as Ru and Ir oxides are still necessary to achieve the desirable current densities.[4]

Controlling metal oxide formation during oxidation reactions affects the electrocatalytic performance.[5–6] The surface structure of the oxide influences the catalytic activity, by changing the electronic properties[7–10] and the density of active sites present at the surface.[11–13] The nature of the Co surface oxide will affect its electrochemical transformation into the Co(OOH) active phase and subsequent formation of Co^{4+} active sites under OER conditions.[3] Recent studies with layered structures such as $Co(OH)_2$ and $CoO_x(OH)_y$ have shown improved OER activity compared to spinel Co_3O_4, which was correlated with a higher density of the active phase formed upon electrochemical oxidation on these more opened, hydrated structures.[3,14] Also, while the spinel Co_3O_4 requires substantial atomic rearrangement in the lattice during the electrochemical redox processes, this happens with minimal structure transformations on the $Co(OH)_2$ layered structure.[15] Therefore, for highly OER active Co-based catalytic nanoparticles, control over the Co-oxide surface structure, with retention of the lower oxidation state $Co(OH)_2$ at the surface as opposite to the more compact Co_3O_4 structure under OER electrochemical conditions in alkaline electrolyte, is a desirable requirement.

We have recently shown that the surface of hcp Ru nanoparticles is more stable against oxidation than polycrystalline Ru, resulting in slower dissolution under OER conditions in acid electrolyte and improved activity and stability.[16–17] Therefore, we expect that obtaining highly crystalline *hcp* Co nanostructures can result in a more resistant-to-oxidation surface under OER conditions, with possible retention of $Co(OH)_2$ at the surface, resulting in increased density of active sites for better OER performance.

In this work, we used a cubic-core hexagonal-branch approach to grow highly-crystalline hcp structured Co branched nanoparticles on *fcc* structured Au nanoparticles as electrocatalysts for the OER in alkaline electrolyte. The highly crystalline surface of the Co branched morphology provided better control of the oxide formation, resulting in an electrochemically stable $Co(OH)_2$ surface and improved OER activity and stability when compared to spherical polycrystalline Co spherical nanoparticles.

[a] M. Myekhlai, Dr. T. M. Benedetti, Dr. L. Gloag, Dr. V. R. Gonçales, H.-S. Chen, Prof. J. J. Gooding, Prof. R. D. Tilley
School of Chemistry
University of New South Wales
Sydney
New South Wales 2052 (Australia)
E-mail: t.benedetti@unsw.edu.au
r.tilley@unsw.edu.au
[b] Dr. S. Cheong, Prof. R. D. Tilley
Electron Microscope Unit
Mark Wainwright Analytical Centre
University of New South Wales
Sydney
New South Wales 2052 (Australia)
[c] Prof. J. J. Gooding
Australian Research Council Centre of Excellence in Convergent Bio-Nano Science and Technology
University of New South Wales
Sydney
New South Wales 2052 (Australia)

Supporting information for this article is available on the WWW under https://doi.org/10.1002/cctc.202000224

Results and Discussion

To synthesize the hcp Co branched nanoparticles, a cubic-core hexagonal-branch growth approach was used to control the growth of hexagonal Co branches on cubic Au seeds. Cobalt(III) acetylacetonate was added to a mixture of monodisperse Au seeds (8.4 ± 1.0 nm, Figure S1), hexadecylamine and mesitylene and heated at 140 °C for 24 h in a hydrogen gas atmosphere of 3 bar, which has been shown to enable the formation of highly crystalline hcp branches. Although Au being a relatively expensive metal, its molar ratio with respect to Co is only 1:100.[16,20] TEM images in Figure 1 show that the branched nanoparticles typically have 3–5 branches, with branch length measured at 63 ± 12 nm and width at 9 ± 1 nm (Figure S2). The branches typically grow from a 28–36 nm nanoparticle core, which itself is of core-shell structure. As shown in Figure 1b, the branches extend from a lighter contrast Co shell around a darker contrast Au core. This is important for branch growth because it offsets the strain between highly mismatched surface atoms at the Au {111} and Co {0001} planes (8.1 % mismatch).[21]

The Co branched nanoparticles each consists of an oxide shell that surrounds the entire core and branches, as shown by the HAADF-STEM image and STEM-EDX elemental maps in Figures 2a–b. The 2–3 nm oxide layer is a result of surface oxidation as the nanoparticles were exposed to air post-synthesis.[22] High-resolution TEM (HRTEM) images in Figures 2c, S3a-b show a highly crystalline Co branch that grows along the *c*-axis of a *hcp* structure, as indicated by the FFT pattern obtained from the core region of the branch (Figure S3c).

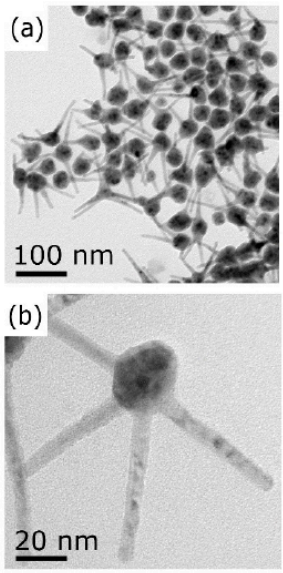

Figure 1. (a) Low resolution TEM image of Co branched nanoparticles, (b) TEM image of a typical Co branched nanoparticle.

Growth along the hexagonal *c*-axis is consistent with other rod-like morphologies observed for *hcp* Co nanoparticles.[23–24] The highly crystalline metallic Co can facilitate the electron transfer processes, contributing to higher activity.[25] The oxide surface adopts a cubic crystal structure with the corresponding FFT showing a rhombic array of spots that can be indexed to a <110> zone axis (Figure S3b). The lattice spacings of 2.1 Å and 2.4 Å are consistent with the {200} and {111} lattices of rock salt CoO, respectively.

Co spherical nanoparticles with an average diameter of 19.4 ± 2.3 nm were formed over the Au seeds when the Co:Au ratio was reduced by 10 fold (Figure S4). STEM-EDX analysis shows that the Au-core-Co-shell structures are surrounded by a 2–3 nm oxide layer (Figures 2d–e). Both the Co and surface oxide layer are polycrystalline or partially crystalline, as shown by the random arrangement of atoms in the HRTEM image in Figure 2f.

The nature of the oxide layer of the Co branched and Co spherical nanoparticles was further analyzed by X-ray photoelectron spectroscopy (XPS). The spectra in the Co 2p region of the as prepared nanoparticles are shown in Figures 3a and 3c for the Co branched and Co spherical nanoparticles, respectively. For both samples, the oxidized Co 2p3/2 and 2p1/2 peaks are centered at 781 eV and 796.7 eV respectively, followed by the satellite peaks at 786 eV and 802.9 eV that are characteristic of predominant Co^{2+},[26–27] in accordance with the CoO structure observed by HRTEM (Figure S3).

Although the composition of the surface oxide revealed by XPS is similar for the as prepared Co branched and Co spherical nanoparticles, the difference in their crystalline structures affects the stability of the surface oxide during electrochemical cycling. This is revealed by XPS analysis of the nanoparticles after 50 voltammetric cycles between −0.3 V and 1.7 V (RHE) in KOH 1 mol L^{-1} electrolyte. Differently from when the Co is oxidized in air to produce CoO, $Co(OH)_2$ is formed by electrochemical oxidation in alkaline electrolytes.[28] While the Co branched nanoparticles still retain the presence of Co^{2+} at the surface (Figure 3b), the Co spherical nanoparticles present predominant features of Co_3O_4 after cycling (Figure 3d), which is similar to that observed for Co_3O_4 nanoparticles (Figure S5). These results show that the highly crystalline *hcp* structure of the Co branched nanoparticles are more stable against oxidation, as previously observed for single-crystalline hcp Ru nanoparticles,[16] preserving the less oxidized $Co(OH)_2$ at the surface with electrochemical cycling.

The changes in the surface oxide structure with electrochemical cycling observed with XPS were monitored by analysis of the cyclic voltammograms during the first 50 cycles. The first cycle for the Co branched nanoparticles (navy line in Figure 4a) presents two defined oxidation peaks at 0.29 V and 1.02 V, corresponding to the formation of $Co(OH)_2$ and its oxidation to Co^{3+} respectively.[29] Both processes are highly irreversible, with the presence of only a small reduction peak at 0.94 V, corresponding to partial reduction of Co^{3+}. In the second cycle (green line in Figure 4a), all peak currents decrease and two defined oxidation peaks at 0.96 V and 1.08 V become evident. These two peaks correspond to the oxidation of $Co(OH)_2$ to

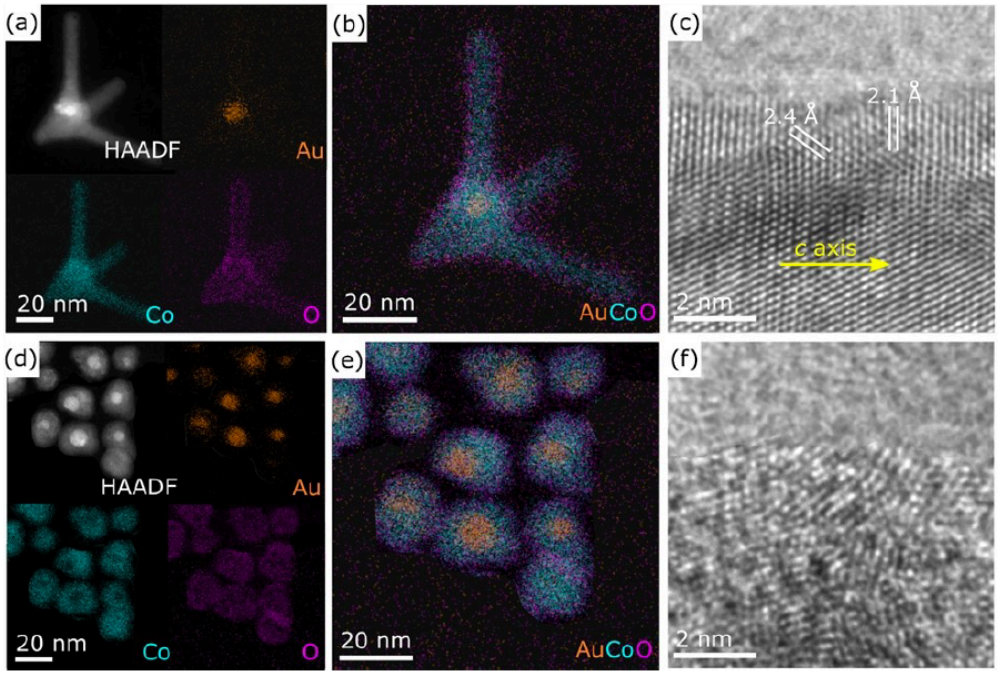

Figure 2. (a) HAADF-STEM image and STEM-EDX elemental maps of Au (orange), Co (cyan) and O (magenta) of a Co branched nanoparticle, (b) Overlay of elemental maps in (a), (c) HRTEM of a Co branch, (d) HAADF-STEM image and STEM-EDX elemental maps of Au (orange), Co (cyan) and O (magenta) of a Co spherical nanoparticle, (e) Overlay of elemental maps in (d), (f) HRTEM of a shell.

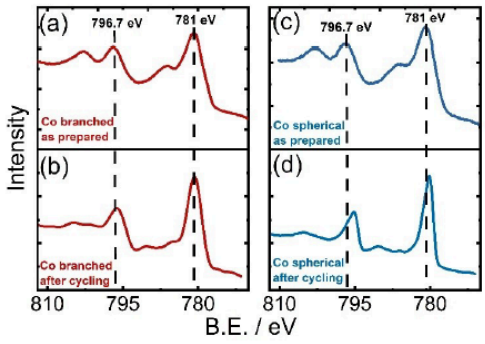

Figure 3. XPS spectra in the Co 2p region of as prepared (a) and after cycling (b) Co branched nanoparticles and as prepared (c) and after cycling (d) Co spherical nanoparticles. Cycling = 50 potentiodynamic cycles in KOH 1 mol L^{-1} between −0.3 V and 1.7 V (RHE) at 50 mV s^{-1}.

Co_3O_4 and oxidation of the tetrahedral Co^{2+} sites of Co_3O_4 to CoOOH respectively.[28] With further cycling (black and red lines for cycles 10 and 50 respectively in Figure 4a), the peak from oxidation of $Co(OH)_2$ to Co_3O_4 vanishes and only the peak from oxidation of Co_3O_4 to CoOOH is evident, with concomitant increase in the formation of Co^{4+} active species at 1.41 V. The tetrahedral Co^{2+} sites from Co_3O_4 are known to be the ones responsible for the formation of CoOOH at 1.08 V, which is the active phase for OER.[13,29] The retention of the more open, layered $Co(OH)_2$ structure in the branched nanoparticles under OER conditions allows the formation of a higher amount of these active sites[14] as evidenced by the higher current densities of the peak at 1.08 V.

For the Co spherical nanoparticles, multiple and less defined oxidation peaks are observed in the first cycle (navy line in Figure 4b), and although a similar amount of Co is present at the electrode surface (as their ECSAs are similar as shown in Figure S6 and Table S1), formation of a lower number of active species at more positive potentials (lines green, black and blue for cycles 2, 10 and 50 respectively in Figure 4b) are observed in the subsequent cycles.

In contrast to the Co spherical nanoparticles and Co branched nanoparticles, no defined oxidation peaks are observed for the Co_3O_4 nanoparticles (yellow line in Figure 4c) and only a capacitive current starting from 0.95 V is present. The absence of defined oxidation peaks is possibly due to predominant capacitive current from –OH adsorption at the non-active octahedral Co^{3+} sites of Co_3O_4.[13] The cyclic

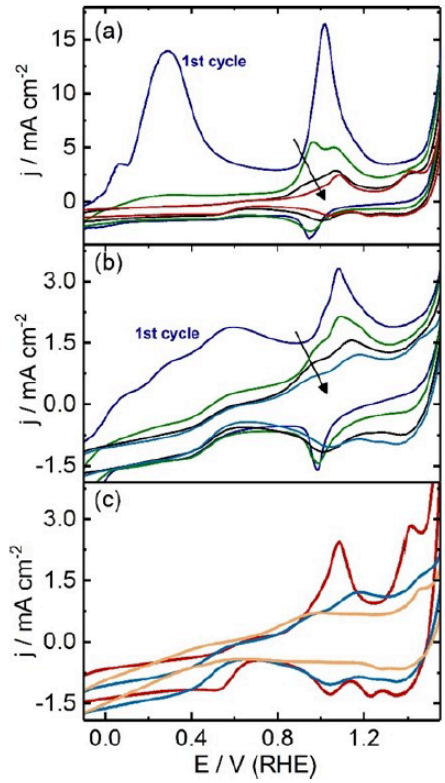

Figure 4. Evolution of the cyclic voltammogram profiles with cycling for the (a) Co branched nanoparticles and (b) Co spherical nanoparticles; (c) Comparison of the 50th cycles for the different nanoparticles. 1st cycle (navy), 2nd cycle (green), 10th cycle (black) and 50th cycle (red for Co branched, blue for Co spherical and yellow for Co_3O_4 nanoparticles). Scan rate = 50 mV s^{-1}, electrolyte = KOH 1 mol L^{-1}.

voltammograms (Figure 4c for comparison of all samples) also show that for the Co branched nanoparticles, the formation of the Co^{4+} active sites occurs at a potential 60 mV more negative, and with charge density significantly higher than for the Co spherical nanoparticles and Co_3O_4 nanoparticles. The fact that more active sites are formed at the surface of the Co branched nanoparticles suggests that their highly crystalline structure enables the retention of the $Co(OH)_2$ at the nanoparticle surface with electrochemical cycling as revealed by XPS; a surface that is known to provide the formation of more OER active sites[3,14] and a resultant higher electrocatalytic activity. Furthermore, the presence of defined reduction peaks corresponding to Co^{3+}/Co^{2+} and Co^{4+}/Co^{3+} denotes the higher reducibility of the Co branched nanoparticles surface, which has been recently identified as a descriptor of higher OER active sites density.[3]

The OER electrocatalysis on the different nanoparticles was evaluated after the 50 voltammetric cycles between −0.3 V and 1.7 V (RHE) in KOH 1 mol L^{-1}, after which changes in the potentiodynamic profiles were no longer observed. The same mass of Co was deposited on the glassy carbon surface for all samples. The anodic scan of the 50th cycle of the voltammograms in Figure 5a shows that the OER starts at lower overpotentials and reaches higher geometric current densities with the Co branched nanoparticles than with the Co spherical and Co_3O_4 nanoparticles. The Co branched nanoparticles reach a geometric current density of 10 mA cm^{-2} at 1.55 V (320 mV overpotential with respect to the thermodynamic OER potential), while at this same potential the Co spherical and Co_3O_4 nanoparticles reach much smaller geometric current densities of 2.63 mA cm^{-2} and 1.91 mA cm^{-2} respectively. The OER activity

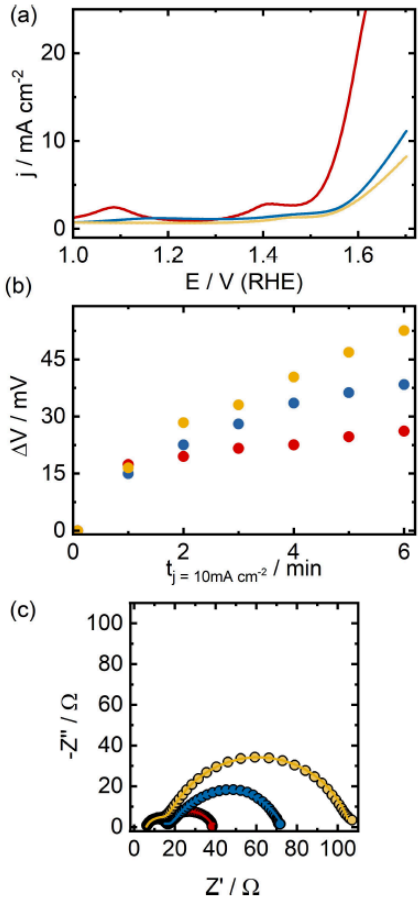

Figure 5. (a) Capacitance subtracted anodic scan of the 50th cycle of cyclic voltammetry to show the OER activities; (b) Changes in overpotential with time at 10 mA cm^{-2}. (c) Fitted Nyquist plots of electrochemical impedance spectroscopy. Co branched nanoparticles (red), Co core-shell nanoparticles (blue) and Co_3O_4 nanoparticles (yellow). Scan rate = 50 mV s^{-1}; electrolyte: KOH 1 mol L^{-1}.

achieved with the Co branched nanoparticles is comparable to that of the noble metal nanoparticles Ir and Ru in acid electrolytes (Figure S7). The activity of the Co branched nanoparticles is also among the highest recently reported for Co based nanoparticles (Table S2),[30–33] showing that designing highly crystalline branched nanoparticles of *hcp* structure is a good strategy to achieve highly active electrocatalysts.

The differences in geometric activities for the different nanoparticles could be also ascribed to differences in their surface areas exposed for the OER. However, the ECSA of the Co branched nanoparticles, obtained from the capacitive current at different scan rates of unsupported nanoparticles, is 6.8 $cm^2 mg^{-1}$, which is similar to the Co spherical nanoparticles and slightly lower than the Co_3O_4 nanoparticles (Figure S6 and Table S1). This means that the higher geometric activity of the Co branched nanoparticles cannot be ascribed to higher surface area. The specific activity (activity normalized by the ECSA) at an overpotential of 400 mV of the Co branched nanoparticles is 9.8 mA cm^{-2} which is 3.8 and 5.8 times higher than the Co spherical and Co_3O_4 respectively (Table S1). This means that the electrocatalytic performance of the different nanoparticles is dictated by the surface structure rather than the electrochemically available surface area.

The stability under a constant geometric current density of 10 mA cm^{-2} (Figure 5b) is initially similar for all nanoparticles, with the overpotential required to keep the applied current density increasing by around 15 mV after 1 h. The overpotential increases faster for the Co_3O_4 and Co spherical nanoparticles than for the Co branched nanoparticles over time, reaching 53 mV, 38 mV and 26 mV after 6 h respectively, suggesting the formation of more active sites due to delayed surface oxide formation with the branched nanoparticles. This indicates that the surface of the Co branched nanoparticles is more stable, resulting in retention of activity for longer times.

All Nyquist plots of the electrochemical impedance spectroscopy (EIS) experiments in Figure 5c show two semi-circle responses that were fitted using a Voigt circuit with two time constants, assuming negligible change in the coverage of intermediates caused by the potential oscillation (10 mV amplitude) and that the catalyst films are thin enough so there is no resistance loss on the catalyst surface (See Table S3 for fitted parameters).[34] The semi-circle at higher frequencies corresponds to the catalyst film and shows similar charge transfer resistance for all samples. The semi-circle at lower frequencies corresponds to the OER process and shows that the resistance to charge transfer for the Co branched nanoparticles is 2.5 and 4.5 times lower than the Co spherical and Co_3O_4 nanoparticles respectively, showing that the OER faradaic process is faster at the Co branched nanoparticles surface. The faster charge transfer is also evident from the Tafel slopes (Figure S8): for the Co branched nanoparticles, this is 117 mV dec^{-1}, slightly lower than the 120 mV dec^{-1} corresponding to the first step of OH adsorption as the rate determining step.[13] The Co spherical and Co_3O_4 nanoparticles present higher Tafel slopes of 192 mV dec^{-1} and 228 mV dec^{-1} respectively, usually observed for pristine Co_3O_4 surfaces,[35] that can be related to the contribution of other processes such as oxide formation.[36]

Conclusion

Using a cubic-core hexagonal-branch growth approach, highly crystalline *hcp* Co branched nanoparticles were synthesized. The obtained nanoparticles presented much higher OER activity than polycrystalline Co spherical and Co_3O_4 nanoparticles. The higher activity is related to the highly crystalline *hcp* structure that retains the presence of $Co(OH)_2$ at the surface of the nanoparticles, enabling the electrochemical formation of higher density of Co^{4+} active sites. These results show that for nanoparticles, engineering metallic nanoparticles with defined surface structure to control the formation of surface oxide is crucial for highly active electrocatalysis and this concept can be extended to a wide range of electrocatalytic reactions that are affected by the oxide formation.

Acknowledgements

This research was financially supported by the Australian Research Council of Centre of Excellence in Convergent Bio-Nano Science and Technology (CE140100036), the ARC Australian Laureate Fellowship (FL150100060), ARC Discovery Project (DP190102659) and the Mark Wainwright Analytical Centre (MWAC) at UNSW. This work used the facilities supported by Microscopy Australia at the Electron Microscope Unit at UNSW and at the Centre for Microscopy & Microanalysis at the University of Sydney.

Conflict of Interest

The authors declare no conflict of interest.

Keywords: Cobalt oxide · Electrocatalysis · Nanoparticles · Oxygen evolution reaction · Surface oxide

[1] T. Reier, H. N. Nong, D. Teschner, R. Schlögl, P. Strasser, *Adv. Energy Mater.* **2017**, 7.
[2] J. Suntivich, K. J. May, H. A. Gasteiger, J. B. Goodenough, Y. Shao-Horn, *Science* **2011**, *334*, 1383–1385.
[3] A. Bergmann, T. E. Jones, E. M. Moreno, D. Teschner, P. Chernev, M. Gliech, T. Reier, H. Dau, P. Strasser, *Nat. Can.* **2018**, *1*, 711–719.
[4] W. T. Hong, M. Risch, K. A. Stoerzinger, A. Grimaud, J. Suntivich, Y. Shao-Horn, *Energy Environ. Sci.* **2015**, *8*, 1404–1427.
[5] C. H. W. Kelly, T. M. Benedetti, A. Alinezhad, J. J. Gooding, R. D. Tilley, *ChemCatChem* **2019**, *11*, 5989–5993.
[6] C. H. W. Kelly, T. M. Benedetti, A. Alinezhad, W. Schuhmann, J. J. Gooding, R. D. Tilley, *J. Phys. Chem. C* **2018**, *122*, 21718–21723.
[7] T. Ling, D. Y. Yan, Y. Jiao, H. Wang, Y. Zheng, X. Zheng, J. Mao, X. W. Du, Z. Hu, M. Jaroniec, S. Z. Qiao, *Nat. Commun.* **2016**, *7*, 12876.
[8] C. S. Tan, S. C. Hsu, W. H. Ke, L. J. Chen, M. H. Huang, *Nano Lett.* **2015**, *15*, 2155–2160.
[9] L. Gloag, T. M. Benedetti, S. Cheong, R. F. Webster, C. E. Marjo, J. J. Gooding, R. D. Tilley, *Nanoscale* **2018**, *10*, 15173–15177.
[10] A. R. Poerwoprajitno, L. Gloag, T. M. Benedetti, S. Cheong, J. Watt, D. L. Huber, J. J. Gooding, R. D. Tilley, *Small* **2019**, *15*, e1804577.

[11] X. W. Xie, Y. Li, Z. Q. Liu, M. Haruta, W. J. Shen, *Nature* **2009**, *458*, 746–749.
[12] J. W. Xiao, Q. Kuang, S. H. Yang, F. Xiao, S. Wang, L. Guo, *Sci. Rep.* **2013**, 3.
[13] H. Y. Wang, S. F. Hung, H. Y. Chen, T. S. Chan, H. M. Chen, B. Liu, *J. Am. Chem. Soc.* **2016**, *138*, 36–39.
[14] J. Yang, J. K. Cooper, F. M. Toma, K. A. Walczak, M. Favaro, J. W. Beeman, L. H. Hess, C. Wang, C. Zhu, S. Gul, J. Yano, C. Kisielowski, A. Schwartzberg, I. D. Sharp, *Nat. Mater.* **2017**, *16*, 335–341.
[15] J. B. Gerken, J. G. McAlpin, J. Y. Chen, M. L. Rigsby, W. H. Casey, R. D. Britt, S. S. Stahl, *J. Am. Chem. Soc.* **2011**, *133*, 14431–14442.
[16] L. Gloag, T. M. Benedetti, S. Cheong, Y. Li, X. H. Chan, L. M. Lacroix, S. L. Y. Chang, R. Arenal, I. Florea, H. Barron, A. S. Barnard, A. M. Henning, C. Zhao, W. Schuhmann, J. J. Gooding, R. D. Tilley, *Angew. Chem. Int. Ed. Engl.* **2018**, *57*, 10241–10245.
[17] L. Gloag, T. M. Benedetti, S. Cheong, C. E. Marjo, J. J. Gooding, R. D. Tilley, *J. Am. Chem. Soc.* **2018**, *140*, 12760–12764.
[18] A. M. Henning, J. Watt, P. J. Miedziak, S. Cheong, M. Santonastaso, M. Song, Y. Takeda, A. I. Kirkland, S. H. Taylor, R. D. Tilley, *Angew. Chem. Int. Ed. Engl.* **2013**, *52*, 1477–1480.
[19] S. Watzele, P. Hauenstein, Y. Liang, S. Xue, J. Fichtner, B. Garlyyev, D. Scieszka, F. Claudel, F. Maillard, A. S. Bandarenka, *ACS Catal.* **2019**, *9*, 9222–9230.
[20] A. Alinezhad, L. Gloag, T. M. Benedetti, S. Cheong, R. F. Webster, M. Roelsgaard, B. B. Iversen, W. Schuhmann, J. J. Gooding, R. D. Tilley, *J. Am. Chem. Soc.* **2019**, *141*, 16202–16207.
[21] A. R. Poerwoprajitno, L. Gloag, S. Cheong, J. J. Gooding, R. D. Tilley, *Nanoscale* **2019**, *11*, 18995–19011.
[22] Z. Yang, N. Yang, J. Yang, J. Bergström, M.-P. Pileni, *Adv. Funct. Mater.* **2015**, *25*, 891–897.
[23] R. K. Ramamoorthy, A. Viola, B. Grindi, J. Peron, C. Gatel, M. Hytch, R. Arenal, L. Sicard, M. Giraud, J. Y. Piquemal, G. Viau, *Nano Lett.* **2019**, *19*, 9160–9169.
[24] M. Pousthomis, E. Anagnostopoulou, I. Panagiotopoulos, R. Boubekri, W. Fang, F. Ott, K. A. Atmane, J.-Y. Piquemal, L.-M. Lacroix, G. Viau, *Nano Res.* **2015**, *8*, 2231–2241.
[25] A. L. Strickler, M. A. Escudero-Escribano, T. F. Jaramillo, *Nano Lett.* **2017**, *17*, 6040–6046.
[26] M. C. Biesinger, B. P. Payne, A. P. Grosvenor, L. W. M. Lau, A. R. Gerson, R. S. C. Smart, *Appl. Surf. Sci.* **2011**, *257*, 2717–2730.
[27] A. Foelske, H. H. Strehblow, *Surf. Interface Anal.* **2000**, *29*, 548–555.
[28] C. Barbero, G. A. Planes, M. C. Miras, *Electrochem. Commun.* **2001**, *3*, 113–116.
[29] C. Li, X. Zhang, K. Wang, H. Zhang, X. Sun, Y. Ma, *RSC Adv.* **2014**, *4*, 59603–59613.
[30] J. Wang, J. Liu, B. Zhang, F. Cheng, Y. Ruan, X. Ji, K. Xu, C. Chen, L. Miao, J. Jiang, *Nano Energy* **2018**, *53*, 144–151.
[31] T. N. Huan, G. Rousse, S. Zanna, I. T. Lucas, X. Xu, N. Menguy, V. Mougel, M. Fontecave, *Angew. Chem. Int. Ed. Engl.* **2017**, *56*, 4792–4796.
[32] R. Zhang, Y.-C. Zhang, L. Pan, G.-Q. Shen, N. Mahmood, Y.-H. Ma, Y. Shi, W. Jia, L. Wang, X. Zhang, W. Xu, J.-J. Zou, *ACS Catal.* **2018**, *8*, 3803–3811.
[33] W. Xu, F. Lyu, Y. Bai, A. Gao, J. Feng, Z. Cai, Y. Yin, *Nano Energy* **2018**, *43*, 110–116.
[34] P. Chakthranont, J. Kibsgaard, A. Gallo, J. Park, M. Mitani, D. Sokaras, T. Kroll, R. Sinclair, M. B. Mogensen, T. F. Jaramillo, *ACS Catal.* **2017**, *7*, 5399–5409.
[35] L. Xu, Q. Q. Jiang, Z. H. Xiao, X. Y. Li, J. Huo, S. Y. Wang, L. M. Dai, *Angew. Chem. Int. Ed.* **2016**, *55*, 5277–5281.
[36] T. Reier, M. Oezaslan, P. Strasser, *ACS Catal.* **2012**, *2*, 1765–1772.

Manuscript received: February 9, 2020
Revised manuscript received: March 18, 2020
Accepted manuscript online: March 20, 2020
Version of record online: April 29, 2020

ChemCatChem

Supporting Information

Increasing the Formation of Active Sites on Highly Crystalline Co Branched Nanoparticles for Improved Oxygen Evolution Reaction Electrocatalysis

Munkhshur Myekhlai, Tania M. Benedetti,* Lucy Gloag, Vinicius R. Gonçales, Soshan Cheong, Hsiang-Sheng Chen, J. Justin Gooding, and Richard D. Tilley*

Supporting Information

Increasing the formation of active sites on highly crystalline Co branched nanoparticles for improved oxygen evolution reaction electrocatalysis

Munkhshur Myekhlai,[a] Tania M. Benedetti,*[a] Lucy Gloag,[a] Vinicius R. Gonçales,[a] Soshan Cheong,[b] Hsiang-Sheng Chen,[a] J. Justin Gooding,[ac] and Richard D. Tilley*[ab]

[a]School of Chemistry, [b]Electron Microscope Unit, Mark Wainwright Analytical Centre and [c]Australian Research Council Centre of Excellence in Convergent Bio-Nano Science and Technology and - The University of New South Wales, Sydney, New South Wales 2052, Australia

*r.tilley@unsw.edu.au, t.benedetti@unsw.edu.au

Experimental Section

Materials.

Gold(III) chloride hydrate ($HAuCl_4 \cdot 3H_2O$, >99.9 %), cobalt(II) acetylacetonate ($Co(C_5H_7O_2)_2$, 97.0 %), hexadecylamine ($CH_3(CH_2)_{15}NH_2$, 90.0 %), and mesitylene ($C_6H_3(CH_3)_3$, 98.0 %) were purchased from Sigma-Aldrich Co., Ltd., Australia. Toluene (99.9%), ethanol (95.0%), and potassium hydroxide (>85.0 %) were purchased from Chem-Supply Pty Ltd Australia.

Synthesis of Au nanoparticles.

Au seeds were prepared according to a previously published method in our group. [1] Hexadecylamine (1.072 g, 4.4 mmol) was firstly dissolved in toluene (4.0 mL). Gold (III) chloride hydrate (0.079g, 0.4 mmol) was then added to the solution. The reaction mixture was then taken place under 3 bar hydrogen at 70°C for 24 hours. After the reaction, H_2 was released and purification was done twice using toluene and ethanol solution (1:1 volume ratio) at 8000 rpm. Then, Au seeds were kept in mesitylene to further syntheses.

Synthesis of Co Nanoparticles.

The syntheses of the Co spherical nanoparticles and Co branched nanoparticles were carried out using an organic-phase solution seed mediated approach. To grow the *hcp* branched and polycrystalline cobalt shell, the Au seed solution was added to a solution containing 0.25 mmol cobalt [2] acetylacetonate (0.065 g) as a precursor and 5 eq. mol of hexadecylamine (0.3018 g) as a surfactant dissolved in 2 mL of mesiltylene. The ratio of cobalt to Au was 10:1 for spherical nanoparticles and 100:1 for branched nanoparticles. The reaction mixture was then taken place under 3 bar hydrogen at 140°C for 24 hours. After the reaction, H_2 was released and purification was done twice using toluene and ethanol solution (1:1 volume ratio) at 8000 rpm. Co_3O_4 nanoparticles were also synthesized, using the same method without the Au seeds.

Characterizations.

TEM Characterization: Low-resolution TEM was performed on a Philips CM200 operated at 200 kV. High-resolution TEM and STEM-EDX were performed on a JEOL JEM-F200 (200 kV, cold field emission gun)c equipped with an annular dark field detector and a JEOL windowless 100 mm^2 silicon drift X-ray detector.

XPS Characterization: X-ray photoelectron spectroscopy (XPS) characterization was performed on an ESCALab 250 Xi (Thermo Scientific) spectrometer with a monochromated Al Kα source. The pressure in the analysis chamber during measurement was < 108 mbar. The pass energy and step size for narrow scans were 20 eV and 0.1 eV respectively, with a take-off

angle normal to the sample surface. Spectral analysis was performed using Avantage 4.73 software and the curve fitting was carried out with a mixture of Gaussian–Lorentzian functions.

ICP-OES Characterization: For the inductively Coupled Plasma-Optical Emission Spectrometry (ICP-OES) the samples were digested in aqua-regia and analyzed using an Optima7300DV- ICP-OES PerkinElmer instrument at the selected wavelengths of Co 228.610 and Au 267.595.

Electrochemical section

Catalysts ink preparation. For the electrochemical studies firstly, the nanoparticles were supported in carbon Vulcan to give 20 wt% Co by sonication of a hexane dispersion of the nanoparticles and carbon followed by centrifugation and washing with ethanol. Then, the carbon loaded nanoparticles (2.5 mg) was dispersed in a solution of an isopropanol (1000 µL) and Nafion 0.5 % v/v (20 µL) to make an ink. The actual wt % of Co was determined by ICP-OES and the same mass of the metal was added on the glassy carbon surface (~20 µL on 5 mm diameter) for all samples as the working electrode.

Electrochemical measurements.

Cyclic voltammetry measurement: The measurements were performed using an Autolab potentiostat running with Nova 2 software. The working electrode was kept rotating at 1600 rpm during the experiments and a 1 mol L^{-1} KOH solution was used as the electrolyte. A Pt-mesh and Hg|HgO|1 mol L^{-1} NaOH were used as a counter electrode and reference electrode, respectively. All potentials were converted to the reversible hydrogen electrode (RHE) by measuring the potential between the reference electrode and a freshly prepared standard reference electrode (SHE) and considering the electrolyte pH. The surface Co oxide due to nanoparticles exposure to air was firstly removed by keeping the potential at -0.3 V (RHE) for 3 minutes. Without opening the electric circuit, the OER activity was then measured by cyclic voltammetry between -0.3 V vs. and 1.7 V (RHE) at 100 mV s^{-1}.

Stability test: The stability was evaluated by chronopotentiometry measured at a geometric current density of 10 mA cm^{-2} for 2 hours. The activity of commercial ruthenium and iridium catalysts were determined using 0.1 M $HClO_4$ as the electrolyte. Other experimental conditions including the amount of particles, scan rate, and electrodes were kept the same.

Electrochemical surface area: The electrochemical surface area (ECSA) of the catalysts were determined from the slope of the capacitive current versus scan rate plots to obtain the capacitance: firstly, the particles without carbon support were dispersed in toluene. The exact

concentration was determined using ICP-OES and the same mass (0.03 mg) of Co was added on the glassy carbon surface for all samples. Cyclic voltammetry measurements in the capacitive potential range were performed at 5, 10, 20, and 50 mV s^{-1}. The obtained capacitance was then used to calculate the ECSA using the specific capacitance of (620 ± 150) µF cm^{-2}. [3]

Electrochemical impedance spectroscopy: Electrochemical impedance spectroscopy (EIS) measurements were carried out with the same experimental setup described above using particles without carbon support. After five potentiodynamic cycles, EIS measurements were performed from 10000 Hz to 0.1 Hz at 1.61 V (RHE) and 10 mV amplitude. Before each EIS measurement, pretreatment was carried out for three minutes at the same potential used for measurement after which the current was constant. The fitting for EIS spectra were done using the Voigt circuit with two time constants (R(QR)(QR)) using the ''ZSimp.Win 3.22'' software.

Supplementary figures:

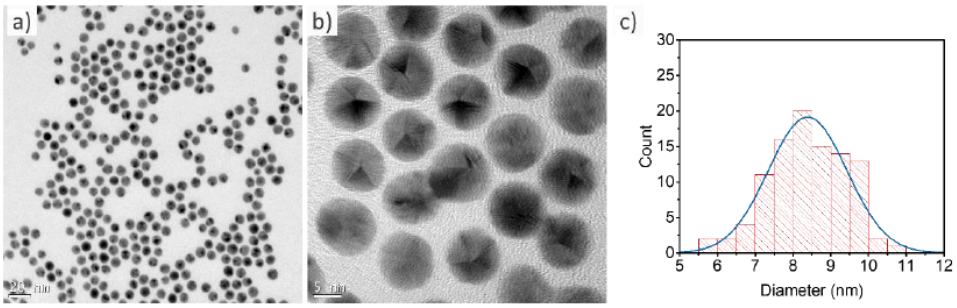

Figure S1: TEM analysis of Au seeds (a-b) TEM images of Au nanoparticles with average diameter of 8.4 ± 1.0 nm used as seeds for Au-Co core-shell and Au-Co branched NPs and (c) Histogram of the size distribution of Au nanoparticles shown in (a-b)

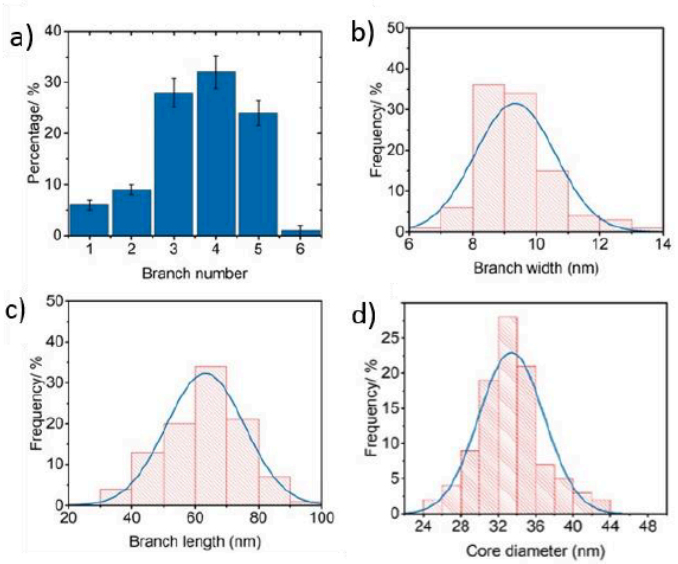

Figure S2: (a) number of branches per particles: the hcp Co branched nanoparticles consists of mostly 3-5 branches (tripod -28 %, tetrapod -32 %, and five branches -24 %), Histograms of the (b) branch width (9±1 nm), (c) branch length (63 ±12 nm) and (d) with average diameter of the core (33.4 ± 3.5 nm).

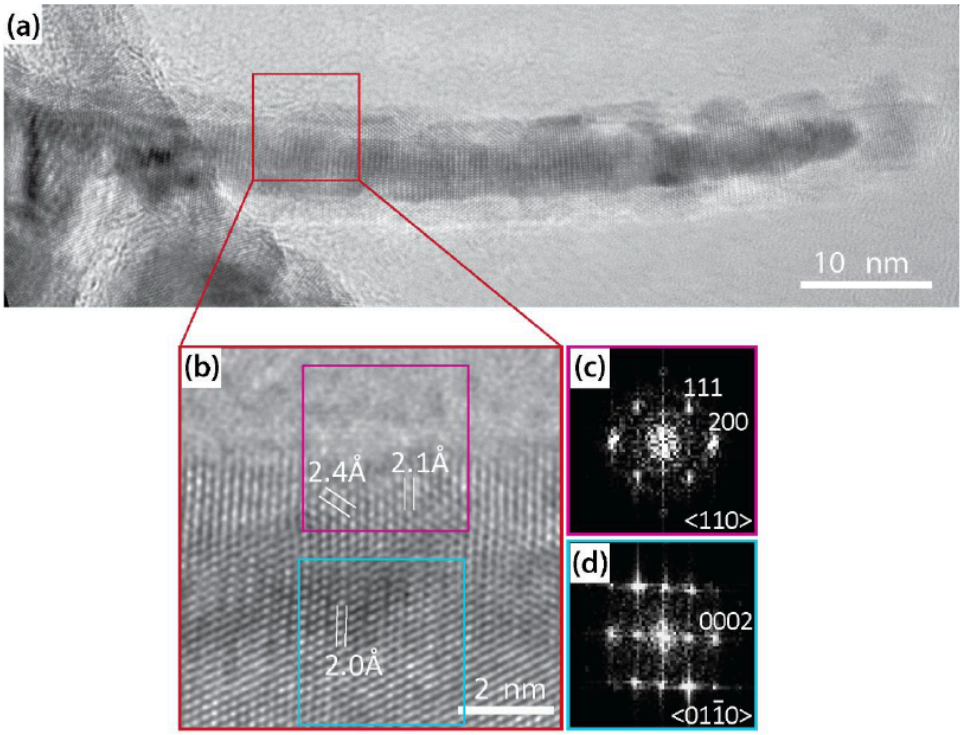

Figure S3: (a) TEM image of a Co branch. (b) HRTEM image of part of the branch in (a) indicated by the red box. (c) FFT of the HRTEM image at the oxide surface (purple box) indexed to a cubic <110> zone axis. (d) FFT of the HRTEM image at the core region (blue box) indexed to a hexagonal <01-10> zone axis. The lattice measurements of 2.0 Å at the core, and 2.1 Å and 2.4 Å at the shell regions are consistent with the lattice spacings of hcp Co{0002}, cubic CoO{200} and cubic CoO{111}, respectively.

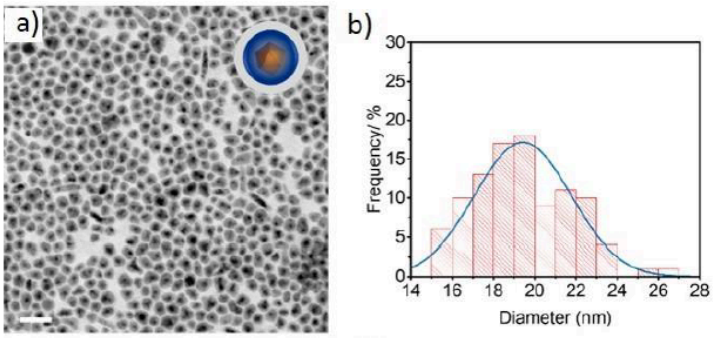

Figure S4: (a) TEM image and (b) histogram (average diameter 19.4 ± 2.3 nm) of polycrystalline Co nanoparticles

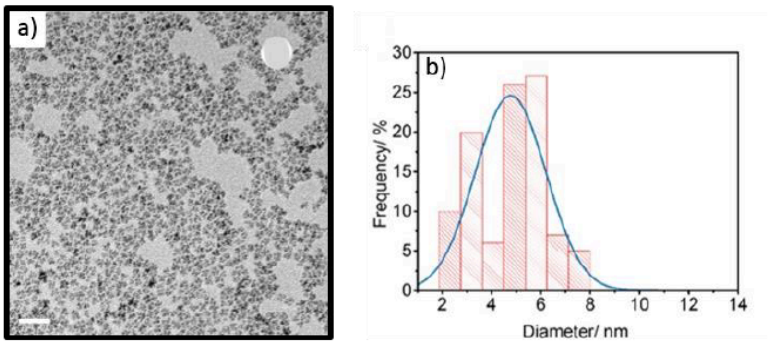

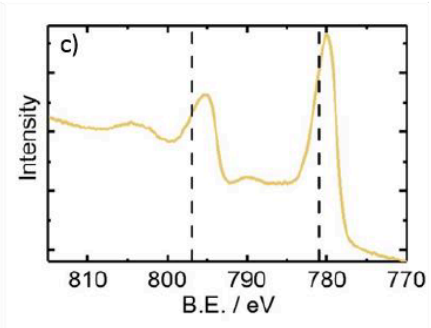

Figure S5: (a) TEM image, (b) histogram (average diameter of 4.8 ± 1.4 nm) and (c) XPS spectrum in the Co *2p* region of the Co_3O_4 nanoparticles. The dashed lines in the XPS plot indicate the position of the XPS peaks for the as prepared Co branched and Co spherical nanoparticles, evidencing the difference with the surfaces containing Co^{2+} species.

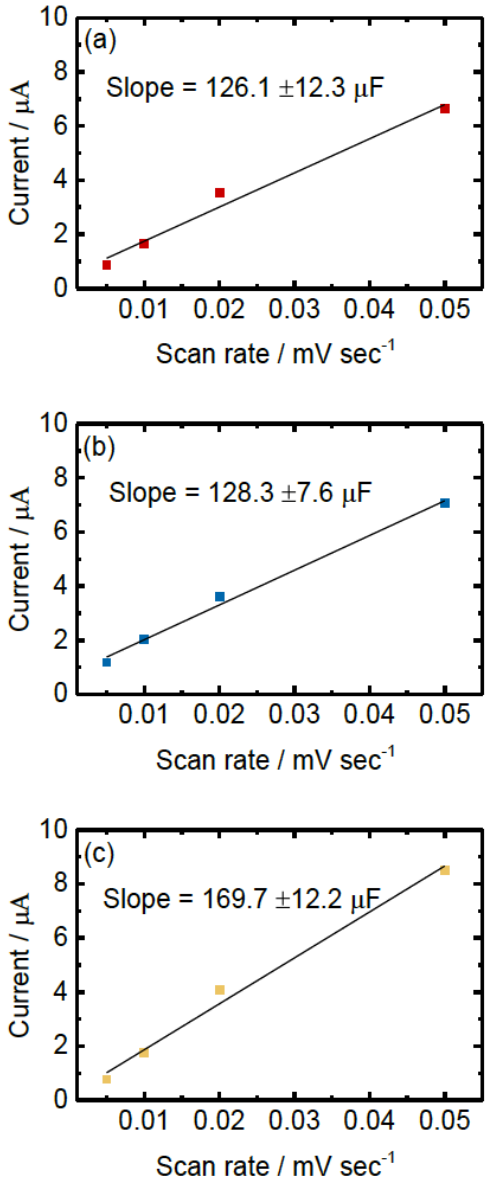

Figure S6: The relationship between current versus scan rate to determine electrochemical surface area. (a) Co branched nanoparticles, (b) Co spherical nanoparticles, and (c) Co_3O_4 nanoparticles.; electrolyte = KOH 1 mol L^{-1}.

Table S1: Electrochemical surface area (ECSA) determined from the graphs shown in Figure S6[3] and specific activity (SA).

Nanoparticle	**ECSA** cm^2/mg	**SA @ η = 400 mV** mA/cm^2_{Co}
Co Branched	6.7±3.0	9.8±3.0
Co spherical	6.9±2.7	2.6±0.7
Co_3O_4	9.1±3.8	1.7±0.5

Table S2. Comparison of catalytic activities of Cobalt -based electrocatalyst materials and commercial electrocatalysts (Ir, Ru) for OER.

Materials	Overpotential to reach 10 mA cm^{-2}	Electrolyte	Ref.
Co branched nanoparticles	320 mV	1M KOH	This work
Co spherical nanoparticles	450 mV	1M KOH	
Co_3O_4 nanoparticles	490 mV	1M KOH	
SnCoFe-Ar	300 mV	1M KOH	[5]
CoNi-SAs/NC	340 mV	1M KOH	[6]
$NiCo_2S_4$@g-C_3N_4CNT	330 mV	O_2-saturated 0.1 M KOH	[7]
SC CoO NRs	330 mV	O_2 saturated 1.0M KOH	[8]
Ce(3)–Co_3O_4	369 mV	1M KOH	[9]
CoO_x-nanoplates	306 mV	1M KOH	[10]
B-NiCoFe	342 mV	O_2 saturated 1.0M KOH	[11]
SCoNC	310 mV	0.1M KOH	[12]
$PrBaCo_2O_{5.75}$	360 mV	O_2 saturated 1.0M KOH	[13]
Co1-yCeyOx/FTO	320 mV	0.1M KOH	[14]

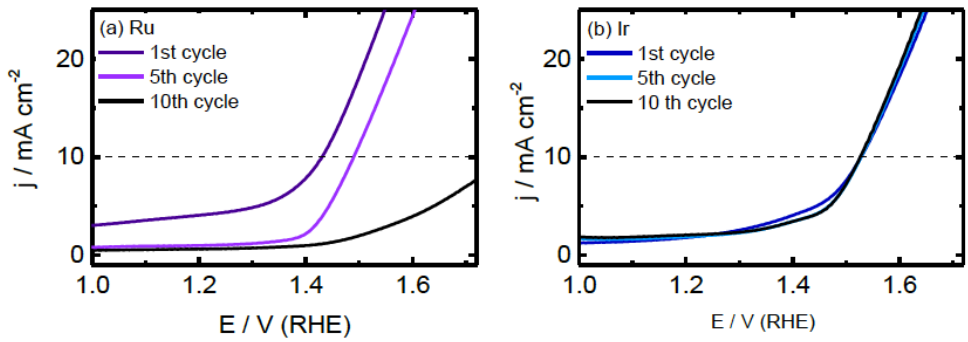

Figure S7: Anodic scan of the 1st, 5th, and 10th cycle of cyclic voltammetry to show the OER activities of commercial (a) ruthenium and (b) iridium catalysts. Cyclic voltammetry measurements were measured in 0.1 M $HClO_4$ at 100 mV sec^{-1} scan rate with rotation speed of 1600 rpm.

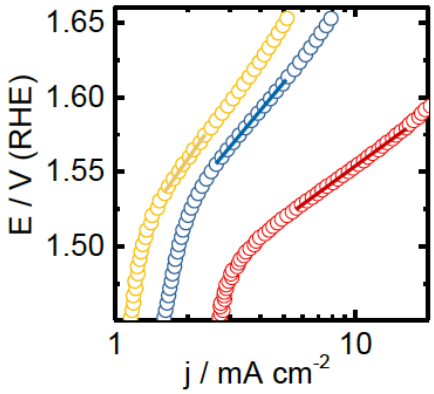

Figure S8: Tafel plots of the catalysts from the 50th cycle of cyclic voltammetry of hcp Co branched nanoparticles (red), Co spherical nanoparticles (blue), and Co_3O_4 nanoparticles (yellow). Scan rate =100 mV s^{-1}.

Table S3. Equivalent circuit and fitted parameters of the impedance diagrams

	Branched	Core-shell	Co_3O_4
R_s / Ω	6.279	0.01	5.959
CPE_1 / S s^n	3.84E-05	0.001472	0.000819
R_1 / Ω	9.175	52.65	89.74
CPE_2 / S s^n	0.002062	1.14E-05	0.000159
R_2 / Ω	23.52	20.74	10.46

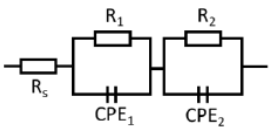

References:

[1] A. M. Henning, J. Watt, P. J. Miedziak, S. Cheong, M. Santonastaso, M. Song, Y. Takeda, A. I. Kirkland, S. H. Taylor, R. D. Tilley, *Angew Chem Int Ed Engl* **2013**, *52*, 1477-1480.

[2] X. Li, P. E. Siegbahn, *J Am Chem Soc* **2013**, *135*, 13804-13813.

[3] S. Watzele, P. Hauenstein, Y. Liang, S. Xue, J. Fichtner, B. Garlyyev, D. Scieszka, F. Claudel, F. Maillard, A. S. Bandarenka, *ACS Catalysis* **2019**, 9222-9230.

[4] Y. Liu, C. Ma, Q. Zhang, W. Wang, P. Pan, L. Gu, D. Xu, J. Bao, Z. Dai, *Adv Mater* **2019**, *31*, e1900062.

[5] D. Chen, M. Qiao, Y. R. Lu, L. Hao, D. Liu, C. L. Dong, Y. Li, S. Wang, *Angew Chem Int Ed Engl* **2018**, *57*, 8691-8696.

[6] X. Han, X. Ling, D. Yu, D. Xie, L. Li, S. Peng, C. Zhong, N. Zhao, Y. Deng, W. Hu, *Adv Mater* **2019**, *31*, e1905622.

[7] X. Han, W. Zhang, X. Ma, C. Zhong, N. Zhao, W. Hu, Y. Deng, *Adv Mater* **2019**, *31*, e1808281.

[8] T. Ling, D. Y. Yan, Y. Jiao, H. Wang, Y. Zheng, X. Zheng, J. Mao, X. W. Du, Z. Hu, M. Jaroniec, S. Z. Qiao, *Nat Commun* **2016**, *7*, 12876.

[9] J. Zhou, H. Zheng, Q. Luan, X. Huang, Y. Li, Z. Xi, G. Lu, L. Xing, Y. Li, *Sustainable Energy & Fuels* **2019**, *3*, 3201-3207.

[10] W. Xu, F. Lyu, Y. Bai, A. Gao, J. Feng, Z. Cai, Y. Yin, *Nano Energy* **2018**, *43*, 110-116.

[11] J. Xie, S. Cao, L. Gao, F. Lei, P. Hao, B. Tang, *Chem Commun (Camb)* **2019**, *55*, 9841-9844.

[12] J. Wu, H. Zhou, Q. Li, M. Chen, J. Wan, N. Zhang, L. Xiong, S. Li, B. Y. Xia, G. Feng, M. Liu, L. Huang, *Advanced Energy Materials* **2019**, *9*.

[13] X. Miao, L. Wu, Y. Lin, X. Yuan, J. Zhao, W. Yan, S. Zhou, L. Shi, *Chem Commun (Camb)* **2019**, *55*, 1442-1445.

[14] L. Pan, Q. Wang, Y. Li, C. Zhang, *Journal of Catalysis* **2020**, *384*, 14-21.

Chapter 5

Controlling the number of branches and surface facets of Pd-core Ru-branched nanoparticles to make highly active oxygen evolution reaction electrocatalysts

Publication One

Munkhshur Myekhlai, Tania M. Benedetti, Lucy Gloag, Agus R. Poerwoprajitno, Soshan Cheong, Wolfgang Schuhmann, J. Justin Gooding, and Richard D. Tilley. ***Chem. Eur.J.*****,** 2020, 26,15501–15504.

Reproduced with the permission from Willey

5.1 Summary

The publication "Controlling the Number of Branches and Surface Facets of Pd-Core Ru-Branched Nanoparticles to Make Highly Active Oxygen Evolution Reaction Electrocatalysts" has been used in lieu of this chapter. This publication aimed to study the effect of surface facets and branch number of Ru-Pd branched nanoparticles for the OER. It was hypothesized that controlling the surface facets and branch number of Ru-Pd branched nanoparticles would influence their catalytic properties. Thus, Ru-Pd branched nanoparticles with controlled branch length and number were synthesized, and their electrocatalytic properties were explored for OER. The results show that Ru-Pd branched nanoparticles with long branches were more catalytically active in comparison to those with short branches, and Ru-Pd branched nanoparticles with 2-3 branches were more catalytically active than those with 5 branches. This study concluded that the density of the more catalytically active $\{10\bar{1}1\}$ facets (side) increased compared to the less active {0001} facets (base) in proportion to an increase of branch length and thereby resulting in an increase in the catalytic activity. In addition, Ru-Pd branched nanoparticles with fewer branches were more accessible to electrocatalysis as compared to nanoparticles with a greater number of branches by promoting the removal of O_2 bubbles and, thus, enhancing the catalytic activity.

Declaration for Chapter 5

Author	Contributions
Munkhshur Myekhlai	Synthesized Pd seeds, Ru-Pd branched nanoparticles Characterized nanocrystals using low-resolution electron microscopy, XRD Performed electrocatalytic experiments including cyclic voltammertry, chronopotentiometry Drafted and proofread manuscript
Tania M. Benedetti	Provided knowledge of electrocatalysis Guidance and direction for project Proofread and writing of manuscript
Lucy Gloag	Experimental design Proofread manuscript
Agus R. Poerwoprajitno	Characterizations of nanocatalysts via high-resolution TEM Proofread manuscript
Soshan Cheong	Characterizations of nanocatalysts via high-resolution TEM and processed the image Proofread manuscript
Wolfgang Schuhmann	Experimental design Provided fundamental understanding of key electrocatalysis ideas Proofread manuscript
J. Justin Gooding	Experimental design Provided fundamental understanding of key electrocatalysis ideas Proofread manuscript
Richard D. Tilley	Experimental design Provided fundamental understanding of key electrocatalysis ideas Proofread manuscript

Inclusion of Publications Statement

UNSW is supportive of candidates publishing their research results during their candidature as detailed in the UNSW Thesis Examination Procedure.

Publications can be used in their thesis in lieu of a Chapter if:

- The candidate contributed greater than 50% of the content in the publication and is the "primary author", ie. the candidate was responsible primarily for the planning, execution and preparation of the work for publication
- The candidate has approval to include the publication in their thesis in lieu of a Chapter from their supervisor and Postgraduate Coordinator.
- The publication is not subject to any obligations or contractual agreements with a third party that would constrain its inclusion in the thesis

Please indicate whether this thesis contains published material or not:

☐ This thesis contains no publications, either published or submitted for publication

☐ Some of the work described in this thesis has been published and it has been documented in the relevant Chapters with acknowledgement

☒ This thesis has publications (either published or submitted for publication) incorporated into it in lieu of a chapter and the details are presented below

CANDIDATE'S DECLARATION

I declare that:

- I have complied with the UNSW Thesis Examination Procedure
- where I have used a publication in lieu of a Chapter, the listed publication(s) below meet(s) the requirements to be included in the thesis.

Candidate's Name	**Signature**	**Date (dd/mm/yy)**
Munkhshur Myekhlai		

POSTGRADUATE COORDINATOR'S DECLARATION

I declare that:

- the information below is accurate
- where listed publication(s) have been used in lieu of Chapter(s), their use complies with the UNSW Thesis Examination Procedure
- the minimum requirements for the format of the thesis have been met.

PGC's Name	**PGC's Signature**	**Date (dd/mm/yy)**
Alex William Donald		

For each publication incorporated into the thesis in lieu of a Chapter, provide all of the requested details and signatures required.

Details of publication #2:

Full title: *Controlling the number of branches and surface facets of Pd-core Ru-branched nanoparticles to make highly active oxygen evolution reaction electrocatalysts*

Authors: *Munkhshur Myekhlai, Tania M. Benedetti, Lucy Gloag, Agus R. Poerwoprajitno, Soshan Cheong, Wolfgang Schuhmann, J. Justin Gooding, and Richard D. Tilley*

Journal or book name: *Chemistry-A European Journal (Chem. Eur.J)*

Volume/page numbers: *Volume 26, Issue. 67, pages 15501-15504*

Date accepted/ published: *25 August, 2020*

Status	*Published*	✗	*Accepted and In press*		*In progress (submitted)*	

The Candidate's Contribution to the Work

- Synthesized Pd seeds, Ru-Pd branched nanoparticles
- Characterized nanocrystals using low-resolution electron microscopy, XRD
- Performed electrocatalytic experiments including cyclic voltammertry, chronopotentiometry
- Drafted and proofread manuscript

Location of the work in the thesis and/or how the work is incorporated in the thesis:

In lieu of Chapter 5

PRIMARY SUPERVISOR'S DECLARATION

I declare that:

- the information above is accurate
- this has been discussed with the PGC and it is agreed that this publication can be included in this thesis in lieu of a Chapter
- All of the co-authors of the publication have reviewed the above information and have agreed to its veracity by signing a 'Co-Author Authorisation' form.

Primary Supervisor's name	**Primary Supervisor's signature**	**Date**
Richard D. Tilley		**(dd/mm/yy)**

Chemistry–A European Journal
Communication
doi.org/10.1002/chem.202003561

Nanotechnology | *Hot Paper*

Controlling the Number of Branches and Surface Facets of Pd-Core Ru-Branched Nanoparticles to Make Highly Active Oxygen Evolution Reaction Electrocatalysts

Munkhshur Myekhlai,[a] Tania M. Benedetti,[a] Lucy Gloag,[a] Agus R. Poerwoprajitno,[a] Soshan Cheong,[b] Wolfgang Schuhmann,[c] J. Justin Gooding,*[a, d] and Richard D. Tilley*[a, b]

Abstract: Producing stable but active materials is one of the enduring challenges in electrocatalysis and other types of catalysis. Producing branched nanoparticles is one potential solution. Controlling the number of branches and branch size of faceted branched nanoparticles is one of the major synthetic challenges to achieve highly active and stable nanocatalysts. Herein, we use a cubic-core hexagonal-branch mechanism to synthesize branched Ru nanoparticles with control over the size and number of branches. This structural control is the key to achieving high exposure of active {10–11} facets and optimum number of Ru branches that enables improved catalytic activity for oxygen evolution reaction while maintaining high stability.

The synthesis of 3D branched metal nanoparticles with well-defined surfaces is important for catalysis.[1] This is because the branch morphology offers high surface area and the surface of the branches can be controlled for active and stable sites.[2] For highly active and stable catalysis, the branch size and the number of branches need to be precisely controlled. These controls enable both the preferential exposure of active facets and increased overall active surface area.

Ruthenium (Ru) is the most active catalyst for the oxygen evolution reaction (OER) in acidic conditions, but Ru is easily dissolved into the electrolyte due to the formation of oxidized Ru species ($Ru^{>4+}$).[3] Recently, faceted Ru nanoparticles have shown to be the most active and stable catalysts to date.[2a, b, 4] The high electrocatalytic performance is due to the presence of branches with low index facets.[2a, b, 5] The next challenge is to precisely control the branch size and number of branches on Ru nanoparticles to further improve the activity and stability.

Cubic-core hexagonal-branch mechanism has been shown as the best approach to synthesize branched nanoparticles with a high level of control.[4, 6] This branching mechanism enables highly uniform hexagonal closed packed (*hcp*) branches to epitaxially grow from a face-centered cubic (*fcc*) core. There is an opportunity to extend this approach to synthesize Ru branched nanoparticles with control over the branch size and number of branches.

Herein, we present a synthetic method to form Pd-Ru core-branched with control over branch size and number of branches. We show that the size of branches controls the relative ratio of {10–11}/{0001} facets and the number of branches controls the size of these facets. Controlling these structural features improves the OER activity by exposing {10–11} active facets and optimizing the release of produced O_2 bubbles to drive the reaction forward.

To synthesize uniform branched Ru nanoparticles, preformed monodispersed Pd nanoparticles of 3.5 ± 0.4 nm were used as seeds (Figure S1, SI). The *fcc*-{111} facets on Pd seeds enables the epitaxial growth of *hcp*-{0001} of branched Ru due to their small lattice mismatch (4%). The Pd seed was mixed with Ru precursor, oleylamine and mesitylene at 140 °C under 3 bar H_2. The use of H_2 as a mild reducing agent is important to ensure that Ru precursor is slowly reduced, which allows heterogeneous nucleation without the formation of homogeneous Ru monometallic nanoparticles.[7]

Uniform Pd-Ru branched nanoparticles were successfully synthesized, as shown in the transmission electron microscopy (TEM) image in Figure 1 a. The branches are hexagonal pyramid shaped (Figure S2, Supporting Information), terminated with 6 low-index facets {10–11} on the sides and a single {0001} on the base, as evidenced by high-resolution TEM (HRTEM) image in Figure 1 b. The presence of Pd and Ru is confirmed by X-ray

[a] M. Myekhlai, Dr. T. M. Benedetti, Dr. L. Gloag, A. R. Poerwoprajitno, Prof. Dr. J. J. Gooding, Prof. Dr. R. D. Tilley
School of Chemistry, The University of New South Wales
Sydney, NSW 2052 (Australia)
E-mail: r.tilley@unsw.edu.au
justin.gooding@unsw.edu.au

[b] Dr. S. Cheong, Prof. Dr. R. D. Tilley
Mark Wainwright Analytical Centre
The University of New South Wales
Sydney, NSW 2052 (Australia)

[c] Prof. Dr. W. Schuhmann
Analytical Chemistry—Center for Electrochemical Sciences (CES)
Faculty of Chemistry and Biochemistry, Ruhr University Bochum
Universitätsstr. 150, D-44780 Bochum (Germany)

[d] Prof. Dr. J. J. Gooding
Australian Research Council Centre of Excellence in
Convergent Bio-Nano Science and Technology, School of Chemistry
The University of New South Wales
Sydney, NSW 2052 (Australia)

Supporting information and the ORCID identification number(s) for the author(s) of this article can be found under:
https://doi.org/10.1002/chem.202003561.

Part of a Special Issue celebrating the 1000th Issue of Chemistry—A European Journal.

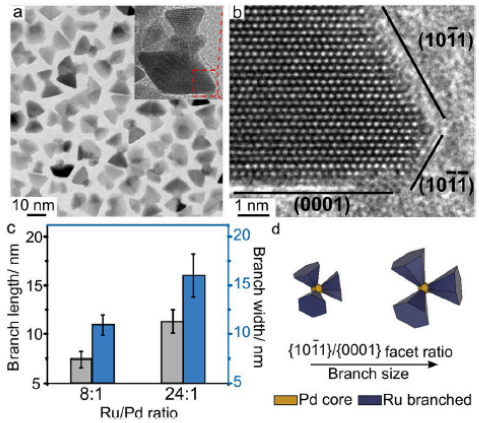

Figure 1. a) TEM image of Pd–Ru branched nanoparticles and HR-TEM image of single Pd–Ru branched nanoparticle (inset). b) Atomic resolution HRTEM image of a branch indicated by the red box in (a) showing the {10–11} and {0001} surface facets. c) Branch length and branch width versus concentration ratio of Ru precursor to Pd seeds. d) Nanoparticle models showing that increasing the branch size results in the higher proportion of {10–11} facets compared to {0001} facets.

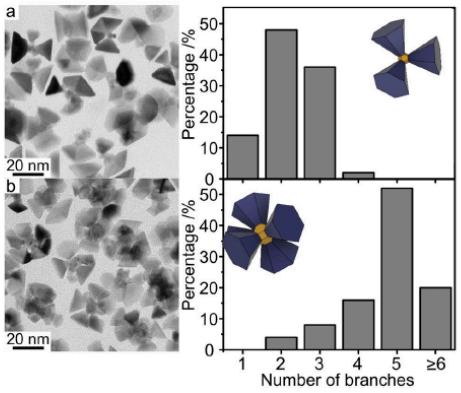

Figure 2. TEM images and corresponding histograms of the number of branches per particle: Pd–Ru nanoparticles with (a) 2—3 branches and (b) 5 branches.

diffraction pattern and energy dispersive X-ray spectroscopy (Figure S2–3, Supporting Information).

Control of branch size was achieved by varying the Ru precursor to Pd seed (Ru/Pd) ratio. The branch size increases from 6.6±0.7 nm in length and 10.1±1.2 nm in width (8:1 Ru/Pd) to 11.0±1.5 nm in length and 17.5±2.2 nm in width (24:1 Ru/Pd), respectively, as shown in Figure 1c and Figure S4 (Supporting Information). The number of branches is kept relatively constant with over 80% of the nanoparticles having 2–3 branches, irrespective of branch size (Figure S5, Supporting Information). The increase in Ru branch size is made possible by making more Ru available per Pd seed during branch growth process.

The increase in branch size results in the higher total surface area of {10–11} facets (sides) compared to {0001} facets (base) as illustrated in Figure 1d. The 6 nm and 11 nm long Pd-Ru branched nanoparticles have {10–11}/{0001} ratios of 1.4 and 1.8, respectively (Table S1, Supporting Information). As the branch size increases, the surface area of the branch sides increases more than the surface area of the base, resulting in an increase in the {10–11}/{0001} facet ratio. This control of facet ratio enables the identification of active facets which has not been achieved by previous Ru branched nanoparticles synthesis.[2a,4]

Control over the number of branches is achieved by introducing different Pd seed sizes (Figure S1, Supporting Information). Increasing the Pd seeds from 3.5 nm to 8.7 nm in diameter, leads to an increase in the number of branches from 2–3 branches to more than 5 branches per nanoparticle, as shown in Figure 2. The branch length and branch width are similar (Figure S5, Supporting Information). When the Pd seed size is increased, there are more nucleation sites available per seed for Ru to form branches. It is more energetically favorable to form new branches than to grow larger branches in order to minimize the total surface energy of the nanoparticles.[8] This condition enables an increase in the number of branches while maintaining the branch size.

The presented synthesis is effective at controlling both the branch size and number of branches, which has not been previously achieved with branched Ru nanoparticles.[9] This high level of control is similar to what has been achieved in the synthesis of state-of-the-art CdSe and PtAu core-branched nanoparticles.[6,8,10] Seeded growth under slow growth conditions are the key to achieve these 3D branched structures with precise control over branch size and number of branches, which are important for highly active and stable OER electrocatalysts.

The catalytic activity and stability of the Pd-Ru branched nanoparticles for the OER was evaluated in acid electrolyte (0.1 M $HClO_4$). The current was normalized by electrochemically active surface area (ECSA) of Ru and the measurements were repeated 4x per sample for consistent results (Table S2, Supporting Information). The effect of branch size was examined by comparing Pd-Ru branched nanoparticles with 2–3 branches that are 6 nm and 11 nm in length. Increasing branch size from 6 nm to 11 nm increased the specific activity at an overpotential of 270 mV by 2.7 times as shown in the anodic scan of the cyclic voltammograms in Figure 3a. This specific activity at an overpotential of 270 mV is 4 times higher than state-of-art IrO_2 nanoparticles.[11] The presence of Pd core is unlikely to contribute to the OER activity because Pd is inactive relative to Ru, requiring a high overpotential of 500 mV.[3a]

The Pd–Ru branched nanoparticles exhibit high stability. The nanoparticles still showed activity even after 1000 potentiodynamic cycles (Figure S6). The activity remains 71% and 75% of the initial activity after 200 cycles for the branched Pd–Ru nanoparticles with 6 nm and 11 nm long branches, respectively. This stability is significantly higher than non-faceted non-

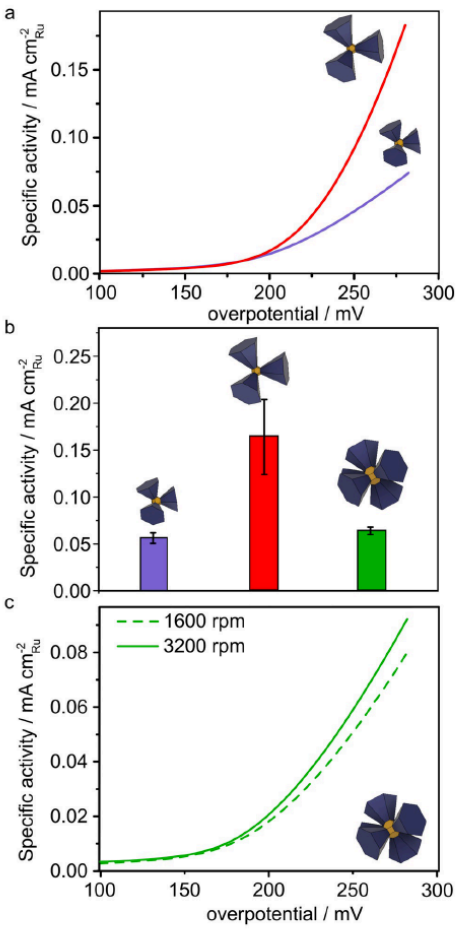

Figure 3. a) Oxidation scan of Pd–Ru 6 nm and 11 nm long branched nanoparticles in 0.1 M $HClO_4$ at 1600 rpm. b) Comparison of specific activity of Pd–Ru nanoparticles with 6 nm long branches, 11 nm long branches and 11 nm long multi-branched nanoparticles obtained at an overpotential of 270 mV. c) Oxidation scan of Pd–Ru 11 nm long multi-branched nanoparticles in 0.1 M $HClO_4$ at 1600 and 3200 rpm.

branched Ru nanoparticles which become completely inactive within the first few cycles.[2a, 4, 12] The high stability of Pd-Ru branched nanoparticles is due to the exposure of low-index facets that minimize the dissolution of $Ru^{>4+}$ into electrolyte (Figure S7, Supporting Information). The Pd–Ru branched nanoparticles have >98% faradaic efficiency (FE) (Table S3, Supporting Information), indicating that Ru atoms involved in the OER are in stable sites instead of dissolving to electrolyte.[2b] A Tafel slope of 69.7 mV dec^{-1} was obtained for the Pd-Ru branched nanoparticles (Figure S8, Supporting Information). The slope is near to 60 mV dec^{-1} and is characteristic of a rate determining step involving the rearrangement of OH prior to second electron transfer reaction and is typical of highly active and stable catalysts.[12a, 13]

The high activity of Pd-Ru branched nanoparticles with larger sized branches is due to the higher relative surface area of {10–11}/{0001} facets as can be seen in Figure S9 (Supporting Information). This result suggests that {10–11} facet is more active than {0001} facet, which is expected due to the lower coordination and slightly higher energy of the {10–11} facet.[5, 14] As both {10–11} and {0001} facets are highly stable, nanoparticles with larger branches that expose a larger surface area of {10–11} facets create stable OER catalysts with improved activity.

The above set of experiments show the importance of synthetically controlling the branch size to increase the exposure of active {10–11} facets. This is vital because unlike isotropic nanoparticles in which the active surface facets can be identified by comparing different shapes,[3b, 15] the active surface facets for anisotropic nanoparticles can only be studied by comparing branch size.[16]

To evaluate the effect of branch number on OER performance, Pd–Ru branched nanoparticles with 2–3 and 5 branches were compared. When the number of branches was increased from 2–3 to 5, the specific activity decreased by 2.6x at an overpotential of 270 mV although the ratio of branch facets remains the same, as shown in Figure 3b and Figure S10 (Supporting Information). It is hypothesized that increasing the number of branches decreases the ability for oxygen molecules to escape from the electrode.[17] It is suggested that as oxygen gas bubbles are formed during OER, they are more easily trapped between the branches of nanoparticles when there are larger numbers of branches. A consequence is that a fraction of active sites becomes blocked by the gas bubbles, which limits the contact between the electrolyte and electrode surface and decreases the specific activity.[17] This is supported by the specific activity increasing from 0.069 to 0.08 mA cm^{-2} (Figure 3c) as the rotation speed of the working electrode was increased from 1600 to 3200 rpm. At higher rotation speeds, the oxygen bubbles are more easily removed from the nanoparticle surface and the specific activity is increased. This result shows the importance of designing nanoparticles with the optimum number of branches (3 Ru branches in this case) to ensure effective gas-bubble detachment.[18]

In conclusion, we show that a cubic-core hexagonal-branch mechanism enables the synthesis of Pd–Ru branched nanoparticles with control of branch size and number of branches. By increasing the ratio of precursor to seed, the branch size could be increased and the relative ratio of active {10–11} to {0001} facets could be controlled. By increasing the size of the Pd seeds, the number of branches could be increased. The high exposure of {10–11} facets improves the catalytic activity without compromising the stability and the optimum number of Ru branches ensure the effective gas bubble detachment. This concept opens up the opportunity to synthesize various well-defined bimetallic branched nanoparticles for different electrocatalytic applications.

Acknowledgements

The authors acknowledge funding under the Australian Research Council Linkage grant (L.G., J.J.G. R.D.T., LP150101014), the Australian Laureate Fellowship (J.J.G., FL150100060) and the Discovery Project (R.D.T., DP190102659 and DP200100143). M.M. and A.R.P. thank to UNSW Scientia Ph.D. scholarship and development Scheme. We also acknowledge support from the Australian Research Council of Centre of Excellence in Convergent Bio-Nano Science and Technology (CE140100036) and Microscopy Australia (formerly AMMRF), as well as the Mark Wainwright Analytical Centre and Electron Microscope Unit at the University of New South Wales.

Conflict of interest

The authors declare no conflict of interest.

Keywords: branched nanoparticles · electrocatalysis · oxygen evolution reactions · ruthenium · surface facets

[1] a) B. Lim, Y. Xia, *Angew. Chem. Int. Ed.* **2011**, *50*, 76–85; *Angew. Chem.* **2011**, *123*, 78–87; b) M. Zhao, Y. Xia, *Nat. Rev. Mater.* **2020**, *5*, 440–459; c) M. Myekhlai, T. M. Benedetti, L. Gloag, V. R. Gonçales, S. Cheong, H.-S. Chen, J. J. Gooding, R. D. Tilley, *ChemCatChem* **2020**, *12*, 3126–3131.

[2] a) L. Gloag, T. M. Benedetti, S. Cheong, Y. Li, X.-H. Chan, L.-M. Lacroix, S. L. Y. Chang, R. Arenal, I. Florea, H. Barron, A. S. Barnard, A. M. Henning, C. Zhao, W. Schuhmann, J. J. Gooding, R. D. Tilley, *Angew. Chem. Int. Ed.* **2018**, *57*, 10241–10245; *Angew. Chem.* **2018**, *130*, 10398–10402; b) A. R. Poerwoprajitno, L. Gloag, T. M. Benedetti, S. Cheong, J. Watt, D. L. Huber, J. J. Gooding, R. D. Tilley, *Small* **2019**, *15*, 1804577; c) A. Alinezhad, T. M. Benedetti, L. Gloag, S. Cheong, J. Watt, H.-S. Chen, J. J. Gooding, R. D. Tilley, *ACS Appl. Mater. Interfaces* **2020**, *3*, 5995–6000.

[3] a) S. Cherevko, A. R. Zeradjanin, A. A. Topalov, N. Kulyk, I. Katsounaros, K. J. J. Mayrhofer, *ChemCatChem* **2014**, *6*, 2219–2223; b) A. R. Poerwoprajitno, L. Gloag, S. Cheong, J. J. Gooding, R. D. Tilley, *Nanoscale* **2019**, *11*, 18995–19011; c) T. Reier, H. N. Nong, D. Teschner, R. Schlögl, P. Strasser, *Adv. Energy Mater.* **2017**, *7*, 1601275; d) X. Wu, C. Tang, Y. Cheng, X. Min, S. P. Jiang, S. Wang, *Chem. Eur. J.* **2020**, *26*, 3906–3929; e) J. Shan, T. Ling, K. Davey, Y. Zheng, S.-Z. Qiao, *Adv. Mater.* **2019**, *31*, 1900510; f) J. Shan, Y. Zheng, B. Shi, K. Davey, S.-Z. Qiao, *ACS Energy Lett.* **2019**, *4*, 2719–2730; g) J. Shan, C. Guo, Y. Zhu, S. Chen, L. Song, M. Jaroniec, Y. Zheng, S.-Z. Qiao, *Chem.* **2019**, *5*, 445–459.

[4] L. Gloag, T. M. Benedetti, S. Cheong, C. E. Marjo, J. J. Gooding, R. D. Tilley, *J. Am. Chem. Soc.* **2018**, *140*, 12760–12764.

[5] S. H. Chang, N. Danilovic, K.-C. Chang, R. Subbaraman, A. P. Paulikas, D. D. Fong, M. J. Highland, P. M. Baldo, V. R. Stamenkovic, J. W. Freeland, J. A. Eastman, N. M. Markovic, *Nat. Commun.* **2014**, *5*, 4191.

[6] L. Manna, D. J. Milliron, A. Meisel, E. C. Scher, A. P. Alivisatos, *Nat. Mater.* **2003**, *2*, 382.

[7] a) T. S. Rodrigues, M. Zhao, T.-H. Yang, K. D. Gilroy, A. G. M. da Silva, P. H. C. Camargo, Y. Xia, *Chem. Eur. J.* **2018**, *24*, 16944–16963; b) L. M. Martínez-Prieto, A. Ferry, P. Lara, C. Richter, K. Philippot, F. Glorius, B. Chaudret, *Chem. Eur. J.* **2015**, *21*, 17495–17502.

[8] C. Wang, W. Tian, Y. Ding, Y.-q. Ma, Z. L. Wang, N. M. Markovic, V. R. Stamenkovic, H. Daimon, S. Sun, *J. Am. Chem. Soc.* **2010**, *132*, 6524–6529.

[9] a) S. Drouet, J. Creus, V. Colliere, C. Amiens, J. Garcia-Anton, X. Sala, K. Philippot, *Chem. Commun.* **2017**, *53*, 11713–11716; b) K. Gao, Y. Wang, Z. Wang, Z. Zhu, J. Wang, Z. Luo, C. Zhang, X. Huang, H. Zhang, W. Huang, *Chem. Commun.* **2018**, *54*, 4613–4616.

[10] K. Cheng, S.-R. Kothapalli, H. Liu, A. L. Koh, J. V. Jokerst, H. Jiang, M. Yang, J. Li, J. Levi, J. C. Wu, S. S. Gambhir, Z. Cheng, *J. Am. Chem. Soc.* **2014**, *136*, 3560–3571.

[11] L. Li, B. Wang, G. Zhang, G. Yang, T. Yang, S. Yang, S. Yang, *Adv. Energy Mater.* **2020**, *10*, 2001600.

[12] a) T. Reier, M. Oezaslan, P. Strasser, *ACS Catal.* **2012**, *2*, 1765–1772; b) C. C. L. McCrory, S. Jung, I. M. Ferrer, S. M. Chatman, J. C. Peters, T. F. Jaramillo, *J. Am. Chem. Soc.* **2015**, *137*, 4347–4357; c) J. Yu, Q. He, G. Yang, W. Zhou, Z. Shao, M. Ni, *ACS Catal.* **2019**, *9*, 9973–10011; d) L. Gloag, T. M. Benedetti, S. Cheong, R. F. Webster, C. E. Marjo, J. J. Gooding, R. D. Tilley, *Nanoscale* **2018**, *10*, 15173–15177.

[13] S. H. Chang, N. Danilovic, K. C. Chang, R. Subbaraman, A. P. Paulikas, D. D. Fong, M. J. Highland, P. M. Baldo, V. R. Stamenkovic, J. W. Freeland, J. A. Eastman, N. M. Markovic, *Nat. Commun.* **2014**, *5*, 4191.

[14] R. R. Rao, M. J. Kolb, L. Giordano, A. F. Pedersen, Y. Katayama, J. Hwang, A. Mehta, H. You, J. R. Lunger, H. Zhou, N. B. Halck, T. Vegge, I. Chorkendorff, I. E. L. Stephens, Y. Shao-Horn, *Nat. Catal.* **2020**, *3*, 516–525.

[15] J. W. Hong, Y. Kim, Y. Kwon, S. W. Han, *Chem. Asian J.* **2016**, *11*, 2224–2239.

[16] a) A. R. Poerwoprajitno, L. Gloag, J. Watt, S. Cychy, S. Cheong, P. V. Kumar, T. M. Benedetti, C. Deng, K.-H. Wu, C. E. Marjo, D. L. Huber, M. Muhler, J. J. Gooding, W. Schuhmann, D.-W. Wang, R. D. Tilley, *Angew. Chem. Int. Ed.* **2020**, *59*, 15487–15491; *Angew. Chem.* **2020**, *132*, 15615–15620; b) A. McLaren, T. Valdes-Solis, G. Li, S. C. Tsang, *J. Am. Chem. Soc.* **2009**, *131*, 12540–12541.

[17] a) A. R. Zeradjanin, A. A. Topalov, Q. Van Overmeere, S. Cherevko, X. Chen, E. Ventosa, W. Schuhmann, K. J. J. Mayrhofer, *RSC Adv.* **2014**, *4*, 9579–9587; b) A. R. Zeradjanin, E. Ventosa, A. S. Bondarenko, W. Schuhmann, *ChemSusChem* **2012**, *5*, 1905–1911.

[18] a) J. Wordsworth, T. M. Benedetti, A. Alinezhad, R. D. Tilley, M. A. Edwards, W. Schuhmann, J. J. Gooding, *Chem. Sci.* **2020**, *11*, 1233–1240; b) E. Fabbri, A. Habereder, K. Waltar, R. Kötz, T. J. Schmidt, *Catal. Sci. Technol.* **2014**, *4*, 3800–3821; c) A. Alinezhad, L. Gloag, T. M. Benedetti, S. Cheong, R. F. Webster, M. Roelsgaard, B. B. Iversen, W. Schuhmann, J. J. Gooding, R. D. Tilley, *J. Am. Chem. Soc.* **2019**, *141*, 16202–16207.

Manuscript received: July 30, 2020
Revised manuscript received: August 24, 2020
Accepted manuscript online: August 25, 2020
Version of record online: October 12, 2020

Chemistry–A European Journal

Supporting Information

Controlling the Number of Branches and Surface Facets of Pd-Core Ru-Branched Nanoparticles to Make Highly Active Oxygen Evolution Reaction Electrocatalysts

Munkhshur Myekhlai,[a] Tania M. Benedetti,[a] Lucy Gloag,[a] Agus R. Poerwoprajitno,[a] Soshan Cheong,[b] Wolfgang Schuhmann,[c] J. Justin Gooding,*[a, d] and Richard D. Tilley*[a, b]

Supporting information

Controlling the number of branches and surface facets of Pd-core Ru-branched nanoparticles to make highly active oxygen evolution reaction electrocatalysts

Munkhshur Myekhlai,[a] Tania M. Benedetti,[a] Lucy Gloag,[a] Agus R. Poerwoprajitno,[a] Soshan Cheong,[b] Wolfgang Schuhmann,[c] J. Justin Gooding,[a,d] and Richard D. Tilley*[a,b]*

[a] School of Chemistry, The University of New South Wales, Sydney, NSW 2052 (Australia).

[b] Mark Wainwright Analytical Centre, The University of New South Wales, Sydney, NSW 2052 (Australia).

[c] Analytical Chemistry - Center for Electrochemical Sciences (CES), Faculty of Chemistry and Biochemistry, Ruhr University Bochum, Universitätsstr. 150, D-44780 Bochum (Germany)

[d] Australian Research Council Centre of Excellence in Convergent Bio-Nano Science and Technology. School of Chemistry, The University of New South Wales, Sydney, NSW 2052 (Australia).

Experimental Section

Synthesis of 3.5 nm Pd seeds. Pd seeds (3.5 ±0.4 nm) were synthesized by a heating-up method according to a previously published method in our group.[1,2] $Pd(acac)_2$ (0.16 mmol, Sigma-Aldrich, 99 %) was dissolved in 5 mL of oleylamine (Sigma-Aldrich, 70 %) in a 25 mL three neck flask using a magnetic stirrer. The reaction mixture was then heated to 100 °C under Ar for 30 min. After that, 0.25 mL of trioctylphosphine (TOP, Sigma-Aldrich, 97 %) was added to the reaction mixture and then the temperature was raised to 250°C at a rate of 2-3 °C min^{-1} and held at this temperature for 30 min. After the reaction, the mixture was cooled down under Ar and purification was done 4-5 times using methanol and toluene (1:1 volume ratio) at 14000 rpm. Then, Pd seeds were kept in mesitylene (Sigma-Aldrich, 98 %) for further syntheses.

Synthesis of 8.7 nm Pd seeds. Pd seeds were synthesized using a seed mediated approach modifying the synthesis of Pd icosahedra nanocrystals[2]. Bis(acetonitrile) dichloropalladium ($PdCl_2(CH_3CN_2)$) (0.05 mmol, Sigma-Aldrich, 99 %) and 10 eq. molar hexadecylamine (0.5 mmol, Sigma-Aldrich, 90 %) were firstly dissolved in toluene (1.0 mL). Pd seeds (3.5 ±0.4 nm) (0.00125 mmol) and toluene (10 mL, Chem-Supply, 99.9 %) were then added to the solution. The reaction mixture was then kept at 3 bar hydrogen at 25°C for 2 hours. After the reaction, H_2 was released and purification was done 4-5 times using toluene and methanol solution (1:1 volume ratio) at 14000 rpm. Then, Pd seeds were kept in mesitylene to further syntheses.

Synthesis of Pd-Ru branched nanoparticles.

Pd-Ru branched nanoparticles. The synthesis of the Pd-Ru branched nanoparticles was firstly carried out using an organic-phase solution seed mediated approach according to a previously published method in our group.[1] To grow the *hcp* branches, the 3.5 nm Pd seed solution (0.00625 mmol was added to a solution containing Ruthenium (III) acetylacetonate (0.05 mmol, Sigma-Aldrich, 97 %) as a precursor and 5 eq. mol of oleylamine (82 µL) as a surfactant dissolved in 1 mL of mesitylene. The ratio of Ru to Pd was 8:1 and 24:1 for Pd-Ru branched nanoparticles with 6 nm and 11 long branches, respectively. The reaction mixture was then kept at 3 bar hydrogen at 140°C for 24 hours. After the reaction, H_2 was released and purification was done twice using methanol and toluene solution (1:1 volume ratio) at 4000 rpm.

Pd-Ru multi-branched nanoparticles with 11 nm long branches. The Pd-Ru multi-branched branched nanoparticles were synthesized using the same protocol for the Pd-Ru branched nanoparticles with 11 nm long branches including same ratio of precursor to seed (24 : 1), however, Pd seeds (8.7 ± 0.7 nm) were used to the synthesis.

Characterizations.

TEM Characterization: Low-resolution TEM was performed on a Philips CM200 operated at 200 kV. High-resolution TEM and STEM-EDX were performed on a JEOL JEM-F200 (200 kV, cold field emission gun) equipped with an annular dark field detector and a JEOL windowless 100 mm^2 silicon drift X-ray detector.

ICP-MS Characterization: For the inductively coupled plasma-mass spectrometry (ICP-MS), a fixed volume of 5 mL of the electrolyte was collected after 5, 10, 100, 200, and 500 OER cycles and analyzed using a Nexlon 300D-ICP-MS PerkinElmer instrument.

XRD Characterization: XRD characterization was performed on an Empyrrean-II powder diffractometer fitted with a 10 mm slit.

Electrochemical procedures

Catalysts ink preparation. For the electrochemical studies, firstly the nanoparticles (about 1 mg) were dispersed in a solution of a toluene (200 µL) to make an ink. The working electrode was prepared by drop casting the electrocatalysts (15 µL) and nafion (0.05 % v/v, 5 µL) onto the glassy carbon surface (0.196 cm^2 area).

Electrochemical measurements

Electrochemical surface area. The electrochemical surface area (ECSA) of the catalysts were determined from the slope of the capacitive current versus scan rate plots to obtain the capacitance. Cyclic voltammetry measurements in the capacitive potential range were performed at 5, 10, 20, and 50 mV s^{-1}. The obtained capacitance was then used to calculate the ECSA using the specific capacitance of 66 µF cm^2. [3]

Oxygen evolution reaction. The measurements were performed using an Autolab potentiostat running with Nova 2 software. The working electrode was kept rotating at 1600 rpm during the experiments and a 0.1 M $HClO_4$ solution was used as the electrolyte. A Pt-mesh and Ag|AgCl|3 M NaCl were used as the counter electrode and reference electrode, respectively. All potentials were converted to the reversible hydrogen electrode (RHE) by measuring the potential between the reference electrode and a freshly prepared standard reference electrode and considering the electrolyte pH. The OER activity was then measured by cyclic voltammetry between 0.0 V vs. and 1.55 V (vs. RHE) at 50 mV s^{-1}.

The stability was evaluated from the difference between the maximum catalytic activity and the activity after 200, 400, 800, and 1000 OER cycles. Cyclic voltammetry measurements for the stability tests were performed under the same conditions used for the activity tests. In addition, to determine faradaic efficiency, the amount of dissolved Ru after 5, 10, 100, 200, and 500 cycles was firstly found using ICP-MS. The faradaic efficiency of the electrocatalysts for the given cycles was then determined from the charge of Ru and total charge.

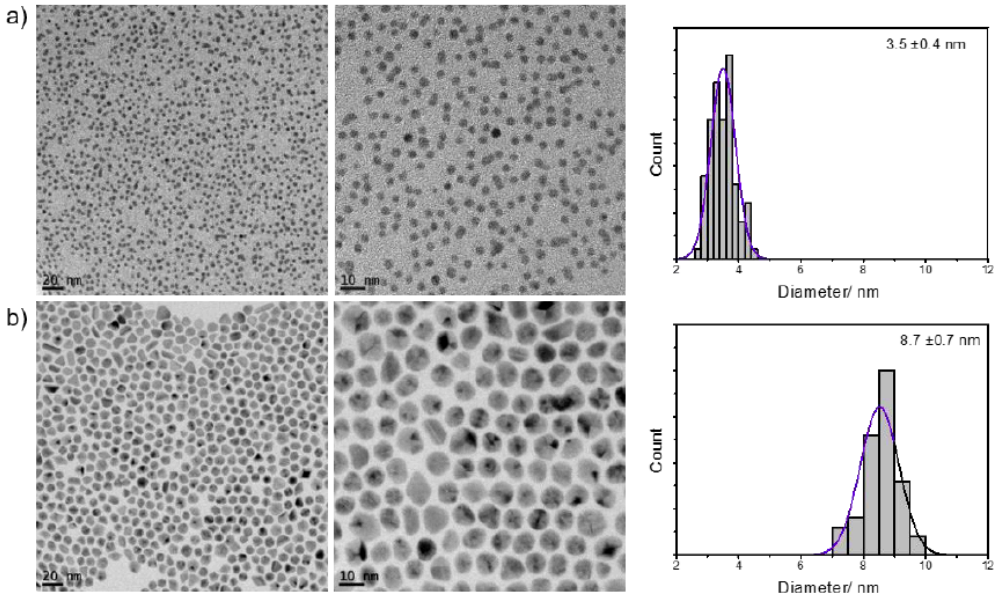

Figure S1. TEM images of Pd seeds with different diameter and related histograms. (a) Pd seeds with average diameter of 3.5 ± 0.4 nm and (b) Pd seeds with average diameter of 8.7 ± 0.7 nm. The histograms were obtained from counting 100 nanoparticles.

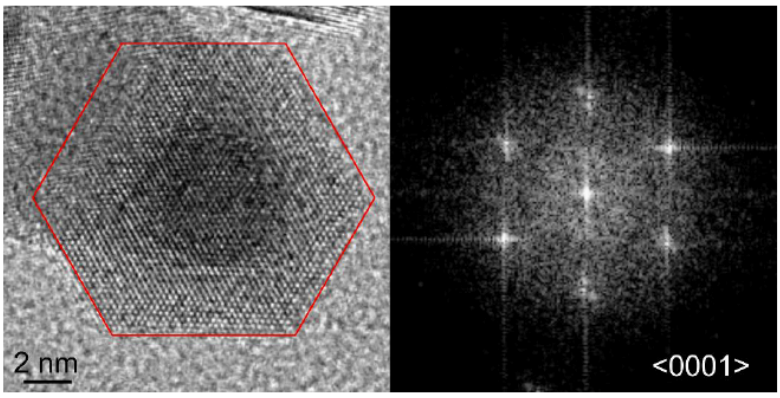

Figure S2. HRTEM image of a single Pd-Ru branched nanoparticle and the corresponding FFT showing the hexagonal pyramid shaped. The atoms are arranged in an hcp crystal structure viewed down the <0001> zone axis.

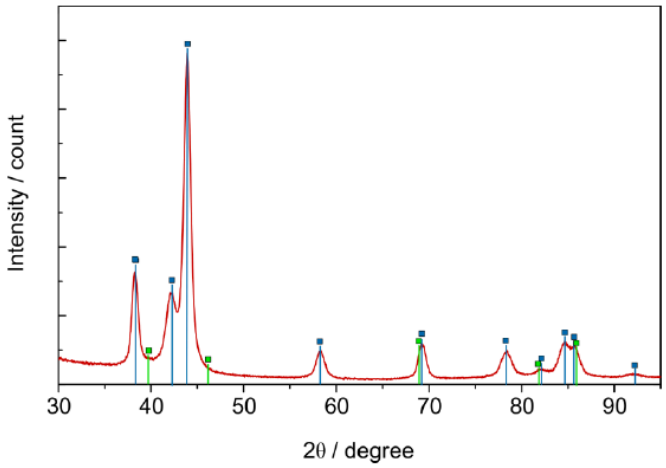

Figure S3. XRD pattern of Pd-Ru branched nanoparticles with 11 nm long branches. Blue - *hcp*-Ru and green *fcc*-Pd.

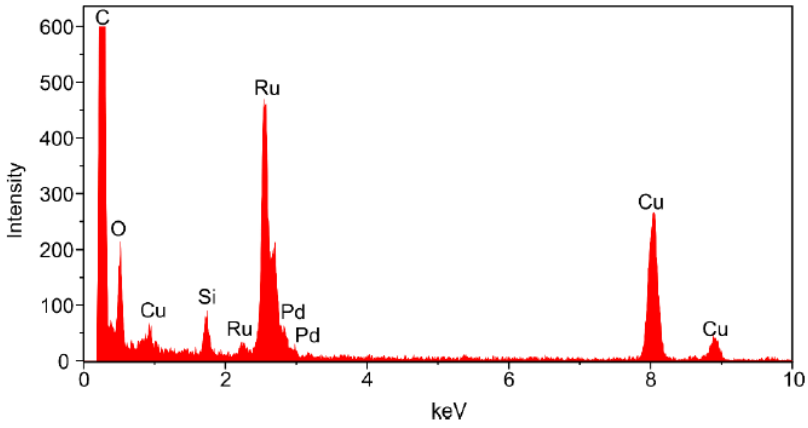

Figure S4. Energy dispersive X-ray spectroscopy of Pd-Ru 6 nm long branched nanoparticles.

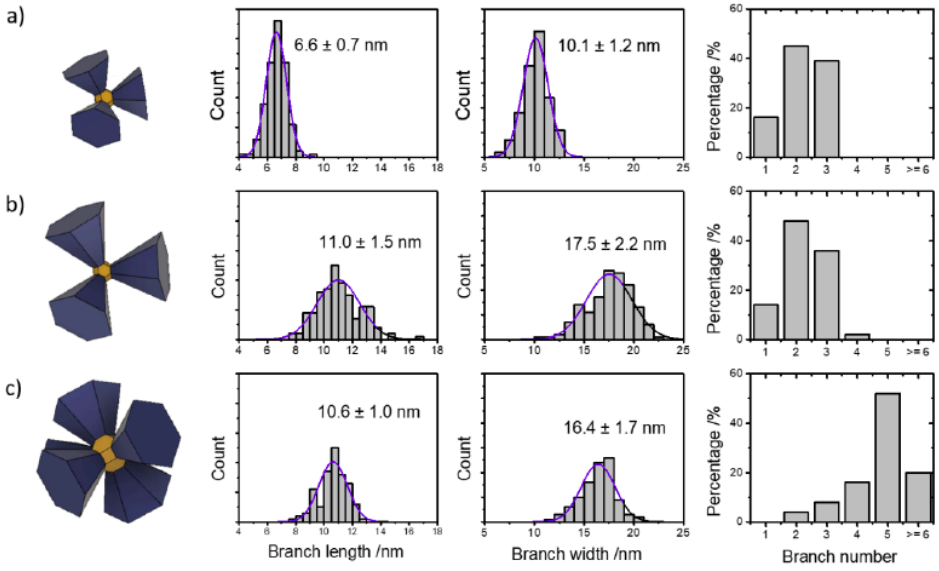

Figure S5. Histograms of branch length, branch width, and branch number of Pd-Ru nanoparticles: a) 6 nm long branches, b) 11 nm long branches and c) 11 nm long multi branches. The histograms were obtained from counting 100 nanoparticles.

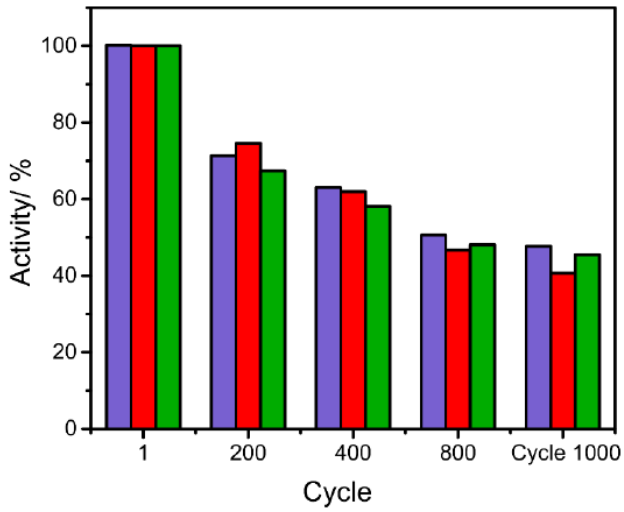

Figure S6. Changes in activity vs. cycle for the Pd-Ru branched nanoparticles. Pd-Ru branched NPs with 6 nm long branches (purple), Pd-Ru branched NPs with 11 nm long branches (red), and multibranched Pd-Ru branched NPs with 11 nm long branches (green). Scan rate = 50 mV s^{-1}; electrolyte =$HClO_4$ 0.1 M.

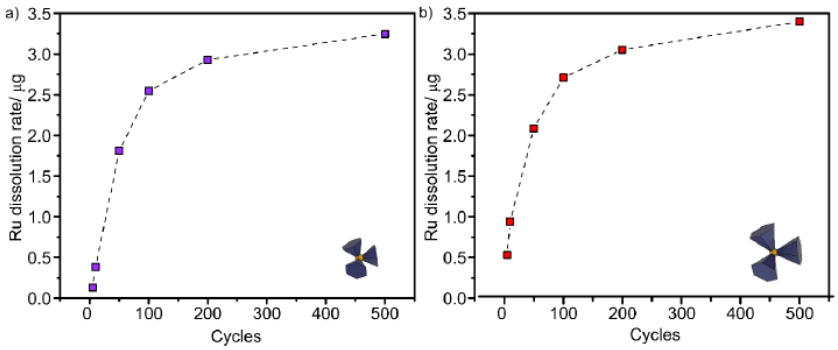

Figure S7. Ru dissolution rate vs. cycle for (a) Pd-Ru branched NPs with 6 nm long branches and (b) Pd-Ru branched NPs with 11 nm long branches. Scan rate: 50 mV s^{-1}; electrolyte: $HClO_4$ 0.1 M.

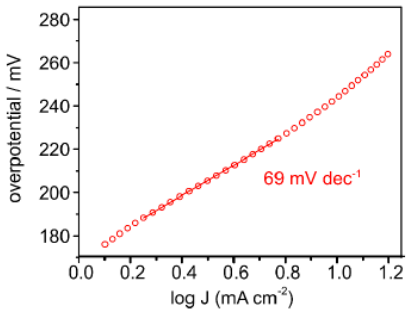

Figure S8. Tafel slope of Pd-Ru branched nanoparticles with 11 nm long branches with a scan rate of 50 mV s^{-1} in 0.1 M $HClO_4$.

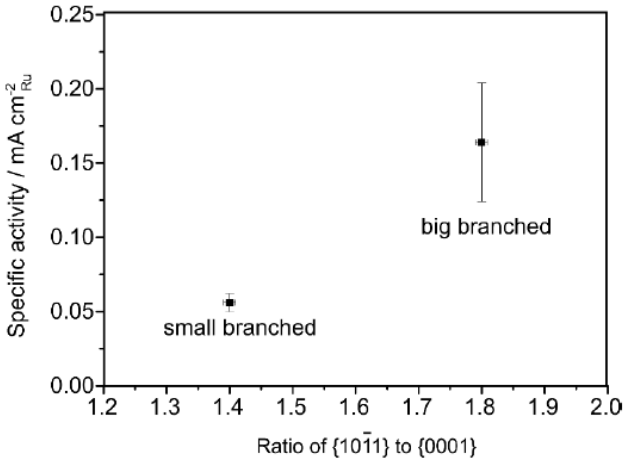

Figure S9. Specific activity versus ratio of {10-11} to {0001} facets showing that the activity increases with increasing of {10-11} facets.

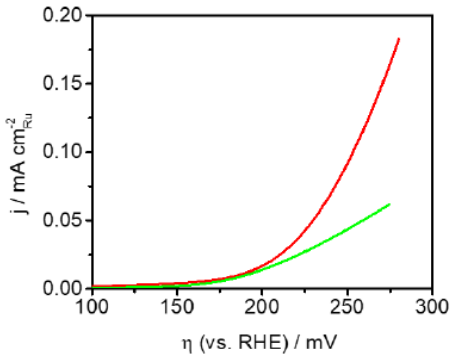

Figure S10. Oxidation scan of Pd-Ru 11 nm long branched (red) and 11 nm long multi-branched (green) nanoparticles in 0.1 M $HClO_4$ at 1600 rpm.

Calculation of facet ratio

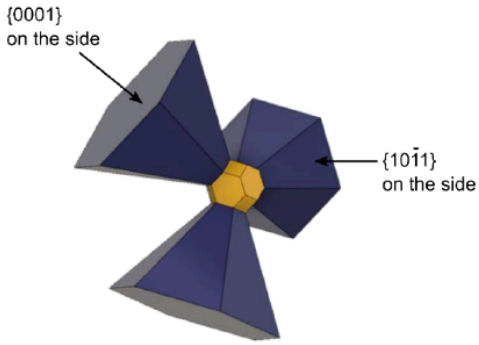

The branches terminated with 6 low-index facets {10-11} on the sides and a single {0001} on the base. Therefore, the {10-11}/{0001} ratios can be calculated by the surface area.

Table S1. Calculation of the facet ratio

Nanoparticles	Side surface area	Base surface area	{10-11}/{0001} ratios
6 nm long branches	188.4	134.7	1.4
11 nm long branches	385.8	219.9	1.8

Table S2. Comparison of experiments of activity measurements for all Pd-Ru branched nanoparticles

No	Sample	Experiment	Specific activity at η=270 mV, $mA\ cm_{Ru}^{-2}$	Average specific activity at η=270 mV, $mA\ cm_{Ru}^{-2}$
1	Pd-Ru branched nanoparticles with 6 nm long branches	1	0.065	0.056 ± 0.006
		2	0.055	
		3	0.052	
		4	0.05	
2	Pd-Ru branched nanoparticles with 11 nm long branches	1	0.22	0.164 ± 0.04
		2	0.152	
		3	0.11	
		4	0.175	
3	Multibranched Pd-Ru branched nanoparticles with 11 nm long branches	1	0.067	0.064 ± 0.004
		2	0.06	
		3	0.07	
		4	0.06	
	Activity at different rotation speed			Activity increase Change, %
	Multibranched Pd-Ru branched nanoparticles with 11 nm long branches	1600 rpm	0.069	14.0
		3200 rpm	0.08	

Table S3. Faradaic efficiency (FE) of Pd-Ru branched nanoparticles at different cycles

	Faradaic efficiency, %	
	6 nm long – Pd-Ru branched NPs	11 nm long – Pd-Ru branched NPs
Cycle 5	87.78716	81.0369
Cycle 10	86.1665	96.28298
Cycle 50	91.53491	98.63798
Cycle 100	96.56537	99.37164
Cycle 200	98.95268	99.80292
Cycle 500	99.64303	99.92314
	98.05254	98.359

[1] L. Gloag, T. M. Benedetti, S. Cheong, C. E. Marjo, J. J. Gooding, R. D. Tilley, *J. Am. Chem. Soc.* **2018**, *140*, 12760-12764.

[2] L. Graham, G. Collins, J. D. Holmes, R. D. Tilley, *Nanoscale* **2016**, *8*, 2867-2874.

[3] S. Watzele, P. Hauenstein, Y. Liang, S. Xue, J. Fichtner, B. Garlyyev, D. Scieszka, F. Claudel, F. Maillard, A. S. Bandarenka, *ACS Catal.* **2019**, 9222-9230.

[4] M. Zhao, L. Xu, M. Vara, A. O. Elnabawy, K. D. Gilroy, Z. D. Hood, S. Zhou, L. Figueroa-Cosme, M. Chi, M. Mavrikakis, Y. Xia, *ACS Catal.* **2018**, *8*, 6948-6960.

Chapter 6

Increasing the exposure of highly active sites on RuCo-Pd alloyed branched nanoparticles for improved oxygen evolution reaction electrocatalysis

6.1 Introduction

Ru nanocrystals are the most active catalysts for OER in acidic conditions owing to their variable redox states during the reaction and moderate binding energy to the intermediates *OH, *O, and *OOH [1-3]. However, Ru-based catalysts have a high dissolution rate in acid electrolytes due to the oxidation to soluble products under OER conditions. This high solution rate affects catalyst stability. Thus, designing catalytically active Ru catalysts while maintaining their stability is of great importance to their potential application.

Designing nanoparticles with well-defined shape[4-6] and highly exposed active sites[7-10] is a promising way to enhance the catalytic performance of electrocatalysts by adjusting surface energy and increasing intrinsic activity. Branched nanoparticles are fascinating catalytic materials owing to their *hcp*-crystal structure, and three-dimensional and faceted structures[4, 5, 11-14]. We have recently synthesized Ru branched nanoparticles, which resulted in the highest OER specific activity and stability reported[4, 5, 12]. This superior catalytic performance can be attributed to the highly exposed surface area in their three-dimensional architecture and the low index facets on *hcp*-branches. Here, the highly exposed surface area provides better accessibility to the catalytic reaction, and the low index facets form a more oxidation resistant surface. However, despite these advancements, the branched nanoparticles have a small number of active sites per area.

Recent studies have also demonstrated that alloyed nanoparticles consisting of a non-noble metal and a noble metal show enhanced catalytic activity for OER in acid solution [7-10]. The leaching of a non-noble metal in an alloyed nanoparticle during the catalyst activation makes defects on the catalysts

surface, increasing the exposure of highly active sites on the surface of a catalyst. For example, Strasser's group found that the electrocatalytic activity toward OER can be significantly enhanced with the incorporation of Ni into Ir nanocrystals for the formation of Ir-Ni oxide catalysts[8-10]. The nickel leaching during catalyst activation generates highly actives sites on the catalyst surface, which enhanced the catalytic activity. Jaramillo's group also confirmed that $SrIrO_3$ catalyst exhibits superior electrocatalytic activity toward oxygen evolution reaction compared with benchmark IrO_x and RuO_x catalysts[7]. The improvement was attributed to the formation of a highly active surface on the catalyst during the catalytic reaction. The Sr leaching and surface rearrangement during the electrochemical pre-treatment enabled the formation of the $IrO_x/SrIrO_3$ catalyst.

Taken together, the number of highly active sites per area on the surface of Ru branch can be increased by incorporating a non-noble metal (M) into Ru nanoparticles for the formation of Ru-M alloyed branched nanoparticles. Possible candidates for the non-noble metal (M) are Co and Ni as they are able to dissolve in acid during the catalytic activation, and form a stable *hcp*-phase, having similar lattice parameters to that of the Ru branch[8, 11, 15].

Nevertheless, making alloyed branched nanoparticles is synthetically very challenging as synthesis of branched and alloyed nanoparticles require different conditions. Minor changes in these reaction conditions could result in non-simultaneous reductions. A classic method to synthesize branched nanoparticles is a cubic-core hexagonal-branch growth approach[4, 5, 11, 15, 16]. In such a synthesis, a weak reducing reagent is used to control the atomic concentration of metallic atoms to prevent homogeneous nucleation during the synthesis. On the other hand, a strong reducing agent and high temperature are suitable for enabling the co-reduction of metallic precursors

during the synthesis of alloyed nanoparticles[17, 18]. Based on the syntheses of Co and Ru branched nanoparticles in Chapters Four and Five of this thesis[11, 12] and the literature on RuCo alloyed catalysts[19, 20], it was expected that the formation of RuCo alloyed branched nanoparticles is synthetically possible due to the following reasons: (i) the decomposition temperature discrepancy of the Co and Ru precursors (135-140°C), (ii) *hcp*-crystalline structure, and (iii) the lattice mismatch difference of less than 2.0 %.

In this work, I demonstrate that the Co leaching in RuCo-Pd alloyed branched nanoparticles during catalytic activation can improve OER activity by increasing the exposure of active sites. I firstly synthesized branched nanoparticles consisting of RuCo alloyed branches on a Pd core. A cubic-core hexagonal-branch growth approach was used to synthesize alloyed branched nanoparticles. The successful synthesis of RuCo-Pd alloyed branched nanoparticles with the Co dispersion around the core region was first achieved by choosing the proper precursors, enabling the simultaneous reduction of two metals in solution. Furthermore, the synthesis of the RuCo-Pd alloyed branched nanoparticles with the Co distribution through branches was achieved by a two-step method where Ru nucleation was followed by the subsequent reduction of Co. The catalytic performance of two types of alloyed branched nanoparticles, for instance, (i) RuCo-Pd alloyed branched nanoparticles with the Co distribution around the core and (ii) RuCo-Pd alloyed branched nanoparticles with the Co distribution through branches, were compared with Ru-Pd branched nanoparticles with long branches[12] as those in Chapter 5. The catalytic performances were improved for both RuCo-Pd alloyed branched nanoparticles compared to the Ru-Pd branched nanoparticles while maintaining their stability. These improvements could be related to the formation of highly active sites on the catalysts's surface

due to Co leaching. The importance of forming highly active sites on the branches rather than the core region has also been demonstrated, as they have better catalytic reaction accessibility. Overall, the results highlight the importance of designing alloyed branched nanoparticles that combine three-dimensional architecture and the exposure of highly active sites. This work can be further extended to other nanoparticles to enhance their catalytic activity by combining well-defined shape and composition.

6.2 Synthesis of RuCo-Pd branched nanoparticles

Several syntheses were performed to achieve the successful synthesis of RuCo-Pd alloyed branched nanoparticles consisting of RuCo branches and a Pd core. The nanoparticles were synthesized using a seed-mediated approach in an organic solution phase. A Fischer-Porter bottle, which is suitable for hydrogenation reactions, is used as the main apparatus for the reactions. The syntheses to grow RuCo branches on a Pd seed were conducted by modifying the synthetic protocol used for the synthesis of Ru branched nanoparticles in Chapter 5 of this thesis.

Firstly, Pd seeds (3.5 nm) were prepared according to a method in Chapter Five. To grow RuCo alloyed branches on a Pd core, several syntheses were conducted by varying reaction conditions, including (i) the ratio of Ru to Co, (ii) the type of Co precursors where the oxidation states of Co are different.

Synthesis of 3.5 nm Pd seeds. Pd seeds (3.5 ±0.4 nm) were synthesized by a heating-up method according to a previously published method in our group.[5, 12, 21] $Pd(acac)_2$ (0.16 mmol, Sigma-Aldrich, 99 %) was dissolved in 5 mL of oleylamine (Sigma-Aldrich, 70 %) in a 25 mL three neck flask using a magnetic stirrer. The reaction mixture was then heated to 100 °C under Ar for 30 min. After that, 0.25 mL of trioctylphosphine (TOP, Sigma-Aldrich,

97 %) was added to the reaction mixture, and then the temperature was raised to 250ºC at a rate of 2-3 ºC min^{-1} and held at this temperature for 30 min. After the reaction, the mixture was cooled down under Ar, and purification was done 4-5 times using methanol and toluene (1:1 volume ratio) at 14000 rpm. Then, Pd seeds were kept in mesitylene (Sigma-Aldrich, 98 %) for further syntheses.

6.2.1 Syntheses using cobalt (II) acetylacetonate as the Co precursor

The first set of syntheses were performed to grow RuCo alloyed branches on a Pd seed using the protocol used for the synthesis of Ru-Pd branched nanoparticles in Chapter 5 except for the use of Co precursor. The syntheses of Ru and Co branched nanoparticles in Chapters 4 and 5 involves the reduction of a metallic precursor by H_2 in the presence of a long-chain amine as the capping agent. In the syntheses, the same reaction temperatures were used to decompose the $Co(acac)_2$ and $Ru(acac)_3$ precursors. Based on the experimental conditions, $Co(acac)_2$ was chosen as the Co precursor.

The effect of Co content on the growth of RuCo-Pd nanoparticles was investigated by varying the molar ratio between $Ru(acac)_3$ and $Co(acac)_2$ precursors. The molar ratio of precursors can affect the formation of the nanoparticles by changing their nucleation rate and growth pattern [22, 23].

Thus, Experiments 1-4 were performed using $Co(acac)_2$ as the Co precursor varying the molar ratio of Ru to Co. The molar ratios of precursors were chosen in the range of Co percentage from 20 to 50 at%.

Experimental

RuCo-Pd nanoparticles. The synthesis of the RuCo-Pd branched nanoparticles was firstly carried out using an organic-phase solution seed-

mediated approach, modifying the protocol in Chapter 5 on the synthesis of Ru branched nanoparticles [5]. To grow the RuCo alloyed branches, the 3.5 nm Pd seed solution (0.0021 mmol) was added to a solution containing ruthenium (III) acetylacetonate (0.025-0.05 mmol, Sigma-Aldrich, 97 %) and cobalt (II) acetylacetonate (0.01-0.025 mmol, Sigma-Aldrich, 97 %) as precursors and 5 eq. mol of oleylamine (82 μL) as a surfactant dissolved in 1 mL of mesitylene. Syntheses were carried out changing the amount of Ru and Co precursors. The reaction mixture was then kept at 3 bar hydrogen at 140ºC for 24 hours. After the reaction, H_2 was released, and purification was performed by centrifuge washing three times using ethanol and toluene solution (1:1 volume ratio) at 4000 rpm for further characterizations.

Table 6.1. The experimental conditions a applied for the synthesis of RuCo-Pd nanoparticles using $Co(acac)_2$ as the Co precursor varying the ratio of $Ru(acac)_3$ to $Co(acac)_2$.

Exp. #	$Ru(acac)_3$, mmol	$Co(acac)_2$, mmol	$[Ru^{3+}]:[Co^{2+}]$	Pd seeds, mmol	Time, h
1	0.04	0.01	4.0	0.0021	24
2	0.035	0.015	2.3	0.0021	24
3	0.03	0.02	1.5	0.0021	24
4	0.025	0.025	1.0	0.0021	24

Results

RuCo-Pd nanoparticles were prepared using $Co(acac)_2$ and $Ru(acac)_3$ as the Ru and Co precursors varying the Ru^{3+} to Co^{2+} molar ratio using an organic solution phase seed-mediated approach in a Fischer-Porter bottle. Figure 6.1 shows the representative TEM images and corresponding particle size

distributions of as-synthesized RuCo-Pd nanoparticles using different molar ratios of Ru^{3+} to Co^{2+}. When the Ru to Co molar ratio was between 4 : 1 and 1.5 : 1, two noticeable features are observed from the TEM images of the particles obtained from Exp 1-3 (Figure 6.1 a-c).

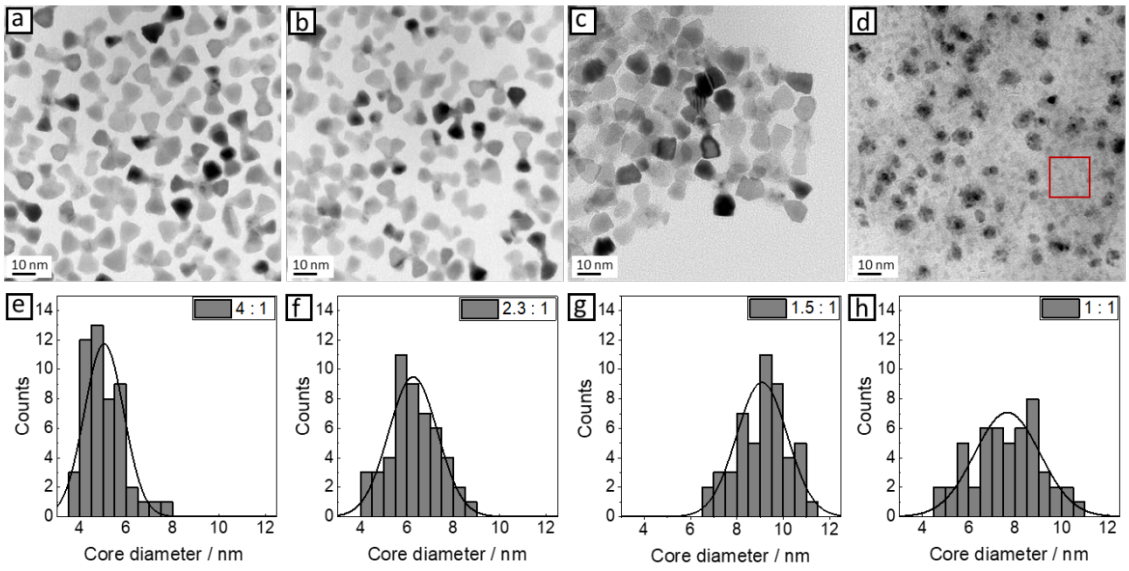

Figure 6.1. (a-d) TEM images of RuCo-*Pd nanoparticles* synthesized using $Co(acac)_2$ and (e-h) corresponding size distributions. Scale bar, 10 nm.

Firstly, the core diameter increases with the increase of Co content. Secondly, in terms of the branch shape, the shape of the branches of RuCo-Pd nanoparticles is similar to the branches of Ru-Pd nanoparticles. As the Co content was further increased to 1:1, core-shell nanoparticles (bigger) and smaller Co nanoparticles highlighted in a red box (with lighter contrast) were obtained (Figure 6.1 d, h). The atomic percentage of the elements (Ru, Co, and Pd) in the resultant nanoparticles was examined by EDX spectra. The results showed that the elemental composition in the final products (Exp.1 - 4) is similar to the value in the initial reaction mixture, indicating that the metallic precursors were completely decomposed in the syntheses.

The elemental distribution and crystalline structure of the sample (Exp.3) were further examined by HAADF-STEM and STEM-EDX mapping.

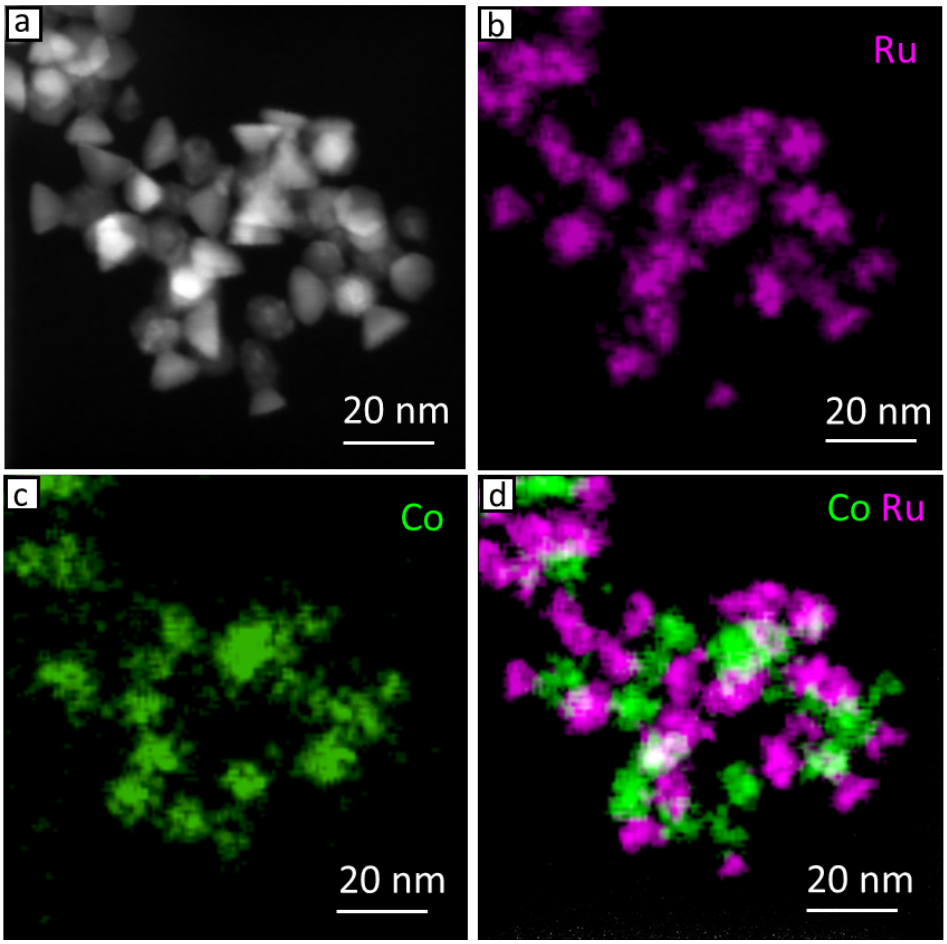

Figure 6.2. (a) HAADF-STEM image and (b-d) corresponding STEM-EDX elemental maps of Ru (pink), Co (green) of RuCo-Pd branched nanoparticles (Exp.3) and overlay of elemental maps in (b) and (c). EDX maps were taken by Hsiang-sheng Chen.

A typical HAADF-STEM image and STEM-EDX elemental map (Figure 6.2a-d) of the RuCo-Pd branched nanoparticles (Exp.3) reveal that the nanoparticle consists of a Co core and Ru branches.

The crystalline structure of the nanoparticles was further examined by SAED and XRD analysis. The SAED patterns of the samples (Figure 6.3 a-d) show that the RuCo-Pd branched nanoparticles synthesized at a lower amount of Co are polycrystalline structure in nature, and the RuCo-Pd nanoparticles

synthesized at a higher amount of Co (Exp.4) are both amorphous and crystalline structures in nature.

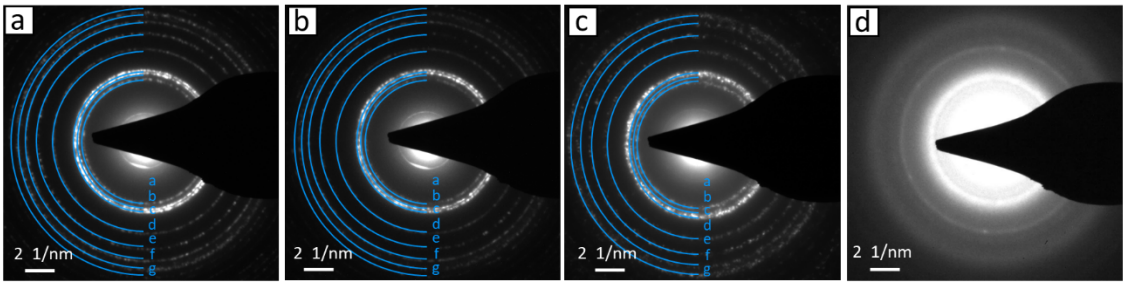

e

Reference Ru	ED spots	Experimental Ru:Co 4:1	Ru:Co 2.3 :1	Ru:Co 1.5 : 1	Ru
d spacing, Å		d spacing, Å	d spacing, Å	d spacing, Å	hkl
2.34	a	2.32	2.32	2.39	$10\bar{1}0$
2.14	b	2.14	2.14	2.22	0002
2.05	c	2.05	2.04	2.09	$10\bar{1}1$
1.58	d	1.57	1.57	1.61	$10\bar{1}2$
1.35	e	1.34	1.33	1.37	$11\bar{2}0$
1.22	f	1.21	1.21	1.24	$10\bar{1}3$
1.17	g	1.13	1.13	1.15	$11\bar{2}2$

f

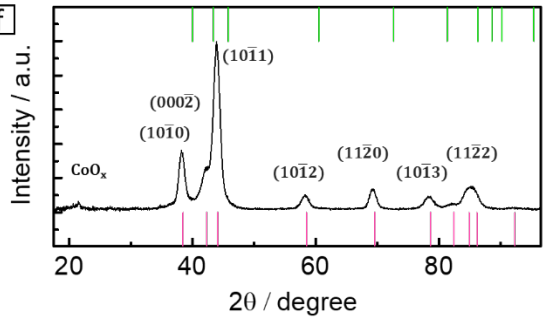

Figure 6.3. (a-d) SAED patterns of RuCo-Pd nanoparticles synthesized using $Co(acac)_2$, (e) SAED indexed to hcp-Ru, and (f) XRD pattern of corresponding SAED pattern. Pink lines: JCPDC no. 06-0663 (hcp-Ru). Green lines: JCPDC no. 65-8976 (hcp-CoRu).

The pattern rings can be indexed to *hcp*-Ru, and shifts at a higher Co content can be associated with the presence of Co. The XRD profile of the RuCo-Pd (Exp.3) branched nanoparticle exhibits a peak pattern consistent with an hcp crystal symmetry, which is in good agreement with its corresponding SAED pattern. A diffraction peak of CoO_x is also observed at approximately 21.4° 2θ, indicating the formation of an oxide layer on the Co shell.

Discussion

The resultant RuCo-Pd branched nanoparticles each consists of a Co shell that surrounds the entire Pd core and Ru branches, indicating that the reduction of Co is followed by the reduction of Ru. Reducing metallic precursors simultaneously in solution is essential for the formation of alloy

nanocrystals[18, 22, 23]. Choosing the proper metallic precursors with reduction kinetics in solution is one of the main factors to adjust the reduction rate of the metallic ions in solution[18, 22, 23]. For example, Xia and co-workers reported a systematic study of the reaction kinetics on the synthesis of Pd-Pt bimetallic nanocrystals[24]. They found that a significant difference in the reduction kinetics of the metallic ions enables the formation of Pd-Pt core-shell nanocrystals. In contrast, similar reduction kinetics promotes the formation of Pd-Pt alloy nanocrystals. Overall, the non-simultaneous reduction of $Co(acac)_2$ and $Ru(acac)_3$ precursors can be related to the difference in their reduction potentials (-0.277 V for Co^{2+}/Co, +0.599V for Ru^{3+}/Ru) and oxidation states (Co^{2+}, Ru^{3+}).

In addition to the nature of precursors, the molar ratio of precursors is crucial for forming alloy nanocrystals by adjusting the reaction kinetics of the metallic ions[23]. Increasing the content of $Co(acac)_2$ in a synthesis increased the core diameter of the particles (Exp.1-3), indicating that there is no change for the growth pattern with the increase of Co content. As the content of $Co(acac)_2$ is further increased, smaller nanoparticles (Co) were obtained, indicating the homogeneous nucleation of Co atoms. At the beginning of the reaction, the burst nucleation of Co occurred and the newly formed Co atoms either deposited on Pd seeds or homogeneously nucleated. Then, Ru is subsequently reduced and deposited on the Co shell over Pd seeds. The results showed that a higher amount of Co does not reduce the discrepancy in the reduction rates of metallic ions in the solution.

Based on the results obtained from Experiment 1-4, I expect that using metallic precursors with the same oxidation states and suitable redox potentials would reduce the difference in the reduction rates of the metallic ions in the solution.

6.2.2 Syntheses using cobalt (III) acetylacetonate as the precursor

The results from the previous syntheses (Exp.1-4) in which $Co(acac)_2$ was used as the Co precursor revealed that Ru and Co do not reduce simultaneously, resulting in Co core formation over Pd seeds and Ru branches. The difference in reduction rate can be related to the oxidation states of the metals in their precursors. Using metallic precursors having the same oxidation states reduces the difference in their reduction rate, increasing the possibility of alloyed nanocrystals formation. Then, to make RuCo-Pd nanoparticles consisting of RuCo alloyed branches and a Pd core, the experiments were further carried out, replacing the $Co(acac)_2$ with $Co(acac)_3$ where the oxidation state of Co is similar to Ru in $Ru(acac)_3$.

Experimental

In these experiments, $Co(acac)_2$ was replaced with $Co(acac)_3$. Experiment 5 used $Ru(acac)_3$ (0.04 mmol), $Co(acac)_3$ (0.01 mmol), 82 μL of oleylamine, 0.0021 mol of Pd seeds suspended in 1 mL of mesitylene in a 4 mL vial (or a small vial). Then, the reaction mixture was transferred to a FP-bottle and was kept at 140°C for 24 h under 3 bar of hydrogen gas. After the reaction, H_2 was released, and purification was done three times using ethanol and toluene solution (1:1 volume ratio) at 4000 rpm for further characterizations.

Table 6-2. The experimental conditions applied to synthesize RuCo-Pd nanoparticles using $Co(acac)_3$ as the Co precursor.

Exp. #	$Ru(acac)_3$, mmol	$Co(acac)_3$, mmol	$[Ru^{3+}]$: $[Co^{3+}]$	Pd seeds, mmol	Time, h
5	0.04	0.01	4.0	0.0021	24

Results

Figure 6.4 a-b show a TEM image of the nanoparticles synthesized using $Co(acac)_3$ as the Co precursor and corresponding size distributions.

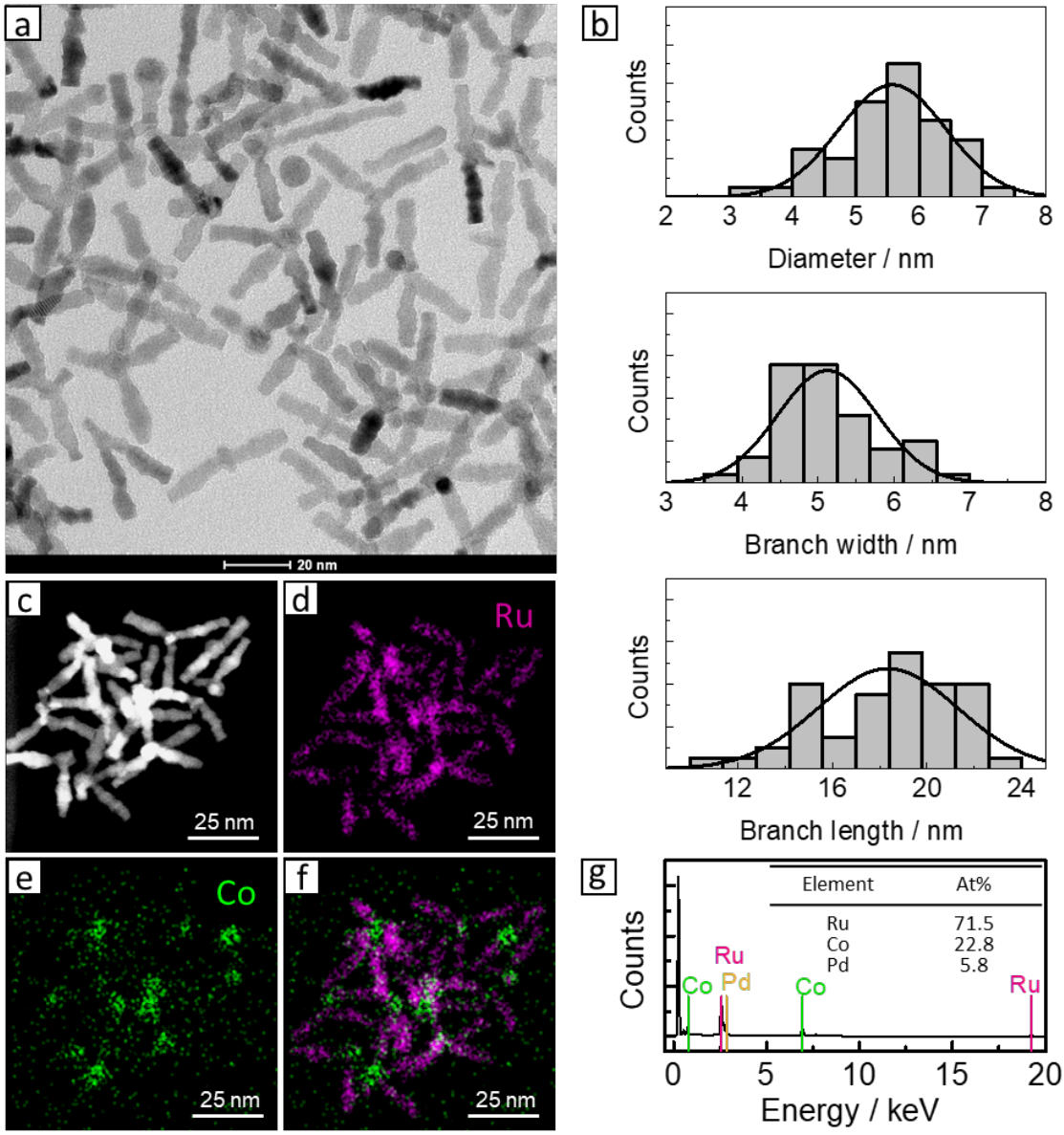

Figure 6.4. (a) TEM image of the particles synthesized using $Co(acac)_3$ as the Co precursor and (b) corresponding size distributions of core diameter (5.1 ± 0.7 nm), branch width (5.6 ± 0.8 nm), and branch length (18.4 ± 3.0 nm), (c-f) HAADF-STEM image, STEM-EDX elemental maps of Co (pink), Ru (green) of RuCo-Pd branched nanoparticles, and overlay of elemental maps, (g) EDX spectrum of the sample and elemental composition in at%. HAADF-STEM image and EDX maps were taken by Hsiang-sheng Chen.

The particles typically have 2-4 branches, with branch width measured at 5.1 ± 0.7 nm and length measured at 18.4 ± 3.0 nm. The branches typically grow from a 5.6 ± 0.8 nm core, which itself is of core-shell structure.

The HAADF-STEM image and STEM-EDX elemental maps in Figures 6.4 c-f show that Co mostly dispersed into the core and Ru dispersed into both core and branches, indicating that the core and branches around the core area are an alloyed structure of CoRu. The elemental composition of the sample was quantified by EDX spectra (in Figure 6.3g), which indicates that the branched nanoparticles consist of Ru (71.5 at%), Co (22.8 at%), and Pd (5.8 at%).

The SAED and XRD patterns in Figure 6.5 reveal the crystalline structure of the RuCo-Pd branched nanoparticles. The rings of SAED pattern in Figure 6.5a can be indexed to *hcp*-Ru and *hcp*-RuCo alloy nanocrystals (Table 6.3).

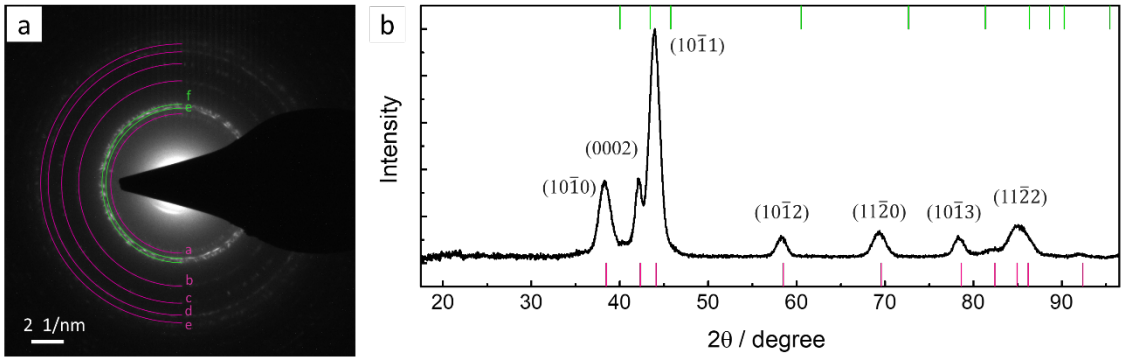

Figure 6.5. (a) SAED and (b) XRD pattern of the sample. The characteristic peaks of hcp-Ru and hcp-RuCo are marked by pink and blue, respectively. Pink lines: JCPDS no. 04-4608 (hcp-Ru). Green lines: JCPDS no. 65-8976 (hcp-CoRu).

Table 6.3. Indexing the diffraction rings of the sample.

Reference		**Experimental**				**Ru/RuCo**	**hkl**
Ru	**CoRu alloy**	**XRD**		**SAED pattern**			
d spacing	d spacing	d spacing	Theta	d spacing	rings	-	-
2.34	2.25	2.36	38.21	2.38	a	Ru	$10\bar{1}0$
-	-	-	-	2.22	f	RuCo	$10\bar{1}0$
2.14	2.08	2.15	42.11	2.11	g	RuCo	0002
2.05	1.98	2.06	43.94	-	-	Ru	$10\bar{1}1$
1.58	1.53	1.58	58.30	1.61	b	Ru	$10\bar{1}2$
1.35	1.30	1.36	69.31	1.40	c	Ru	$11\bar{2}0$
1.22	1.18	1.22	78.19	1.25	d	Ru	$10\bar{1}3$
1.17	1.13	1.18	81.77	1.17	e	Ru	$20\bar{2}0$
1.14	1.10	1.15	84.64	-	-	Ru	$11\bar{2}2$
1.13	1.09	-	-	-	-	-	-
1.07	1.04	1.07	91.86	-	-	Ru	0004

The XRD for the sample shows peaks at 38.2°, 42.1° 43.9°, 58.3°, 69.3°, 78.2°, 81.7°, and 84.6° in the range from 17.5 to 96.5°. These peaks are consistent with the $10\bar{1}0$, 0002, $10\bar{1}1$, $10\bar{1}2$, $11\bar{2}0$, $10\bar{1}3$, and $11\bar{2}2$ reflections of *hcp*-Ru (P63/mmc, a = 0.27 nm) and *hcp*-RuCo alloys (P63/mmc, a = 0.27 nm), which are consistent with the diffraction rings.

Discussion

In experiment 5, $Co(acac)_2$ was replaced with $Co(acac)_3$ to reduce the difference in Ru and Co's reduction rates and grow alloyed RuCo branches on a Pd core.

Significant changes were observed in the shape and surface of the nanoparticles' branches compared to the branch morphology of the Ru nanoparticles previously synthesized [5, 12] and nanoparticles synthesized using $Co(acac)_2$. The branch morphology of the particles synthesized using $Co(acac)_3$ is cylindrical and the branch width is consistent from the beginning to the end of the branch. In addition, the branch surface is rough and jagged, indicating the faceted structure. The changes in the branch shape and surface of the sample can be attributed to the presence of Co in the branches. In Chapters 4 and 5, it was observed that the Co branch is thinner towards the tip while the Ru branch is wider. Thus, the difference in the shape of the alloyed branch compared to the Ru and Co branches can be explained by the different growth mechanisms of Ru and Co atoms. The alloyed structure was confirmed by morphological and structural analysis, as mentioned in the results section. However, the distribution of Co is mostly around the core region, which can be attributed to the lower amount of Co precursor.

Overall, using metallic precursors where the oxidation states and reduction potentials of the metals are closer enable simultaneous reduction of the metallic ions to metallic atoms, increasing the possibility of forming an alloyed structure. Additionally, the molar ratio of precursors is a key factor that can affect the distribution of metals in the alloy.

6.2.3 Two-step synthesis using $Co(acac)_3$ as the precursor.

The results from experiment 5 showed that RuCo-Pd branched nanoparticles consisting of alloyed RuCo branches and a Pd core can be achieved using the Co and Ru precursors in which Co and Ru have the same oxidation states in the precursor. Although alloyed RuCo branches on a Pd core were obtained from experiment 5, Co mostly distributed around the core region or beginning of branches. The dispersion of Co around the core area can be related to the molar ratio of precursors, the initial molar ratio of Ru : Co was 4 : 1. The goal of the following experiments is to increase the Co dispersion through the branches. To disperse Co through the branches, two-step reaction was performed. In the reaction, the Co precursor was added to the reaction mixture just after the decomposition of Ru precursor and formation of Ru branches.

Experimental

Experiment 6 used $Ru(acac)_3$ (0.04 mmol), 82 μL of oleylamine, 0.0021 mol of Pd seeds suspended in 1 mL of mesitylene in a 4 mL vial. Then, the reaction mixture was transferred to a FP-bottle and was kept at 140°C for 4 h under 3 bar of hydrogen gas. After 4 h, $Co(acac)_3$ (0.01 mmol) was added to the reaction mixture and kept at 140°C for 20 h under 3 bar of hydrogen gas. After the reaction, H_2 was released, and purification was done three times using ethanol and toluene solution (1:1 volume ratio) at 4000 rpm for further characterizations.

Table 6.4. The experimental conditions applied for the synthesis of RuCo-Pd nanoparticles using $Co(acac)_3$ as the Co precursor.

Exp. #	Step. #	$Ru(acac)_3$, mmol	$Co(acac)_3$, mmol	$[Ru^{3+}]$: $[Co^{3+}]$	Pd seeds, mmol	Time, h
6	1	0.04	-	-	0.0021	4
	2	-	0.01	4.0	-	20

Results

A TEM image and typical EDX spectra of the nanoparticles synthesized using a two-step reaction in figure 6.6 a-b show that the particles typically have 2-4 branches and consist of Ru (71.7 at%), Co (21.5 at%), and Pd (6.8 at%). As shown in Figure 6.6 c-f, the HAADF-STEM image and STEM-EDX elemental maps of the nanoparticles reveal that Co and Ru dispersed through the branches.

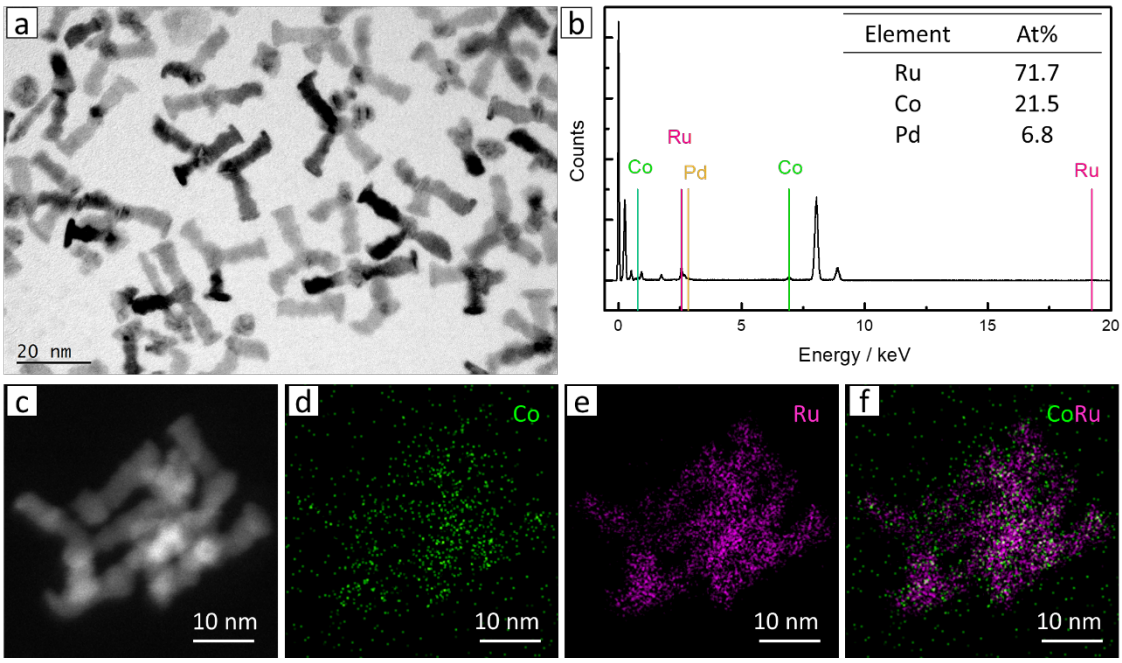

Figure 6.6. (a) TEM image of the particles synthesized using $Co(acac)_3$ as the Co precursor and (b) EDS spectrum of the sample and elemental composition in at%, (c-f) HAADF-STEM image, STEM-EDX elemental maps of Co (green), Ru (pink) of RuCo-Pd branched nanoparticles, and overlay of elemental maps. HAADF-STEM image and EDX-maps were taken by Zeno Rizqi Ramadhan.

The rings of SAED pattern in Figure 6.7a can be indexed to *hcp*-Ru and *hcp*-RuCo alloy nanocrystals (Table 6.5). An XRD pattern of the sample in Figure 6.7b shows peaks at 37.9°, 40.8°, 42.1°, 43.9°, 58.3°, 69.1°, 78.4°, 84.6°, and 92.1°.

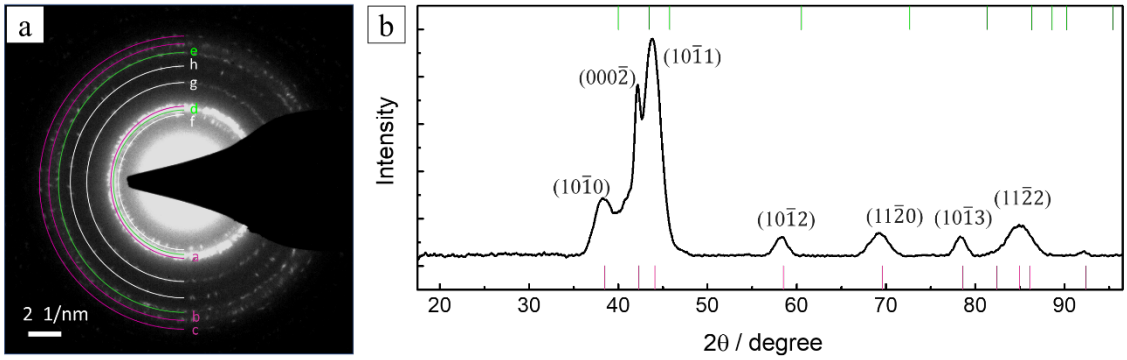

Figure 6.7. (a) SAED and (b) XRD pattern of the sample. The characteristic peaks of hcp-Ru and hcp-RuCo are marked by pink and blue, respectively. Pink lines: JCPDS no. 04-4608 (hcp-Ru). Green lines: JCPDS no. 65-8976 (hcp-CoRu).

Table 6.5. Indexing the diffraction rings of the sample.

Reference		**Experimental**				**Ru/ RuCo**	**hkl /hkil**
Ru	**CoRu alloy**	**XRD**		**SAED pattern**			
d spacing	d spacing	d spacing	Theta	d spacing	ring	-	-
-	-	-	-	2.48	f	-	-
2.34	2.25	2.38	37.87	-	-	Ru	$10\bar{1}0$
-	-	2.25	40.80	2.27	d	CoRu	$10\bar{1}0$
2.14	2.08	2.14	42.11	2.16	a	Ru	0002
2.05	1.98	2.06	2.06	1.66	g	Ru	$10\bar{1}1$
1.58	1.53	1.58	58.31	1.42	h	Ru	$10\bar{1}2$
1.35	1.30	1.36	69.12	-	-	Ru	$11\bar{2}0$
-	-	-	-	1.30	e	CoRu	$11\bar{2}0$
1.22	1.18	1.22	78.40	1.21	b	Ru	$10\bar{1}3$
1.14	1.10	1.15	84.64	1.14	c	Ru	$11\bar{2}2$
1.07	1.04	1.07	92.06	-	-	Ru	0004

These peaks are consistent with the $10\bar{1}0$, 0002, $10\bar{1}1$, $10\bar{1}2$, $11\bar{2}0$, $10\bar{1}3$, $11\bar{2}2$, and 0004 reflections of hcp-Ru (P63/mmc, a = 0.27 nm) and hcp-RuCo alloys (P63/mmc, a = 0.27 nm), which are basically consistent with the diffraction rings. The slight shift in the peaks' position and the presence of the diffraction rings of CoRu alloy can be associated with the CoRu alloyed crystal.

HRTEM of an individual RuCo-Pd branched nanoparticle is shown in Figure 6.8a. HRTEM image reveals that highly crystalline *hcp*-RuCo branches grow

along the c-axis of an *hcp* structure, as indicated by the FFT pattern (Figure 6.8b). The Pd core adopts an *fcc* structure, as indicated by the FFT pattern (Figure 6.8c).

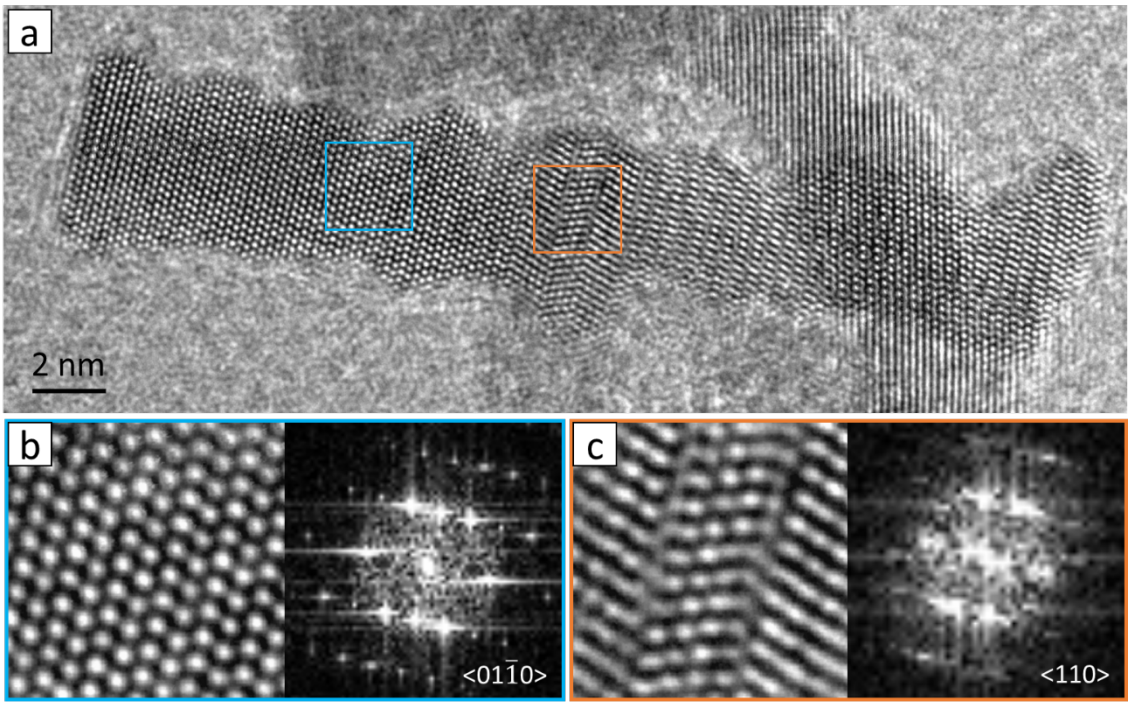

Figure 6.8. (a) HRTEM image of a branched nanoparticle. (b) HRTEM image of part of the branch in (a) indicated by the blue box and corresponding FFT indexed to a hexagonal <01$\bar{1}$0> zone axis. (c) HRTEM image of the core region in (a) indicated by the orange box and corresponding FFT indexed to a cubic <110> zone axis. HRTEM image was taken by Zeno Rizqi Ramadhan.

The growth of *hcp* branches on an *fcc* core is consistent with the other branched morphologies observed from a cubic-core hexagonal-branch growth approach[4, 5, 11, 12].

Figures 6.9 a-b and 6.10 a-b depict TEM images of the nanoparticles after the reaction of 4 h and 24 h, and corresponding size distributions to further understand the continuous growth of Ru and Co adatoms on the intermediate after 4 h.

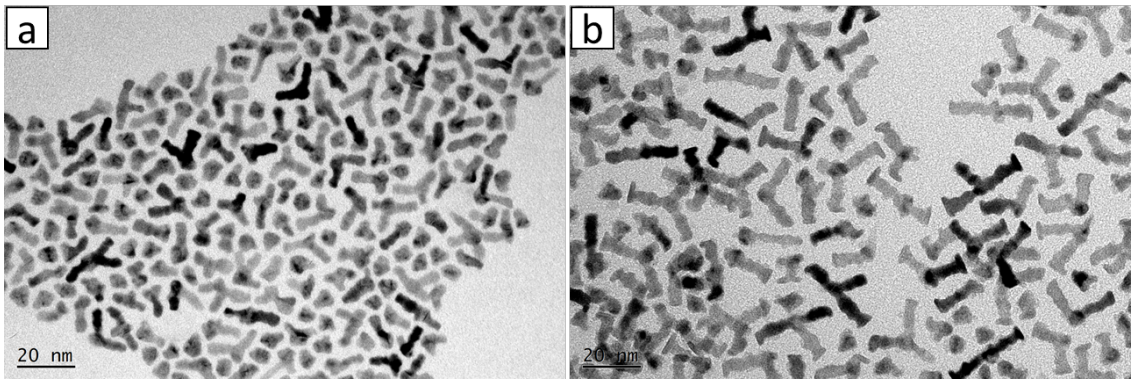

Figure 6.9. TEM images of the particles (a) after 4 h reaction and (b) after 24 h reaction.

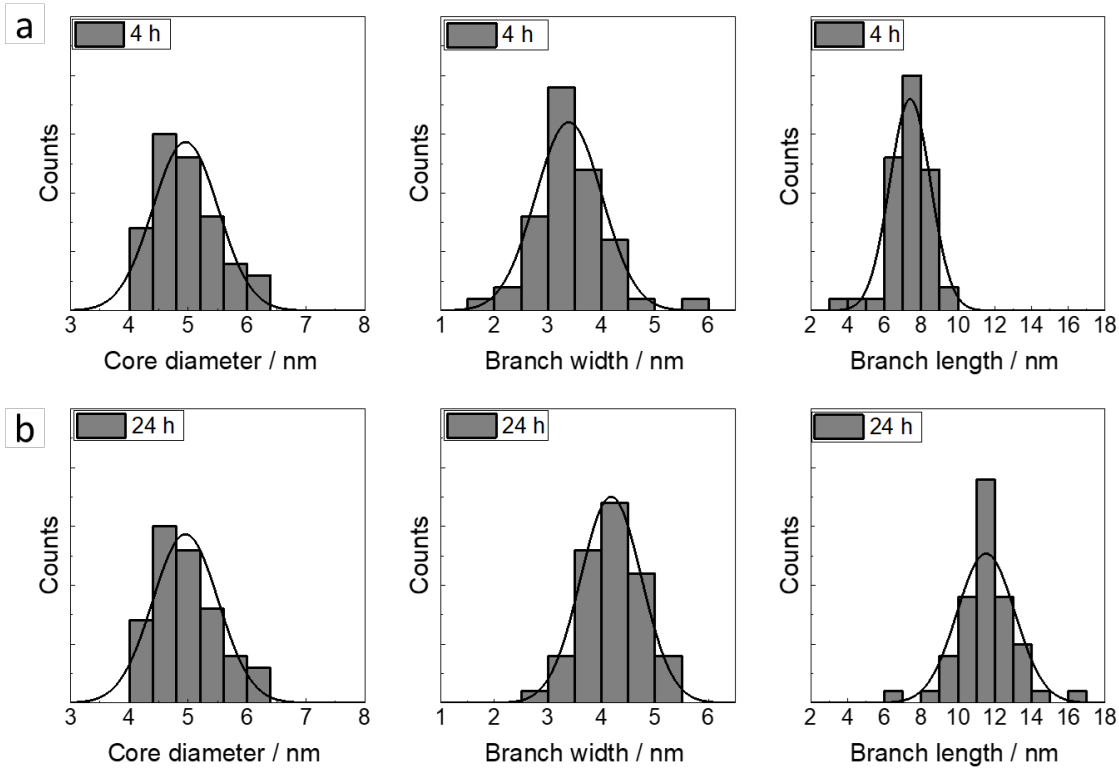

Figure 6.10. Size distributions of core diameter, branch width, and branch length of the particles (a) after 4 h reaction and (b) after 24 h reaction.

The results show a significant change in the branch length of the final product (24 h), indicating that adatoms of Ru and Co grew along the c-axis extending the branch length.

Discussion

The two-step synthesis resulted in RuCo-Pd branched nanoparticles with Co distribution through the branches. After a 4 h of reaction, spherical nanoparticles and nanoparticles with short branches were obtained. In this stage, the Ru precursor is reduced to Ru nucleus, following the subsequent growth of Ru atoms on the surface of Pd seeds. In the next step, Co precursor was added to a reaction mixture containing Ru atoms, Ru precursor, and nanoparticles (4 h). After 24 h of reaction, a significant increase was observed in the size of branched nanoparticles in terms of branch length. Increased branch length for the nanoparticles (24 h) indicates the growth of Ru and Co adatoms from the branches along the c-axis.

6.3 Electrocatalytic properties of RuCo-Pd branched nanoparticles

Experimental

Catalysts ink preparation. For the electrochemical studies, firstly, the nanoparticles (about 0.2 mg) were dispersed in toluene (100 μL) to make an ink. The working electrode was prepared by drop-casting the electrocatalysts ink (15 μL) and nafion (0.05 % v/v, 5 μL) onto the glassy carbon surface (0.196 cm^2 area).

Electrochemical measurements. The measurements were performed using an Autolab potentiostat running with Nova 2 software. The working electrode was kept rotating at 1600 rpm during the experiments, and a 0.1 mol L^{-1} $HClO_4$ solution was used as the electrolyte. A Pt-mesh and Ag|AgCl|3 mol L^{-1} NaCl were used as the counter electrode and reference electrode, respectively. All potentials were converted to the reversible hydrogen electrode (RHE) by measuring the potential between the reference

electrode and a freshly prepared standard reference electrode and considering the electrolyte pH. The equation for converting the potential to RHE is shown below:

$$E_{RHE} = E_{Ag/AgCl} + 0.059pH + E^0_{Ag/AgCl} \quad (6.1)$$

where E_{RHE} denotes the potential (vs.RHE), $E_{Ag/AgCl}$, $E^0_{Ag/AgCl}$ is standart potential, and $E_{Ag/AgCl}$ is the working potential (vs.RHE).

The OER activity was then measured by cyclic voltammetry between 1.0 V vs. and 1.55 V (vs. RHE) at 50 mV s^{-1}.

Electrochemical surface area. The electrochemical surface area (ECSA) of the catalysts was determined by cyclic voltammetry at different scan rates from the slope of the capacitive current versus scan rate plots to obtain the capacitance. Cyclic voltammetry measurements in the capacitive potential range were performed at 5, 10, 25, 50, 100, and 200 mV s^{-1}. The obtained capacitance was then used to calculate the ECSA using the specific capacitance of 66 μF cm^{-2}. [25, 26]

The stability was evaluated from the difference between the maximum catalytic activity and the activity after 200 and 400 OER cycles. Cyclic voltammetry measurements for the stability tests were performed under the same conditions used for the activity tests.

Results

Electrochemical measurements were conducted on RuCo-Pd 1 (Co is highly distributed at the beginning of branches), RuCo-Pd 2 (Co is well distributed through branches) catalysts to elucidate the effect of the Co distribution in alloyed branches on OER performance. Ru-Pd branched nanoparticles with

long branches, the same particles as those in Chapter 5, were used for comparison. Cyclic voltammograms of the three catalysts were firstly measured using a three-electrode system in 0.1 $HClO_4$ at 50 mV s^{-1}. Similar amounts of nanoparticles were deposited on all electrodes.

The anodic scans of the 5th cycle of the voltammograms, in which the current normalized with the geometric surface area (0.196 cm^2), are shown in Figure 6.11. The anodic scans of the 5th cycles of the voltammograms are shown in Figure 6.11.

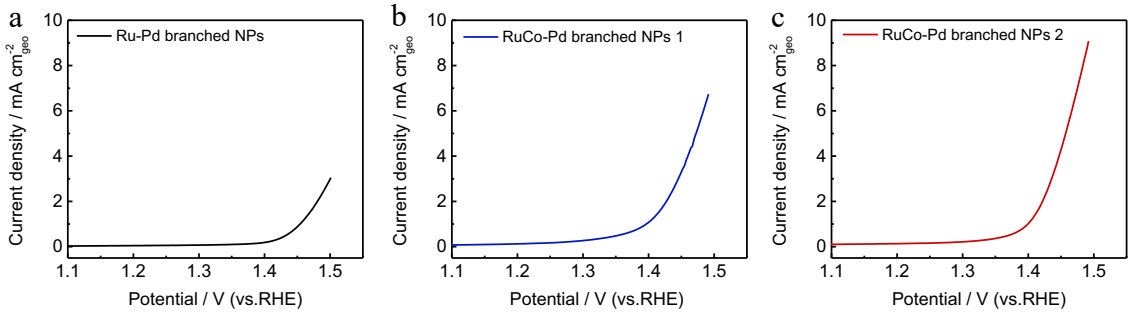

Figure 6.11. Anodic scan of the 5th cyclic voltammetry to show the geometric activities (a) Ru-Pd branched nanoparticles, (b) RuCo-Pd branched nanoparticles 1, and (c) RuCo-Pd branched nanoparticles 2.

The RuCo-Pd branched nanoparticles-2 exhibit higher geometric activity than RuCo-Pd branched nanoparticles-1 and Ru-Pd branched nanoparticles. As shown in the anodic scan of the cyclic voltammograms in Figure 6.11, the RuCo-Pd 2 catalyst reaches a geometric current density of 8.0 mA cm^{-2} at 1.48 V (250 mV overpotential with respect to the thermodynamic OER potential), while at this same potential, the RuCo-Pd 1 and Ru-Pd catalysts reach much smaller geometric current densities of 6.15 mA cm^{-2} and 2.18 mA cm^{-2}, respectively. The geometric activities achieved with the RuCo-Pd 2 and RuCo-Pd 1 catalysts are approximately 6.8 and 5.2 times higher than that of Ru-Pd catalyst, respectively. As the same amount Ru was deposited

on all electrodes, the difference in activity can be due to the exposure of new sites, which are highly active, because of the dissolution of Co.

A specific activity represents the catalysts' intrinsic activities, giving more accurate results for determining the catalytic activity[27]. Evaluating the catalytic activity based on a specific activity can provide more precise information on the formation of more active new sites when Co is removed. The specific activity of a catalyst is determined by normalizing the current density to the surface area of the catalyst. As shown in Figure 6.12, the surface areas of the three catalysts, obtained from the capacitance current at different scan rates of the particles, are 3.07 cm^2_{Ru}, 4.38 cm^2_{Ru}, and 2.75 cm^2_{Ru} for Ru-Pd, RuCo-Pd-1, and RuCo-Pd-2 catalysts, respectively.

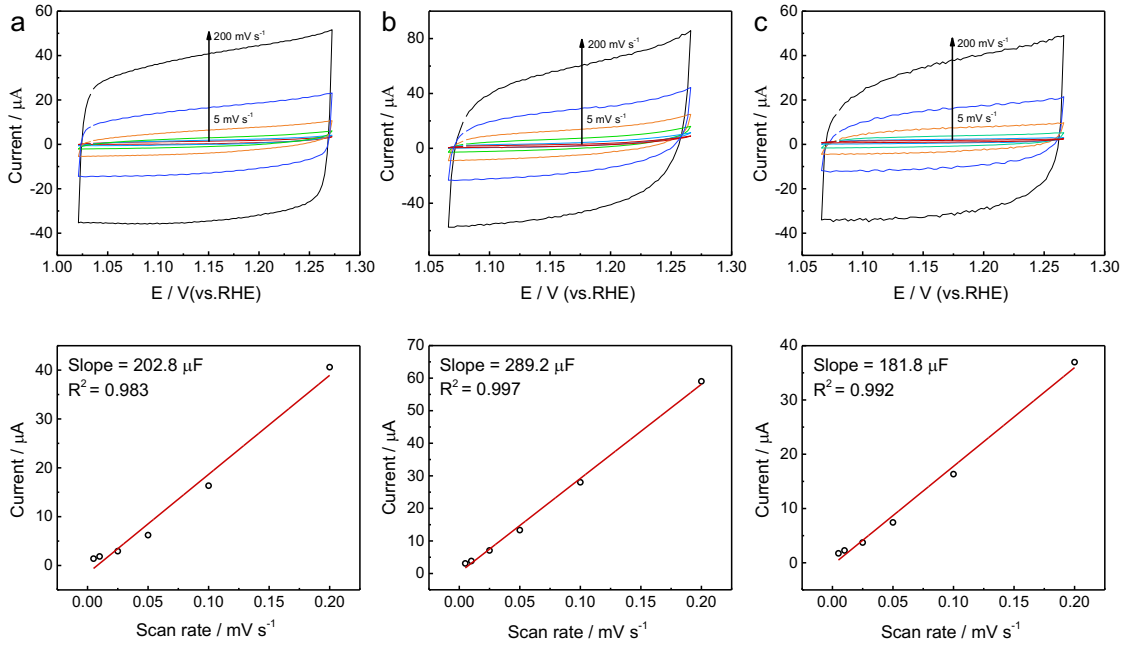

Figure 6.12. CVs measured for (a) Ru-Pd branched nanoparticles, (b) RuCo-Pd branched nanoparticles 1, and (c) RuCo-Pd branched nanoparticles 2 in 0.1 M $HClO_4$. Corresponding plots of the current at 1.15 V vs. the scan rate.

Figure 6.13 depicts the anodic scan of the cyclic voltammograms, in which current density is normalized by the surface area of catalysts.

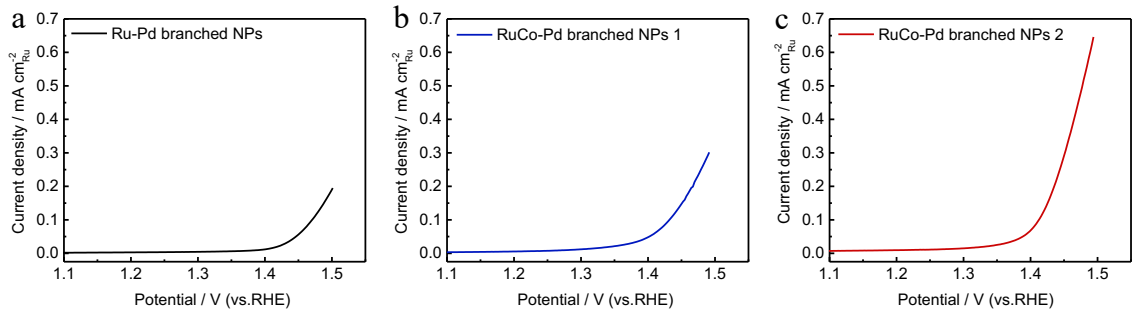

Figure 6.13. Anodic scan of the 5th cycle of cyclic voltammetry to show the specific activities (a) Ru-Pd branched nanoparticles, (b) RuCo-Pd branched nanoparticles-1, and (c) RuCo-Pd branched nanoparticles-2.

The RuCo-Pd-2 catalyst with the Co distribution through branches exhibits a specific activity of 0.6 mA cm^{-2} at 1.49 V (260 mV overpotential with respect to the thermodynamic OER potential), which is about 2.0-fold relative to RuCo-Pd-1 catalyst with the Co distribution around the core, and about 4.0-fold relative to Ru-Pd catalyst at the same potential, respectively. To conclude, the new sites being exposed are more active, and the higher geometric activity is then a combination of higher surface area and higher intrinsic activity of the new sites exposed.

As shown in the plot of changes in activity vs. cycle in Figure 6.14a, The RuCo-Pd-1 catalysts retain 70 % of initial activity after 200 OER cycles, 50 % after 400 cycles, and the RuCo-Pd-2 catalysts retain 64 % of initial activity after 200 OER cycles, 46.8 % after 400 cycles, respectively. Both particles are slightly less stable than the Ru-Pd branched nanoparticles (74.6 % activity after 200 cycles, 62.0 % after 400 cycles). Although RuCo-Pd-1 and RuCo-Pd-2 catalysts are less stable than that of Ru-Pd catalyst, these catalysts still show higher specific activities after 200 and 400 cycles than the Ru-Co catalysts (Figure 6.14b).

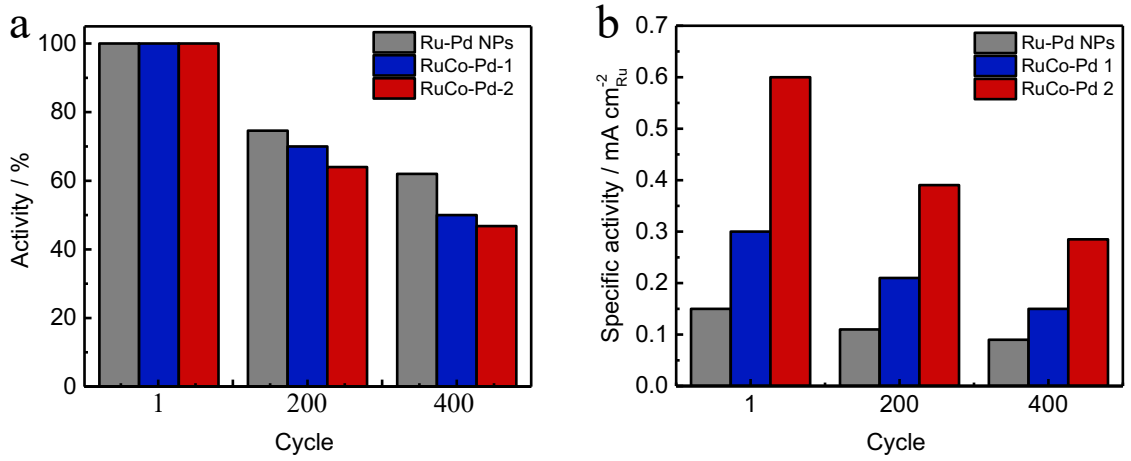

Figure 6.14. Catalytic stability tests for the catalysts. (a) changes in activity vs. cycle and (b) changes in specific activity vs. cycle. Ru-Pd branched nanoparticle (grey), RuCo-Pd branched nanoparticles 1 (blue), and (c) RuCo-Pd branched nanoparticles 2 (red).

Discussion

Electrochemical activity and stability were investigated for the two types of RuCo-Pd branched nanoparticles, for instance, (i) RuCo-Pd alloyed branched nanoparticles with the Co distribution around the core region/beginning of branches and (ii) RuCo-Pd alloyed branched nanoparticles with the Co distribution through branches. Ru-Pd branched nanoparticles with long branches, the same particles as those in Chapter 5, were used as a benchmark catalyst. The hypothesis for the enhanced specific activities of the RuCo-Pd-1 and RuCo-Pd-2 catalysts is that Co leaching during OER increases the number of defects and active sites. Previous studies have reported that the leaching of non-noble metal in alloyed nanoparticles during electrocatalytic reaction makes surface defects and increases the number of active sites on the surface, enhancing catalytic activity [7-9]. To elucidate the origin of the higher activity of the alloyed RuCo-Pd branched nanoparticles compared to the Ru-Pd branched nanoparticles, the leaching of cobalt in RuCo-Pd catalysts, and the ECSAs of the catalysts

were examined by measuring CVs in an alkaline solution before and after running CVs in acid solution. Both Co and Ru catalysts are stable in the potentials range (0.9 -1.25 V vs.RHE) of the ECSAs measurements in alkaline solution according to their Pourbaix diagrams whereas only Co is soluble in the potential range in acid solution. The results are shown in Figure 6.15 and Figure 6.16.

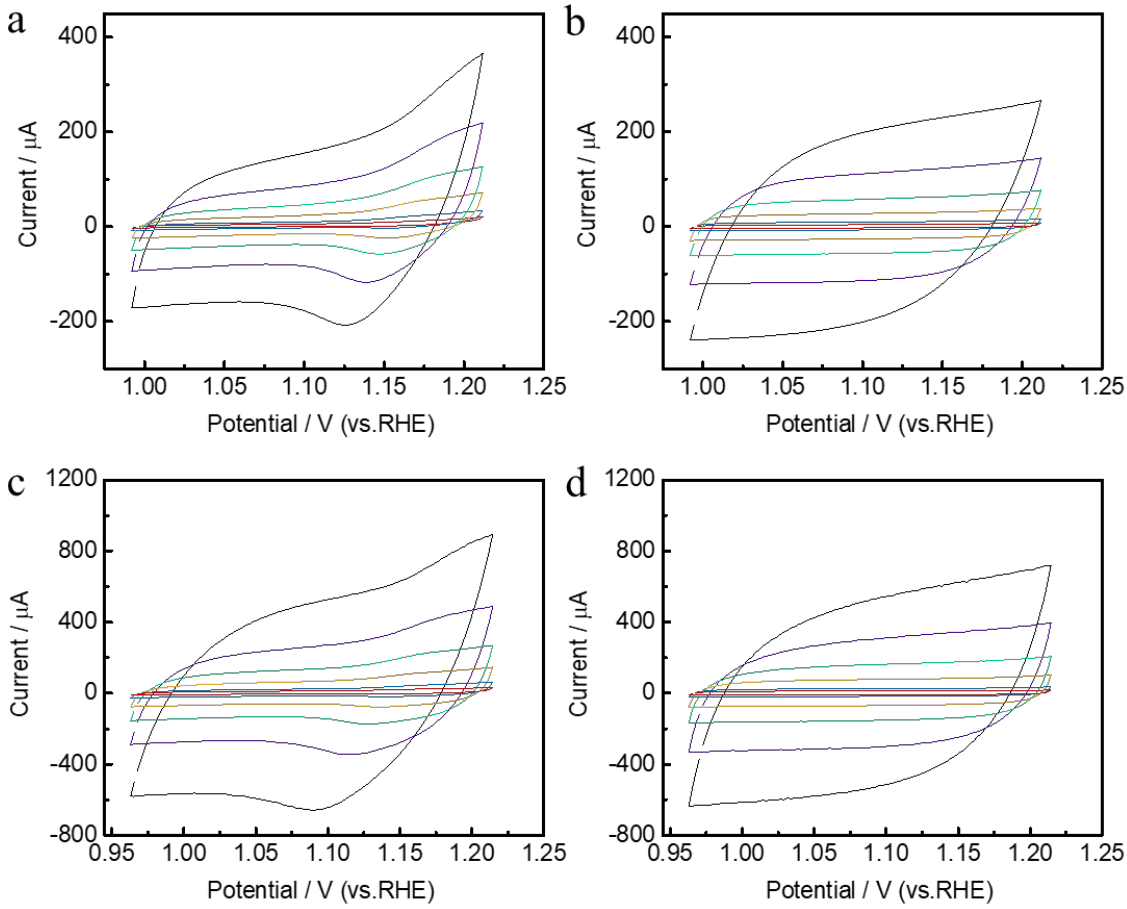

Figure 6.15. CVs measured in alkaline alkaline solution (0.1 M NaOH) before and after running CVs in acid solution (0.1 M $HClO_4$) for (a-b) RuCo-Pd branched nanoparticles-1 and (c-d) RuCo-Pd branched nanoparticles-2.

A peak at ~1.1 V for the CVs of RuCo-Pd-1 and RuCo-Pd-2 before running CVs in acid solution can be assigned to the oxidation of cobalt, indicating the presence of Co in the catalysts. The peak was not present after running

CVs in acid solution, indicating the Co leaching in the catalysts. The ECSAs of the catalysts were further determined to investigate the change in actives sites.

As shown in Figure 6.16, the ECSAs increased for both RuCo-Pd-1 and RuCo-Pd-2 catalysts after Co leaching.

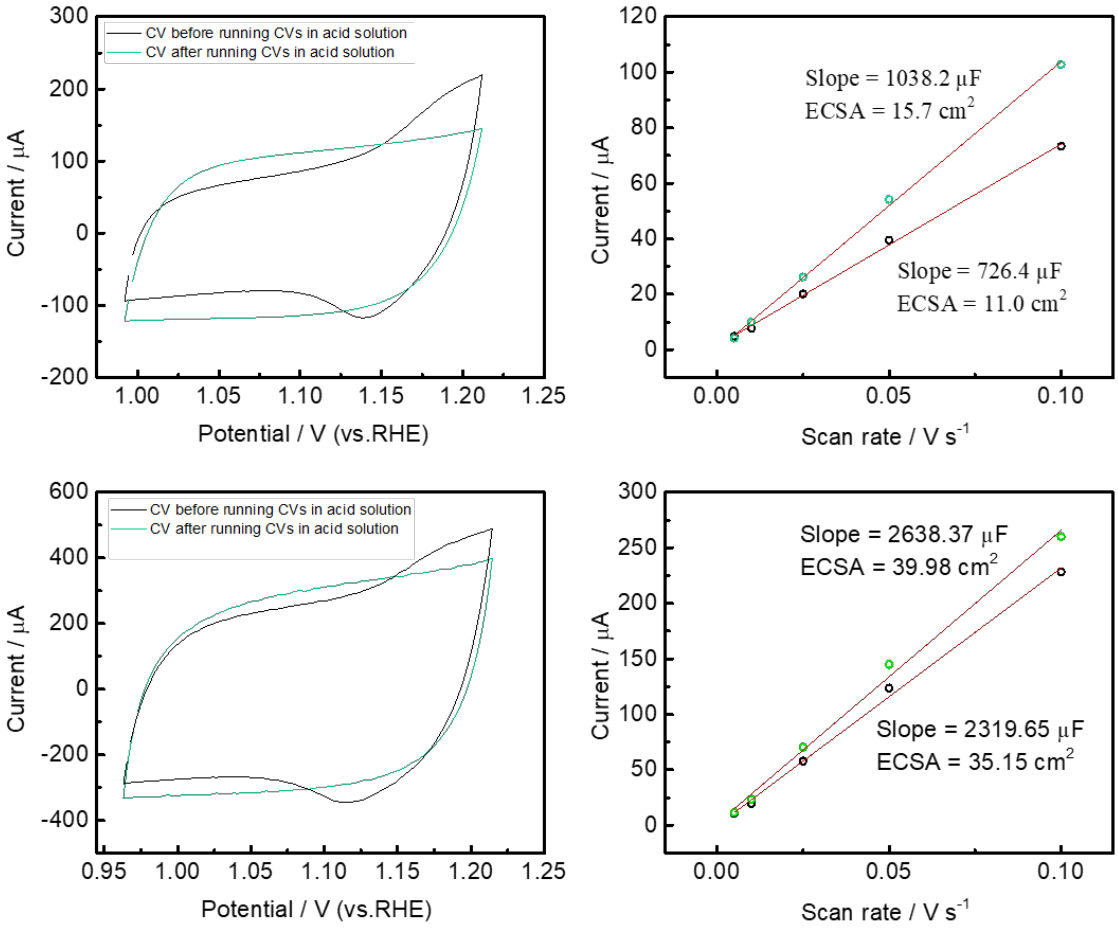

Figure 6.16. Comparison of surface areas before and after Co leaching. CVs measured in alkaline solution (0.1 M NaOH) at 100 mV s^{-1} before and after running CVs in acid solution (0.1 M $HClO_4$), and the plots of current at 1.05 V vs. the scan rate for (a-b) RuCo-Pd branched nanoparticles-1 and (c-d) RuCo-Pd branched nanoparticles-2.

These changes illustrate that the Co leaching in the catalysts exposes more active sites on the catalyst's surface. Overall, enhanced OER activities of the catalysts are related to the exposure of highly active sites with the removal

of cobalt. The RuCo-Pd-2 catalyst exhibited 2x fold higher OER activity than the RuCo-Pd 1 catalyst and 4x higher activity than the Ru-Pd catalysts, which can be related to the Co distribution on the more accessible sites of the branches. Notably, although the higher exposition of more active facets, the alloyed RuCo-Pd catalysts maintained their stability, exhibiting higher activity than the benchmark catalysts after 400 cycles. Therefore, alloyed branches show enhanced OER activity because the leaching of the non-noble metal in the branches makes defects during OER, generating highly active sites and increasing the intrinsic activity.

The Co content in the RuCo-Pd-2 catalyst was further quantified by EDS spectrum before and after catalyst activation to confirm the Co leaching from the particles (Figure 6.17 a-b).

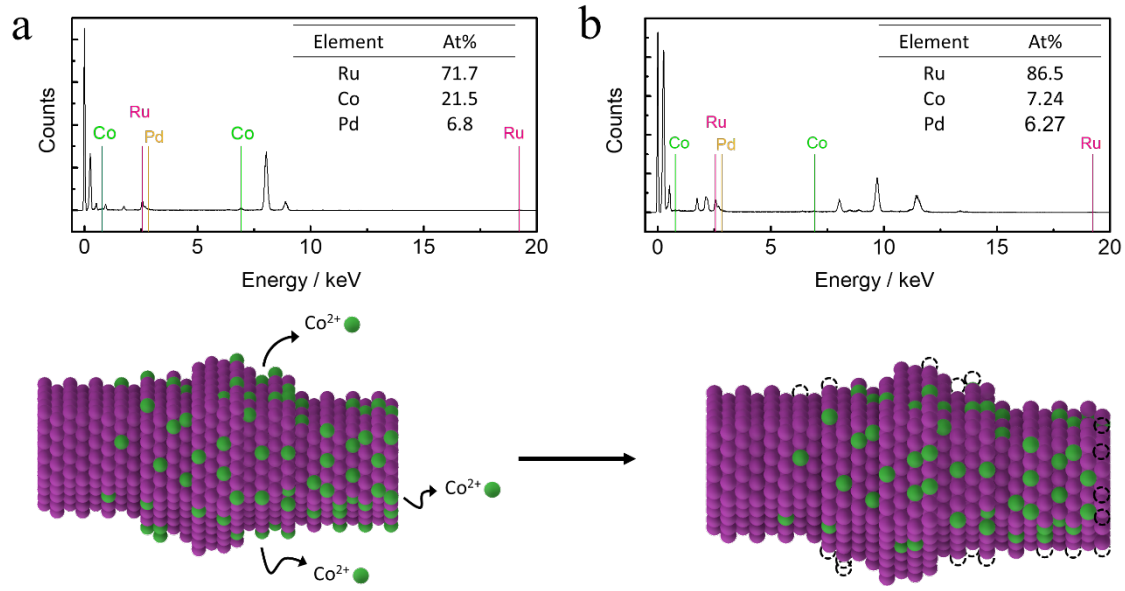

Figure 6.17. Comparison of the Co content in the RuCo-Pd-2 catalyst before and after electrochemical activation. (a-b) Eds spectras of the catalysts before and after running CVs in acid solution (0.1 M $HClO_4$), and (c) the schematic illustration of the formation of active surface after running CVs in acid solution. Black circles indicated that the vacancies of Co after Co leaching from the catalyst's surface.

The results showed that the Co content in the RuCo-Pd-2 catalyst decreased from 21.5 to 7.24 at%. The change in the Co content indicates that the Co atoms were leached out during the catalytic activation from the catalysts forming highly active surfaces on the branches. The Co is not totally removed. The Co in inner layers might be related to maintaining the stability by adjusting the binding energy of the catalyst surface with oxygen intermediates.

6.4 Conclusions

A cubic-core hexagonal-branch growth approach was used to grow RuCo alloyed branches on a Pd seed.

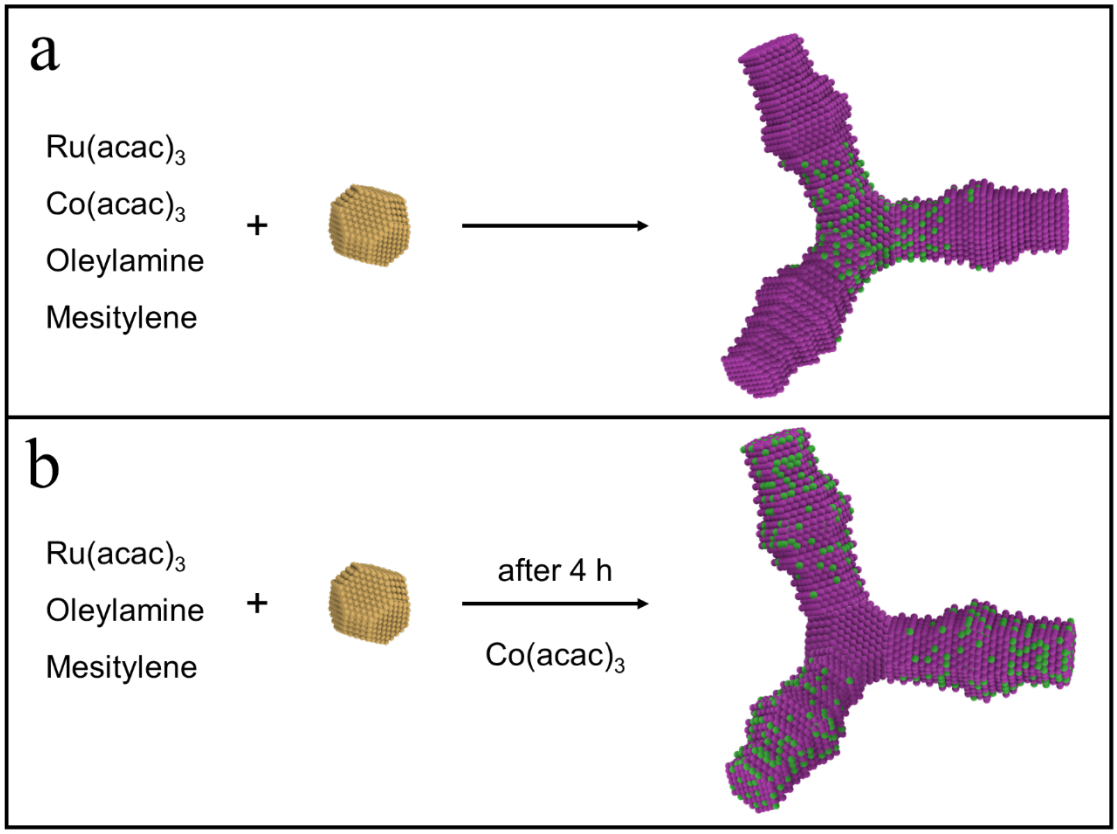

Figure 6.18. Schematic illustration of the synthesis for (a) RuCo-Pd alloyed branched nanoparticles with the Co distribution around the beginning of branches and (b) RuCo-Pd alloyed branched nanoparticles with the Co distribution though branches.

Two types RuCo-Pd alloyed branched nanoparticles, including (i) Co distribution around the beginning of branches and (ii) Co distribution through branches, were successfully synthesized by optimizing the reaction conditions, including the molar ratio of Ru to Co, the oxidation states of Co in the precursor, and the nucleation steps of the metals.

The RuCo-Pd alloyed branched nanoparticles-2 with the Co distribution through branches presented much higher OER activity than RuCo-Pd alloyed branched nanoparticles-1 with the Co distribution around the beginning of the branches and Ru-Pd branched nanoparticles.

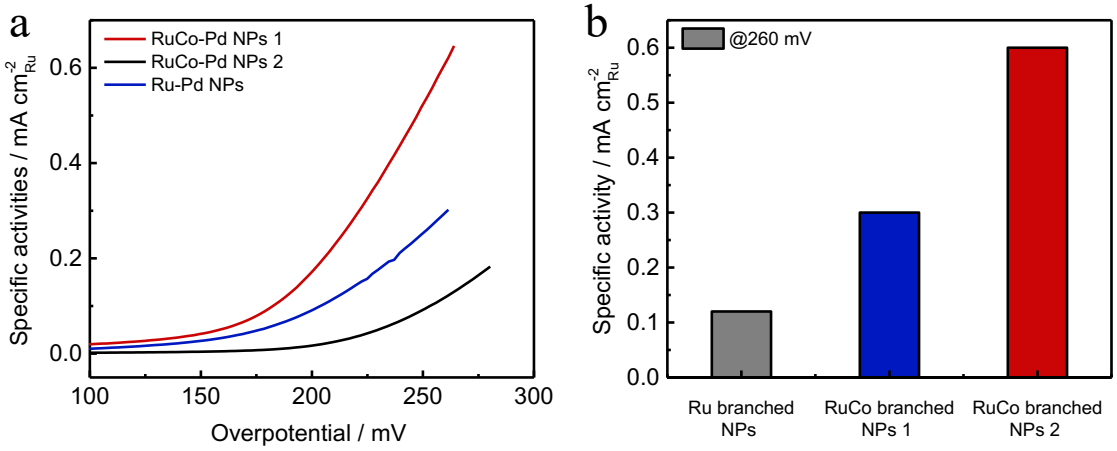

Figure 6.19. Catalytic activities of the catalysts. (a) anodic scan of the 5th cycle of cyclic voltammetry to show the OER activities and (b) Comparison of the specific activities of RuCo-Pd-1, RuCo-Pd-2, and Ru-Pd catalysts obtained at an overpotential of 260 mV.

The higher activity of alloyed nanoparticles is related to the leaching of Co during the OER that makes defects at the surface of the nanoparticles, enabling the high exposure of active sites. The higher activity of alloyed nanoparticles with the Co distribution through branches can be ascribed to their better accessibility of exposed active sites and higher intrinsic activity of the newly exposed sites.

These results show that for nanoparticles, engineering alloyed nanoparticles with well-defined shape to enable the exposure of active sites is crucial for highly active electrocatalysis and this concept can be extended to a wide range of electrocatalytic reactions.

References

1. Man, I. C.; Su, H. Y.; Calle-Vallejo, F.; Hansen, H. A.; Martínez, J. I.; Inoglu, N. G.; Kitchin, J.; Jaramillo, T. F.; Nørskov, J. K.; Rossmeisl, J., Universality in Oxygen Evolution Electrocatalysis on Oxide Surfaces. *ChemCatChem* **2011,** *3* (7), 1159-1165.

2. Yao, Y.; Hu, S.; Chen, W.; Huang, Z.-Q.; Wei, W.; Yao, T.; Liu, R.; Zang, K.; Wang, X.; Wu, G.; Yuan, W.; Yuan, T.; Zhu, B.; Liu, W.; Li, Z.; He, D.; Xue, Z.; Wang, Y.; Zheng, X.; Dong, J.; Chang, C.-R.; Chen, Y.; Hong, X.; Luo, J.; Wei, S.; Li, W.-X.; Strasser, P.; Wu, Y.; Li, Y., Engineering the electronic structure of single atom Ru sites via compressive strain boosts acidic water oxidation electrocatalysis. *Nature Catalysis* **2019,** *2* (4), 304-313.

3. Yu, J.; He, Q.; Yang, G.; Zhou, W.; Shao, Z.; Ni, M., Recent Advances and Prospective in Ruthenium-Based Materials for Electrochemical Water Splitting. *ACS Catalysis* **2019,** *9* (11), 9973-10011.

4. Gloag, L.; Benedetti, T. M.; Cheong, S.; Li, Y.; Chan, X. H.; Lacroix, L. M.; Chang, S. L. Y.; Arenal, R.; Florea, I.; Barron, H.; Barnard, A. S.; Henning, A. M.; Zhao, C.; Schuhmann, W.; Gooding, J. J.; Tilley, R. D., Three-Dimensional Branched and Faceted Gold-Ruthenium Nanoparticles: Using Nanostructure to Improve Stability in Oxygen Evolution Electrocatalysis. *Angew Chem Int Ed Engl* **2018,** *57* (32), 10241-10245.

5. Gloag, L.; Benedetti, T. M.; Cheong, S.; Marjo, C. E.; Gooding, J. J.; Tilley, R. D., Cubic-Core Hexagonal-Branch Mechanism To Synthesize Bimetallic Branched and Faceted Pd-Ru Nanoparticles for Oxygen Evolution Reaction Electrocatalysis. *J Am Chem Soc* **2018,** *140* (40), 12760-12764.

6. Strasser, P.; Gliech, M.; Kuehl, S.; Moeller, T., Electrochemical processes on solid shaped nanoparticles with defined facets. *Chem Soc Rev* **2018,** *47* (3), 715-735.

7. Seitz, L. C.; Dickens, C. F.; Nishio, K.; Hikita, Y.; Montoya, J.; Doyle, A.; Kirk, C.; Vojvodic, A.; Hwang, H. Y.; Norskov, J. K.; Jaramillo, T. F., A highly active and stable IrOx/SrIrO3 catalyst for the oxygen evolution reaction. *Science* **2016,** *353* (6303), 1011-1014.

8. Nong, H. N.; Gan, L.; Willinger, E.; Teschner, D.; Strasser, P., IrOx core-shell nanocatalysts for cost- and energy-efficient electrochemical water splitting. *Chem. Sci.* **2014,** *5* (8), 2955-2963.

9. Reier, T.; Pawolek, Z.; Cherevko, S.; Bruns, M.; Jones, T.; Teschner, D.; Selve, S.; Bergmann, A.; Nong, H. N.; Schlogl, R.; Mayrhofer, K. J.; Strasser, P., Molecular Insight in Structure and Activity of Highly Efficient, Low-Ir Ir-Ni Oxide Catalysts for Electrochemical Water Splitting (OER). *J Am Chem Soc* **2015,** *137* (40), 13031-40.

10. Nong, H. N.; Reier, T.; Oh, H.-S.; Gliech, M.; Paciok, P.; Vu, T. H. T.; Teschner, D.; Heggen, M.; Petkov, V.; Schlögl, R.; Jones, T.; Strasser, P., A unique oxygen ligand environment facilitates water oxidation in hole-doped IrNiOx core–shell electrocatalysts. *Nature Catalysis* **2018,** *1* (11), 841-851.

11. Myekhlai, M.; Benedetti, T. M.; Gloag, L.; Gonçales, V. R.; Cheong, S.; Chen, H. S.; Gooding, J. J.; Tilley, R. D., Increasing the Formation of Active Sites on Highly Crystalline Co Branched Nanoparticles for Improved Oxygen Evolution Reaction Electrocatalysis. *ChemCatChem* **2020,** *12* (11), 3126-3131.

12. Myekhlai, M.; Benedetti, T. M.; Gloag, L.; Poerwoprajitno, A. R.; Cheong, S.; Schuhmann, W.; Gooding, J. J.; Tilley, R. D., Controlling the

Number of Branches and Surface Facets of Pd-Core Ru-Branched Nanoparticles to Make Highly Active Oxygen Evolution Reaction Electrocatalysts. *Chemistry* **2020,** *26* (67), 15501-15504.

13. Cao, Z.; Chen, Q.; Zhang, J.; Li, H.; Jiang, Y.; Shen, S.; Fu, G.; Lu, B. A.; Xie, Z.; Zheng, L., Platinum-nickel alloy excavated nano-multipods with hexagonal close-packed structure and superior activity towards hydrogen evolution reaction. *Nat Commun* **2017,** *8*, 15131.

14. Zhang, Z.; Liu, G.; Cui, X.; Chen, B.; Zhu, Y.; Gong, Y.; Saleem, F.; Xi, S.; Du, Y.; Borgna, A.; Lai, Z.; Zhang, Q.; Li, B.; Zong, Y.; Han, Y.; Gu, L.; Zhang, H., Crystal Phase and Architecture Engineering of Lotus-Thalamus-Shaped Pt-Ni Anisotropic Superstructures for Highly Efficient Electrochemical Hydrogen Evolution. *Advanced Materials* **2018,** *30* (30), 1801741.

15. LaGrow, A. P.; Cheong, S.; Watt, J.; Ingham, B.; Toney, M. F.; Jefferson, D. A.; Tilley, R. D., Can polymorphism be used to form branched metal nanostructures? *Adv Mater* **2013,** *25* (11), 1552-6.

16. Manna, L.; Milliron, D. J.; Meisel, A.; Scher, E. C.; Alivisatos, A. P., Controlled growth of tetrapod-branched inorganic nanocrystals. *Nat Mater* **2003,** *2* (6), 382-5.

17. Gilroy, K. D.; Yang, X.; Xie, S.; Zhao, M.; Qin, D.; Xia, Y., Shape-Controlled Synthesis of Colloidal Metal Nanocrystals by Replicating the Surface Atomic Structure on the Seed. *Adv Mater* **2018,** *30* (25), e1706312.

18. Zhou, M.; Li, C.; Fang, J., Noble-Metal Based Random Alloy and Intermetallic Nanocrystals: Syntheses and Applications. *Chem Rev* **2021,** *121* (2), 736-795.

19. Feng, T.; Yu, G.; Tao, S.; Zhu, S.; Ku, R.; Zhang, R.; Zeng, Q.; Yang, M.; Chen, Y.; Chen, W.; Chen, W.; Yang, B., A highly efficient

overall water splitting ruthenium-cobalt alloy electrocatalyst across a wide pH range via electronic coupling with carbon dots. *Journal of Materials Chemistry A* **2020,** *8* (19), 9638-9645.

20. Zhang, F.; Zhu, Y.; Chen, Y.; Lu, Y.; Lin, Q.; Zhang, L.; Tao, S.; Zhang, X.; Wang, H., RuCo alloy bimodal nanoparticles embedded in N-doped carbon: a superior pH-universal electrocatalyst outperforms benchmark Pt for the hydrogen evolution reaction. *Journal of Materials Chemistry A* **2020,** *8* (25), 12810-12820.

21. Graham, L.; Collins, G.; Holmes, J. D.; Tilley, R. D., Synthesis and catalytic properties of highly branched palladium nanostructures using seeded growth. *Nanoscale* **2016,** *8* (5), 2867-2874.

22. Huang, X.; Li, Y.; Li, Y.; Zhou, H.; Duan, X.; Huang, Y., Synthesis of PtPd bimetal nanocrystals with controllable shape, composition, and their tunable catalytic properties. *Nano Lett* **2012,** *12* (8), 4265-70.

23. Wang, C.; Yin, H.; Chan, R.; Peng, S.; Dai, S.; Sun, S., One-Pot Synthesis of Oleylamine Coated AuAg Alloy NPs and Their Catalysis for CO Oxidation. *Chemistry of Materials* **2009,** *21* (3), 433-435.

24. Zhou, M.; Wang, H.; Vara, M.; Hood, Z. D.; Luo, M.; Yang, T. H.; Bao, S.; Chi, M.; Xiao, P.; Zhang, Y.; Xia, Y., Quantitative Analysis of the Reduction Kinetics Responsible for the One-Pot Synthesis of Pd-Pt Bimetallic Nanocrystals with Different Structures. *J Am Chem Soc* **2016,** *138* (37), 12263-70.

25. Watzele, S.; Hauenstein, P.; Liang, Y.; Xue, S.; Fichtner, J.; Garlyyev, B.; Scieszka, D.; Claudel, F.; Maillard, F.; Bandarenka, A. S., Determination of Electroactive Surface Area of Ni-, Co-, Fe-, and Ir-Based Oxide Electrocatalysts. *ACS Catalysis* **2019**, 9222-9230.

26. Łosiewicz, B.; Martin, M.; Lebouin, C.; Lasia, A., Kinetics of hydrogen underpotential deposition at ruthenium in acidic solutions. *Journal of Electroanalytical Chemistry* **2010,** *649* (1-2), 198-205.
27. Wei, C.; Sun, S.; Mandler, D.; Wang, X.; Qiao, S. Z.; Xu, Z. J., Approaches for measuring the surface areas of metal oxide electrocatalysts for determining their intrinsic electrocatalytic activity. *Chem Soc Rev* **2019,** *48* (9), 2518-2534.

Chapter 7

Conclusions and Future Work

7.1 Conclusions

Hydrogen can be used as an efficient fuel in fuel cells and is regarded as an energy dense, sustainable, and clean energy source. The electrochemical water splitting process is one of the most promising methods for producing hydrogen. However, the kinetically slow OER at the anode limits this reaction's efficiency as its is slower than the HER at the cathode. To overcome the challenges associated with oxygen electrocatalysis, this thesis focused on the development of both earth-abundant and noble metals branched nanoparticles as highly active and stable electrocatalysts in alkaline and acidic media, respectively, and understanding their electrocatalytic reactions that occur on these electrocatalysts. This thesis investigated three different catalyst systems for OER, including Co branched nanoparticles in alkaline media, Ru-Pd branched nanoparticles in acid, and alloyed RuCo-Pd branched nanoparticles in acid.

Co and Ru were chosen as the earth-abundant and noble metal electrocatalysts, respectively, owing to their promising catalytic activities for OER in acidic and alkaline environments. A recent study by our group has demonstrated that a cubic-core hexagonal-branch strategy is an effective way to synthesize Ru branched nanoparticles[1, 2]. The present study showed that this method could also be applied to make Co branched nanoparticles successfully and, thus, RuCo-Pd alloyed branched nanoparticles. In this study, the Fischer-Porter bottle method was proved to be an effective strategy for synthesizing both Ru and Co branched nanoparticles in the presence of H_2 as a weak reducing agent, which enabled the slow growth of the secondary metal on cubic seeds and, thereby, the formation of branches. First of all, in the synthesis of these branched nanoparticles, long-chain amines were found to be appropriate capping agents for stabilizing side facets and

promoting the growth of the second metal along the c-axis, thus allowing for the formation of branches. In addition, the precursor to seed ratio was a critical factor in the growth pattern of the secondary metal, resulting in either core-shell nanoparticles or branched nanoparticles with controlled branch sizes.

After developing the electrocatalysts, their catalytic properties were investigated in order to gain a better understanding of the catalytic reactions on the catalysts and to evaluate their catalytic performance. The branched nanoparticles exhibited improved catalytic activity and stability for OER. The highly crystalline *hcp* branches enclosed by low indexed $\{10\bar{1}0\}$ and $\{0001\}$ facets of branched nanoparticles were determined to have highly resistant to oxidation, which results in enhanced stability. Having these stable surfaces reduced the dissolution of the Ru catalyst, thus improving its stability, and provided the formation of active $Co(OH)_2$ surface on Co branches, enhancing the catalytic activity and stability of the catalyst. Furthermore, 3D branched nanoparticles exhibited improved catalytic activity due to their larger exposed surface area. It was also obtained that the catalytic activity of branched nanoparticles could be enhanced by tuning surface facets, branch number of the nanoparticles, and by designing alloyed branched nanoparticles. The following sections provide a conclusion regarding each of these three catalyst systems.

7.1.1 Co branched nanoparticles

A hypothesis described in Chapter 1.4.1 suggested that Co branched nanoparticles may provide excellent catalytic properties. Then, Chapter 3 established a synthetic protocol for synthesizing highly crystalline *hcp* Co branched nanoparticles, and Chapter 4 explored their catalytic properties. In Chapter 3, I demonstrated that a cubic-core and hexagonal growth approach could be extended to the synthesis of new *hcp* Co branched nanoparticles by optimizing the experimental conditions to grow Co branches on an Au core. It was found that the precursor to seed ratio, the type of precursor, and reaction time were critical parameters in the reaction to grow Co branches on an Au core. Co spherical and Co_3O_4 oxide nanoparticles were also synthesized for further comparison with the branched nanoparticles in electrocatalytic studies. In Chapter 4, I investigated the role of the 3D structure of the branched nanoparticles and the crystalline structure of the branches in the formation of active sites and, thus, electrocatalytic properties of OER. The Co branched nanoparticles exhibited the highest activity and stability for OER, followed by Co spherical and Co_3O_4 nanoparticles. The activity achieved with the Co branched nanoparticle is comparable to that of the noble metal nanoparticles Ir and Ru in acidic electrolytes. This improved activity is attributed to the highly crystalline *hcp* structure that retains the presence of $Co(OH)_2$ at the surface of the nanoparticles enabling the electrochemical formation of greater density of Co^{4+} active sites and 3D morphology that provides a higher surface area. These results demonstrated that designing highly crystalline branched nanoparticles with well-defined surface structures could be an effective strategy for making highly active electrocatalysts. This concept can be applied to a variety of electrocatalytic reactions that are influenced by the formation of oxide species.

7.1.2 Ru-Pd branched nanoparticles

As discussed in Chapter 1.4.2, the electrocatalytic properties of previously synthesized Ru-Pd branched nanoparticles can be improved by tuning their surface facets and branch numbers. Therefore, Chapter 2 focused on developing methodologies for synthesizing Au and Pd cubic seeds with controlled size and Ru-Pd branched nanoparticles with tunable branch length and number and Chapter 5 investigated the effect of branch number and surface facets of Ru-Pd branched nanoparticles for OER. In Chapter 3, reaction temperature and the precursor to seed ratio were first determined to be the key factors in controlling the size of seeds during a seed-mediated growth approach in an organic solution phase. The precursor to seed ratio and the seed size were further found to be critical variables for tuning branch length and branch number, respectively. Chapter 5 explored the electrocatalytic properties of the Ru-Pd branched nanoparticles with controlled branch length and branch number for OER. The specific activity of Ru-Pd branched nanoparticles with long branches was found to be 2.7 times higher than that of short branches and 4 times greater than that of the best commercially available IrO_2 nanoparticles. This greater activity can be attributed to the increased exposure of more active $\{10\bar{1}1\}$ facets (sides) compared to less active {0001} facets (base) as branch length increases. It was also observed that the specific activity decreased by 2.6 times as the number of branches was increased from 2-3 to 5. This decreased activity was likely caused by the limited accessibility of the branched nanoparticles with multi-branches to the catalytic reaction.

These results showed the importance of the control of surface facets and branch number to exploit the advantage of branched nanoparticles for OER,

and this work is applicable across a wide range of nanoparticles to engineering efficient electrocatalysts.

7.1.3 RuCo-Pd alloyed branched nanoparticles

On the basis of the discussion presented in Chapter 1.4.2, the exposure of active sites on Ru branches per area can be increased by alloying Ru with Co. Chapter 6 focused on developing RuCo-Pd branched nanoparticles consisting of RuCo branches and a Pd core and understanding the OER on the nanoparticles. A cubic-core hexagonal-branch approach in an organic solution phase was found to be an effective approach to synthesize the alloyed branched nanoparticles. Two types of alloyed RuCo-Pd branched nanoparticles were synthesized, including (i) Co distribution around the beginning of branches (RuCo-Pd-1) and (ii) Co distribution throughout branches (RuCo-Pd-2) by optimizing reaction parameters. The oxidation state of Co in the precursor and the nucleation steps were determined to be decisive parameters for enabling the growth of RuCo branches on a Pd core. In addition, a two-step reaction was used to achieve to distribute Co throughout the branches. The electrocatalytic properties of RuCo-Pd-1 and RuCo-Pd-2 were then compared to those of the Ru-Pd branched nanoparticles with long branches described in Chapter 5. RuCo-Pd-2 and RuCo-Pd 1 catalysts exhibited a 4- and 2-times greater OER activity than the Ru-Pd catalyst, respectively. This enhancement in the OER activity of the alloyed catalysts is due to the formation of new active sites on Ru branches as a result of the Co leaching during the catalytic activation. The excellent catalytic activity of RuCo-Pd is attributed to the distribution of Co throughout the branches of the catalyst, which allows the exposure of new active sites at the more accessible areas. In this study, alloying a noble metal

with a non-noble metal proved to be an effective method of exposing more active sites. This method can be further applied to different nanoparticles to design highly active electrocatalysts.

7.2 Future work

These fundamental studies enable us to gain a better understanding of OER catalysts. However, we still have a great deal more to learn about these systems. Although OER on the branched nanoparticles was evaluated in terms of catalytic activity and stability, operando analysis and computational studies are further needed to explore the mechanisms of electrocatalytic reactions on these branched nanoparticles and the changes in catalyst structures during electrocatalysis. As mentioned in Chapter 1, several studies have been conducted in order to understand the mechanism of OER on the surfaces of CoO_x and RuO_2. Thus, combining operando and computational analysis can help gain insight into the interaction between water and the surface of the nanoparticles.

In the case of Co catalysts, HRTEM characterizations are required following catalytic activity and stability tests on Co-branched nanoparticles to determine the thickness of the Co_3O_4 layer on the branches and the structural changes in the catalyst. It may be possible to enhance the catalytic activity of Co further branched nanoparticles by controlling the thickness of the oxide layer and depositing a conductive metal (Au, Pt, etc.) onto the surface. In addition, in terms of synthesis, the effect of seed material and shape can be investigated to improve the shape of Co branched nanoparticles.

The leaching of Co from the RuCo-Pd alloyed branched nanoparticles during catalytic activation significantly increased the exposure of active sites and, consequently, the catalytic activity of the catalyst. There is approximately 20 at% of Co in the branched nanoparticles. Hence, there remains a question about how the amount of Co affects the density of newly formed active sites during the electrochemical pre-treatment. Therefore, I propose the following

step to be a systematic investigation of the effect of the amount of Co on the catalytic performance.

Overall, this work demonstrated that engineering 3D bimetallic branched nanoparticles with well-defined shapes and crystalline structures could significantly improve their electrocatalytic properties for OER. For instance: (i) highly crystalline metallic hcp branches with low indexed facets improves the surface resistance to oxidation, enhancing the catalytic stability, (ii) 3D structure of branched nanoparticles enables highly exposed surface area, improving their catalytic activity, (iii) 1D branch morphology and highly crystalline surface enhance charge transfer properties, resulting in enhanced reaction kinetics and improved catalytic activities. Nevertheless, there are still further opportunities to improve the catalytic performance of 3D bimetallic branched nanoparticles and explore their use in various catalytic reactions. First, in terms of designing nanoparticles, great control over well-defined surfaces and crystalline structures of 3D branched nanoparticles can be combined with different approaches to boost their catalytic properties, such as doping heteroatoms[3, 4], creating oxygen vacancies[5, 6], and supporting single atoms on the branches[7, 8]. Furthermore, in terms of catalytic reactions, Co and Ru nanocatalysts have been proven as an efficient electrocatalyst for various catalytic reactions, including HER[9, 10], ORR[9, 10], and CO_2 reduction reaction (CO_2RR)[9, 10], and nitrogen reduction reaction (NRR)[11, 12]. Therefore the catalytic properties of Co, Ru, and RuCo branched nanoparticles can be further explored in different catalytic reactions.

7.3 References

1. Gloag, L.; Benedetti, T. M.; Cheong, S.; Marjo, C. E.; Gooding, J. J.; Tilley, R. D., Cubic-Core Hexagonal-Branch Mechanism To Synthesize Bimetallic Branched and Faceted Pd-Ru Nanoparticles for Oxygen Evolution Reaction Electrocatalysis. *J Am Chem Soc* **2018,** *140* (40), 12760-12764.

2. Gloag, L.; Benedetti, T. M.; Cheong, S.; Li, Y.; Chan, X. H.; Lacroix, L. M.; Chang, S. L. Y.; Arenal, R.; Florea, I.; Barron, H.; Barnard, A. S.; Henning, A. M.; Zhao, C.; Schuhmann, W.; Gooding, J. J.; Tilley, R. D., Three-Dimensional Branched and Faceted Gold-Ruthenium Nanoparticles: Using Nanostructure to Improve Stability in Oxygen Evolution Electrocatalysis. *Angew Chem Int Ed Engl* **2018,** *57* (32), 10241-10245.

3. Shan, J.; Ling, T.; Davey, K.; Zheng, Y.; Qiao, S. Z., Transition-Metal-Doped RuIr Bifunctional Nanocrystals for Overall Water Splitting in Acidic Environments. *Adv Mater* **2019,** *31* (17), e1900510.

4. Wang, Z.; Liu, H.; Ge, R.; Ren, X.; Ren, J.; Yang, D.; Zhang, L.; Sun, X., Phosphorus-Doped Co3O4 Nanowire Array: A Highly Efficient Bifunctional Electrocatalyst for Overall Water Splitting. *ACS Catalysis* **2018,** *8* (3), 2236-2241.

5. Ling, T.; Yan, D. Y.; Jiao, Y.; Wang, H.; Zheng, Y.; Zheng, X.; Mao, J.; Du, X. W.; Hu, Z.; Jaroniec, M.; Qiao, S. Z., Engineering surface atomic structure of single-crystal cobalt (II) oxide nanorods for superior electrocatalysis. *Nat Commun* **2016,** *7*, 12876.

6. Liu, Y.; Ma, C.; Zhang, Q.; Wang, W.; Pan, P.; Gu, L.; Xu, D.; Bao, J.; Dai, Z., 2D Electron Gas and Oxygen Vacancy Induced High

Oxygen Evolution Performances for Advanced Co3 O4 /CeO2 Nanohybrids. *Adv Mater* **2019,** *31* (21), e1900062.

7. Sultan, S.; Tiwari, J. N.; Singh, A. N.; Zhumagali, S.; Ha, M.; Myung, C. W.; Thangavel, P.; Kim, K. S., Single Atoms and Clusters Based Nanomaterials for Hydrogen Evolution, Oxygen Evolution Reactions, and Full Water Splitting. *Advanced Energy Materials* **2019,** *9* (22).

8. Shan, J.; Ye, C.; Chen, S.; Sun, T.; Jiao, Y.; Liu, L.; Zhu, C.; Song, L.; Han, Y.; Jaroniec, M.; Zhu, Y.; Zheng, Y.; Qiao, S. Z., Short-Range Ordered Iridium Single Atoms Integrated into Cobalt Oxide Spinel Structure for Highly Efficient Electrocatalytic Water Oxidation. *J Am Chem Soc* **2021,** *143* (13), 5201-5211.

9. Zhao, M.; Xia, Y., Crystal-phase and surface-structure engineering of ruthenium nanocrystals. *Nature Reviews Materials* **2020**.

10. Yu, J.; He, Q.; Yang, G.; Zhou, W.; Shao, Z.; Ni, M., Recent Advances and Prospective in Ruthenium-Based Materials for Electrochemical Water Splitting. *ACS Catalysis* **2019,** *9* (11), 9973-10011.

11. Yang, B.; Ding, W.; Zhang, H.; Zhang, S., Recent progress in electrochemical synthesis of ammonia from nitrogen: strategies to improve the catalytic activity and selectivity. *Energy & Environmental Science* **2021,** *14* (2), 672-687.

12. Liu, D.; Chen, M.; Du, X.; Ai, H.; Lo, K. H.; Wang, S.; Chen, S.; Xing, G.; Wang, X.; Pan, H., Development of Electrocatalysts for Efficient Nitrogen Reduction Reaction under Ambient Condition. *Advanced Functional Materials* **2020,** *31* (11).